UNIVERSITY OF CALIFORNIA

Los Angeles

External Asymmetric Forcing of Convectively Unstable Transverse Jets

A dissertation submitted in partial satisfaction

of the requirements for the degree

Doctor of Philosophy in Aerospace Engineering

by

Andrea Celeste Besnard

2019

ABSTRACT OF THE DISSERTATION

External Asymmetric Forcing of Convectively Unstable Transverse Jets

by

Andrea Celeste Besnard
Doctor of Philosophy in Aerospace Engineering
University of California, Los Angeles, 2019
Professor Ann R. Karagozian, Chair

This work describes the experimental exploration of the influence of external asymmetric excitation on the equidensity gaseous jet in crossflow (JICF). Asymmetric forcing was applied via an array of speakers flush mounted around the exterior of the jet exit, each embedded in the injection wall of the wind tunnel. The speakers were individually operated with sinusoidal temporal excitation at differing phases with respect to one another, allowing for controlled directional azimuthal forcing about the jet exit, for example, in counterclockwise or clockwise directions, and with variable forcing amplitudes and frequencies. Operation of one, two, or all four speakers was explored here in terms of the influence of local or more circumferential asymmetric excitation on transverse jet response. The amplitudes of pressure perturbation were very low as compared to previous axisymmetric forcing studies by Shoji (2017) and Shoji et al. (2019c), in many cases by at least an order of magnitude. There was a special focus here on high jet-to-crossflow momentum flux ratios (e.g., $J = 61$ and 41), which are known to have a convectively unstable upstream shear layer (USL) and to create asymmetric cross-sections with typically poorer mixing characteristics (Gevorkyan et al., 2016) than for lower J values with an absolutely unstable USL.

The results of hotwire-based spectral measurements in the transverse jet's upstream shear layer revealed that asymmetric forcing at a frequency f_f within the fundamental range of the jet USL instability created a strong lock-in of the USL to the forcing frequency, as expected,

whereas excitation at frequencies f_f further from f_o required higher amplitude excitation for clear lock-in. Similar to sinusoidal excitation studies on the free jet (Li and Juniper, 2013c) and JICF subject to axisymmetric forcing (Shoji et al., 2019b), quasiperiodic behavior on the run-up to lock-in was observed for forcing cases outside the fundamental range. While forcing frequencies below the fundamental tended to enable lock-in for sufficiently high amplitudes, for forcing frequencies f_f that were well above f_o, as f_f approached $2f_o$, the jet USL did not lock-in to the external forcing, even at relatively high pressure perturbation amplitudes. Additionally, differing shear layer responses were often observed when employing different directional forcing strategies for a fixed forcing frequency f_f and amplitude P', suggesting a different susceptibility to clockwise and counter-clockwise orientations of flow perturbation and thus differing rates of growth of asymmetric instabilities under these high J conditions.

Acetone planar laser induced florescence (PLIF) imaging showed that asymmetric forcing at frequencies near the fundamental frequency associated with the USL can greatly influence jet cross-sectional structure. In many cases such forcing creates enhanced symmetrization of the counter-rotating vortex pair (CVP), more typical of transverse jets at lower J values and a naturally absolutely unstable USL. Symmetrization of the jet cross-sectional structure at high J values with asymmetric forcing was associated with improvements in molecular mixing, as had been seen for the unforced JICF at low J values (Gevorkyan et al., 2016). For all forcing conditions in which 1:1 lock-in of the USL occurred, mixing was generally enhanced in both the centerplane and cross-sectional views. Moreover, results in this study show that in general, asymmetric forcing enhanced mixing to some degree, even in instances when the USL was known to exhibit quasiperiodic behavior or was not locked-in to the asymmetric forcing. Yet cases where the USL was locked-in to the forcing virtually always provided better mixing enhancement (lower Unmixedness) than cases where the USL exhibited quasiperiodic behavior in the USL in response spectra, or cases which were neither locked-in or quasiperiodic.

Simultaneous acetone PLIF and stereo particle image velocimetry (PIV) measurements quantified the interaction of the transverse jet's velocity field and scalar concentration field in

response to asymmetric forcing for the $J = 41$ condition. Asymmetric forcing clearly demonstrated influence on the flowfield velocity and a moderate influence on the local associated strain rate, primarily causing the spatial rate of increase in local strain rate to occur closer to the jet exit than in the absence of forcing. Cross-sectional PLIF/PIV results showed small natural asymmetries in both the mean vorticity field and mean scalar concentration field at the upstream edge of the jet orifice, and that asymmetric forcing influenced these natural structures in different ways, depending on the orientation and localization of the excitation.

Proper orthogonal decomposition (POD) analysis of the transverse jet's near-field scalar and velocity fields was performed, and the phase space of POD mode coefficients was mapped for dominant modes associated with in a given forcing condition. Hence the dynamics of a larger region than just the upstream shear layer could be quantified here. Sometimes, coherent shapes emerged from the POD coefficient phase space, and those shapes strongly resembled a variety of strange attractors, potentially representing non-periodic solutions. All forcing cases which produced strange attractor-like structures had a strongly locked-in upstream shear layer. Other groups (Bonetti and Boon, 1989; Williams-Stuber and Gharib, 1990; Aref et al., 1987; Guzman and Amon, 1994; Guan et al., 2018) have found evidence for strange attractors in other flowfields in the run-up to chaotic behavior, which may suggest that the asymmetric forcing cases for the transverse jet in which coherent phase space shapes appear may be associated with a transition of the flow, especially but not exclusively in the transverse jet's upstream shear layer.

Overall, then, asymmetric perturbations of the flow in the vicinity of the exit of the flush-injected transverse jet can have a substantial impact on many key aspects of jet behavior: the dynamical character of the upstream shear layer and near-field dynamics, the jet centerplane and especially cross-sectional structure, and molecular mixing characteristics of the jet. This study provides evidence of the rich potential that strategic asymmetric perturbations can provide in both understanding and controlling key features of the transverse jet, opening new questions worthy of future exploration.

The dissertation of Andrea Celeste Besnard is approved.

John Kim

Robert Thomas M'Closkey

Joseph M. Teran

Ann R. Karagozian, Committee Chair

University of California, Los Angeles

2019

TABLE OF CONTENTS

LIST OF FIGURES

LIST OF TABLES

ACKNOWLEDGMENTS

I sincerely appreciate the support I have received during my time here at UCLA, which enabled me to pursue my ambitions. I would like to thank my advisor Professor Ann Karagozian for her encouragement and guidance, and for lessons that extend far beyond the classroom or laboratory. I would like to thank my committee members Professors John Kim, Robert M'Closkey, and Joseph Teran for their input on this work, as well as Professor Owen Smith for his endless ideas on experimental techniques. I would also like to thank Professor Leo Alves for inspiring new ideas on this research.

My labmates in the Energy and Propulsion Research Laboratory have contributed technical ideas and assistance. A special thank you to Elijah Harris for being such a great research partner over the last four years. Thank you to Levon, Takeshi, Dario, John, Andres, Miguel, Sal, Stephen, Richard, Ayaboe, Sim, David, and Aly for years of input and smiles. I would like to acknowledge Michael Andonian for his contributions to the waveform control circuit.

Thank you to my friends and family. I could not have completed this work without the support of my husband Eric, who encouraged me when I needed it, and knew when to just listen. Thank you to the older girls who pitched in too. Most of all I would like to thank my young daughters, who made the adventure of having two babies while in grad school equally easier and as difficult as it sounds.

Thank you to Mr. Foster Stanback for his generous donation to the Energy and Propulsion Research Lab, which contributed to the purchase of test equipment used extensively in this research.

I was supported by the Department of Defense (DoD) through the National Defense Science & Engineering Graduate Fellowship (NDSEG) Program, as well as by the Eugene V. Cota-Robles Fellowship.

Financial support for this project has come from the National Science Foundation under grants CBET-1437014 and from the Air Force Office of Scientific Research under grant FA9550-15-1-0261.

VITA

2007	NASA/Space Grant Summer Scholarship Recipient
2007-2008	Undergraduate Research Assistant, California State University Foundation, Long Beach
2009	B.S. (Aerospace Engineering), California State University, Long Beach. A.E. Outstanding B.S. Graduate Recipient
2009-2013	Development Engineer, SpaceX, Hawthorne, CA. Spacecraft Propulsion Components, Responsible Engineer (RE)
2012	NASA JSC Acheivement Award, Member of SpaceX Dragon Demo Flight Control Team
2013-2014	Development Engineering Manager, Flight Works, Inc., Irvine, CA
2014-2019	Fellowship, Eugene V. Cota-Robles, UCLA
2015-2018	Fellowship, National Defense Science and Engineering Graduate (NDSEG)
2017	M.S Aerospace Engineering, UCLA

PUBLICATIONS AND PRESENTATIONS

A. Besnard, T. Shoji, S. T. Schein, E. W. Harris and A. R. Karagozian. Exploration of Asymmetric Forcing on Mixing and Structural Characteristics for Transverse Jets. AIAA SciTech Forum, San Diego, CA 2019. DOI: 10.2514/6.2019-0321

T. Shoji, A. Besnard, E. W. Harris, R. T. M'Closkey and A. R. Karagozian. Effects of axisymmetric square-wave excitation on transverse jet structure and mixing. *AIAA Journal*, 2019. DOI: 10.2514/1.J057982

A. Besnard, T. Shoji, E. W. Harris, R. T. M'Closkey and A. R. Karagozian. Exploration of Asymmetric Forcing on Mixing and Structural Characteristics for Transverse Jets, presented at the 70$^{\text{th}}$ APS/DFD Meeting, Denver, CO, November 2017.

A. Wilson (Besnard), J. Clark, E. Besnard, and M. Baker. CFD Analysis of a Mulit-Chamber Aerospike Engine in Over-Expanded, Slipstream Conditions. *Paper AIAA-2009-5486*, 2009

A. Wilson (Besnard), C. Bostwick, E. Besnard, and R. Shinavski. Ceramic Matrix Composite as Liners for Improved Ablative Chambers. *Paper AIAA-2009-5478*, 2009

CHAPTER 1

Introduction and Background

The transverse jet, also called jet in crossflow (JICF), consists of a fluid jet having mean velocity U_j injected perpendicularly or at an angle with respect to a crossflow of velocity U_∞. Example variants on the fundamental transverse jet system include: combinations on fluid phase, such as gaseous jet injected into gas crossflow, or liquid jet into a crossflow of liquid or gas; reactions within the flowfield; supersonic and compressible flows; or jets with varying geometric shapes and injection configurations.

The jet in crossflow appears in many energy, propulsion, and environmental control applications, most of which desire either enhanced or suppressed mixing of the fluids (Margason, 1993; Karagozian, 2010). In space technology jets in crossflow have been utilized in liquid rocket engines for thrust vector control by deflection of the flow within the nozzle, in preburner diluent injection systems, and in liquid fuel film cooling to reduce nozzle wall temperatures and heat flux (Terry and Caras, 1966). Additional cooling applications where transverse jets have been employed include in gas turbine combustors for dilution air jet injection to control temperature pattern factor and/or NOx emissions, and high pressure turbine blade fuel film cooling. In the latter case, arrays of JICF injectors create a cool boundary layer along the blades, enabling improved temperature uniformity, reduction in local temperature hotspots, improved efficiency, reduced fuel consumption, and prolonged blade lifetime (Vermeulen et al., 1992). Contrary to film cooling applications where low jet penetration into crossflow and delayed mixing is desired, transverse jets are utilized as fuel injectors in high speed combustion of ramjets and scramjets, where enhanced, rapid mixing as well as deep penetration are desired to facilitate stable combustion. For most propulsion system applications, if a more deeply penetrating jet is utilized, enhanced mixing is sought,

while for applications where a low degree of penetration is sought, e.g., for film cooling, enhanced mixing is not as much desired as is surface cooling.

1.1 Jet in Crossflow Characteristics

The varied jet interactions produced by the injection of the transverse jet generates complex flow structures as in Figure 1.1, where the coordinate system shown is identical to the coordinate system of the current study. The jet upstream shear layer (USL) trajectory is defined in terms of the parameter s, and the trajectory of the jet centerline, s_c, is determined by applying a best fit power-law curve (Margason, 1993) to the loci of maximum jet fluid concentration in the vertical column of the jet mean centerplane image, as described by Gevorkyan et al. (2016).

Non-dimensional parameters commonly used to characterize the transverse jet include the jet-to-crossflow density ratio $S = \rho_j/\rho_\infty$, jet-to-crossflow velocity ratio $R = U_j/U_\infty$, and the jet-to-crossflow momentum flux ratio $J = \rho_j U_j^2/\rho_\infty U_\infty^2$. Other parameters which characterize various features of the transverse jet interactions and behaviors include jet Reynolds number based on jet diameter D, $Re_j = U_j D/\nu$, momentum thickness of the upstream region of the jet θ_j, the crossflow boundary layer thickness θ_∞ and Strouhal number $St_o = f_o D/U_j$ where f_o is the natural frequency of the jet's upstream shear layer instability. A corresponding St_f based on a forcing frequency f_f is also used in the present study. Each of these parameters play roles in the transverse jet trajectories, mixing, and penetration, enabling the optimization of molecular mixing for specific fixed flow conditions.

The transverse jet flowfield is dominated by vortical structures identified in Figure 1.1 including the counter-rotating vortex pair (CVP) associated with the jet cross-section (Cortelezzi and Karagozian, 2001), ring-like shear layer vortices, wrap-around horseshoe vortices, and upright wake vortices known to draw wall boundary layer fluid into the jet (Fric and Roshko, 1994). The CVP dominates the jet cross-section in the far-field, and its structure is of interest to the current study. The CVP is thought to form via rollup of the upstream shear

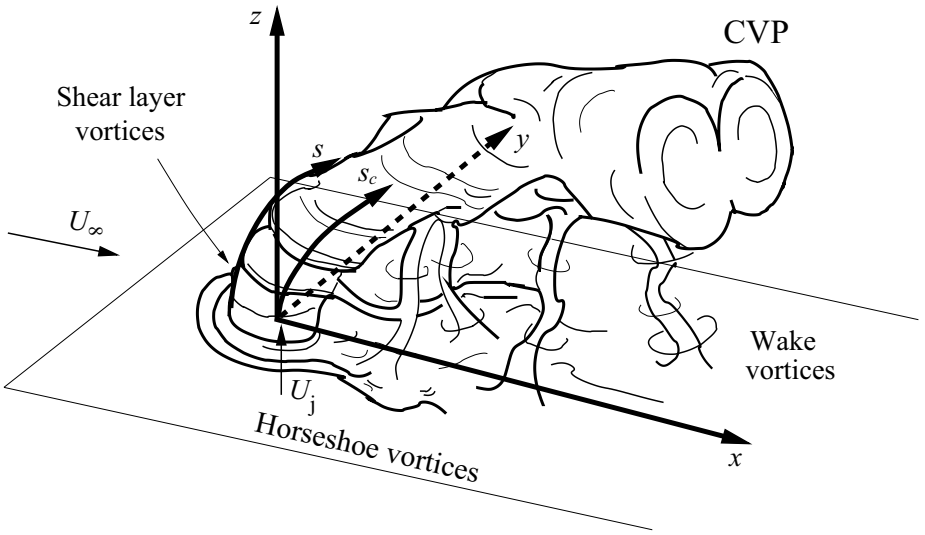

Figure 1.1: Schematic of the flush injected transverse jet and associated vortical flow structures. Orientation of coordinate axes x, y, z, jet upstream shear layer trajectory s, and jet centerline trajectory s_c are shown. Adapted from Fric and Roshko (1994).

layer and distortion by the crossflow, initiating in the jet near-field, and becoming more dominant in the farfield. The CVP is thought to promote entrainment of crossflow fluid into the jet, thereby enhancing mixing as compared with the free jet in quiescent surroundings (Moussa et al., 1977; Kelso et al., 1996; Cortelezzi and Karagozian, 2001; Karagozian, 2010). Horseshoe vortices are also formed in the jet near-field, wrapping around the jet similar to a flow past a cylinder, and observed to have modes which are steady, oscillatory, or coalescing, depending on flow conditions such as Re and R (Kelso and Smits, 1995). Wake vortices, which appear as tornado-like upright structures in the jet downstream, have been attributed to separation of the wall boundary layer, resulting in boundary layer fluid begin drawn upwards into the jet (Fric and Roshko, 1994; Smith and Mungal, 1998). The rolled-up shear layer vortices have been thought by some to be generated by a Kelvin-Helmholtz instability (Kelso et al., 1996; Yuan and Street, 1998), however recent evidence suggests the interaction is far more intricate, and the upstream shear layer instabilities have been the focus of many studies by our group (Megerian et al., 2007; Davitian et al., 2010a; Getsinger et al., 2012, 2014). The behavior of the USL instabilities and their response to external forcing are fundamentally influential in the current study.

1.2 Shear Layer Instabilities in the Transverse Jet

The evolution of the upstream shear layer vortices in the transverse jet have been thought to contribute significantly to development of the CVP (Kelso et al., 1996; Cortelezzi and Karagozian, 2001). Upstream shear layer stability characteristics enable an understanding of shear layer dynamics and, ultimately, JICF structure. In open system shear flows which are spatially developing, such as the JICF, the instability can be characterized as either local or global within the flowfield, and as either absolutely unstable, convectively unstable, or in a state of transition between the two (Huerre and Monkewitz, 1990). A flow instability which is considered to be absolutely unstable (AU) is one in which a disturbance becomes self-sustained, spreading the disturbance upstream and downstream and behaving as a dynamical oscillator. A convectively unstable (CU) shear flow is one in which the disturbance is amplified as it is advected downstream, and hence is classified as a dynamical amplifier.

Early studies by our group (Megerian et al., 2007) utilize hotwire anemometry to explore spectral based characteristics of the JICF upstream shear layer for the equidensity jet (emanating from either a flush nozzle or elevated nozzle) for velocity ratios in the range $1.15 \leq R \leq \infty$. For a fixed jet Reynolds number, as velocity ratio R, and therefore J, is reduced, the nature of the spectra changes, as shown in Figure 1.2 for the flush nozzle injected nitrogen jet into a crossflow of air. For the free jet, when $R \rightarrow \infty$ as in (a) and (b), no significant disturbances were observed near the jet exit plane ($s/D = 0$), while weak amplitude oscillations spanning a broadband frequency range began to develop at approximately $s/D = 3.0$. In the presence of a crossflow, transverse jets with high R or J values such as $R = 6.4$ or $J = 41$ in Figure 1.2 (c-d), have a convectively unstable upstream shear layer, with developing oscillations in a broadband frequency range around f_o, downstream development of a "preferred mode" near a subharmonic of f_o, and higher harmonics. In this flow regime ($R \gtrsim 3.1$), tonal interference between the hotwire probe and strengthening shear layer instabilities creates frequency shifting in the broadband range around f_o, as seen in the dominant disturbance which develops at $s/D \approx 2.0$ in 1.2 (d), which is notably closer to the jet exit than the initiation of the disturbance for the free jet.

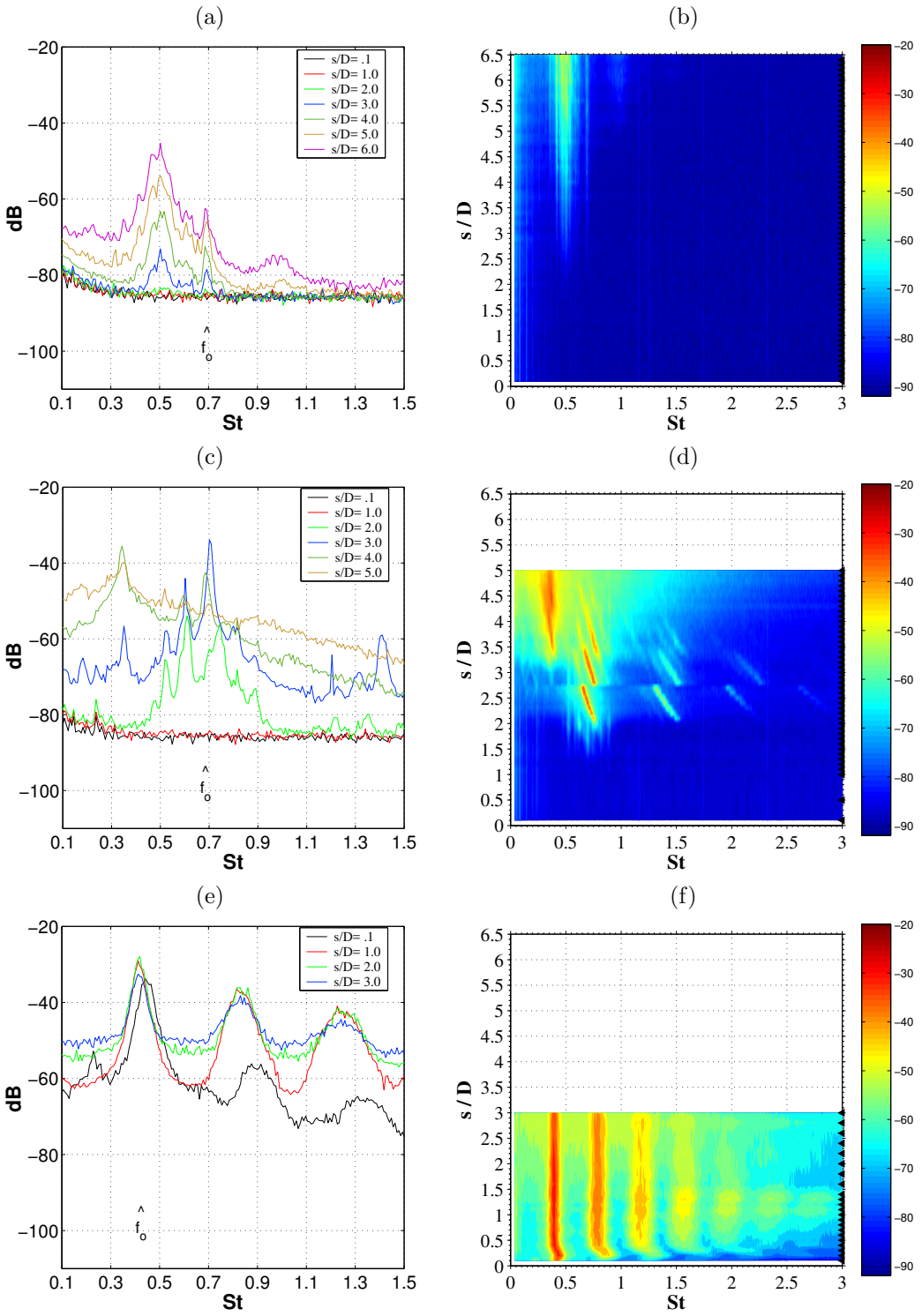

Figure 1.2: Power spectra plots of vertical velocity disturbances along the USL coordinate s for the unforced equidensity flush nozzle injected $Re_j = 2000$ Nitrogen jet for velocity ratio (a,b) $R = \infty$, (c,d) $R = 6.4$, (e,f) and $R = 1.15$. Left column represents power spectra at discrete s/D USL trajectory locations. Right column represents spectral contour maps with 0.1 s/D spatial resolution with color bar indicating disturbance amplitude in dB. From Megerian et al. (2007).

When one increases the crossflow velocity U_∞ at a fixed Re_j, strong, pure tone disturbances at f_o initiate close to the jet exit and persist along the upstream shear layer trajectory, consistent with an absolutely unstable shear layer, as demonstrated in Figure 1.2 (e-f) for $R = 1.15$. There are clear higher harmonics of the fundamental frequency f_o, and reduction of the energy transfer from fundamental f_o to the subharmonic (Davitian et al., 2010a) as well as evidence of a Hopf bifurcation near $R_{cr} = 3.1$. For low density transverse jets, the transition from convective to absolute instability is observed for $S \lesssim 0.4$ or $J \lesssim 10$ (Getsinger et al., 2012). Absolutely unstable flows are known to be resistant to applied excitation, depending on the regime, while convectively unstable flows can be altered more readily with low level axisymmetric excitation (Megerian et al., 2007; Davitian et al., 2010a; Getsinger et al., 2012).

Computational studies on the transverse jet shear layer instabilities have also been performed to investigate the nature of the dominant disturbances in the USL. Direct numerical simulation (DNS) was performed in exploring the $R = 2$ (AU), and $R = 4$ (CU) transverse jets (where $Re_j = 2000$) in the study by Iyer and Mahesh (2016), corresponding to conditions of the experimental study by Megerian et al. (2007). The simulations reproduce the USL instability, and compare the experimental data to the USL vertical velocity power spectra of the numerical results at discrete s/D USL trajectory locations. For $R = 2$ the dominant instability recovered was found to agree with the results of Megerian et al. (2007) remarkably well, where $St_o = 0.65$. For $R = 4$, the frequency of the dominant disturbance was seen to shift over the evolution of the USL trajectory, qualitatively similar to what has been observed for the CU JICF. Dynamic mode decomposition (DMD) of the DNS-generated flowfield enabled exploration of dominant instability modes under various flow conditions and in various regions of the flowfield. LSA of the transverse jet, again incorporating mean data from the DNS, by Regan and Mahesh (2019) show that the dominant modes of the $R = 4$ and $R = 2$ JICF are indeed shear layer modes, whose frequencies agree with previous experiments and simulations of the same flow conditions (Megerian et al., 2007; Iyer and Mahesh, 2016). Interestingly, Regan and Mahesh (2019) observed asymmetric linear stabil-

ity and adjoint sensitivity modes, which reside on the CVP. Examination of the the USL mode and asymmetric mode growth rates suggest that asymmetric modes and sensitivity to experiential asymmetries are more significant for the convectively unstable JICF than the absolutely unstable case.

1.3 Jet Structure and Mixing Studies

Structural aspects of the JICF are affected by the USL stability characteristics, as observed via laser diagnostics in experiments at UCLA (Getsinger et al., 2014) and also as suggested in recent simulations by Regan and Mahesh (2019). Acetone planar laser-induced fluorescence (PLIF) imaging of the gaseous jet in crossflow by Getsinger et al. (2014), Figure 1.3 (a), shows that in the instantaneous centerplane ($x-z$) images, the rolled up vortical structures on the upstream shear layer of the jet are clearly seen. As the momentum flux ratio J is reduced, initiation of clear vortex roll up occurs closer to the jet exit, eventually initiating nearly at the jet exit plane for $J = 3$[1]. This is consistent with the upstream shear layer power spectral data (Megerian et al., 2007), where the pure tone disturbance moves closer to the jet exit as R or J are reduced. Mean acetone PLIF cross-section images in the $y-z$ plane capture out-of-plane structures such as the CVP at downstream location $x/D = 10.5$, shown in Figure 1.3 (b). A strongly asymmetric cross sectional vortical structure is seen quite repeatably for high J values, e.g., $J = 61$. Such asymmetries have been noted previously by other researchers at relatively high J values but typically at higher Reynolds numbers (Kamotani and Greber, 1972; Smith and Mungal, 1998; Kuzo, 1996; Narayanan et al., 2003; Shan and Dimotakis, 2006; Muldoon and Acharya, 2010). The experiments in Getsinger et al. (2014) show a relatively symmetric CVP structure when the USL is absolutely unstable. The shear layer's stability characteristics thus have an important influence on JICF structure, seen in both the centerplane and cross-sectional views.

[1]Since publication of this article, updates have been made to a flow condition calculation code for acetone PLIF imaging experiments, to properly account for acetone as a jet constituent. Values shown in this thesis reflect the updated values of flow velocity parameters (Re_j, U_j and J) corresponding to the experimental data, which we believe to be more accurate.

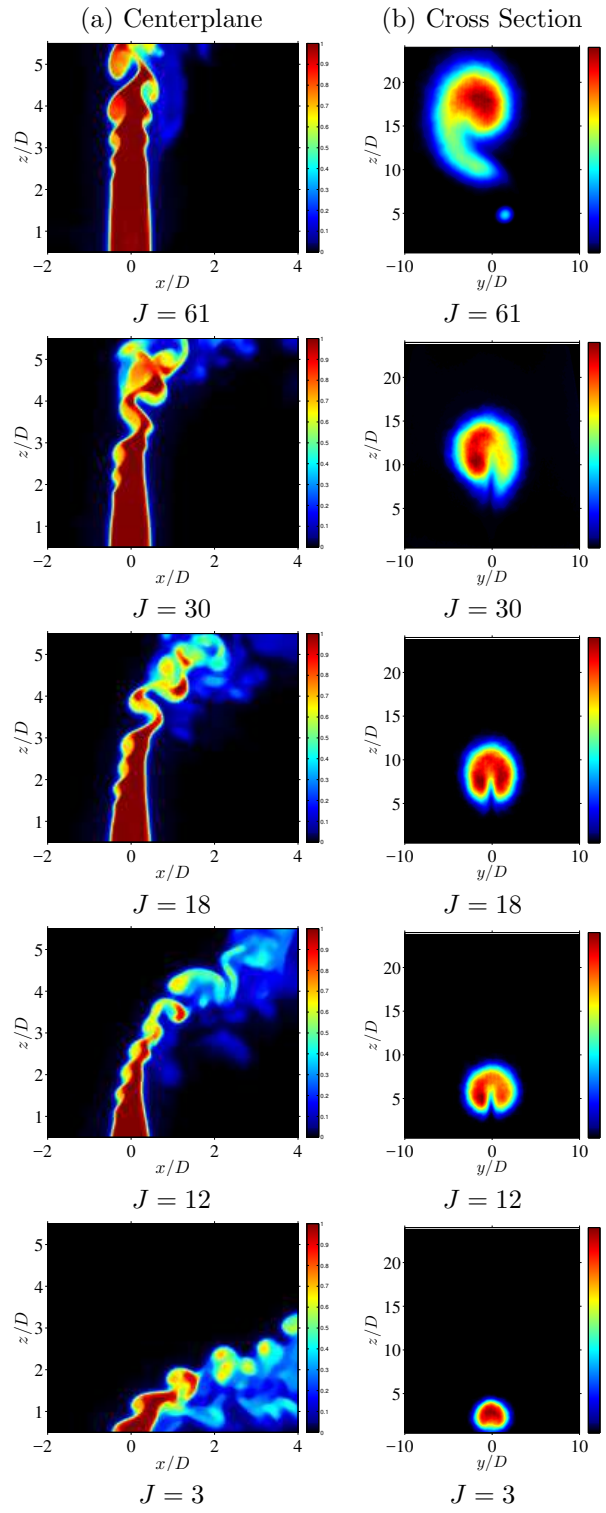

Figure 1.3: Instantaneous centerplane (a) and mean cross sectional at x/D=10.5 (b)PLIF images for the $S = 1$ $\mathrm{Re}_j = 2300$ flush nozzle injected transverse jet with various jet-to-crossflow momentum flux ratios, J. From Getsinger et al. (2014).

A number of researchers have suggested that the transverse jet enhances mixing via increased entrainment of crossflow fluid by the jet, and evolution of jet structures such as the CVP (Kamotani and Greber, 1972; Broadwell and Breidenthal, 1984; Karagozian and Marble, 1986). Relating these structural characteristics to their influence on mixing can be explored by quantifying various mixing metrics. The physical mixing process can be described from a variety of viewpoints. A simple example is the break-up of a clump of fluid to smaller scales, thus reducing the scale of segregations, or the distribution of length scales (Danckwerts, 1952). In addition to length scales, some consider the stirring, swirling, folding, rate of stretching, and striations of the concentration field in mixing quantifications (Mathew et al., 2005; Gubanov and Cortelezzi, 2010). Kukukova et al. (2009) introduce the mixing metric "exposure", which correlates the contact area between fluids, their concentration gradients, and the rate of change of the segregation into a potential-like parameter.

Global metrics such as jet penetration and spread have been traditionally used to estimate transverse jet mixing (Margason, 1993; Davitian et al., 2010a; Narayanan et al., 2003), as well as mean centerplane characteristics such as centerline concentration decay (Smith and Mungal, 1998; Gevorkyan et al., 2016). But statistical quantification of instantaneous scalar field measurements can quantify molecular mixing more accurately. As noted by Gevorkyan et al. (2016), the transport processes of the low Reynolds number flow field are mainly diffusion limited. JICF acetone PLIF data can be used to determine the scalar concentration field and thus to calculate local Unmixedness, U, as done for the transverse jet for unforced conditions by Gevorkyan et al. (2016). Unmixedness is a molecular mixing metric defined per (Danckwerts, 1952; Dimotakis and Miller, 1990; Smith et al., 1997):

$$U = \frac{1}{L_y L_z} \int \int \frac{(C/C_0 - \bar{C}/C_0)^2}{\bar{C}/C_0(1 - \bar{C}/C_0)} dydz \tag{1.1}$$

where C/C_0 is the local normalized value of scalar (acetone) concentration at a pixel element at (y,z), $\bar{C}/C_0$ is the spatial average over the domain, C_o is the concentration at the jet exit, and L_y and L_z are the length scales of the local jet interrogation area over which data are

quantified. The local U can be evaluated in both cross-sectional and centerplane views, with a matching of the mean concentration $\bar{C}$ at all locations and flow conditions achieved by altering the local interrogation area (e.g., $L_y L_z$) by adding or subtracting zero-valued pixels, thus enabling comparison of molecular mixing for different cases. The Unmixedness calculation is applied to each scaled instantaneous image at each location and then averaged over the entire data set, typically consisting of 500 images (Gevorkyan et al., 2016; Gevorkyan, 2015). A low value of Unmixedness corresponds to a more homogeneous, or well mixed field, while higher U means greater segregation of fluids and a lesser degree of molecular mixing.

The Spatial Mixing Deficiency (SMD) is defined by:

$$SMD = \left[\frac{1}{L_y L_z} \int \int \left\{ \frac{C/C_0 - \bar{C}/C_0}{\bar{C}/C_0} \right\}^2 dydz \right]^{\frac{1}{2}} \tag{1.2}$$

and is a measure of local concentration variance from the mean concentration value. Another metric, the Mix-Norm (Mathew et al., 2005; Gubanov and Cortelezzi, 2010), requires the mean value concentration, $\bar{C}/C_0$ to be subtracted from the field. The Mix-Norm is typically evaluated for variable scale lengths, not just the minimum pixel size (as in the algorithm for Unmixedness), in order to study phenomenon such as stirring. Both SMD and Mix-Norm result in similar or identical results to Unmixedness when the mean value is matched (Getsinger, 2012; Gevorkyan, 2015).

The rate at which mixing occurs is also of interest in reactive flowfields, for example. For a conserved scalar, the rate at which scalar fluctuations are destroyed, or scalar dissipation rate χ (Su and Clemens, 1999) is defined by:

$$\chi = \hat{D} \left(\frac{\partial \zeta}{\partial x_i} \right) \left(\frac{\partial \zeta}{\partial x_i} \right) \tag{1.3}$$

where ζ is the mixture fraction and $\hat{D}$ is the binary mass diffusivity. Also contributing to the

scalar mixing process is the underlying strain rate, where the strain rate is the symmetric portion of the velocity gradient tensor defined:

$$\epsilon_{ij} = \frac{1}{2}\left(\frac{\partial u_i}{\partial x_j} + \frac{\partial u_j}{\partial x_i}\right) \tag{1.4}$$

Variations in strain cause variations in the scalar dissipation rate χ and hence scalar variance, or Unmixedness. Gevorkyan et al. (2018) examined the dynamical character between the transverse jet instantaneous velocity fields and scalar concentration fields through comparison of simultaneously acquired PLIF and PIV imaging of the unforced JICF at various J values. The extraction of local scalar dissipation rates and strain rates along the jet upstream and downstream shear layers show good correspondence of these metrics for locations of shear layer vorticity roll up, demonstrating the interaction of the strain field with scalar gradients, and ultimately influencing molecular mixing of the scalar field.

1.4 Axisymmetric and Asymmetric Jet Excitation, Mixing and Dynamic Response

Forced excitation of the transverse jet has been seen to alter the flowfield, vortical structure interactions, and global (mean) mixing properties (Narayanan et al., 2003; Eroglu and Breidenthal, 2001; Johari, 2006). Earlier studies at UCLA show that axisymmetric temporal square wave excitation can create deeply penetrating vortical structures, thus increasing jet spread (M'Closkey et al., 2002; Shapiro et al., 2006). Axisymmetric forcing studies at UCLA define the amplitude of excitation as the root mean square (RMS) of the jet velocity perturbation relative, to the mean jet velocity U_j:

$$U'_{j,rms} = \sqrt{\frac{1}{T}\int_{t_1}^{t_1+T} (u_j - \bar{U_j})^2 dt} \tag{1.5}$$

where period T is the inverse of forcing frequency f_f. Smoke visualization of the JICF square wave forcing experiments by M'Closkey et al. (2002), where the amplitude of the velocity perturbation $U'_{j,rms}$ =1.7 m/s was matched across all images, are shown in Figure 1.4, demonstrating the puff-like vortical structures in (e)-(g). Making use of the knowledge of transverse jet upstream shear layer instabilities (Megerian et al., 2007; Davitian et al., 2010a; Getsinger et al., 2012) enables strategic forcing to be employed to alter and tailor the penetration and spread of the JICF Davitian et al. (2010b), quantified via smoke visualization.

Results of studies using acetone PLIF (Shoji et al., 2019c,a) demonstrate that penetration, spread, and Unmixedness can be affected by either square wave or sine wave excitation, depending on the flow conditions, e.g., J, and thus shear layer stability characteristics. These recent axisymmetric forcing studies via acoustic excitation (Shoji, 2017) investigates the influence of sinusoidal as well as square wave forcing on jet structure and mixing characteristics for various flow and excitation conditions. Results show that forcing with axisymmetric sinusoidal excitation near the $J = 61$ USL fundamental frequency range f_o = 1600-1900 Hz for the naturally convectively unstable jet ($J > 12$) with a relatively low velocity perturbation has a significant impact on the jet cross-section structure and asymmetry. The naturally asymmetric CVP, seen in Figure 1.5 (a) for the $J = 61$ JICF, can become nearly symmetric and the jet fluid concentration more evenly distributed in response to axisymmetric forcing, as seen in 1.5 (b). Interestingly, the Unmixedness for such forcing frequencies f_f which are close to the fundamental f_o also correspond to better molecular mixing, in both the centerplane (Figure 1.5 (c)) and cross-sectional plane (Figure 1.5 (d)) views. These results reinforce the traditional view that a symmetric CVP cross-sectional structure for the transverse jet leads to improved mixing over the free jet (Karagozian, 2010; Broadwell and Breidenthal, 1984). Square wave forcing, with an additional temporal pulse width as a variable, often but not always shows a correspondence between cross-sectional symmetry and mixing (Shoji et al., 2019c).

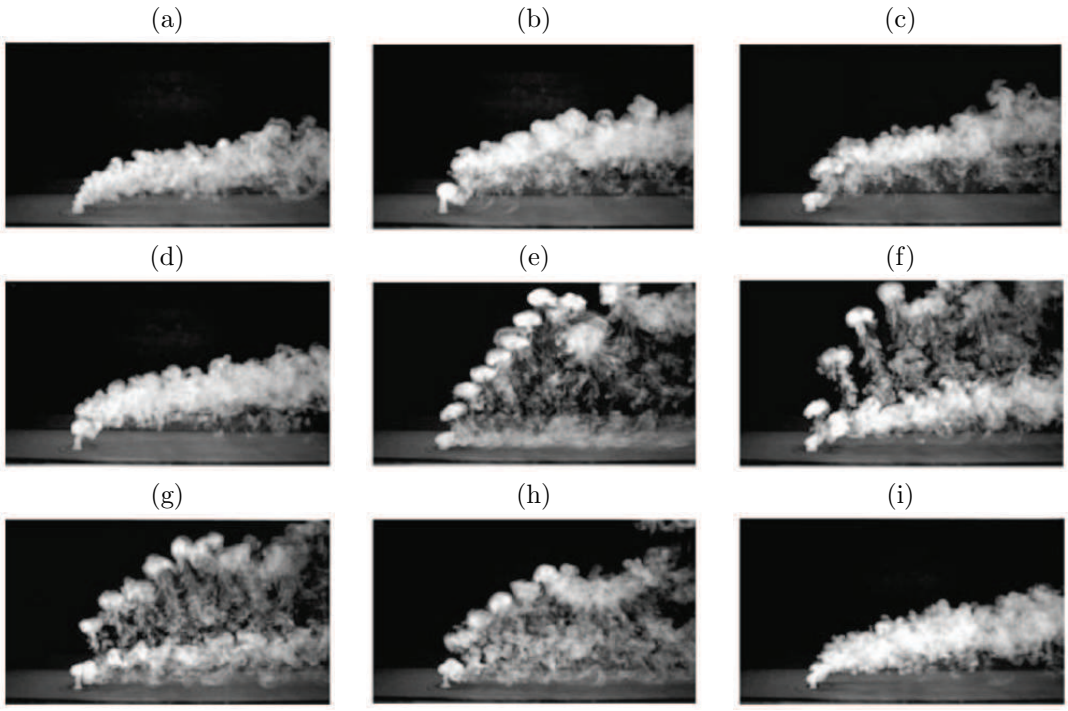

Figure 1.4: Instantaneous smoke visualization of unforced and forced jets in crossflow at jet-to-crossflow velocity ratio of $R = 2.58$, with matched root-mean-squared of jet velocity perturbation of $U'_{j,rms} = 1.7\ m/s$ amongst all excitation cases. Each image represents: (a) unforced jet, (b) uncompensated forced jet by sine wave at forcing frequency of $f_f = 735\ Hz$, (c) compensated forced jet by sine wave at $f_f = 735\ Hz$, (d) uncompensated forced jet by square wave at $f_f = 110\ Hz$ and duty cycle of $\alpha = 31$ %, (e) compensated forced jet by square wave at $f_f = 110\ Hz$ and $\alpha = 31$ %, (f) compensated forced jet by square wave at $f_f = 55\ Hz$ and $\alpha = 15$ %, (g) compensated forced jet by square wave at $f_f = 735\ Hz$ and $\alpha = 22$ %, (h) compensated forced jet by square wave at $f_f = 85\ Hz$ and $\alpha = 24$ %, and (i) compensated forced jet by square wave at $f_f = 220\ Hz$ and $\alpha = 62$ %. From M'Closkey et al. (2002)

Axisymmetric sinusoidal excitation has been studied for jets with naturally absolutely unstable shear layers, including the low density or reactive free jet (Li and Juniper, 2013c,b) and the absolutely unstable transverse jet (Davitian et al., 2010a; Getsinger et al., 2012). The studies by Shoji et al. (2019c,a) also have focused on the dependence of sinusoidal forcing frequency and amplitude as well as temporal square wave characteristics at which a jet will become influenced by such forcing. If the transverse jet shear layer is absolutely or globally unstable, an applied sinusoidal forcing frequency f_f close to the fundamental frequency f_o could lead to "lock-in" of the upstream shear layer, in which the applied excitation overtakes

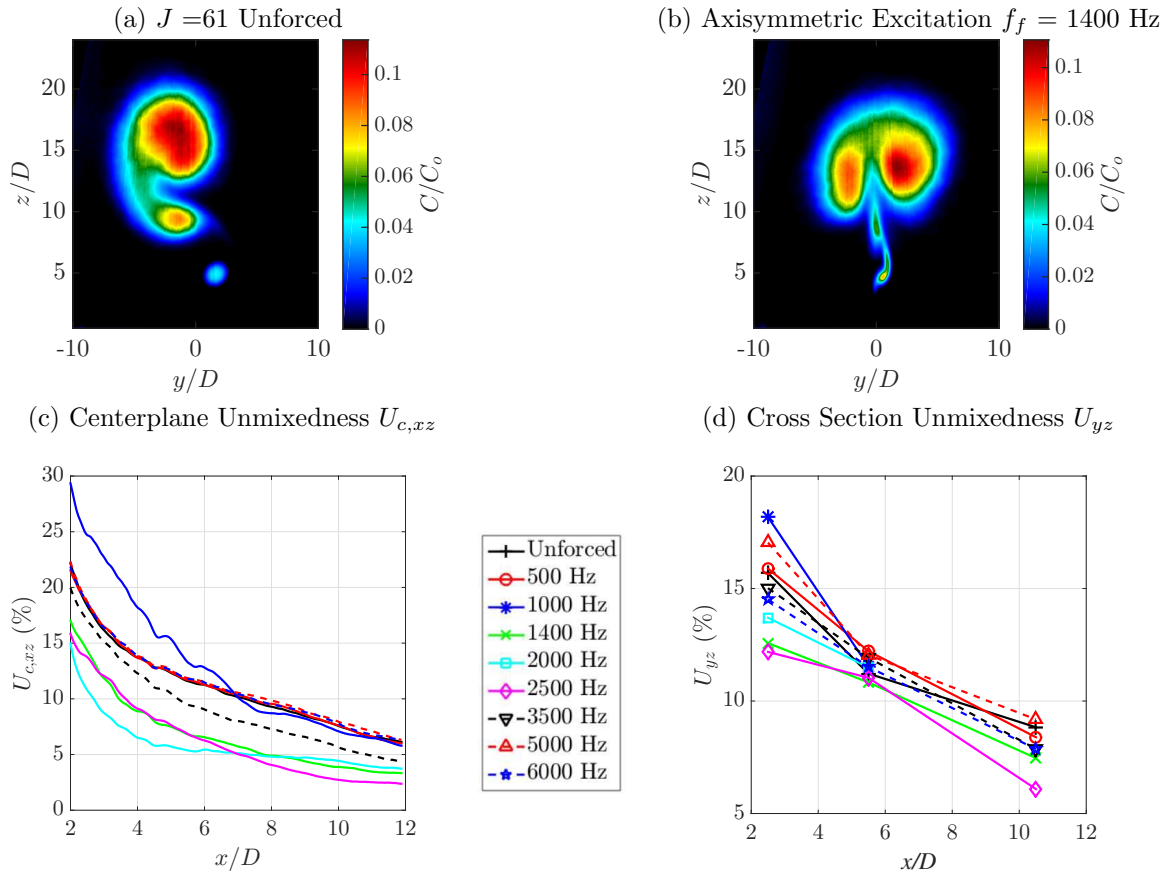

Figure 1.5: Comparison of $S = 1$, $J = 61$ JICF (a) unforced mean cross-sectional PLIF image at $x/D = 10.5$, (b) $f_f = 1400$ Hz, $U'_{j,rms} = 0.07$ m/s excitation mean cross-sectional PLIF image at $x/D = 10.5$, (c) $x - z$ centerplane-based Unmixedness $U_{c,xz}$ associated with sinewave forcing at various frequencies, $U'_{j,rms} = 0.07$ m/s, and (d) $y - z$ cross-section based Unmixedness U_{yz} associated with sinewave forcing at various frequencies, $U'_{j,rms} = 0.07$ m/s. From Shoji (2017).

the natural mode, depending on the amplitude of the applied f_f, as is commonly demonstrated for other AU flows such as wakes or low density free jets (Li and Juniper, 2013c). When the USL is naturally absolutely unstable, the shear layer becomes increasingly resistant to sinusoidal forcing, requiring a greater amplitude at a given f_f to influence the jet (Getsinger et al., 2012; Davitian et al., 2010a; Shoji, 2017), and as with other lock-in phenomena (Cohen and Wygnanski, 1987), it is found that f_f values further from the fundamental frequency f_o require a greater amplitude to achieve lock-in.

A lock-in diagram can be created showing the critical forcing condition in which the

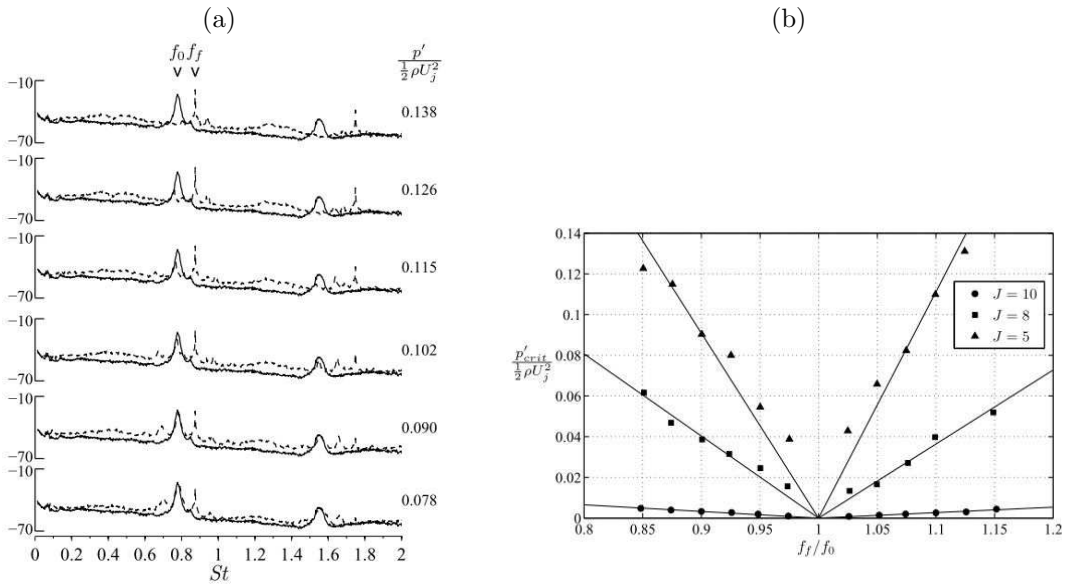

Figure 1.6: (a) Power spectra of $J = 7$, $S = 0.55$, $\mathrm{Re}_j = 2200$ jet upstream shear layer; unforced (solid line) and forced (dashed line) at $s/\mathrm{D} = 2$ for several forcing amplitudes. (b) Forcing amplitude at which lock-in is achieved for several $S = 0.55$ jets. From Getsinger et al. (2012).

applied excitation, f_f, overtakes the natural mode of the jet, f_o. Typically this diagram takes on a V shape centered about f_0 with a linear relationship between amplitude and $|f_f$ - $f_o|$, as observed in Figure 1.6 (b). The non-reactive low density transverse jet (Getsinger et al., 2012) and free jet (Li and Juniper, 2013c) appear to be more readily locked in with axisymmetric excitation below the natural frequency ($f_f < f_o$) than that above natural mode ($f_f > f_o$). For equidensity transverse jets (Shoji et al., 2019a) asymmetric lock-in diagrams with the opposite character are seen, and somewhat unexpectedly, lock-in diagrams for the convectively unstable jet are seen, with quasiperiodic behavior (as described below) in the run-up to lock-in conditions.

There are several mechanisms by which lock-in can occur. The phenomenon of lock-in is the forced synchronization of periodic oscillations, where one system influences the other, but does not experience any influence from the other system in return (Balanov et al., 2009). In the case of the transverse or free jet, the influenced system is the shear layer instability, which does not provide feedback to the forcing source, i.e. the acoustic speaker. 1:1 lock-in,

as observed by Li and Juniper (2013c) in low density free jet experiments, is a specific case of the more general $n : m$ lock-in which can occur when the forcing frequency f_f is not close to the unforced system's fundamental frequency f_o, but instead f_f is close to $\frac{n}{m}\ f_o$.

Lock-in of the frequency can be accomplished via frequency pushing/pulling, or by frequency suppression. In frequency pushing/pulling, as the amplitude of excitation is increased, the dominant frequency of the system incrementally shifts from the natural f_o to that of the forcing f_f, until they are coincident. In frequency suppression, as the amplitude of excitation is increased, the peak associated with the natural frequency f_o (almost) does not move, but becomes reduced until vanishing (Balanov et al., 2009). Although the dominant frequency can become locked-in to an external forcing source, as described above, locking of the phase between the system natural dynamics and imposed oscillation may occur. When a system is phase-locked, the difference between the instantaneous phase of the system and that of the external forcing perturbation is constant. Phase-locking requires frequency locking, but lock-in of the frequency does not require phase-locking (Li and Juniper, 2013a). A system is considered fully synchronous when both the phase and frequency are locked. Phase "trapping" occurs when the frequency is locked but the phase is not locked, where the oscillations have the same average frequency (Aronson et al., 1990; Balusamy et al., 2015). The evaluation of the synchronization and phase-locking for the current study could be enabled by diagnostics such as simultaneous time series data for both the forced system (USL instability) and the oscillator (acoustic speaker system output pressure perturbation), however as pointed out by Li and Juniper (2013a), differentiating between phase trapping and standard frequency locking requires delicate control of the experimental conditions.

Prior studies for the transverse jet (Davitian et al., 2010a; Getsinger et al., 2012; Shoji et al., 2019b) and the low density free jet (Li and Juniper, 2013c) demonstrate frequency lock-in occurs through frequency suppression, where the frequency of forcing f_f overcomes and diminishes the fundamental frequency f_o. However it has been observed by Li and Juniper (2013c) for the low density free jet and Shoji et al. (2019b) for the equidensity transverse jet that the path to lock in can include quasiperiodicity, in which two incommensurate

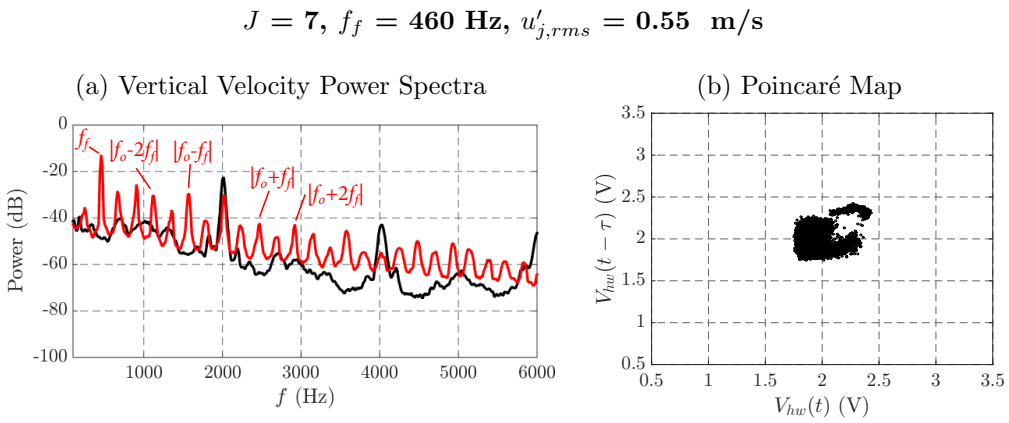

Figure 1.7: Quasiperiodic behavior of the USL demonstrated by hotwire voltage-based measurements at $s/D = 2$ for the $J = 7$ equidensity JICF subject to $f_f = 460$ Hz axisymmetric sinusoidal forcing at amplitude $u'_{j,rms} = 0.55$ m/s; (a) vertical velocity power spectra of unforced (black line) and forced (red line), and (b) Poincaré map. From Shoji et al. (2019b).

frequencies appear (f_o and f_f), as well as linear combinations of the two. Quasiperiodic behavior has been observed in other flow fields subject to excitation, such as harmonically excited cylinder wakes (Atta and Gharib, 1987; Karniadakis and Triantafyllow, 1989), where as the excitation approached the lock-in boundary, an intermediate situation develops in which the two frequencies (f_o and f_f) become of comparable importance. Quasiperiodic behavior can be observed in the frequency spectra of the system, demonstrated in Figure 1.7 (a), where multiple instances of linear combinations of f_f and f_o appear in the forcing case shown. Quasiperiodicity can also be observed through Poincaré maps such as those by Li and Juniper (2013c) and Shoji et al. (2019b), shown in Figure 1.7 (b), in which the onset of quasiperiodicity is indicated by torus birth, and lock-in the the external forcing is subsequently indicated by torus death and restoration of a fixed-point dot on the mapping. Here, the fixed point represents intersections of a periodic system through a slice of its three-dimensional phase space.

Relevant to the current study, where much of the applied external asymmetric excitation corresponds to an USL which is locked-in to an external oscillating signal, is the question of "what happens within the flowfield when the amplitude of forcing is well above that of the lock-in boundary, at a given frequency?". As noted by Guan et al. (2018), studies have

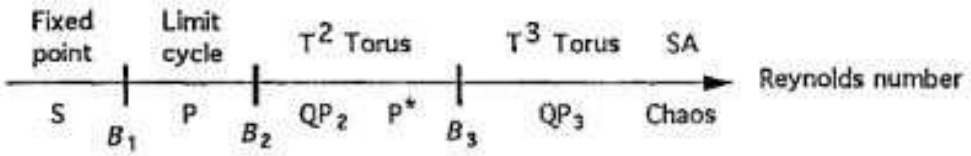

Figure 1.8: Schematic representations of successive bifurcations (B_x) leading to chaos with increasing Reynolds number in a convergent divergent channel flow, where S= steady state; P= periodic state, QP_2 = quasiperiodic regime with two incommensurate frequencies; P^* = frequency-locked periodic state; QP_3 = quasiperiodic regime with three incommensurate frequencies; SA = strange attractor. From Guzman and Amon (1994).

primarily focused exclusively on the dynamics before and en route to lock-in, not after it, perhaps on the assumption that a locked-in system will remain locked-in even with further increases in forcing amplitude. In previous studies such as by Li and Juniper (2013c), quasiperiodicity was observed as an intermittent stage of flow between states dominated by a single frequency, from f_o to f_f, on the path to lock-in. However quasiperiodicity may also be associated as an intermittent stage of flow on the path from laminar to irregular or chaotic behavior. The power spectrum of a dynamical system on this such path, as proposed by Newhouse et al. (1978), evolves as consisting of one frequency, then two and sometimes three frequencies, and the presence of a third frequency signifies that chaos should begin to appear (Ruelle and Takens, 1971). Hopf bifurcations and flow states associated with these events, as shown in Figure 1.8, are identified for the evolution of flow such as seen by Guzman and Amon (1994) in converging-diverging channel flow of increasing Reynolds number, and can in theory be applied to the forced jet system: (i) laminar steady state flow; first bifurcation; (ii) periodic flow with one fundamental frequency (f_o); second bifurcation, (iii) quasiperiodic flow with two incommensurate fundamental frequencies and their linear combinations (f_o and f_f); (iv) frequency-locked periodic state (f_f); third bifurcation, (v) quasiperiodic flow with three incommensurate fundamental frequencies and their linear combinations; and (vi) aperiodic chaotic state.

Aref et al. (1987) experimentally observed incommensurate frequencies and interesting flow patters with the transition to chaos for thin airfoil wakes. Williams-Stuber and Gharib

(1990) were the first to demonstrate three incommensurate frequencies in the transition to chaos for an open fluid system in experiments examining the wake of an airfoil when two forcing frequencies were simultaneously applied. Conversely, external forcing has been shown to transition a chaotic system to a synchronized system (Balanov et al., 2009). While Williams-Stuber and Gharib (1990) saw the appearance of three incommensurate frequencies due to a single fundamental and 2 forced modes, in a laminar pre-mixed flame Guan et al. (2018) also observes three frequencies despite periodic forcing at a single frequency f_f. In this study f_1 corresponds to the initial natural mode, and a second natural mode f_2 (which is at a lower frequency than f_1) arises alongside the natural frequency due to increased forcing at amplitudes in excess of the lock-in threshold, which combined with the f_f represent three incommensurate frequencies whose presence are consistent with Grebogi et al. (1984) for a system forced with a single external frequency. Guan et al. (2018) find that this state, which has the coexistence of three incommensurate frequencies (and their linear combinations), corresponded to an aperiodic chaotic state, associated with a strange attractor, whose properties will be further discussed in the results of Chapter 5. Furthermore, Guan et al. (2018) conclude that when the forcing amplitude is sufficiently higher than that required for onset of lock-in, the system does not necessarily remain locked-in but can transition to other, more complex states.

1.5 Helical Mode Studies

Given the evidence that forcing can act to make the JICF cross-section more symmetric, which in turn can improve molecular mixing, it is of interest to explore the effect of asymmetric (external helical) forcing of the jet at a low to moderate amplitude, especially for the JICF at larger momentum flux ratios (eg., $J \geq 30$) where the cross-section is naturally asymmetric for a flush nozzle-injected jet (Getsinger et al., 2014). The present experimental study focuses on such asymmetric excitation, making use of the knowledge of stability characteristics of shear layers associated with both free and transverse jets. Studies on the stability modes, m, of free jets investigate azimuthal, spinning, and helical modes (Batchelor

and Gill, 1962; Mattingly and Chang, 1974; Plaschko, 1979; Leibovich, 1983; Strange and Crighton, 1983; Gallaire and Chomaz, 2004) via linear stability analysis (LSA), where the axisymmetric stability mode is $m = 0$ and the first helical modes are $m = \pm 1$, in which one wavelength travels azimuthally, with a positive wave number m traversing in the clockwise direction (Kusek et al., 1990). Experiments in Gursul (1996) note that azimuthal forcing of the free jet induces helical and radial velocity fluctuations due to non-uniformity around the jet, exciting the helical first mode and enhancing jet spread. Kusek et al. (1990) utilize twelve mini speakers to excite helical modes by varying amplitude in the azimuthal direction, while Cohen and Wygnanski (1987) in earlier studies use eight azimuthal speakers designed to blow air through narrow slits around the lip of the jet nozzle. They see that when the axisymmetric mode is excited, but not simultaneously with the helical mode, higher amplification rates for the $m = +1$ mode as compared to the m = -1 are observed, indicating a potential preference for the +1 azimuthal mode in the free jet. Additional studies in Cohen and Wygnaski (1987) in which axisymmetric $m = 0$ and helical m = -1 modes are excited simultaneously at subharmonics of each other show the azimuthal mode to gain energy from the excitation, indicating nonlinear interaction between the two disturbance modes. Other studies by Corke and Kusek (1993) show that weak helical excitation with axisymmetric perturbations can lead to subharmonic helical mode amplification.

While the studies discussed above are for free jets ($J \rightarrow \infty$), LSA by our group shows for $R > 3$, that the transverse jet instabilities can be fundamentally different from those for the free jet, even for very weak crossflows (Alves et al., 2007, 2008). Due to the presence of the crossflow, the shear force from the axial jet flow and circumferential flow about the jet gives rise to transverse jet instabilities when viscous effects are represented (Alves et al., 2008), with the axisymmetric mode first becoming destabilized before the helical modes, where the axisymmetric mode is thus the most unstable. The growth rates and Strouhal numbers for the $m = 0$ mode are qualitatively and quantitatively consistent with the experimental measurements by Megerian et al. (2007), where the instability is strengthened with increased crossflow velocity as the jet approaches absolutely unstable conditions while still convectively

unstable. The inviscid stability analysis shows that the positive and negative helical modes in the JICF have different spatial growth rates (Alves et al., 2007), although the differences are small. This suggests a potential lack of symmetry in the instability evolution of the transverse jet at high J values, which could suggest reasons for the experimentally observed CVP asymmetries in the jet cross-section (Getsinger et al., 2014). Direct numerical simulations by Regan (2018) suggest similar types of USL symmetries for a convectively unstable condition (R = 4).

1.6 Current Study

The current study is directed at investigating the effect of external helical mode forcing on the transverse jet via acoustic excitation, where the resulting influence on jet structure and mixing are of interest. For the free jet, helical forcing enhancing the helical mode instabilities is observed to be the key to entrainment and enhanced mixing (Gursul, 1996). The intent of the present research is to employ similar asymmetric helical forcing for the JICF, potentially exciting the $m = \pm 1$ modes at various amplitudes, frequencies, and orientation of perturbation. The $J = 61$, $S = 1$ flush injected transverse jet is the primary focus here, as it has a highly asymmetric cross-section as well as poorer mixing characteristics than absolutely unstable jets with a more symmetric cross-sectional CVP structure (Gevorkyan et al., 2016). It is of interest to examine influences external asymmetric forcing has on the stability character of the JICF USL, centerplane and cross-sectional view structural changes, as well as molecular mixing and associated phenomenon such as strain and scalar dissipation rate, induced by the helical excitation, as part of a larger study on strategic control of the transverse jet.

CHAPTER 2

Experimental Setup and Equipment

2.1 Wind Tunnel and Flow Control

The transverse jet experimental study was conducted in a low speed wind tunnel whose general setup is shown in Figure 2.1. A radial centrifugal industrial fan (New York Blower Company size 125 Compact GI fan), driven by a speed adjustable AC motor (Baldor Industrial M3546T-8) was controlled by a variable frequency drive (ABB ACS355-03U-04A7-2), using laboratory air to generate the crossflow. The crossflow stream passed through honeycomb flow straighteners and screens to condition the flow before entering a 9:1 area ratio contraction section. This configuration had the capacity to generate crossflow speeds ranging from $U_\infty = 1.0$ m/s to 7 m/s. For a fixed Reynolds number, varying the crossflow velocity was the means of controlling J or R in this experiment, depending on the density of the jet fluid. The crossflow entered a 80 cm x 12 cm x 12 cm test section where the transverse jet issued perpendicularly. The test section floor had a 22 cm x 9 cm removable portion which enabled multiple and varied test configurations within the overall wind tunnel framework, the specific floor used in this study will be described in Section 2.4. The test section floor and support beams were black anodized aluminum to minimize laser light reflections during optical diagnostics. The upper surface of the test section consisted of a quartz window for laser sheet access. The side walls were removable; as such, Plexiglas acrylic or quartz sheets were used where camera access was required. Blackout boards provided a uniform background for imaging; sections with access ports for instrumentation, such as a hotwire probe or piezoelectric microphone, were interchangeable with the blackout boards. A plenum for tunnel exhaust was situated far downstream, with a 90 cm x 90 cm quartz window for cross

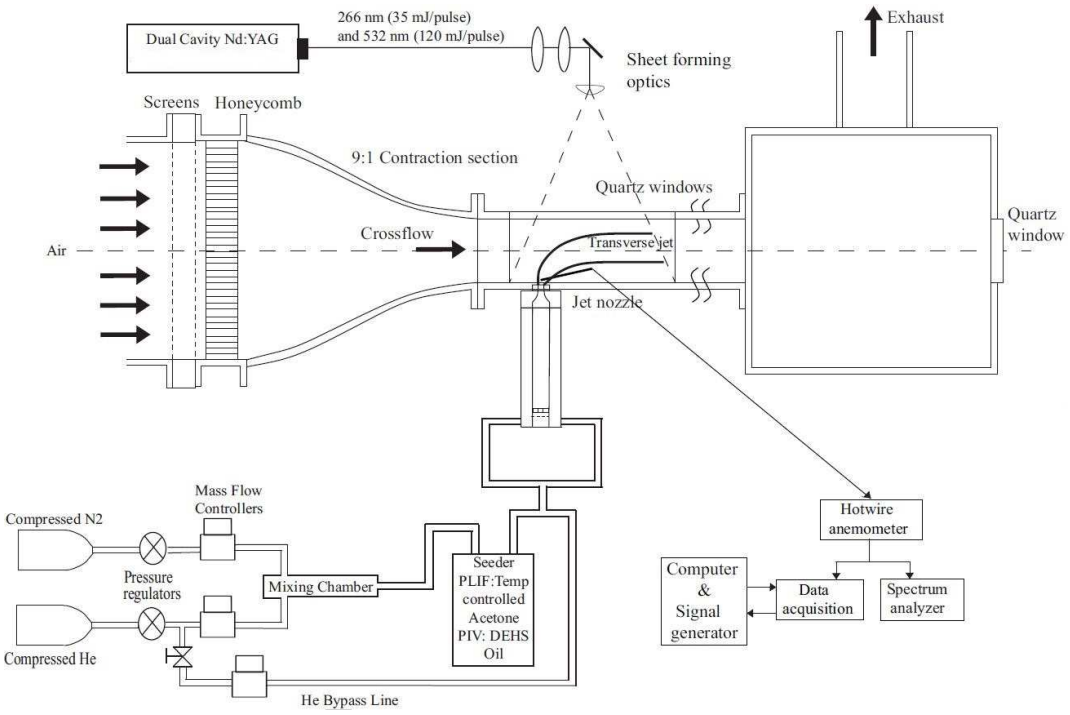

Figure 2.1: Low velocity wind tunnel and associated experimental diagnostics for hotwire anemometry, acetone PLIF, and stereo particle image velocimetry (PIV).

sectional jet visualization. The entire wind tunnel could be moved along the x-coordinate axis in order to fix the optical setup while interrogating different downstream cross-sectional $y-z$ planes at different x locations using a linear stage controlled by a stepper motor.

The filtered supply gases for the transversely injected jet consisted of helium (He) and gaseous nitrogen (N_2), whose proportions (along with acetone vapor for PLIF) were varied as the primary means of controlling jet-to-crossflow density ratio S in the experiment. Mass flow meters (Tylan FC-260, 0-5 NLPM; MKS Instruments GM50A, 0-50 NLPM) with 1% accuracy determined the jet flow conditions, producing the desired JICF flow field within the test section (S=1, Re_j=1900, with J varied via altering the crossflow velocity for this study). Flow meters are controlled by a data acquisition module further described in Section 2.2. The general flow schematic of the experiment is shown in Figure 2.2. By opening or closing various hand valves in the plumbing lines, the outlet of the flow meters could either have been routed into a passive mixing chamber, or alternately bypass the mixing chamber. Flow

Table 2.1: Typical flow conditions used during jet hotwire anemometry, acetone PLIF, and simultaneous PLIF/PIV imaging for the $S = 1$ jet with $Re_j = 2300$ for high resolution PLIF-only data sets, or $Re_j = 1900$ for simultaneous PLIF/PIV data sets.

Experiment	J	U_j (m/s)	U_∞ (m/s)	$\Psi_{acetone}$	ρ_j (kg/m^3)	μ_j (kg/ms)
USL Velocity Spectra	61	7.91	1.01	0.218	1.198	$1.653x10^{-5}$
PLIF-only	61	7.91	1.01	0.218	1.198	$1.653x10^{-5}$
PLIF-only	24	7.91	1.62	0.218	1.198	$1.653x10^{-5}$
PLIF-only	6	7.91	3.25	0.218	1.198	$1.653x10^{-5}$
PLIF/PIV	41	6.78	1.06	0.112	1.198	$1.727x10^{-5}$

could be passed through acetone and/or PIV flow seeding chambers to introduce particle tracers into the flow and enable optical diagnostics.

Jet and crossflow flow conditions used in the present experiments are shown in Table 2.1. The viscosity and other properties of the mixture were determined via the Reichenberg method (Bruce E. Poling, 2001) so that jet Reynolds number could be determined accurately. In the PLIF-only experiments, helium and nitrogen flow rates were controlled by the Tylan flow meters; the gases were mixed in the mixing chamber, then bubbled through the acetone seeding chamber, and subsequently fed to the jet plenum for injection into the wind tunnel. The gas mixture of He and N2 was bubbled through two separate seeders connected in series, to ensure saturation of acetone vapor in the jet fluid. In the simultaneous PLIF/PIV flow experiments, helium flow was controlled by the He Tylan flow meter while nitrogen flow was split between the N_2 Tylan flow meter and the MKS flow meter. The flow line controlled by the N_2 Tylan flow meter was directed into the mixing chamber, then bubbled through the acetone seeding chamber, and fed to the jet line. The flow of nitrogen controlled by the MKS flow meter was combined with the helium, downstream of the flow meters. A portion of this combined flow was passed through the PIV seeding chamber and then to the jet line, while the remainder of the He/N_2 flow was bypassed directly to the jet line. All three flow paths (acetone seeded, PIV seeded, and bypassed He/N_2) were combined upstream of the jet plenum.

At the jet plenum, the jet fluid was fed through a symmetric four-way injection system

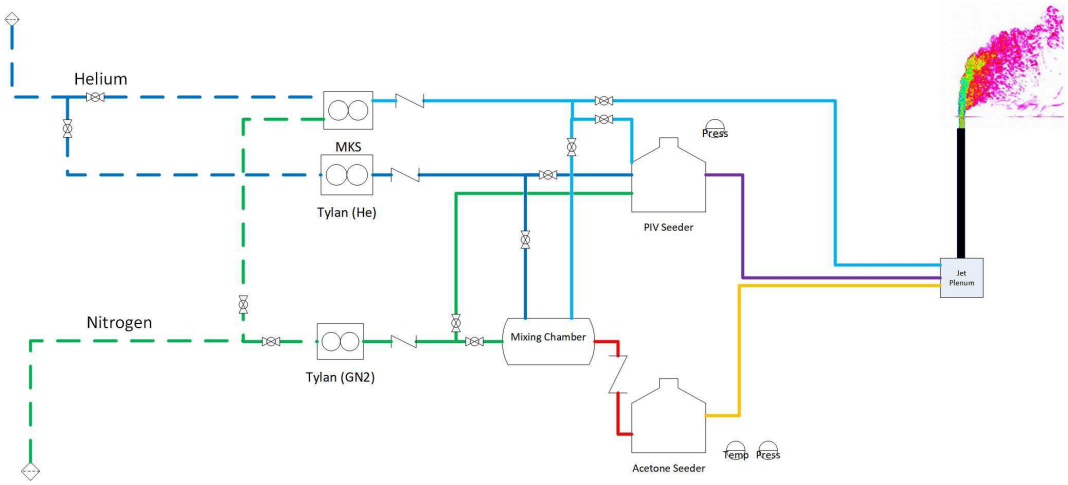

Figure 2.2: Fluid flow control schematic associated with experimental wind tunnel.

into the jet plenum which could be either directly connected to the jet injector, or as in the current experiments, passed through a long development section (L/D=155) containing honeycomb flow straighteners to minimize swirl and ensure a spatially uniform jet. The conditioned flow was then fed into an injector seen in Figure 2.3, whose outlet issued perpendicularly into the test section where interaction with the crossflow occurred. The nozzle (D = 4.04 mm) exit plane was flush with the test section floor. The flush nozzle used in the current study was designed with a fifth-order polynomial contraction to generate thin jet boundary layers at the exit, resulting in a free jet top-hat velocity profile in the absence of crossflow, as documented in prior studies (Megerian et al., 2007; Gevorkyan et al., 2016). The polynomial contraction nozzle was designed to create a thin jet shear layer, enabling the development of strengthening upstream shear layer instabilities as crossflow velocity was increased. A straight pipe to create the flush-injected JICF was examined in separate studies (Getsinger et al., 2014; Gevorkyan et al., 2016, 2018), and the much thicker jet shear layer had a significant influence on the USL instabilities in the convectively unstable regime, but transition to global instability tended to occur under similar overall flow conditions. In the present study, only the flush nozzle was explored due to its distinctive USL instability characteristics, especially at high momentum flux ratios.

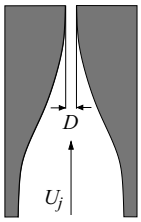

Figure 2.3: flush nozzle injector.

2.2 Measurement and Instrumentation

In order to evaluate, quantify, and control the flowfield, various analog and digital sensors, tools, and equipment were used. For general jet flow control and monitoring a dSPACE 1104 DSP data acquisition (DAQ) and controller board were used in conjunction with Simulink environment and ControlDesk graphical user interface which provided automatic control and digital signal processing. Jet line pressure was monitored by an Omega 0-15 psi gauge pressure transducer located in the acetone seeding chamber, and temperature monitored by an Omega T-type thermocouple and Omega HH91 digital thermometer. In order to control the mole fraction of seeded acetone vapor in the jet flow, the acetone seeding chamber was thermally conditioned using a recirculator (Cole-Parmer Ploystat CR250WU), with a cooling and heating range from 5°C to 80°C, to flow water through a copper coil heat exchanger within the acetone chamber.

To measure velocity characteristics of the flowfield such as boundary layer profiles, jet velocity profiles, jet trajectory, and jet velocity spectra, a miniature constant temperature boundary layer hotwire probe (Dantec 55P15) was used, mounted on a three axes linear platform traversal mechanism with 1μm accuracy. The hotwire signal was fed to a Dantec StreamLine 90N10 frame and then passed through an AC/DC signal splitter for signal conditioning, developed by Hendrickson (2012). Hotwire anemometry was also used in conjunction with a dual channel signal analyzer (HP 36665A) to capture velocity spectral measurements and frequency response of the jet upstream shear layer or other locations of interest. The hotwire signal, with a gain of 10 applied via the signal splitter/conditioner was fed to the signal analyzer and velocity power spectral measurements were captured at 20kHz acquisi-

tion rate over the range of 300Hz to 6.7 kHz (8Hz step size increments), and averaged over 40 readings.

For crossflow velocity calibration, Omega differential pressure transducers (models PX653, 3" and 25" water column full range) are used in-line with a static pitot tube system. This calibration process correlates the input setting (rotational frequency) of the AC motor driving the centrifugal fan to a crossflow velocity in the wind tunnel, and simultaneously calibrates the hotwire velocity probe.

To control jet external forcing described in Section 2.4, a dual output signal generator (HP 8904A Multifunction Synthesizer) generated input waveforms in a frequency range of approximately 875 Hz to 3.5kHz. Each output channel was capable of independent amplitude, frequency, and phase control. Critical to the experiment, the internal clocks of the dual channels were synced with one another, such that they could be accurately offset by a 90° phase shift. Forcing and response signal amplitude, frequency, and phase could be independently verified via a four channel analog input oscilloscope (Keysight InfiniiVision MSOX2024A) with 2 GSPS sample rate. The pressure perturbation amplitude created by acoustic forcing was measured by a free-field piezoelectric microphone/amplifier (PCB Piezotronics 377C01/426B03), whose signal was passed through a conditioner (PCB Piezotronics 484B11) on a gain setting of 100. The raw voltage signal was converted to sound pressure level (dB) or sound pressure (Pa) using the calibrated microphone sensitivity and reference sound pressure for air, $P_o = \mu 20$ Pa.

2.3 Laser Diagnostics and Imaging

Non-intrusive optical diagnostics have the advantage of enabling spatial and temporal flow measurements without physically interfering with the flowfield. The laser diagnostics used in this study facilitate the examination of jet structure and mixing metrics via acetone planar laser-induced fluorescence (PLIF); and flow velocity via particle image velocimetry (PIV). The experimental setup for laser imaging is shown in Figure 2.4. In this study, two different

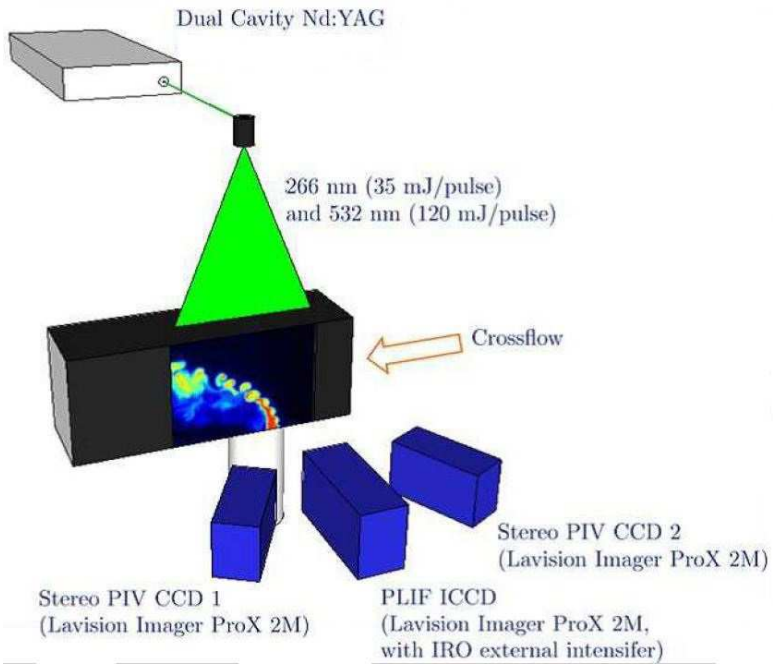

Figure 2.4: Laser and camera setup for PLIF and PIV diagnostics.

dual cavity Q-switched Nd:YAG lasers were used at different periods of the experiment due to equipment issues. A Litron Nano-L PIV laser was used for the vast majority of the 4-speaker studies. The Litron laser was eventually replaced with a Quantel Evergreen 30266 laser, which was used to acquire data during the localized 2-speaker and 1-speaker studies. Both lasers have comparable beam diameter, output energy (mJ) specifications, and were operated with the same triggering software. Each of these lasers produced monochromatic laser light at 1064 nm, which passed through a second harmonic generator at 532 nm and a fourth harmonic generator at 266 nm, the latter for acetone PLIF imaging in the UV. The laser beam passed through two spherical lenses and a turning mirror before being formed into a sheet using a $f =$ -10 mm cylindrical lens. The sheet passed through the quartz window at the top of the test section, and could be rotated to create a very thin divergent sheet in the centerplane $(x - z)$ or cross-sectional $(y - z)$ view of interest. A quartz window was used so that the beam was not reflected or attenuated in the ultra-violet. DaVis 8.2 software and an external programmable timing unit (PTU), both by produced LaVison, were used to operate the laser and synchronize the camera(s).

2.3.1 PLIF

Planar laser-induced fluorescence (PLIF) is a non-intrusive imaging technique which can be used for structure visualization as well as quantitative concentration or temperature measurements (Lozano, 1992). A flow tracer is seeded which is then excited to a higher energy state by laser light whose wavelength is in the florescence band of the tracer molecule. As the molecules return to the original energy state they fluoresce and emit light which can be captured with optics and cameras. Unlike phosphorescence, fluorescence acts on a short timescale (general order of ns) and so is ideal to capture seemingly instantaneous images of the JICF. The intensity of the florescence indicates concentration of the tracer and hence for the seeded flow stream.

Acetone ($CH_3 - CO - CH3$) was used in these PLIF studies as a tracer for jet fluid. Acetone is widely available and is easy to handle from a health hazards perspective. With acetone saturation vapor pressure a function of temperature (e.g. 3.5 psig (22.9 kPa) at $20°C$), acetone could be seeded into the flow in varied concentrations (Lozano et al., 1992). The presence of oxygen in the flowfield quenches the phosphorescence of the acetone, but not the fluorescence whose lifetime is 4 ns. Florescence occurs when the acetone was excited by UV light of 225-320 nm, emitting 300-500 nm visible light which was captured by camera optics.

532 nm and 266 nm combined laser beam described above passed through two 266 nm dichroic mirrors to remove the majority of the 532 nm light and pass the 266 nm beam to the sheet forming optics. The 266 nm wavelength laser sheet thickness was measured to be 600-1000 μm throughout the test section's area of interest. A very thin laser sheet is necessary to acquire sufficiently high spatial resolution images to capture mixing trends. Details on the knife-edge technique for measuring and quantifying the laser sheet thickness may be found in Shoji (2017). Where PLIF and PIV measurements are acquired simultaneously the thickness of the 266 nm laser sheet is required to be approximately doubled to 1.4-2.0 mm such that there is sufficient thickness of the laser sheet in the 532 nm visible light wavelength for reasonable PIV window correlation (see Section 2.3.2).

Acetone images during PLIF-only experiments were acquired using a 14-bit charge-coupled device (CCD) camera (LaVision Imager proX) with 1600 x 1200 pixel resolution. An external intensifier (LaVision IRO) was used to amplify the fluorescence intensity and increase the signal to noise ratio. The image intensifier was gated for 200 ns in order to capture the acetone florescence lifetime but not the 200 μs lifetime of the phosphoresce (Lozano, 1992). 2 x 2 hardware binning was used to further increase the signal to noise ratio, which provided an in-plane resolution of 140-170 μm per pixel for jet centerplane PLIF images, and a resolution of 120-160 μm per pixel for cross-sectional PLIF images. Since the intensifier has a 1500 pixel circular aperture, a digital mask was applied to the pixels outside this region during post processing. For the PLIF portion of simultaneous PLIF/PIV experiments, the acetone images were acquired with a 12-bit CCD camera (LaVison NanoStar) with a 1280 x 1024 pixel resolution, using 2 x 2 hardware binning. For PLIF-only jet centerplane images, a Nikon 50 mm lens at $f/2.0$ and a Vivitar +2 diopter close-up lens were attached to the camera. For centerplane images of the PLIF portion of simultaneous PLIF/PIV experiments, a Sigma AF 90 mm lens at $f/2.8$ with a Vivitar +2 diopter close-up lens were used. For all jet cross-sectional PLIF images a Nikon 200 mm lens at $f/4.0$ was used. For all PLIF experiments, the camera was fitted with a UV bandpass filter to pass only the acetone fluorescence wavelength of light.

The captured PLIF data images require post-processing corrections to obtain accurate scalar concentration values, therefore during PLIF-only experiments, laser energy was monitored by splitting off a small portion of the beam and directing it to a pyroelectric joule meter (Newport 818E-10-50-S), where shot-to-shot energy pulses were recorded. Within the DaVis 8.2 software, camera bias noise (dark image) and background images were subtracted and flat field (white image) corrected. The images were then normalized by the mean shot-to-shot laser energy. For the PLIF portion of simultaneous PLIF/PIV experiments, since the UV wavelength was not separated from the green visible light in the laser beam, UV laser energy could not be monitored, and therefore images for these experiments were not normalized by the shot-to-shot mean laser energy. Therefore the PLIF images from the simultaneous data

sets were used for scalar gradient measurements and not mixing quantification.

Critical to the accuracy of concentration values, especially near the jet potential core, is correction for the absorption of the laser sheet as it passes from wind tunnel top to bottom through the flow media. A mean image of the laser sheet, acquired with the test section filled with acetone, is used to track the intensity decay of the laser along each angled ray. The location of the center of these divergent rays is determined by tracing the edges of an object in the path of the laser sheet beam (Figure 2.5), following the line trace to an imaginary point laser light "source". From this point light source, a coordinate transformation was applied along radial lines to produce a collimated laser sheet, in which energy decay from absorption could be calculated from the Beer-Lambert law:

$$E(x) = E_o e^{-\sigma n x} = E_o e^{-\alpha x} \tag{2.1}$$

where σ is the absorption cross-section, n the number density of acetone, and $\alpha{=}\sigma n$, the absorption coefficient. Further absorption correction details described in Getsinger (2012); Gevorkyan (2015); Shoji (2017).

Following absorption correction all images were normalized such that the concentration of the jet potential core was shown to contain only jet fluid, defining the scalar concentration of the fluid in the potential core as C_o, and $C/C_o{=}1$ in the jet potential core. Concentration values were averaged in a small interrogation area in the jet potential core to calculate C_o, and that average was used to normalize all pixels within the image. This process was performed on each instantaneous centerplane image. Since in general, a cross-sectional image does not contain the jet potential core, a different process was followed. The associated mean centerplane image is used as reference, and concentration mean of that centerplane image is evaluated in the vertical direction at the same x/D location as the cross-sectional plane being corrected. The mean of that local vertical slice is then correlated to the mean cross-sectional image, thus enabling calibration of concentrations in the cross-sectional images. Further details on calibration and image post-processing can be found in Getsinger (2012); Gevorkyan (2015); Shoji (2017). It should noted that some cross-sectional images were unable to be calibrated with a reasonable correlation to the centerplane, likely due to

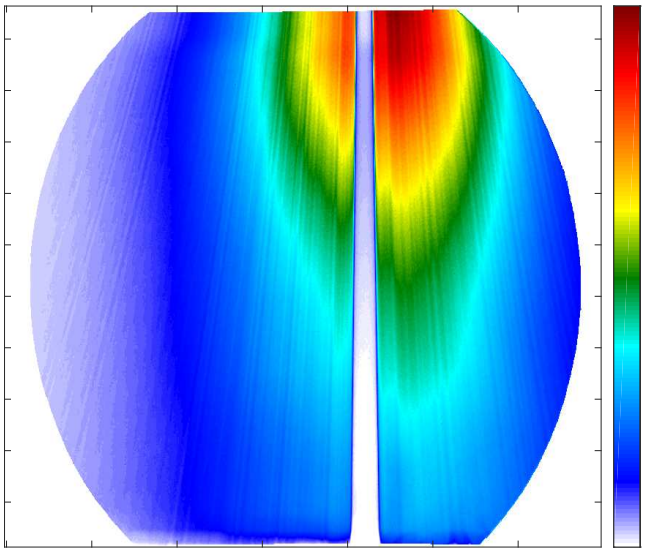

Figure 2.5: PLIF source image for determining imaginary location of divergent sheet laser light source.

asymmetric jet structure in the cross-section view. In these cases since a large portion of the total jet concentration was off-center, the centerplane images in the y=0 plane did not capture sufficient jet concentration to match the mean in the cross-section. Non-normalized cross-section data could not be used for mixing quantification since concentration values were not directly comparable to other data, however the data could still be used to examine jet cross-sectional structure.

Following absorption correction and concentration normalization, PLIF images were then filtered using a 5 x 5 median filter which calculated the median value of a local 5 x 5 pixel region, or window. The center pixel of the 5 x 5 region was replaced with this median value. The window shifted pixel by pixel over the entire image. This process removed any locally abnormal values and reduced the noise in the images, particularly outside of the jet in the crossflow region.

2.3.2 PIV

Particle image velocimetry (PIV) is another optical diagnostic method that utilizes a tracer in the fluid to enable visualization. Local fluid velocity (and hence vorticity) can be extracted by tracking the motion of individual flow tracer particles over a known, short time step. The tracer particles should be sufficiently small such that they are entrained in the flow and do not interfere with the flow or each other, but be large enough to be visible via light scattering. The velocity field is estimated by capturing the displacement of tracer particles over two pulses of light. In these experiments the displacement was captured via two camera frames with a single exposure, a technique called cross-correlation. The resulting image pair is divided into multiple small interrogation areas or windows and a fast Fourier transform (FFT) algorithm computes the velocity vector of the few particles within the window. The resolution of the measurement is determined by the diameter of the tracer particle in comparison to the interrogation window (Westerweel, 1997).

The general setup, including the dual-cavity Quantel Evergreen Nd:YAG laser described in Section 2.3 was again utilized for PIV. PIV requires 532 nm wavelength visible light, therefore dichroic mirrors used to dump excess green light during PLIF measurements were removed. In these experiments, the laser sheet was measured to be approximately 1.5-2 mm thick in the imaging area field of view. A slightly thicker laser sheet was required to adequately capture small out-of-plane components of particle displacement during stereo PIV. To introduce light scattering tracers into the jet, a portion of the flow was rerouted as described in Section 2.1 through a TSI particle generator, which utilized Di-Ethyl-Hexyl-Sebacat (DEHS) oil, creating an aerosol of oil and this portion of jet fluid was then returned to the jet flow path. The seeding density of the jet was determined by the proportion of flow that was diverted through the PIV seeding line. The tracer oil particles were on the order of 1 μm diameter. The crossflow was seeded using a commercial portable smoke machine (Pea Soup Rocket) using glycol based artificial smoke fluid which was directed to the air intake of the crossflow centrifugal fan. The artificial smoke tracer particles were non-toxic with a particle size of 0.2 to 0.3 μm in diameter.

Similar to JICF experiments described in Getsinger (2012), Gevorkyan (2015), Shoji (2017), and Gevorkyan et al. (2018), a 2D3C stereoscopic PIV setup was used in which two cameras imaged the flow from different angles to capture the out-of-plane particle displacement for measurements of all three components of velocity. Here the two cross-correlation CCD cameras (LaVision Imager proX, 1600 x 1200 pixel resolution) were offset approximately 60° from the jet. The two different camera views of the flowfield captured the out-of-plane component of the tracer particle movement, which reduced bias-errors of the in-plane velocity component. In jet centerplane imaging, one camera was upstream the jet and the other downstream as shown in Figure 2.4. In jet cross-sectional PIV imaging, one camera was mounted on ether side of the test section, downstream of the jet looking towards the upstream. Nikon 60 mm lenses at $f/11.0$ and 532 nm narrowband filters were attached to the cameras. Scheimpflug mounts were used to adjust the angle between the cameras and their lenses to avoid off-axis image blurring by the CCD. As with PLIF, PIV cameras require calibration in order to spatially map the camera coordinate system to the geometric setup. Further details on calibration (including self-calibration technique) can be found in Getsinger (2012) and Gevorkyan (2015).

From each instantaneous image pair, velocity vectors were calculated using LaVision's DaVis 8.2 software. Using the spatial calibration, images were mapped to real-world coordinates, then a mean background image from the experiment was subtracted to remove extraneous light reflections within the wind tunnel and enhance tracer particle visibility. Processing software further enhanced contrast by applying and 8x8 pixel sliding background removal and 5x5 min/max filtering scheme. Vector calculations utilized multi-pass stereo cross-correlation; 2 passes with a 32x32 pixel interrogation window and 50% overlap, followed by 4 passes with a 24x24 interrogation window and 75% window overlap. The time separation of the two laser pulses Δt was 12 μs for centerplane images and 15 μs for cross-sectional images, in order for the maximum particle displacement to be less than 1/4 of the initial interrogation window Adrian and Westerweel (2011). Vectors with low correlation values were removed, empty space filled by interpolation, and a 3x3 smoothing filter was

applied to all images.

2.4 Jet Forcing Scheme

The current study focused on the effects of external asymmetric forcing on mixing and structural changes for the JICF, primarily at conditions where J=61, S=1, Re_j=2300. This convectively unstable condition had a highly asymmetric mean jet cross-section without forcing, so effects of the jet perturbation would be potentially easier to visualize and quantify, in addition to being more impactful. A very limited study investigated other S=1, Re_j=1900 transverse jets: the J=24 jet, which is convectively unstable yet has a fairly symmetric cross section, and the J=6 jet, which is absolutely unstable. Asymmetric excitation external to the flush-injected jet was created using four mini-speakers (Tymphany PMT-30N18AL03-04) recessed into the test section floor, spaced circumferentially 90° with respect to the jet exit as seen schematically in Figure 2.6. To distinguish individual speakers they were numbered using the test section floor's $x-y$ plane coordinate system, where the jet exit center served as the origin. The speakers were mounted recessed within the test section floor and covered by a 0.002" thick thin Teflon membrane so as not to disturb the JICF flow field and floor boundary layer. The speakers were tested to ensure minimal damping of the frequency response and good sine wave response correlation for the output acoustic wave. The Teflon membrane was locally painted black with high heat aerosol paint to absorb the laser sheet, minimizing reflections from the test section floor.

Each speaker could be individually operated with independent frequency, amplitude, and phase inputs, hence a wide feasible range of forcing schemes could be employed. The current study operated each speaker with calibrated frequency and amplitude signals via a specially designed control circuit; detailed design of the control circuit and speaker calibration procedure is found in Appendix A. In these studies each speaker could be operated 90° out of phase with those adjacent to it (or at any other specified phase difference). This allowed controlled, relatively uniform, helical-like excitation of the crossflow fluid surrounding the jet in both clockwise (speaker sequence 2-1-4-3) and counterclockwise (2-3-4-1) directions

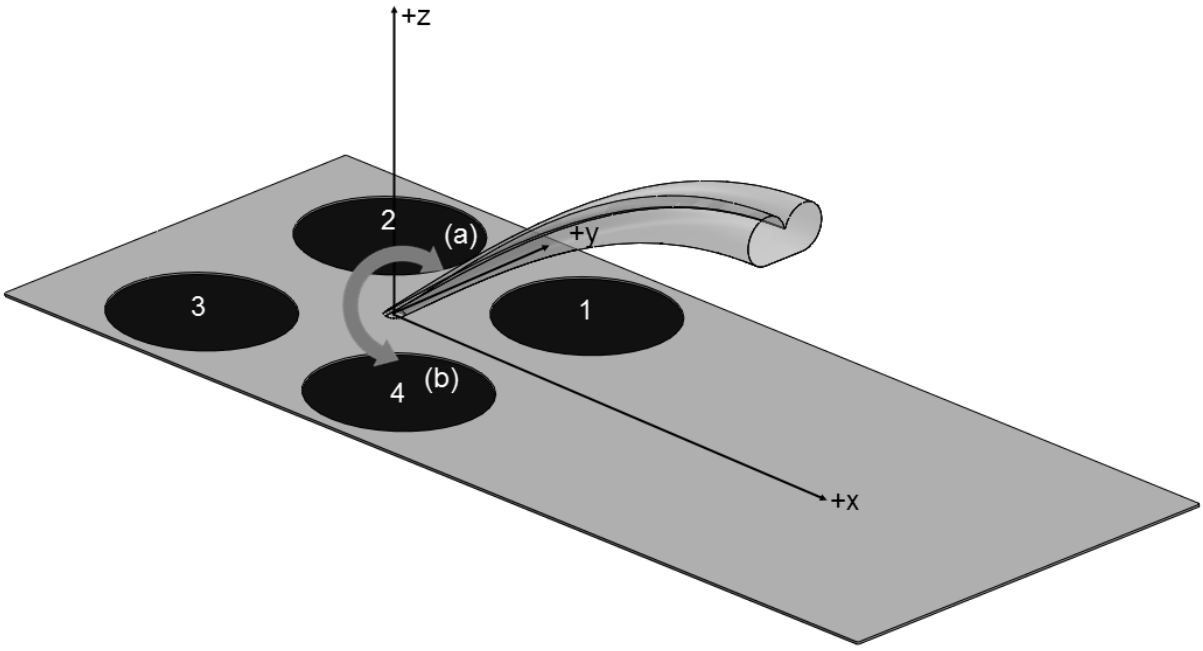

Figure 2.6: Speaker configuration and numbering convention associated with external asymmetric forcing of the JICF, where the crossflow acts in the positive x-direction. Operation of speakers in the sequence 2-1-4-3 created clockwise excitation (a), and 2-3-4-1 created counterclockwise jet excitation (b).

about the jet as shown in Figure 2.6; this is also the same directional convention as one sees when viewing the jet cross section from the downstream end of the tunnel. The operation of the 4 speakers 90°out of phase with each other, sequentially, causes the temporal peak of the forcing sine wave to travel around the jet as the out-of phase speakers operate at a given frequency. The control circuit enabled the amplitudes of the perturbations by each speaker to be matched, as measured by a microphone placed at the center of the jet exit. Speakers could also be operated individually, e.g., only speaker 2 or 3 or both, to study localized external perturbation effects. For example, clockwise directional forcing on the jet windward side-only was accomplished by triggering the peak perturbation amplitude at speaker 3, followed by speaker 90° later, then speakers 1 and 4 remained off during the remainder of the cycle. A comprehensive list of all speaker sequences used in this study are summarized in Table 2.2.

For these experiments, the J=61 equidensity jet was excited with precisely controlled

Table 2.2: Speaker operation sequences used to create directional or localized external perturbations.

Forcing Scheme	Abbreviation	Speaker Sequence
Clockwise, 4 speakers	CW 4	2-1-4-3
Counterclockwise, 4 speakers	CCW 4	2-3-4-1
Clockwise, upstream speakers	CW U	3-2-(1 off)-(4 off)
Counterclockwise, upstream speakers	CCW U	2-3-(4 off)-(1 off)
Clockwise, downstream speakers	CW D	1-4-(3 off)-(2 off))
Counterclockwise, upstream speakers	CCW D	4-1-(2 off)-(3 off)
Right side, upstream	R U	2
Left side, upstream	L U	3
Upstream speakers together	R&L	2 and 3 in-phase
Right side, downstream	R D	1
Left side, downstream	L D	4

waveforms in the range of the fundamental frequency per upstream shear layer spectral measurements, $f_o \approxeq$ 1600-1900 Hz, as well as below and above this range. Assuming the fundamental to be around the mean of this range, $f_o \approxeq$ 1750 Hz, we also force at the subharmonic f_f=875 Hz, and above this range up to the first harmonic f_f=3500 Hz. A more limited study of the J=24 equidensity jet was conducted, exciting the jet at $f_o \approxeq$ 1900 Hz, or the mean of the J=24 fundamental frequency range of $f_o \approxeq$ 1750-2050 Hz. In another very limited study the J=6 jet was excited at $f_o \approxeq$ 1900Hz. Details on the determination of transverse jet fundamental frequencies are described in Section 3.1.1.

CHAPTER 3

Upstream Shear Layer Instabilities and Response to Excitation

This section discusses hotwire-based upstream shear layer (USL) spectral characteristics of the unforced transverse jet and of the transverse jet subject to external asymmetric excitation. Results focus on upstream shear layer instability characteristics for the $J = 61$ equidensity jet, and the response of those USL instabilities to the external disturbances created by the applied asymmetric forcing. Understanding alterations in the transverse jet's USL shear layer instabilities, and their response to asymmetric/helical excitation, will help us to interpret the structural and mixing alterations in the JICF during such excitation.

3.1 Unforced Jet Flowfield Characteristics

Prior experimental studies on USL stability characteristics for the unforced transverse jet with varying fluid properties have been conducted by our group using hotwire anemometry (Megerian et al., 2007; Davitian et al., 2010a; Getsinger et al., 2012; Shoji, 2017). These studies include the present flush nozzle with an exit diameter of 4.0 mm, in addition to a flush round pipe and a nozzle elevated from the injection wall by around 4 jet diameters. For the present hotwire-based investigation, and all subsequent experiments presented in this study, the jet Reynolds number was fixed at $Re_j = 2300$, determined by the mean (profile-averaged) bulk jet velocity, U_j, and the density ratio was fixed at $S = 1$, by proportioning of jet fluid constituents (acetone, He, and N_2). Hotwire studies were conducted on a jet seeded with a mole fraction of acetone Ψ=0.218 , to replicate the jet flow conditions of PLIF-based

studies. The crossflow (laboratory air) velocity was varied to achieve the desired momentum flux ratios $6 \leq J \leq 61$.

3.1.1 Crossflow Characteristics

The wind tunnel test section design described in Chapter 2 was newly constructed with the intent to have versatile floor and sidewall configurations for experimental flexibility. Another advantage of this new design was increased optical access downstream of the jet exit which enabled cross-sectional PLIF and stereo PIV diagnostics to be acquired simultaneously. The external asymmetric forcing experiments were the first to utilize this new test section, therefore the new test setup was characterized to ensure consistency and provide confidence in the results of this study. Velocity profiles of the lowest incoming crossflow typically explored in the JICF studies, U_∞ = 1.01 m/s, were measured using a calibrated hotwire previously described in Chapter 2. This very low velocity crossflow condition corresponded to high momentum flux ratio J=61, for which cross-sectional asymmetries were repeatedly observed (Getsinger et al., 2014; Gevorkyan et al., 2016; Shoji, 2017). Figures 3.1 (a) and (b) show the incoming streamwise velocity, at various vertical distances z/D from the test section floor, as the hotwire was traversed from one side of the test section across the spanwise dimension of the floor, in the y-direction. Results ("New Tunnel") are compared with results from the previous wind tunnel test section setup ("Old Tunnel"). Figure 3.1 (a) measurements were taken at x/D = -6.78 (upstream of the jet exit), which was directly over the centerline of the upstream speakers, and (b) measurements were measured at a typical upstream location from prior studies by our group, x/D = -5.0, closer to the jet orifice. These locations were 16.22 and 18 jet diameters downstream distance from the wind tunnel contraction section, respectively.

Both plots in Figure 3.1 (a) and (b) showed relatively close agreement in the magnitude of the streamwise velocity at given upstream locations and distances from the floor between the old and new wind tunnel. There was especially good agreement and clear spanwise flatness of the velocity at the edge of the crossflow boundary layer in the spanwise direction, at a

vertical height from the floor of z/D=3.0. There were very slight velocity asymmetries along the y-coordinate closer to the injection wall (z/D=0.5), and interestingly these asymmetries were of opposite trend between the old and new wind tunnel. The old wind tunnel crossflow velocity skewed very slightly negative in the $+y$ direction, while the new wind tunnel crossflow velocity skewed slightly positive. However, the orientation of the J=61 structural asymmetry remained the exact same, suggesting that some small imperfection very close to the centerline of the jet may be triggering different growth rates for the upstream shear layer, rather than asymmetries in the crossflow spanwise direction.

Figures 3.1 (c) and (d) compare the crossflow (streamwise) velocity boundary layer profiles at the jet centerline (y/D = 0.0) plane and at same x/D measurement locations as in (a) and (b). The Blasius boundary layer solution for a flat plate is shown as a solid black line for reference. In both cases the boundary layer was $\approx$ 2.5-3.0 jet diameters in thickness. The boundary layer measurements from the new and old wind tunnels agreed closely with each other and also the Blasius solution fairly well. Deviations in measurements in all Figure 3.1 plots at low velocities within the boundary layer ($U/U_\infty \lesssim 0.5$) are possibly attributed to a decrease in accuracy of the hotwire measurements at very speeds, due to calibration limitations using the crossflow blower at very low rotational frequencies. The good agreement in crossflow boundary layers between data sets and correspondence to theory verify that the new tunnel floor section was sufficiently flat and flush, and the Teflon membrane which covered the speakers did not interfere with the incoming flow.

3.1.2 Spectral Character of the Transverse Jet Upstream Shear Layer

The evolution of the upstream shear layer vortices in the transverse jet have been thought to contribute significantly to development of the CVP (Kelso et al., 1996; Cortelezzi and Karagozian, 2001). Upstream shear layer stability characteristics enable an understanding of shear layer dynamics and, ultimately, JICF structure. Early studies by our group (Megerian et al., 2007) utilized hotwire anemometry to explore spectral based characteristics of the JICF upstream shear layer for the equidensity jet (emanating from either a flush nozzle

(a) Streamwise Velocity, x/D = -6.78

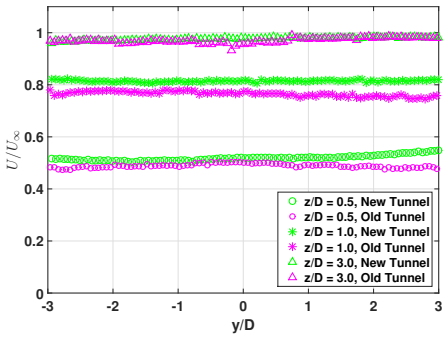

(b) Streamwise Velocity, x/D = -5.0

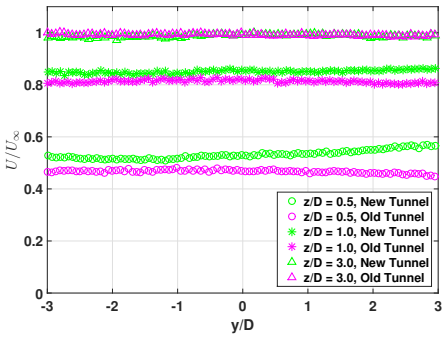

(c) Crossflow Boundary Layer, x/D = -6.78

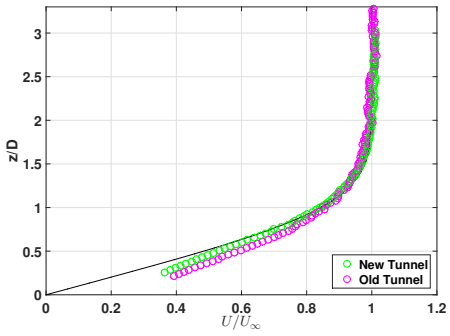

(d) Crossflow Boundary Layer, x/D = -5.0

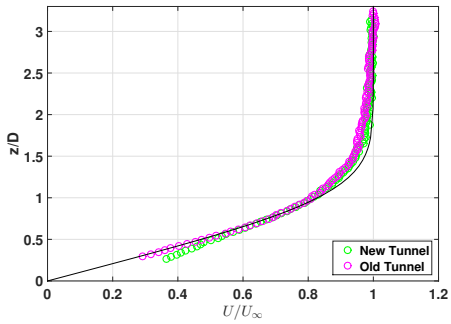

Figure 3.1: Comparison of crossflow boundary layer measurements upstream of nozzle orifice for U_∞ = 1.01 m/s: (a) streamwise velocity vs. spanwise direction y/D for various vertical z/D locations, at x/D = -6.78, (b) streamwise velocity vs. spanwise direction y/D for various vertical z/D locations, at x/D = -5.0, (c) crossflow boundary layer profiles at $y/D = 0$ jet centerline plane at x/D = -6.78, and (d) crossflow boundary layer profiles at $y/D = 0$ jet centerline plane at x/D = -5.0, where solid line is Blasius solution.

or elevated nozzle) for velocity ratios in the range $1.15 \leq R \leq \infty$. For a fixed jet Reynolds number, as the crossflow velocity was increased and thus jet-to-crossflow velocity ratio R and momentum flux ratio J were reduced, the nature of the spectra changed. Transverse jets with high J values had a convectively unstable upstream shear layer, with developing oscillations in a broadband frequency range around f_o, downstream development of a "preferred mode" near a subharmonic of f_o, and higher harmonics. In this flow regime ($R \gtrsim$ 3.1), tonal interference between the hotwire probe and strengthening shear layer instabilities created frequency shifting in the broadband range around f_o. When one continues to increase the crossflow velocity U_∞ at a fixed Re_j, for $R < 3.1$,, strong, pure tone disturbances at f_o initiated close to the jet exit and persisted along the upstream shear layer trajectory,

consistent with an absolutely unstable shear layer. There were clear higher harmonics of the fundamental frequency f_o, and reduction of the energy transfer from fundamental f_o to the subharmonic (Davitian et al., 2010a), as well as evidence of a Hopf bifurcation near R_{cr} = 3.1 for a Nitrogen jet. For low density transverse jets, the transition from convective to absolute instability was observed for $S \lesssim 0.4$ or $J \lesssim 10$ (Getsinger et al., 2012).

As in prior studies, the hotwire was used to acquire an average of 40 temporal velocity fluctuations along the upstream shear layer, and the signal was then analyzed via the Fast Fourier Transform (FFT), which produced a power spectral density (magnitude and frequency) for a given measurement location. The trajectory of the upstream shear layer was determined by applying a power law fit to the error function profile centroids of the horizontally traversed hotwire as it is passed far upstream and downstream of the upstream shear layer, for fixed vertical location slices (Megerian et al., 2007; Davitian et al., 2010a). From this trajectory the hotwire was then traversed along the jet coordinate direction s, with spatial resolution increments of s/D=0.1. A boundary layer hotwire probe was used such that the first measurement could be acquired very close to the upstream edge of the jet exit orifice, at a location $s/D = 0.1$.

Figures 3.2 (a), (c), and (e) represent the magnitude of the local velocity perturbation in dB as a function of upstream shear layer (USL) trajectory locations s/D and $St = \frac{fD}{U_j}$, or normalized frequency, where D is the jet diameter (4.04 mm) and U_j is the velocity of the jet. For the spectra shown here, the jet fluid was seeded with acetone at a mole fraction of $\psi = 0.218$ and mole fractions of helium of $\psi = 0.234$ and nitrogen of $\psi = 0.548$, corresponding to acetone PLIF-only experiments to be discussed later. These conditions produced a jet density that was approximately equal to that of air, so that $S = 1$, with a jet Reynolds number of $Re = 2300$. Figures 3.2 (b), (d), and (f) are more finely resolved spectral magnitude contour plots, in trajectory increments of $s/D = 0.1$, where the color bar corresponds to the disturbance magnitude. Spectral measurements are shown for momentum flux ratios of $J = 61$ (Figures 3.2 (a) and (b)), $J = 24$ (Figures 3.2 (c) and (d)), and $J = 6$ (Figures 3.2 (e) and (f)). The $J = 61$ and $J = 24$ transverse jets showed frequency hopping

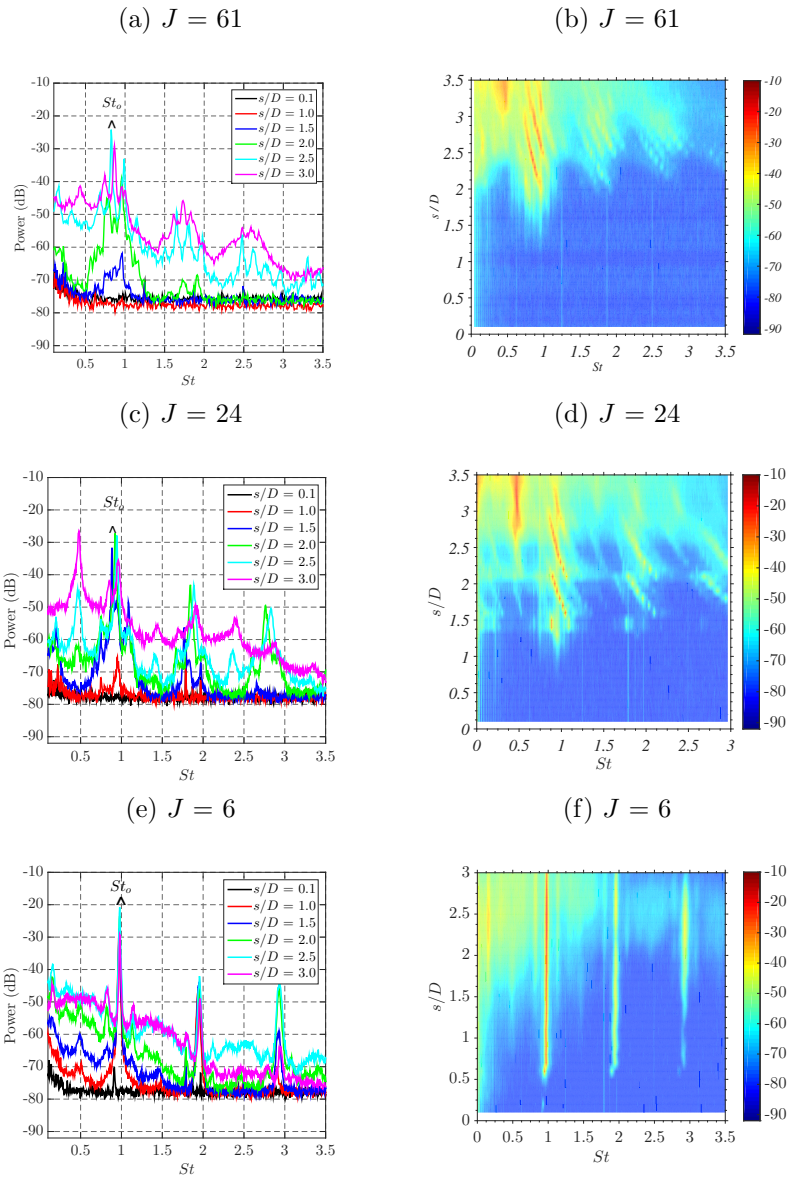

Figure 3.2: Power spectra of vertical velocity disturbances along the USL coordinate s for the unforced $Re_j = 2300$ and acetone mole fraction $\Psi = 0.218$ JICF for (a,b) $J = 61$, (c,d) $J = 24$, and (e,f) $J = 6$. Left column represents power spectra at discrete s/D USL trajectory locations. Right column represents spectral contour maps with 0.1 s/D spatial resolution with color bar indicating disturbance amplitude in dB.

or shifting of the dominant disturbance along the shear layer. This has been attributed to tonal effects of the hotwire probe's presence within the flow, interacting with the shear layer instabilities (Hussain and Zaman, 1978; Getsinger et al., 2012). The fundamental frequency of the instability, St_o or f_o, was estimated as the mean of this broadband frequency

Table 3.1: Fundamental (natural) frequencies f_0 of the upstream shear layer with the $\Psi = 0.218$ acetone vapor seeded jet.

	J=6	J=24	J=61
f_0 (Hz)	1900	1750-2050	1600-1900

shifting range. Farther downstream along the s coordinate, for $J = 61$, a subharmonic of this fundamental mode developed, $f_{1/2}$, indicating the onset of energy transfer from the fundamental frequency to the subharmonic, corresponding to vortex pairing of the upstream shear layer instability structures. These spectral features are characteristic of a convectively unstable shear layer (Megerian et al., 2007; Davitian et al., 2010a; Getsinger et al., 2012). As the momentum flux ratio J decreased from $J = 61$ to $J = 24$ (U_∞ increased), frequency shifting still occurred, however the initiation of USL disturbances developed closer to the jet exit, signaling strengthening of the shear layer instability. In Figures 3.2 (e) and (f), $J = 6$ showed strong, pure-tones of the dominant disturbance which initiated close to the jet exit, at s/D ≈ 0.5, and persisted far downstream. Higher harmonics of St_o appeared while growth of the subharmonic was suppressed, consistent with an absolutely unstable upstream shear layer.

The natural, unforced jet's upstream shear layer's fundamental frequency or range of frequencies, f_0, for each momentum flux ratio J discussed, are summarized in Table 3.1. For a jet with a convectively unstable USL, the fundamental is taken to be around the mean of this range, for $J = 61$ $f_o = 1750$ Hz and for $J = 24$ $f_o = 1900$ Hz, which informed this experimental study on discrete values at which to target forcing frequency f_f.

3.2 Upstream Shear Layer Response to Single Tone External Acoustic Forcing

Absolutely unstable (AU) flows are known to be resistant to applied excitation, depending on the regime, while convectively unstable (CU) flows can be altered more readily with

low level axisymmetric excitation, for example, as observed for the transverse jet (Megerian et al., 2007; Davitian et al., 2010a). As seen in more extensive studies by Shoji (2017), sinusoidal forcing applied to the transverse jet has the ability to change the dynamics of the flowfield, due to the interactions of the jet fundamental mode and the forced mode. The frequency of forcing f_f can overcome the jet's natural mode f_o, this condition is known as "lock-in", as discussed in Chapter 1 and as studied by Shoji et al. (2019b) for axisymmetric excitation of the jet fluid. In the present study, the upstream shear layer behavior of the J= 61 equidensity JICF with acetone mole fraction $\Psi = 0.218$, subject to external asymmetric forcing, was investigated. The jet response was measured via a hotwire in the vicinity of the jet exit, at the upstream shear layer trajectory location of $s/D = 2.0$ and positioned with the wire oriented along the x-axis, above the jet exit, to effectively capture perturbations in the shear layer resulting from external excitation.

The upstream shear layer response can be characterized as locked-in, quasiperiodic, or not locked-in. For asymmetric forcing, lock-in of the USL to sinusoidal forcing is considered to occur when the applied forcing frequency f_f causes the peak of the fundamental mode f_o to be diminished by three orders of magnitude or more, and no quasiperiodic spectral behavior is present. This criterion for lock-in was used in axisymmetric JICF excitation studies (Getsinger et al., 2012; Shoji, 2017; Shoji et al., 2019b), and is similar to criteria used for lock-in studies involving the low density or reactive free jet (Li and Juniper, 2013c). As an example of the velocity power spectra for the locked-in upstream shear layer, Figure 3.3 (a) shows locked-in condition where the applied forcing frequency f_f, resulting from operation of all 4 speakers in a clockwise manner at amplitude P'=0.19 Pa, dominates the flow, where numerous higher harmonics of f_f are seen, and the fundamental mode f_o has been reduced by three orders of magnitude. Quasiperiodicity occurs on the way to lock-in, when the upstream shear layer responds moderately to the applied forcing, resulting in nonlinear interactions between the fundamental and forced mode, however the amplitude of forcing is not large enough to induce lock-in. Quasiperiodic spectral behavior is characterized by the appearance of linear combinations of the fundamental frequency f_o and forcing frequency

f_f, $|pf_o + qf_f|$ where p and q are integers. Figure 3.3 (b) shows quasiperiodic response of the jet USL to asymmetric forcing at f_f = 875 Hz P'=0.025 Pa, resulting from operation of 2 upstream speakers in a clockwise manner, where spectral peaks appear at f_o+f_f and $2f_o$+f_f, the fundamental mode f_o is only diminished by $\approx$ 10 dB, and the magnitude of f_f has not become dominant over f_o. Figure 3.3 (c) shows an USL response which is not locked-in to the applied perturbation, f_f = 1900 Hz, P'= 0.15 Pa, resulting from operation of the right upstream speaker. The forcing frequency f_f = 1900 Hz has become dominant, however the fundamental mode f_o is only diminished by approximately an order of magnitude, and linear combinations of f_o and f_f are not yet evident in the spectral behavior.

3.2.1 4-Speaker Study

Clockwise and counterclockwise asymmetric forcing utilizing the 4 speaker system was applied to the $J = 61$ equidensity jet at discrete frequencies in the range $0.5 \lesssim f_f/f_o \lesssim 2$, or 875 Hz $< f_f <$ 3500 Hz, and the velocity perturbations were measured via hotwire at the upstream shear layer trajectory coordinate s/D = 2.0. Various combinations of forcing frequencies and amplitudes were applied, which corresponded to excitation conditions studied in PLIF experiments, discussed in Chapters 4 and 5. Upstream shear layer power spectra for 4 speaker directional forcing at various forcing frequencies are shown in Figure 3.4; here the amplitudes of forcing pressure perturbation were similar, P'$\approxeq$ 0.15 Pa. In Figure 3.4 black lines represented the unforced jet's natural upstream shear layer velocity spectra, with a fundamental frequency f_o = 1725 Hz, and red and blue lines represented the USL spectra of the $J = 61$ jet subject to clockwise (CW 4) and counterclockwise (CCW 4) directional asymmetric excitation, respectively. When forcing at f_f = 1000 Hz, P'= 0.19 Pa in Figure 3.4 (a), the forced spectra showed the fundamental mode diminished by three orders of magnitude, and no evidence of quasiperiodicity for both the clockwise and counterclockwise forcing directions, hence the USL exhibits 1:1 lock-in, as described by Li and Juniper (2013c). Interestingly, forcing in the clockwise direction produces a disturbance at f_f = 1000 Hz which is approximately an order of magnitude greater than the response for the

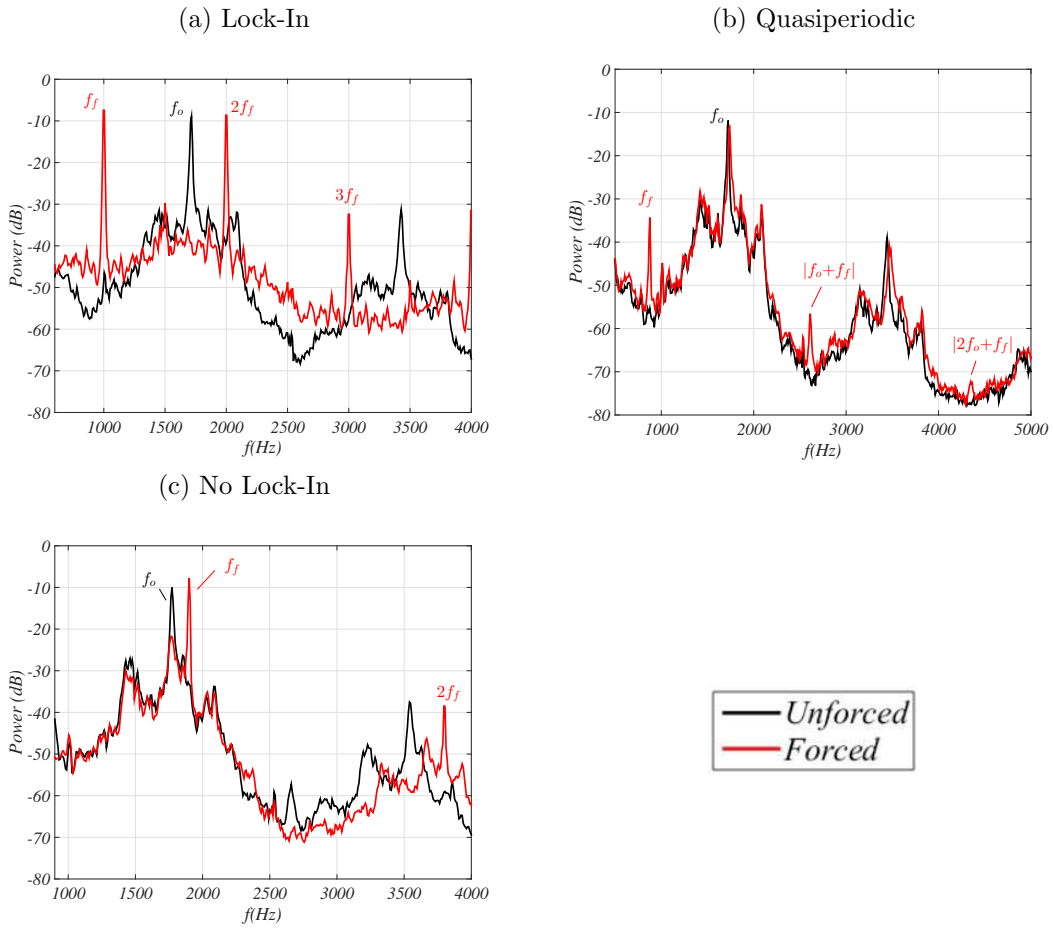

Figure 3.3: $J = 61$ example power spectra of vertical velocity disturbances in response to in response to various asymmetric excitation speaker operation strategies, demonstrating (a) USL locked-in to external asymmetric forcing at $f_f = 1000$ Hz P'= 0.19 Pa, CW 4, (b) quasiperiodic spectral response to external asymmetric forcing at $f_f = 875$ Hz P'= 0.025 Pa , CW U, and (c) non locked-in USL response to external asymmetric forcing $f_f = 1900$ Hz P'= 0.15 Pa, R U.

counterclockwise forcing, despite the same input amplitude for each of the speakers, with control-based operation for each speaker at 90 °with respect to one another. Higher harmonics of forcing f_f were seen, where the amplitudes of the counterclockwise disturbances was consistently greater than that of the counterclockwise for the odd harmonics ($3f_f$ and $5f_f$), but not so much at the even harmonics. These differences suggested that upstream shear layer rollup and merger of vortical structures could be different between CW and CCW asymmetric excitation conditions.

In Figure 3.4 (b), external excitation at $f_f = 1600$ Hz, P'= 0.15 Pa was applied, which re-

sulted in a locked-in USL for both clockwise and counterclockwise directional forcing. Here, f_o was essentially vanished, and narrow peaks at $f_f = 1600$ Hz and higher harmonics appeared. Since $f_f = 1600$ Hz in this case was close to the USL fundamental frequency $f_o = 1725$ Hz, this strong 1:1 lock-in behavior was not surprising, although it is interesting that CW and CCW excitation produce virtually identical responses, as opposed to the 1:1 lock-in behavior in 3.4(a). In Figure 3.4 (c) the forcing frequency $f_f = 1900$ Hz was again very close to the USL fundamental frequency, and again lock-in was observed at pressure perturbation P'= 0.15 Pa. The clockwise directional forcing saw the emergence of the forcing frequency subharmonic $1/2f_f$, as well as combinations of this subharmonic with f_f and higher harmonics. This behavior was not observed for the equivalent counterclockwise forcing, suggesting the likelihood of greater shear layer vorticity rollup and merger for the CW case than for the CCW case with the same frequency and input amplitude. As the forcing frequency was increased higher above f_o to $f_f = 2600$ Hz, with P'= 0.15 Pa, the USL did not lock-in to the external asymmetric forcing, as shown in Figure 3.4 (d). The fundamental mode f_o, though slightly shifted, was only reduced by one order of magnitude and quasiperiodic behavior was exhibited in the velocity spectra. Linear combinations of the fundamental and forced frequencies appeared as a result of forcing in both clockwise and counterclockwise directions, indicating the amplitude of applied forcing was not sufficient to overcome the fundamental instability, but was high enough to create interactions between the natural and forced modes, as observed for axisymmetric sinusoidal excitation of the transverse jet for both convectively unstable and absolutely unstable shear layer conditions (Shoji et al., 2019b) and for the low density free jet for absolutely unstable conditions (Li and Juniper, 2013c). The present results demonstrated that for a fixed forcing amplitude, the response of the USL was frequency dependent, as is typically seen for lock-in types of dynamical response in a flowfield.

Figure 3.5 investigates the effect of the USL spectra in response to 4-speaker clockwise and counterclockwise directional forcing for a fixed forcing frequency, $f_f = 1000$ Hz, subject to two different amplitudes of excitation, (a) P'= 0.065 Pa and (b) P'= 0.19 Pa. In Figure 3.5 (a), the USL spectra was quasiperiodic in nature, as seen by the linear combinations of the

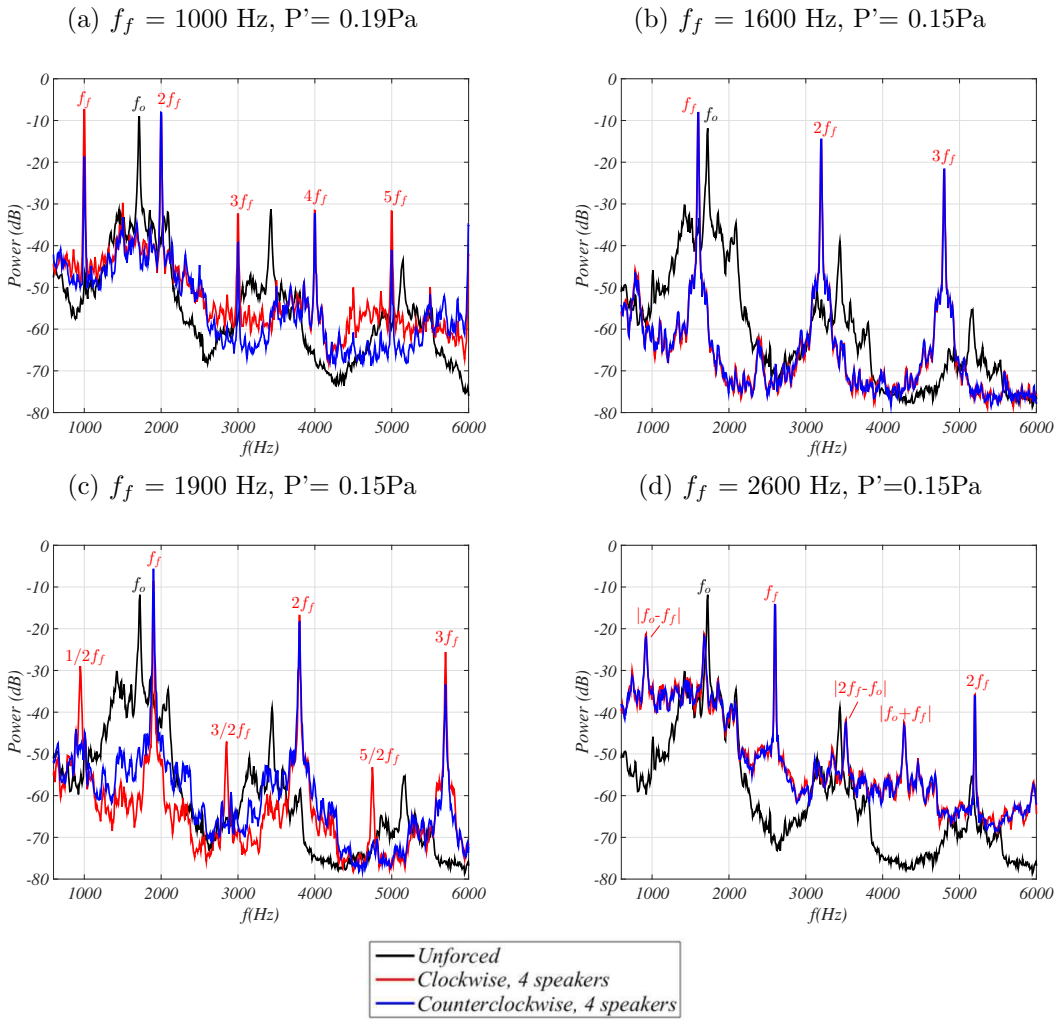

Figure 3.4: Power spectra of vertical velocity disturbances at the USL trajectory coordinate s/D = 2.0 for the $J = 61$ transverse jet with and without 4 speaker clockwise and counterclockwise directional external asymmetric forcing, at various frequencies with similar pressure perturbation amplitudes as indicated. The USL had a natural frequency of $f_o = 1725$ Hz.

unforced frequency f_o and the f_f, similar to observations of quasiperiodicity in response to axisymmetric excitation in low density free jets by Li and Juniper (2013c) for an absolutely unstable shear layer and for the transverse jet for both CU and AU conditions by Shoji et al. (2019b). Under the present asymmetric forcing a slightly different response between the clockwise and counterclockwise forcing directions was again observed; the clockwise forced USL responded with greater amplitude at all peaks induced by the excitation and even away from the spectral peaks. When the pressure perturbation amplitude was increased to P'=

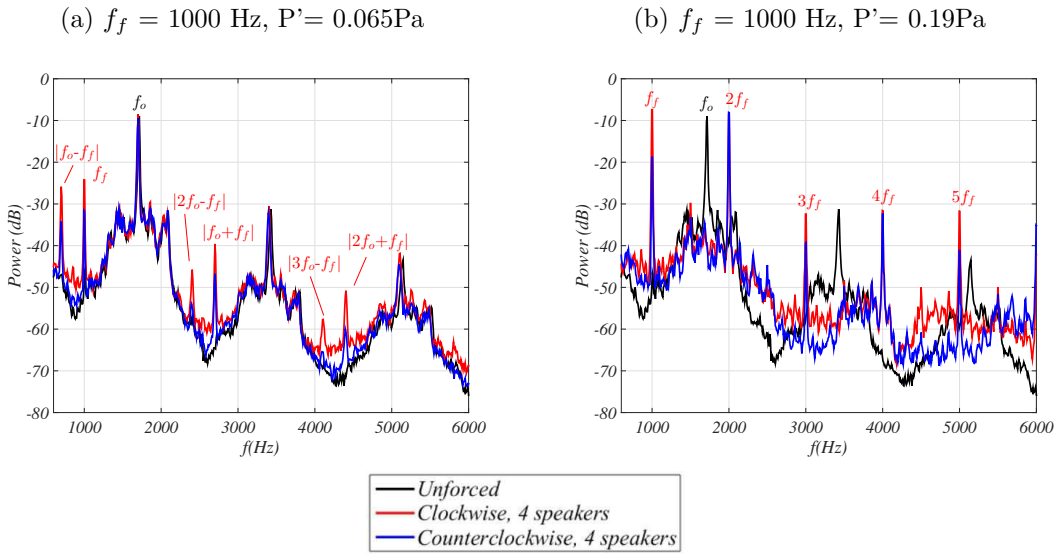

Figure 3.5: Power spectra of vertical velocity disturbances at the USL trajectory coordinate s/D = 2.0 for the J = 61 transverse jet with and without 4 speaker clockwise and counterclockwise directional external asymmetric forcing, at f_f = 1000 Hz with different pressure perturbation amplitudes. The USL had a natural frequency of f_o = 1725 Hz.

0.19 Pa in Figure 3.5 (b) the USL was clearly locked-in with a sufficiently diminished f_o, and f_f and higher harmonics dominated the velocity power spectra. This demonstrated that for a fixed forcing frequency, the response of the USL was amplitude dependent and with quasiperiodicity prior to 1:1 lock-in, again consistent with dynamical lock-in behaviors of other types of shear layers.

As the forcing frequency moved farther above the fundamental frequency f_o, it became increasingly difficult to elicit a response of the USL to very low level external forcing. Greater amplitudes of forcing were applied at frequencies high above f_o (f_f approaching $2f_o$), yet these amplitudes were still very low as compared to those of the axisymmetric sinusoidal forcing studies by Shoji (2017) required to produce lock-in and/or changes in jet behavior. In Figure 3.6 the JICF was subjected to asymmetric forcing at frequencies above the fundamental (f_o<f_f<$2f_o$), (a) f_f = 2900Hz, P'= 1.4 Pa, and (b) f_f = 3500 Hz, P'= 2.0 Pa. Note these forcing amplitudes are an order of magnitude greater than the excitation seen in Figure 3.4. Excitation at f_f = 2900 Hz P'= 1.4 Pa, seen in Figure 3.6 (a), led to quasiperiodicity, with disturbances appearing at linear combinations of the forcing and the fundamental fre-

quencies. For this excitation condition there were virtually identical responses of the USL to either CW or CCW asymmetric forcing, in contrast to the results in Figures 3.4 and 3.5. When forcing at $f_f = 3500$ Hz, with even further increased amplitude P'= 2.0 Pa, the USL did not lock into the frequency of forcing; f_o was not diminished, nor did f_f dominate the power spectra. The results of Figure 3.6 show that the $J = 61$ convectively unstable shear layer does not lock-in to low level asymmetric forcing when forcing high above the fundamental range, again consistent with typical lock-in limitations for both AU and CU shear layers in response to axisymmetric excitation.

In general, the USL velocity power spectra showed differing behavior when excited in the clockwise direction vs. counterclockwise excitation. The differences ranged from slight, as in Figure 3.4 (a), to obvious, as in Figure 3.4 (c). Possible reasons for these dissimilar responses to a given forcing frequency and amplitude may be related to the asymmetric nature of the naturally unforced $J = 61$ jet, and possible positive, uneven growth rates of the m=$\pm$1 helical modes as suggested by Alves et al. (2007) for the equidensity transverse jet. Therefore forcing in one direction may enhance such natural asymmetries in the helical mode growth rates, while forcing in the opposite direction may work to suppress any uneven instability growth rates, which could lead to differences in the USL spectral character for a given forcing frequency and amplitude. Another possibility to explain the differing jet responses to directional forcing may be that since the nature of the jet is associated with the upstream shear layer, perhaps when applying external directional forcing, the overall azimuthal excitation about the jet exit is not the driving influence on the USL, but rather the last speaker in the sequence the USL layer "sees" locally, such as the R speaker (R U) or left speaker (L U). Investigations of the differences in directional forcing led to the detailed study of localized forcing on the upstream shear layer in the 2-speaker and 1-speaker studies.

3.2.2 2-Speaker and 1-Speaker Study

The dissimilarity in the response of the USL to directional application of forcing led to the investigation of localized external forcing strategies. The two upstream speakers were oper-

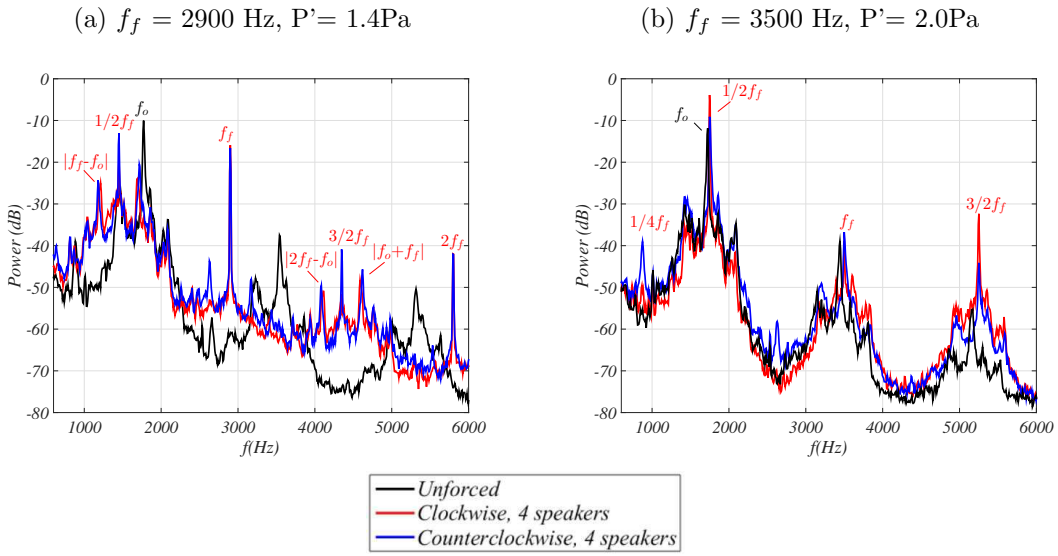

Figure 3.6: Power spectra of vertical velocity disturbances at the USL trajectory coordinate $s/\mathrm{D} = 2.0$ for the $J = 61$ transverse jet with and without 4 speaker clockwise and counterclockwise directional external asymmetric forcing, at frequencies above far f_o, with relatively large perturbation amplitudes for this study. The USL had a natural frequency of $f_o = 1725$ Hz.

ated in a semi-clockwise or semi-counterclockwise way in which the upstream speakers were tuned to be 90° out of phase with each other, as in 4-speaker operation schemes, but the two downstream speakers were turned off, leading to directional forcing in the upstream portion of the flowfield. Other forcing strategies were employed, such as the two upstream speakers forcing together in-phase, with the downstream speakers turned off, to create symmetric (equal forcing on either side) external excitation in the jet exit upstream region. Additionally, upstream forcing intended to introduce asymmetric perturbations was applied, either with the left upstream speaker only, or the right upstream speaker only. As in the 4-speaker study, the USL velocity power spectra was measured at the upstream shear layer trajectory coordinate of $s/D = 2.0$ for the J=61 transverse jet, in both the unforced condition and for the jet subject to the upstream 2-speaker or 1-speaker forcing.

USL velocity spectral evaluation for upstream external excitation is shown in Figure 3.7. Figure 3.7 (a) shows upstream power spectra for $f_f = 875$ Hz with different forcing strategies utilizing the upstream speakers, and all cases were seen to exhibit quasiperiodic behavior, with combined interactions of the fundamental frequency f_o and the forcing frequency f_f

and with similar trends in amplitudes in the spectra. The fact that the USL did not lock-in was perhaps unsurprising given the very low amplitude of excitation, P'= 0.025 Pa. An examination of the USL power spectra at f_f reveals some differences in the response amplitude of the jet to different localized forcing strategies. Upstream speaker in-phase forcing (R&L together) and counterclockwise upstream forcing (CW U, trace directly under R&L) led to the greatest amplitude in shear layer response at $f_f = 875$ Hz. Perturbing the upstream flowfield with the left speaker only (L U) lead to the weakest amplitude response in the USL at $f_f = 875$ Hz, an order of magnitude lower than the forced response of R&L and CW U. In contrast, upstream forcing at $f_f = 1600$ Hz, P'= 0.15 Pa seen in Figure 3.7 (b) resulted in USL power spectra with very similar response to all forcing strategies. All cases are clearly locked-in with the vanishing of f_o, and dominance of f_f higher harmonics, sub harmonics, and combinations of both is seen. At $f_f = 1600$ Hz, forcing with the L U condition produced a slightly larger amplitude response, but the difference in response of the USL instability overall was 3dB or less between all compared upstream forcing cases.

The upstream shear layer power spectra results for Figure 3.7 (c)-(e) are quite interesting as they demonstrated more dissimilar responses to the different forcing strategies. Upstream forcing at $f_f = 1900$ Hz, P'= 0.15 Pa seen in Figure 3.7 (c) shows the condition where upstream right (R U) was not locked in, while all other upstream local forcing strategies exhibited 1:1 lock-in. For $f_f = 1900$ Hz R U, f_o was only reduced by approximately an order of magnitude. The lack of clear lock-in for R U forcing for $f_f = 1900$ Hz was a surprising result due to the fact that the forcing frequency was quite near the fundamental f_o, the amplitude of perturbation was not particularly low for this study, and quasiperiodicity was not seen, meaning the R U case did not appear to be approaching dynamical lock-in. In Figure 3.7 (d) upstream excitation was applied at $f_f = 2300$ Hz, P'= 0.28 Pa, and while CCW U, L U, and R&L were locked-in, R U and CW U exhibited quasiperiodic behavior in the USL spectra. For R U and CW U, $f_f = 2300$ Hz excitation resulted in a reduction of f_o by only 15 dB, and also resulted in interactions of f_f and f_o as seen by the peaks of combined frequencies. However, R U was only weakly quasiperiodic as the spectra peaks at

(a) f_f = 875 Hz, P'= 0.025Pa

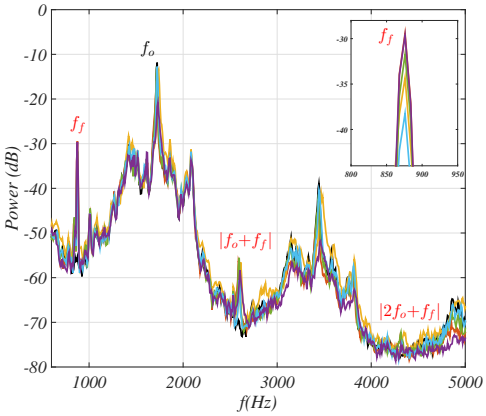

(b) f_f = 1600 Hz, P'= 0.15Pa

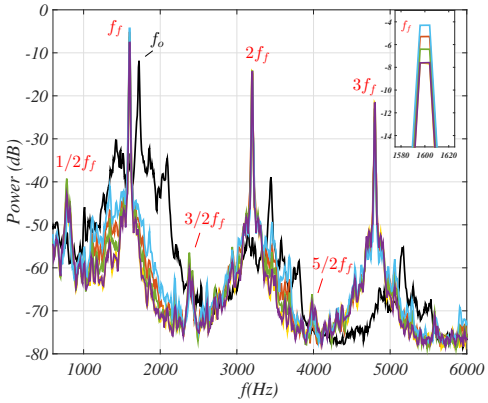

(c) f_f = 1900 Hz, P'= 0.15Pa

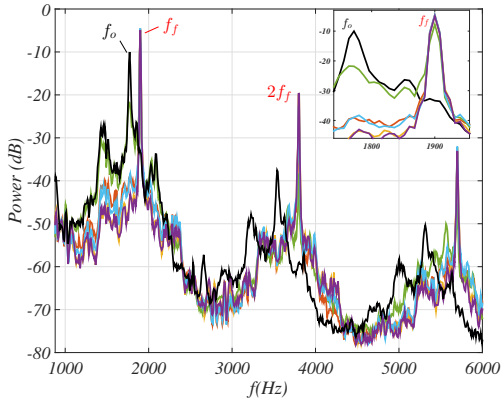

(d) f_f = 2300 Hz, P'=0.28

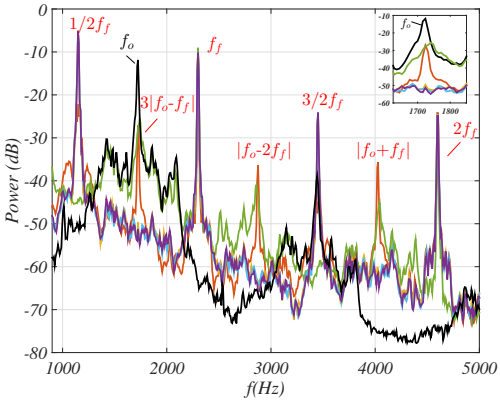

(e) f_f = 2900 Hz, P'= 1.4Pa

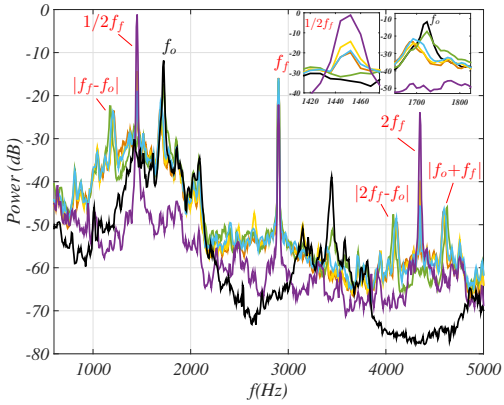

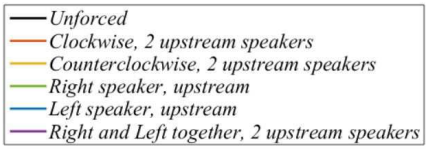

Figure 3.7: Power spectra of vertical velocity disturbances at the USL trajectory coordinate s/D = 2.0 for the J = 61 transverse jet with and without 2-speaker and 1-speaker upstream external asymmetric forcing, at various frequencies and pressure perturbation amplitudes. The USL had a natural frequency of f_o = 1725 Hz.

$|pf_o+qf_f|$ were very broadband. It is interesting that both R U and CW U respond similarly, since in the CW U forcing strategy, the USL would "see" the excitation of R U last in the operation sequence. The fact that localized L U and R U 1-speaker forcing often resulted in differing power spectra traces suggest that perhaps more than unequal m=±1 helical growth rates contribute to the dissimilar jet responses and natural asymmetric structure of the J = 61 jet cross-section, since 1-speaker operation would not induce a directional excitation azimuthally about the jet exit. Perhaps the mere existence of a small asymmetry in the incoming crossflow boundary layer (Figure 3.1(a)-(b)) induced small perturbations which may trigger instabilities, and those instabilities result in the consistent orientation of the J = 61 unforced jet's cross-section asymmetry, despite opposite trends in the small boundary layer irregularities between the old and new wind tunnel sections.

Furthering the investigation of differences in USL response to upstream localized external excitation, Figure 3.7 (e) shows the shear layer power spectra for f_f = 2900 Hz, P'= 1.4 Pa. Note the relatively high amplitude of forcing for this condition and excitation applied well above the natural mode f_o. Here, only the two upstream speakers operating in phase (R&L) exhibit 1:1 lock-in of the USL, while all other forcing strategies (CW U, CCW U, R U, and L U) responded with low amplitude f_f and f_o combined peaks, and a reduction in f_o less than 3 orders of magnitude. R U responded especially weakly, which only reduced f_o by a few dB, thus R U was consistently the least effective at altering the natural USL when excitation was applied at frequencies above the fundamental, f_f>f_o. Interestingly, in Figure 3.7 (e), the forcing frequency did not dominate the power spectra for the locked-in case R&L, but rather the subharmonic $1/2f_f$ was dominant in the amplitude of response, perhaps because $1/2f_f$ = 1450 Hz, was much closer to the USL fundamental range ($f_o \approx$ 1600 - 1900 Hz) than f_f = 2900 Hz, and therefore was easier for the USL to lock-in to; this also suggests that this forcing condition could trigger stronger shear layer vortex pairing. Upon examination of the velocity spectra responses at $1/2f_f$, it was seen that R&L U responds strongly with a magnitude of -1 dB, while CW U, CCW U, and L U response at $1/2f_f$ was similar to their response at f_f, approximately -20 dB. And notably the USL power spectra for R U

had virtually no response (same magnitude response as the unforced case) at $1/2f_f$, adding to the evidence that excitation in the upstream right side of the jet is less influential on the $J = 61$ equidensity transverse jet when $f_f > f_o$.

The effect of localized downstream forcing on the USL velocity spectra was also explored. The two downstream speakers were operated in a semi-clockwise or semi-counterclockwise way in which the downstream speakers were operated 90° out of phase with each other, as in 4-speaker operation schemes, but the two upstream speakers were turned off, leading to directional forcing in the wake portion of the flowfield. Additionally, asymmetric downstream forcing was applied, operating either the left downstream speaker only, or the right downstream speaker only. The USL velocity power spectra was measured at the USL trajectory coordinate of $s/D = 2.0$. In Figure 3.8 (a), response to downstream forcing at $f_f = 875$ Hz, P'= 0.225 Pa showed peaks at $f_f = 875$ Hz and its higher harmonics, however this case was not considered to be locked-in because the amplitude of f_o was only reduced by at most a factor of 10 dB, less than the three orders of magnitude criteria for lock-in. In fact what may be represented around $f_o = 1725$ Hz may be "pulling" of the frequency, where when f_f is close to f_o, the fundamental shifts slightly towards f_f (or in this case $2f_f = 1750$ Hz), as seen by Li and Juniper (2013c) for the absolutely unstable low density free jet. Examination of the USL power spectra at $f_f = 875$ Hz showed that the USL response to different wake area forcing strategies resulted peaks of somewhat similar magnitudes, the greatest magnitude response was downstream counterclockwise forcing (CW D), while the weakest magnitude response was for the right downstream speaker (R D), with a 6 dB spread between the two. This result agrees with upstream speaker forcing, in that the right side of the jet tends to have a weaker effect on the USL for a given f_f and P' combination. Downstream forcing shown in Figures 3.8 (b) ($f_f = 1600$ Hz) and (c) ($f_f = 1900$ Hz), both with P'= 0.15 Pa, show the USL clearly locked in to f_f. Notable in both cases under was R D forcing, the USL response at f_f was more broadband than other speaker operation strategies which exhibited more pure tone spectral behavior, another supporting piece of evidence that the jet USL is not as readily locked-in to external forcing on the right side (starboard), even when excited

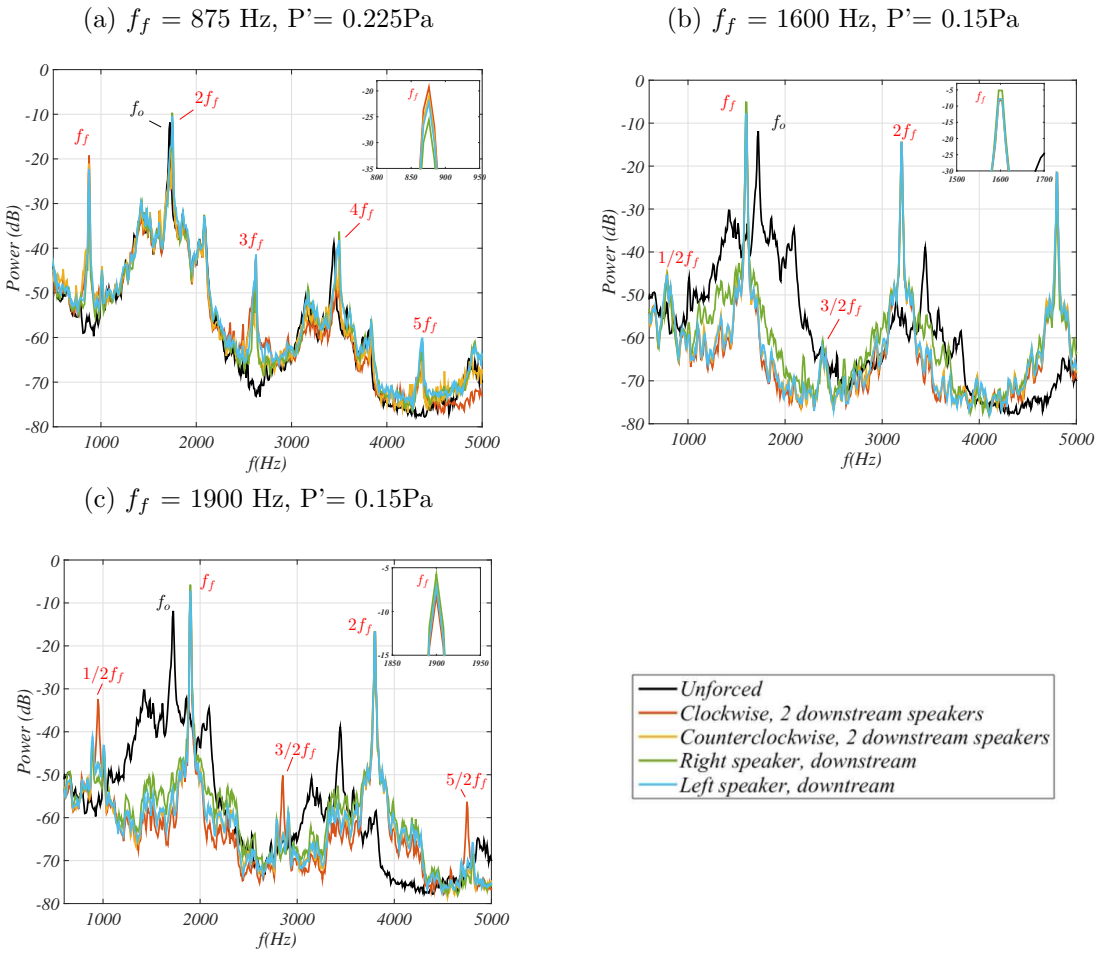

Figure 3.8: Power spectra of vertical velocity disturbances at the USL trajectory coordinate $s/D = 2.0$ for the $J = 61$ transverse jet with and without 2-speaker and 1-speaker downstream external asymmetric forcing, at various frequencies and pressure perturbation amplitudes. The USL had a natural frequency of $f_o = 1725$ Hz.

in the wake region.

Based on results shown in Figures 3.4-3.8, maps of USL lock-in conditions was extracted for various forcing strategies. Figure 3.9 represents this mapping for the (a) 4-speakers study, (b) upstream speaker study, (c) downstream speaker study, and (d) superposition of all forcing conditions; where green symbols correspond to 1:1 lock-in of USL power spectra, blue symbols correspond to quasiperiodicity in the run-up to 1:1 lock-in, and red symbols correspond to no lock-in of USL. The results in Figure 3.9 show that in general, when forcing near the fundamental frequency f_o, the USL locked-in to the forcing readily, with the

exception of $f_f = 1900$ Hz, P'=0.15 Pa, R U. Also observed is that when forcing high above the fundamental, as f_f approached $2f_o$, the jet USL did not lock-in to the external forcing, even at relatively high pressure perturbation amplitudes. This suggests that the jet USL may not be able to respond to external forcing at frequencies high above the fundamental. This also suggests that a more detailed lock-in diagram for external asymmetric forcing, if centered around f_o, may have a somewhat steep slope of the lock-in boundary for $f_f > f_o$. The general asymmetry of the maps in Figure 3.9 are similar to results of previous studies with axisymmetric sinusoidal jet excitation by Shoji et al. (2019b), where asymmetric V-like shape lock-in diagrams were produced. Also similar to to the results of the study by Shoji et al. (2019b), quasiperiodicity in the run-up to 1:1 lock in for the equidensity $J = 61$ transverse jet was observed, as well as conditions producing no lock-in for this study, adding to evidence that the convectively unstable USL is not always locked-in, in contrast to expectations for CU shear layers in general (Sreenivasan et al., 1989; Huerre and Monkewitz, 1990; Juniper et al., 2009) and unlike the somewhat limited results of Davitian et al. (2010a) for the $J = 61$ equidensity transverse jet.

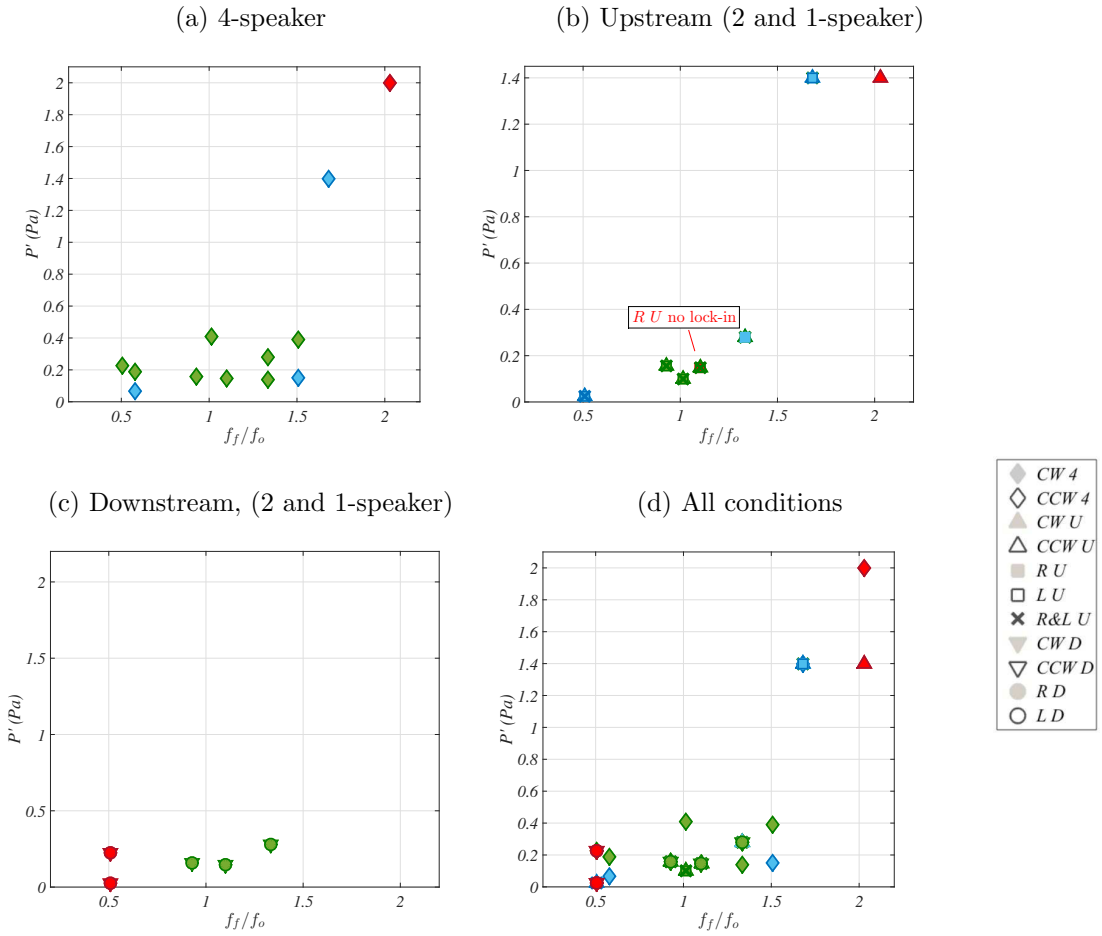

Figure 3.9: Maps of the USL response to external forcing at various forcing frequencies and perturbation amplitudes P', measured at shear layer location $s/D = 2.0$. Green colored symbols represent 1:1 lock-in of the USL, blue symbols represent quasiperiodic behavior of the USL power spectra, and red symbols represent no lock-in of the USL to external forcing.

CHAPTER 4

Effects of Asymmetric Forcing on Transverse Jet Structure

This section discusses the influence of external asymmetric acoustic forcing on transverse jet structure, based on instantaneous centerplane and mean cross-sectional acetone PLIF images. Strategic forcing of the transverse jet can be used to tailor or optimize the flowfield for aerospace engineering or other applications, and axisymmetric sinusoidal forcing has been shown to have a profound affect on jet structure for a jet whose USL is convectively unstable (Davitian et al., 2010b; Shoji, 2017). For the JICF with an absolutely unstable USL, square wave excitation is typically observed to have the most significant effect (Shoji et al., 2019c) in order to overcome the naturally strong shear layer instabilities. This study investigates the affect of externally applied sinusoidal forcing to the jet structure, depending on forcing frequency f_f and pressure perturbation amplitudes P' as well as the nature of asymmetric application of this forcing.

External asymmetric forcing was accomplished by the operation of the control scheme discussed in Chapter 2, utilizing varied forcing strategies summarized in Table 2.2. Very small profile speakers were used; the frequency response (phase and magnitude) for a sample speaker, quantified via piezoelectric free-field microphone measurement, is shown in Figure 4.1. Here, the magnitude of the frequency response was fairly flat ($\pm$ 7 dB) in the range of $\approx$ 750-7000 Hz, while the phase of the frequency response was linear within a similar range. This flat response region captured the range of USL fundamental frequencies, $f_o \approx$ 1600-1900 Hz for the $J = 61$ jet, and set a lower bound of speaker operation around $f_f \geq 800$ Hz. All PLIF and PLIF/PIV imaging was acquired without phase-locking to f_f, at a recording

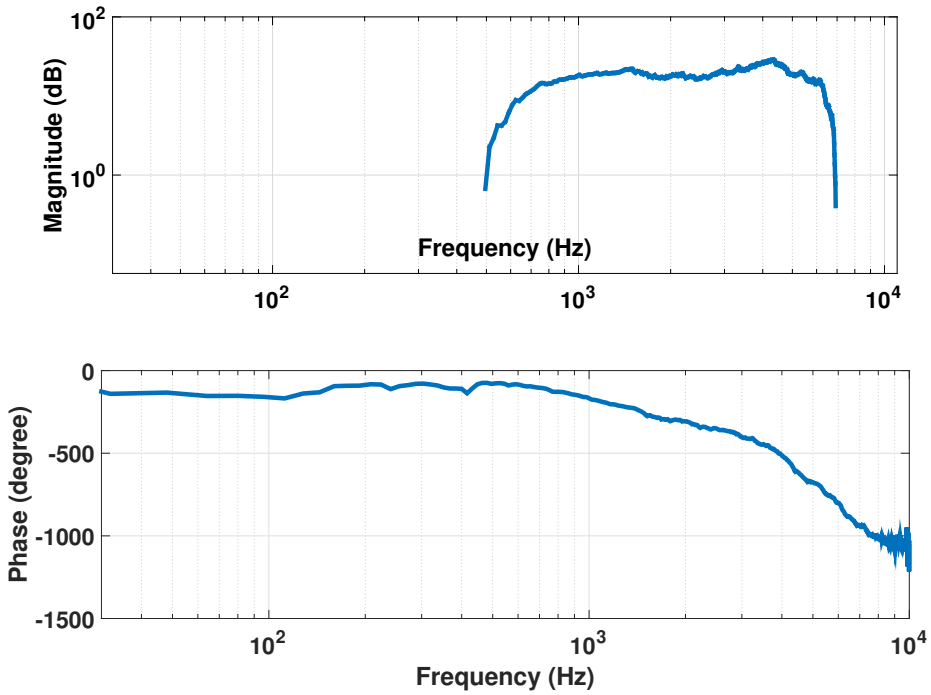

Figure 4.1: Magnitude (in dB) and phase (in degrees) frequency response for a sample mini-speaker, as measured by a free-field piezoelectric microphone and calculated via a dynamic signal analyzer.

rate of 7.5 Hz with the Litron laser, or approximately 5.4 Hz with the Quantel laser. These recording rate frequencies were chosen such that any f_f used in this study would not be divisible by the recording rate, in order to capture all phases of the flow with respect to the forcing.

4.1 4-Speaker Study, Structural Characteristics

Visualization of the jet centerplane images has the potential to illustrate the influence of external forcing on the JICF upstream shear layer vortex formation, and hence the evolution of the CVP, as well as other structural effects. Figure 4.2 shows a sample of instantaneous centerplane acetone PLIF images for the $J = 61$ jet, both without and with external asymmetric forcing, using the 4-speaker clockwise and counterclockwise operation schemes, for various forcing frequencies f_f. The scalar concentration field C is normalized by the mean concentration in the jet potential core C_o, where C_o=1. Mean centerplane images are shown

in Appendix C. The unforced case is shown in Figure 4.2 (a), where the highly concentrated jet potential core extends to a vertical height of approximately $z/D \approx 4.5$. The upstream shear layer instability roll up is observed to initiate at a vertical height of approximately $z/D \approx$ 2-2.5, which is consistent with initiation of the dominant instability in Figure 3.2 (b) for the unforced J= 61 transverse jet.

The changes in jet structure due to asymmetric forcing were subtle when examining the forced jet instantaneous centerplane image, as seen in Figures 4.2 (b)-(c). This outcome was perhaps not particularity surprising due to the very low forcing amplitudes employed in this study. When the transverse jet was externally forced at f_f = 875 Hz, 1600 Hz, 1900 Hz, and 2300 Hz with forcing amplitude P'$\approx$ 0.15 Pa, the upstream shear layer roll up initiated closer to the jet exit, at a vertical height of approximately $z/D\approx$ 1.5. The height of the jet potential core was fairly unaffected by the external asymmetric forcing, except in the case of f_f= 1600 Hz at amplitude P'=0.15 Pa, where the jet potential core appeared thinner and extended to a vertical height of $z/D\approx$5.5, and in the case of f_f= 875 Hz at amplitude P'=0.15 Pa, where the jet potential core was slightly reduced to approximately $z/D\approx$4.0.

Perhaps the most obvious and unusual feature of the J = 61 equidensity JICF is the highly asymmetric cross-section, and this asymmetry in the CVP amplifies as the flow evolves spatially (Kuzo, 1996; Getsinger et al., 2014; Gevorkyan et al., 2016). Visualization of mean cross-sectional slices at x/D = 2.5, 5.5, and 10.5 downstream of the jet exit thus has the potential to illustrate the influence of helical forcing on jet structure. Results are shown in Figures 4.3 through 4.6 for a selection of excitation amplitudes and forcing frequencies studied, additional images are shown in Appendix C. Figures 4.3 through 4.6 show the mean cross-sectional images for asymmetric excitation of the J = 61 jet, in both the 4-speaker clockwise and counterclockwise directions for x/D =2.5, x/D = 5.5, and x/D =10.5; the naturally occurring unforced jet's mean images are shown in Figure 4.3 (a) as reference. Note that the cross-sectional scalar images were quantified using calibrated centerplane images (which included a known concentration in the potential core) with a thin 7-pixel wide slice of the jet image at the same average x-location (Gevorkyan et al., 2016). Figures 4.3-4.6

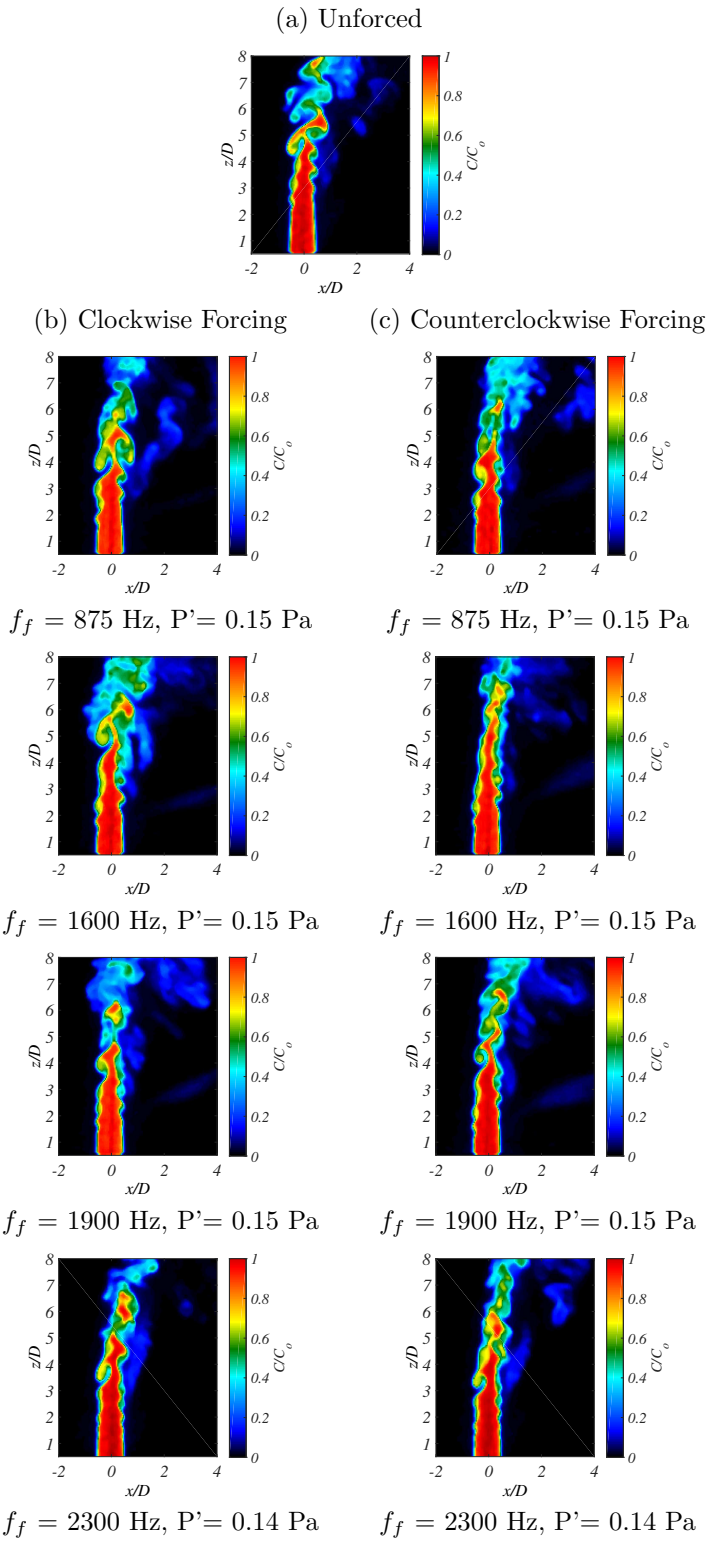

Figure 4.2: Instantaneous centerplane acetone concentration images in the regular plane (x/D - z/D) for the $J = 61$ jet for (a) the unforced case (where f_o = 1600 - 1900 Hz) as well as 4-speaker (b) clockwise and (c) counterclockwise forcing for various f_f forcing frequencies, where P'≈0.15 Pa.

show asymmetric forcing for a fixed forcing frequency f_f, while the pressure perturbation P' was increased sequentially.

Figure 4.3 shows the unforced jet cross-section and the effects of forcing on cross-sectional structure at f_f = 1600 Hz at P'= 0.075 Pa and 0.15 Pa, where f_f = 1600 Hz, P'=0.15 Pa corresponded to lock-in of the USL per Figure 3.4 (b). When forcing at f_f = 1600 Hz, at the lower end of the USL fundamental range, with a low pressure perturbation amplitude P'=0.075 Pa (4.3 (c) and (d)), there were minimal differences observed between the effects of clockwise and counterclockwise forcing on the jet cross-section. However when the forcing amplitude was increased to P'=0.15 Pa, the far field for both clockwise and counterclockwise forcing conditions resulted in a symmetrized structure, as compared to the unforced case, yet the clockwise direction produced a fairly organized CVP structure, with two clear lobes, while the counterclockwise direction produced a more uniform structure. The observed differences in jet cross-sectional structure under directional forcing in this case is interesting, since the USL vertical velocity power spectra associated with this case (Figure 3.4 (b)) showed no difference in the clockwise vs. counterclockwise response.

In Figure 4.4, 4-speaker forcing f_f = 875 Hz at amplitudes P'= 0.025 Pa, 0.15 Pa, and 0.225 Pa, where f_f = 875 Hz at P'= 0.225 Pa corresponded to lock-in of the USL per Figure 3.9 (a), there were again differences observed between the effects of clockwise and counterclockwise forcing on the jet cross-section. Forcing at f_f = 875 Hz, P'= 0.225 Pa in the clockwise direction (Figure 4.4 (e)), for example, showed symmetrization beginning at x/D = 5.5, while the counterclockwise forcing (Figure 4.4 (f)) showed CVP symmetrization in the near field at x/D=2.5, with the asymmetry temporarily reversed at x/D = 5.5. The associated USL velocity spectra for this case showed little differences in response between clockwise vs. counterclockwise forcing.

Figure 4.5 shows clockwise and counterclockwise directional forcing for f_f = 1000 Hz with pressure perturbation amplitudes P'= 0.19 Pa, 0.50 Pa, and 0.65 Pa, where f_f = 1000 Hz P'= 0.19 Pa corresponded to lock-in of the USL per Figure 3.5 (b). There were again differences observed between the effects of clockwise and counterclockwise forcing on the jet

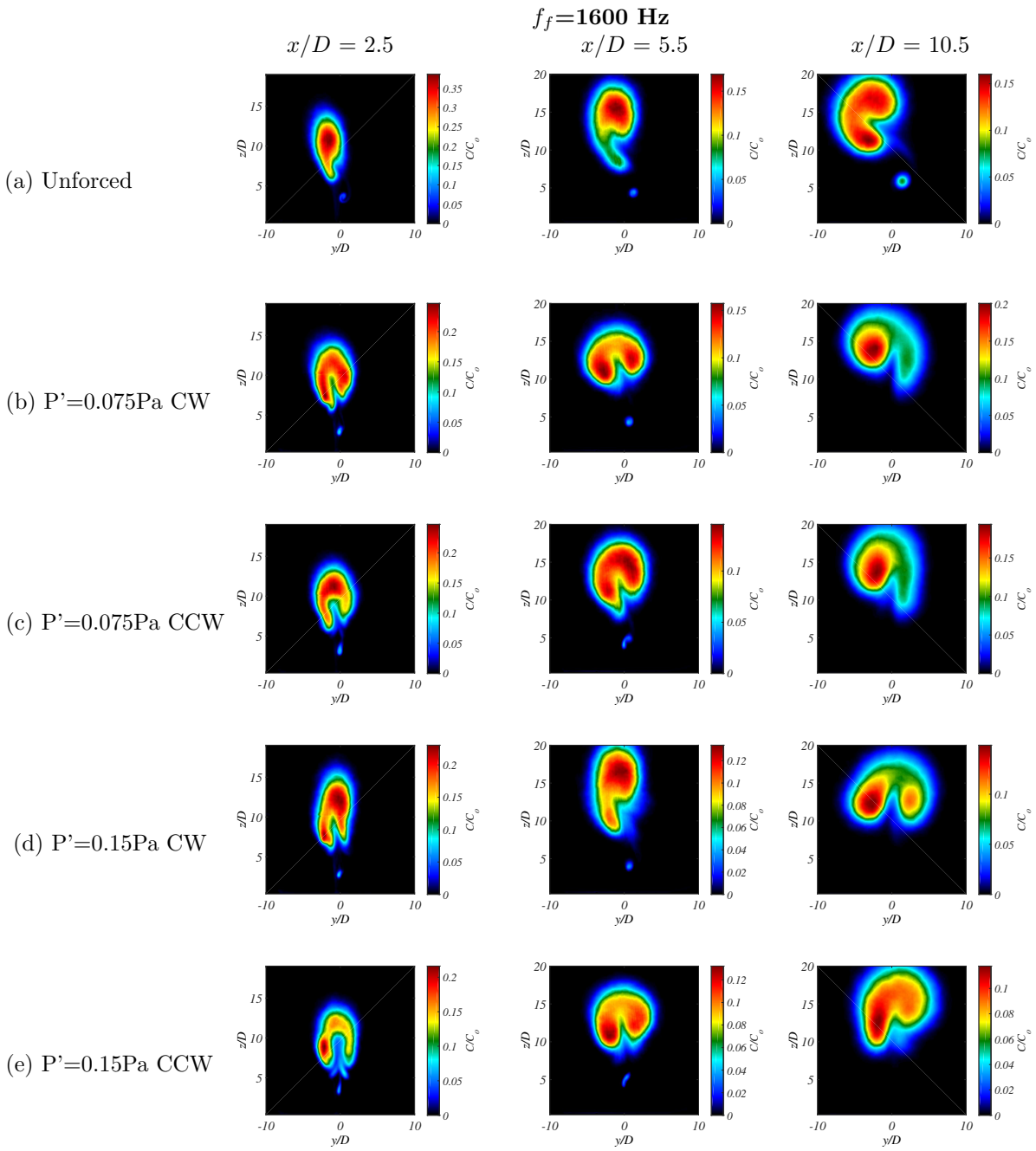

Figure 4.3: Mean PLIF images in the cross-sectional y/D-z/D plane for the J=61 JICF with natural frequency is the range of f_o=1600-1900 Hz. (a)Unforced jet top row, (b)-(e) f_f=1600Hz for different pressure perturbations P' and speaker operational orientation as shown.

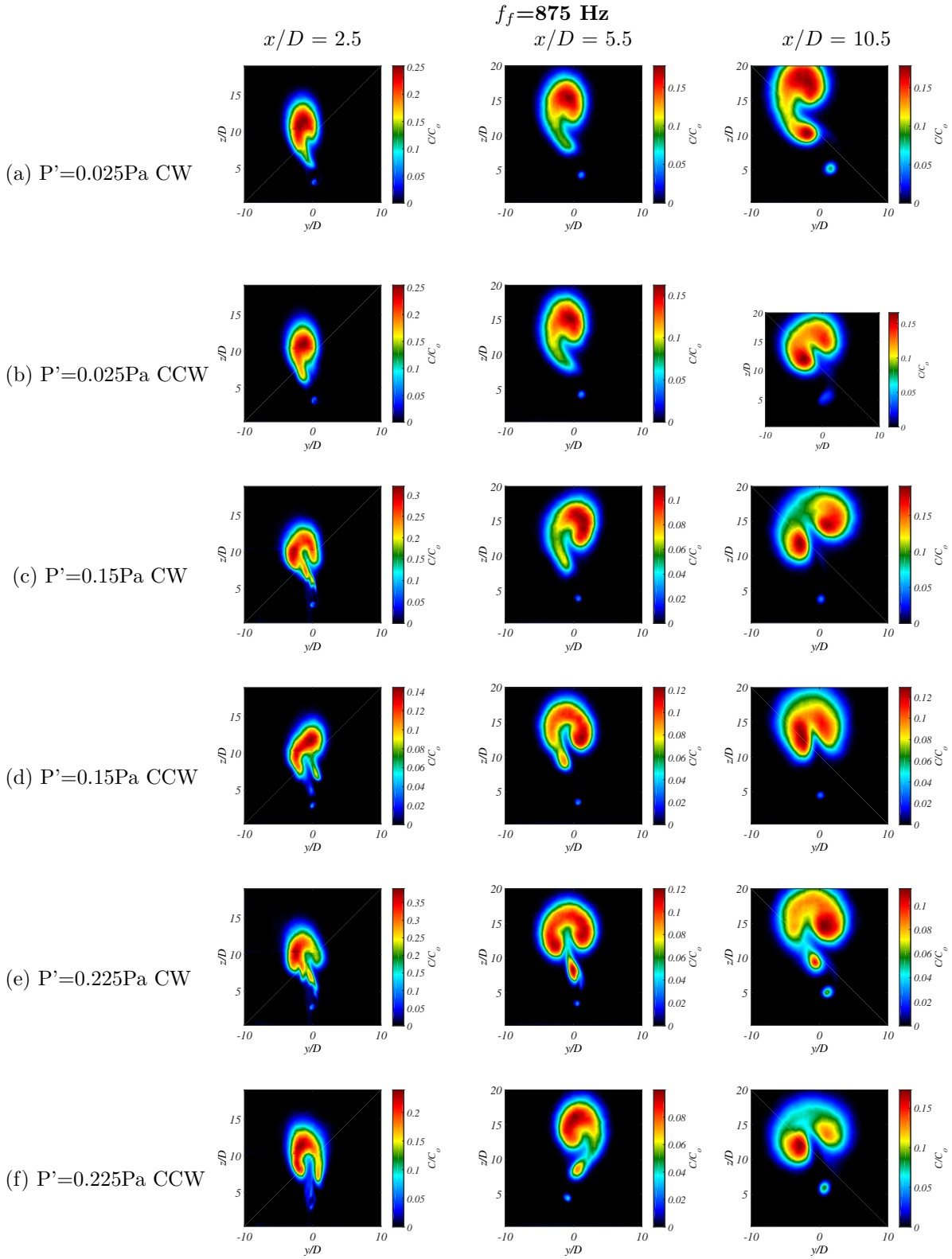

Figure 4.4: Mean PLIF images in the cross-sectional y/D-z/D plane for the J=61 JICF with natural frequency is the range of f_o=1600-1900 Hz. f_f=875 Hz for different pressure perturbations P' and speaker operational orientation as shown.

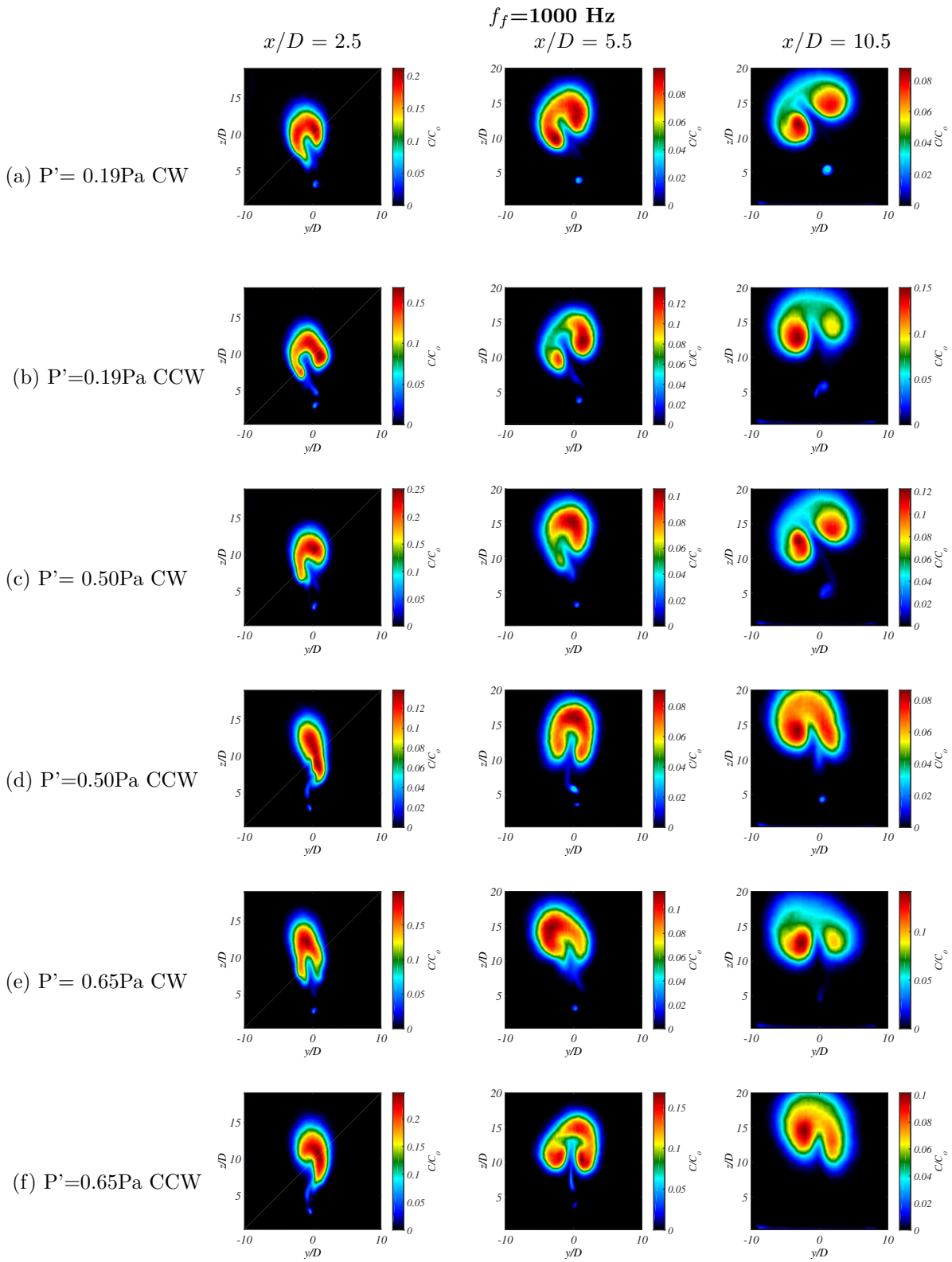

Figure 4.5: Mean PLIF images in the cross-sectional y/D-z/D plane for the J=61 JICF with natural frequency is the range of f_o=1600-1900 Hz. f_f=1000 Hz for different pressure perturbations P' and speaker operational orientation as shown.

cross-section. External excitation at f_f = 1000 Hz in the clockwise and counterclockwise conditions resulted in a symmetrized structure, as compared to the unforced case, yet the clockwise direction produced a fairly organized CVP structure with two clear lobes, while the counterclockwise direction in Figure 4.5 (d) and (e) produced a more uniform structure. The observed differences in jet cross-sectional structure under directional forcing in this case was not unexpected since per Figure 3.5, the general trend in response of the USL vertical velocity spectra under f_f = 1000 Hz asymmetric forcing showed the amplitudes of the counterclockwise disturbances was consistently greater than that of the counterclockwise for the odd harmonics ($3f_f$ and $5f_f$).

Figure 4.6 shows the effects of forcing at f_f = 2600 Hz, at amplitudes P'= 0.39 Pa, 0.65 Pa, and 0.79 Pa, all of which correspond to USL lock-in per Figure 3.9 (a). Forcing at f_f = 2600 Hz similarly showed little difference between clockwise and counterclockwise excitation effects, which produced a more singular structure in the far-field. The results of 4-speaker external excitation for f_f=2600 Hz, well above f_o, may indicate that a symmetrized 2-lobed CVP structure may be hard to produce at high frequencies, despite the USL exhibiting 1:1 lock-in to the applied forcing.

All excitation conditions in Figures 4.3-4.6 produced more symmetric cross-sections, though the improvements in Figure 4.6 (a) and (b) were very slight, despite lock-in of the jet upstream shear layer to f_f = 2600 Hz at amplitudes P' $\geq$ 0.39 Pa subject to CW 4 and CCW 4 forcing conditions. Figure 4.7 revisits the map of USL response to 4-speaker external forcing, with examples correlating the character of the USL response to the changes in jet mean cross-sectional structure under specific forcing conditions. The condition which did not result in lock-in, f_f = 3500 Hz with high amplitude pressure perturbation P'= 2.0 Pa for both CW 4 and CCW 4 speaker operation, did not result in any structural changes of the jet as shown in the inset image. However, forcing at a much lower amplitude P'=0.19 Pa, but with a locked-in USL at f_f = 1000 Hz, resulted in a dramatically altered cross sectional structure that was symmetrized. All forcing conditions which resulted in a locked-in USL as shown in Figure 4.7 produced more symmetric cross sections as compared to the unforced

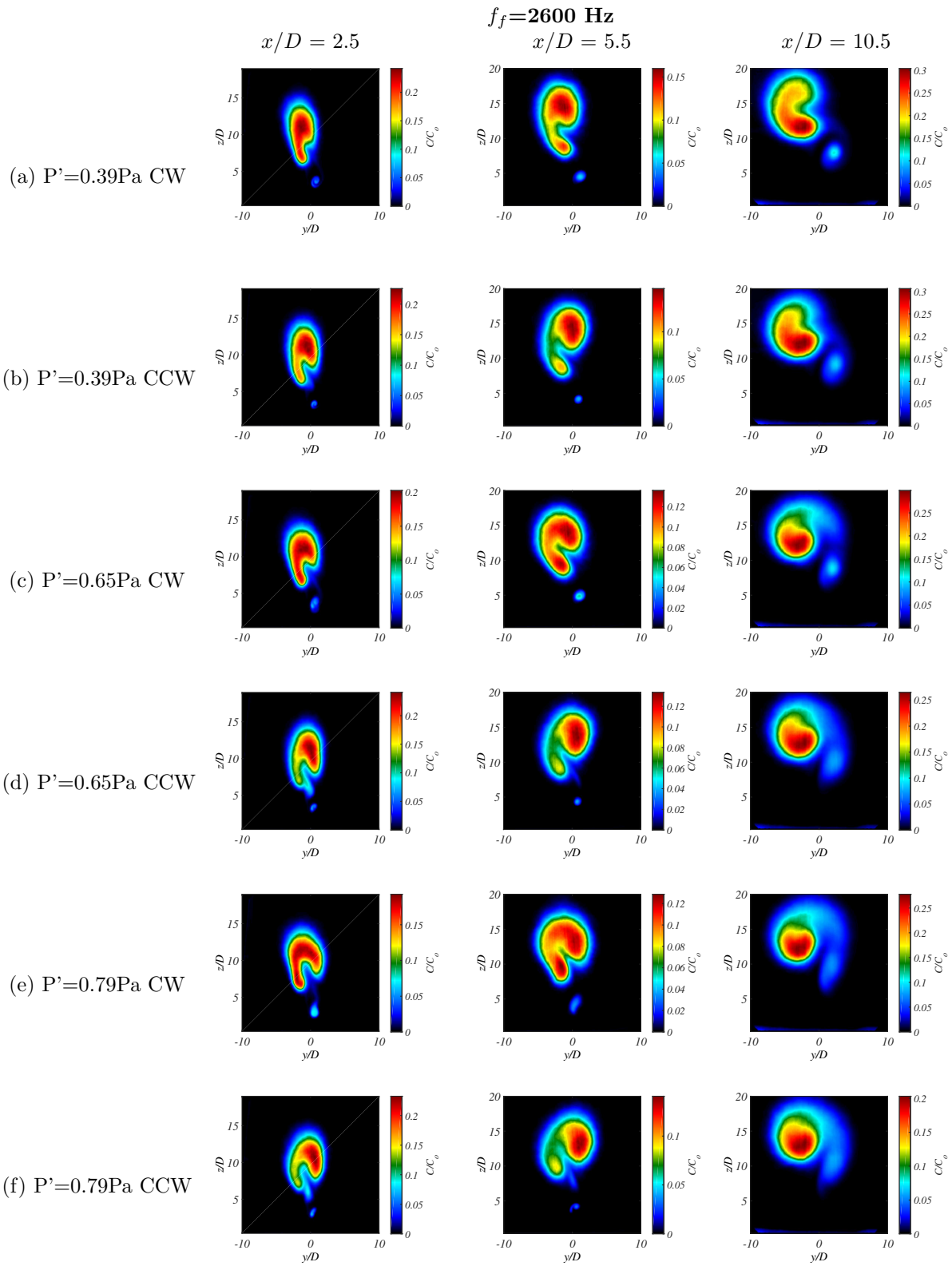

Figure 4.6: Mean PLIF images in the cross-sectional y/D-z/D plane for the J=61 JICF with natural frequency is the range of f_o=1600-1900 Hz. f_f=2600 Hz for different pressure perturbations P' and speaker operational orientation as shown.

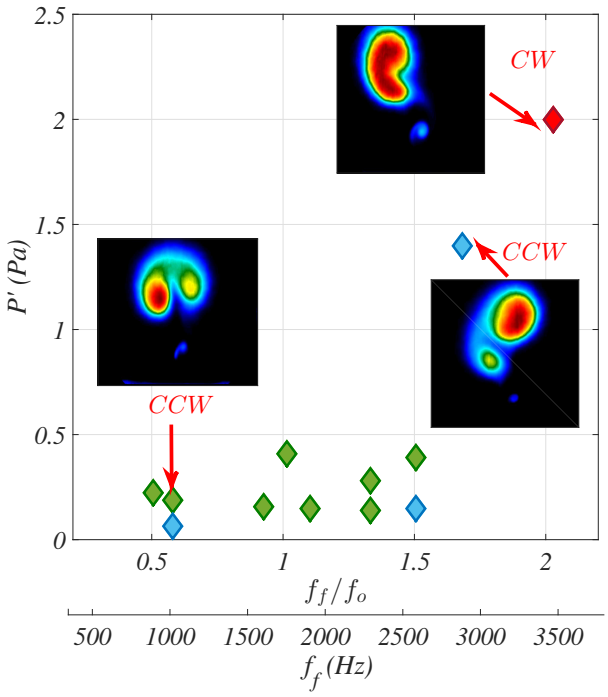

Figure 4.7: Map of USL response to 4-speaker external forcing, as shown in Figure 3.9, with inset of sample jet mean cross-sectional PLIF images taken at downstream location x/D=10.5. Green colored symbols represent 1:1 lock-in of the USL, blue symbols represent quasiperiodic behavior of the USL power spectra, and red symbols represent no lock-in of the USL to external forcing.

case, with the extent of symmetrization and overall shapes varied, which align with the PLIF imaging results of axisymmetric sinusoidal forcing by Shoji et al. (2019a), in which the $J = 61$ cross-sectional structure was altered when the USL was locked-in to the applied forcing.

4.2 2-Speaker and 1-Speaker Study

The influence of external asymmetric forcing on jet cross-sectional structure and relationships with USL velocity spectra lock-in was further explored with localized upstream and downstream forcing strategies. Jet instantaneous centerplane images for 2-speaker and 1-speaker forcing conditions were acquired and any changes in jet structure were very subtle as in Figure 4.2, therefore will not be discussed in detail here. Again the minimal changes in jet centerplane images was not surprising due to the very low forcing amplitudes employed

in these studies. Mean centerplane images for the 2-speaker and 1-speaker forcing are shown in Appendix C. As discussed previously in the 4-speaker study, due to the highly asymmetric cross-section of the naturally occurring $J = 61$ JICF, visualization of mean cross-sectional slices at $x/D = 2.5$, 5.5, and 10.5 downstream of the jet exit thus has the potential to illustrate the influence of localized external asymmetric forcing.

Figure 4.8 shows the effects of forcing the upstream region of the jet at $f_f = 875$ Hz, with amplitude P'= 0.025 Pa, which corresponded to quasiperiodicity of the USL per Figure 3.7 (a). It was observed in Figure 4.8 (e) that the evolution of the jet cross-sectional structure appeared almost unchanged in the case of L U forcing, while all other forcing conditions resulted in some degree of structural changes. Meanwhile, CW U and R&L showed highly symmetrized cross-sections in the near field at $x/D = 2.5$ and in the far-field at $x/D = 10.5$. These variations in structure changes to the $J = 61$ equidensity jet, subject to localized upstream forcing at $f_f = 875$ Hz and amplitude P'= 0.025 Pa, are consistent with the associated USL velocity power spectra, in which the response amplitude of the jet at $f_f = 875$ Hz to L U forcing was the lowest in magnitude, followed by the CCW U, while amplitudes of USL responses to CW U and R&L forcing were the greatest, with an order of magnitude difference between the overall minimum and maximum response. It is interesting and important to note that excitation at the right upstream side has a much more significant effect on symmetrizing the JICF cross-section than the LU forcing at the same amplitude. The localized R U forcing produced a response amplitude in the USL power spectra which was approximately 6 dB greater at f_f than the response induced by LU, again suggesting inherent natural asymmetries in the upstream region of the jet. Although none of the conditions in Figure 4.8 had an USL which was locked-in to the forcing, and all conditions exhibited quasiperiodicity, it appeared that in this case there may exist a minimum threshold amplitude of the response disturbance at f_f required to affect the jet cross-sectional structure, and the response in the USL for L U did not meet this threshold amplitude. Furthermore, as the response amplitude of the USL at f_f increased sequentially for other upstream speaker

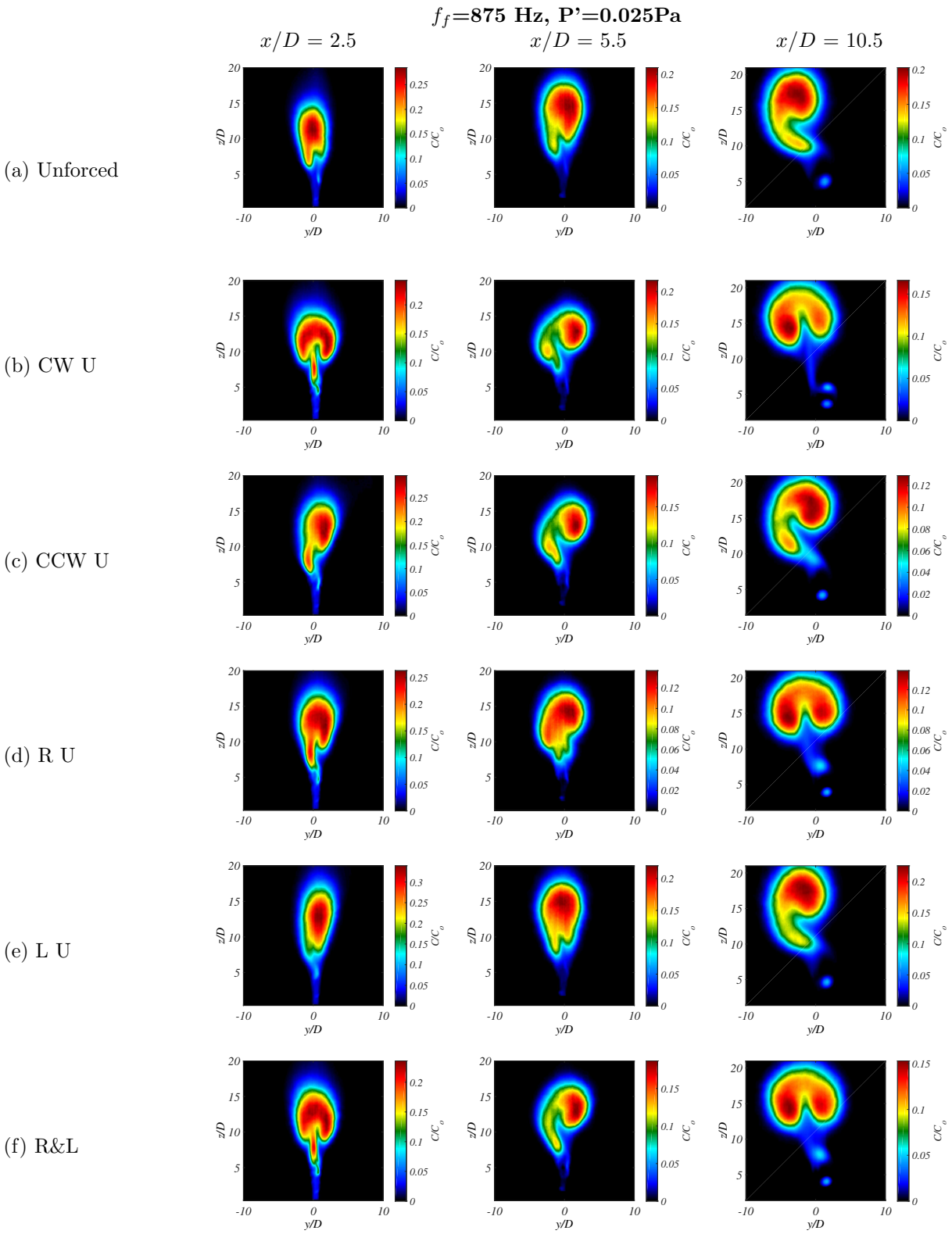

Figure 4.8: P'=0.025 Pa Mean PLIF images in the cross-sectional y/D-z/D plane for the J=61 JICF with natural frequency is the range of f_o=1600-1900 Hz. f_f=875 Hz for different pressure perturbations P' and upstream speaker operational orientation as shown.

operation strategies at the fixed forcing frequency and pressure perturbation, the degree of symmetrization in the associated jet cross-sections was also increased.

The acetone PLIF images in Figure 4.9 demonstrated the evolution of the jet cross-section when subject to upstream external asymmetric forcing at f_f = 1600 Hz (at the lower end of the USL fundamental range $f_o \approx$ 1600-1900 Hz) with forcing amplitude P' = 0.15 Pa, all conditions of which corresponded to USL lock-in per Figure 3.7 (b). All speaker operation strategies led to increased symmetrization of the jet cross-section. Upon examination of the USL response spectra to these forcing conditions, although the amplitude of disturbance at the forcing frequency was similar for each speaker operation strategy (within 4dB), the CCW U and R&L responded identically at f_f, with the lowest response amplitude of -8 dB. Interestingly the CCW U and R&L forcing also resulted in nearly identical cross-sections at x/D = 10.5, appearing as symmetrized, uniform structure without clear CVP lobes. CW U, R U, and L U forcing resulted in slightly increased amplitude responses of the USL at f_f (-6 dB to -4 dB), and as seen in Figure 4.9 (b), (d), and (e), produced more symmetrized cross-sections in the far-field at x/D = 10.5, as compared to CCW U and R&L, yet with clear CVP lobes. Thus it is interesting that 2 different speaker operation strategies with identical response of the USL disturbance at f_f produced nearly identical changes to the jet structure, while speaker operation strategies with slightly greater amplitude in the USL response at f_f produced different, more CVP-like structures, suggesting that the exact amplitude of USL response is important to jet structure, even when the USL is locked-in to the forcing.

The PLIF cross-sectional evolution images for what is perhaps the most interesting USL response to asymmetric forcing, upstream speakers subject to f_f = 1900 Hz at amplitude P'= 0.15 Pa, are shown in Figure 4.10. The PLIF images clearly showed all forcing conditions produced nearly identical cross-section structures at all imaged downstream locations. However, these forcing conditions corresponded to USL velocity power spectra shown in Figure 3.7 (c), in which all forcing conditions exhibited 1:1 lock-in of the USL, with the exception of R U which was not locked-in. The weak response of the USL to R U f_f = 1900 Hz forcing condition led to the prediction that any changes in the jet structure would not be as

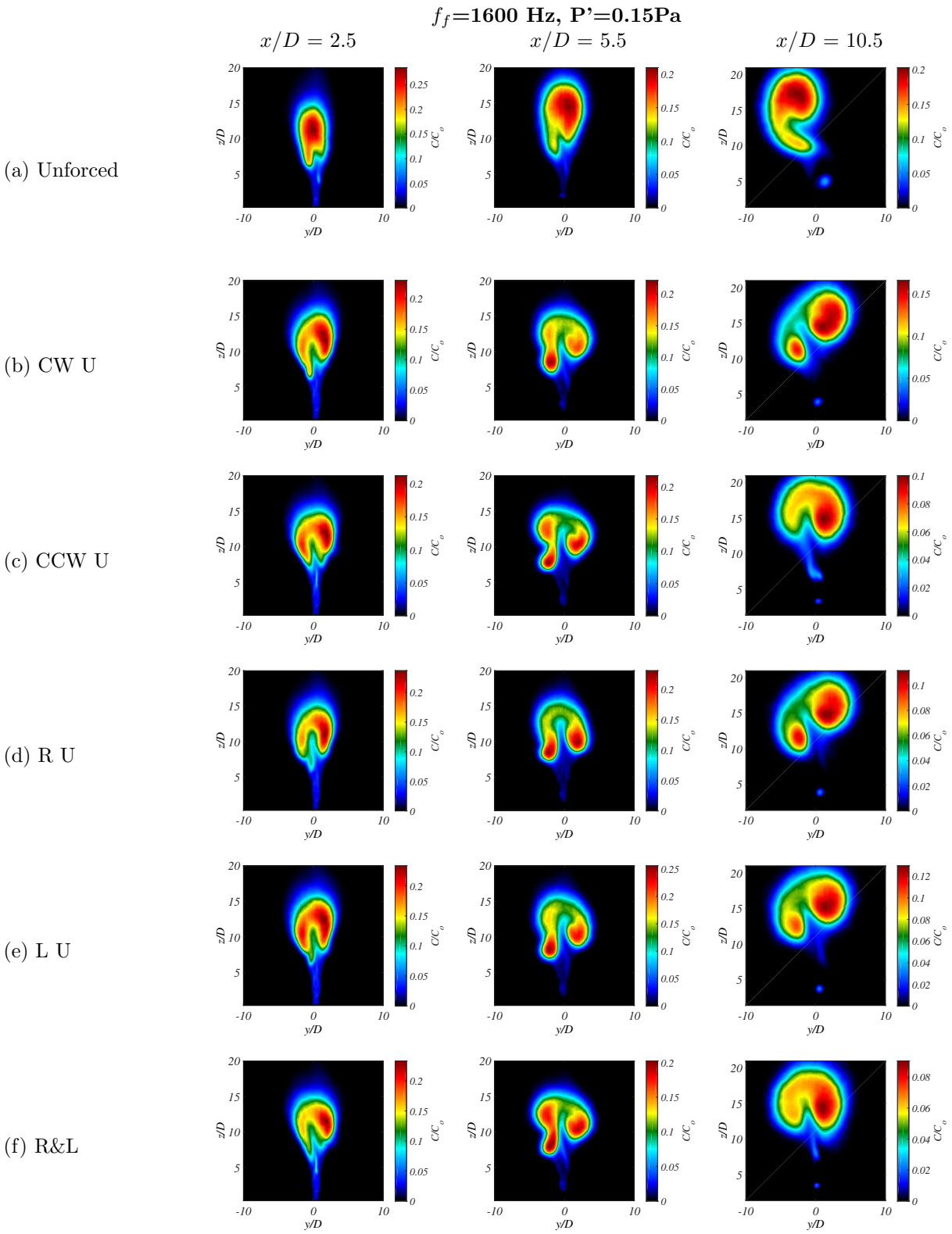

Figure 4.9: P'=0.15 Pa Mean PLIF images in the cross-sectional y/D-z/D plane for the J=61 JICF with natural frequency is the range of f_o=1600-1900 Hz. f_f=1600 Hz for different pressure perturbations P' and upstream speaker operational orientation as shown.

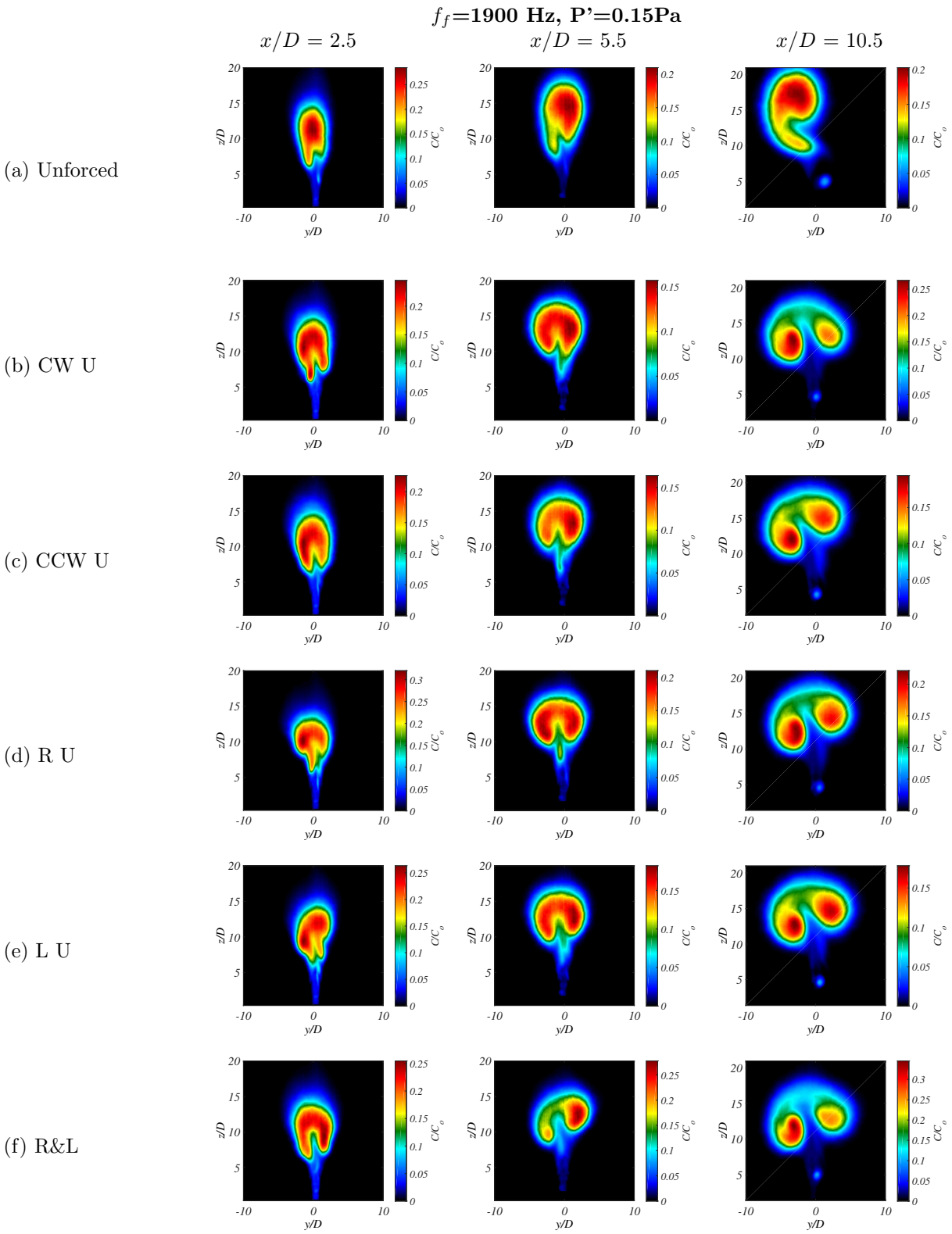

Figure 4.10: P'=0.15 Pa Mean PLIF images in the cross-sectional y/D-z/D plane for the J=61 JICF with natural frequency is the range of f_o=1600-1900 Hz. f_f=1900 Hz for different pressure perturbations P' and upstream speaker operational orientation as shown.

enhanced as for other speaker operation strategies, or perhaps no changes would be observed at all as in Figure 4.8 (e), where the USL was not locked-in to the applied forcing. Yet interestingly, the changes in structure under R U asymmetric excitation were as equally profound as the cases in which the USL was locked-in. Re-examination of the USL power spectra for upstream speaker operation at f_f = 1900 Hz with amplitude P'= 0.15 Pa in Figure 3.7 (c) showed that although R U did not meet the definition of lock-in since the magnitude of f_o was not sufficiently diminished, there was only a single order of magnitude reduction in the response of the upstream shear layer at f_o for this forcing condition (green line in Figure 3.7 (c)), and the response of the USL at f_f was quite similar for all speaker operation cases (within 3 dB), and the response of the vertical velocity power spectra at f_f was of greater amplitude than the response at f_o, even in the case of R U. This suggests that as long as f_f dominates over f_o, structural changes might be expected regardless of whether or not the USL exhibits 1:1 lock-in to the forcing.

Figure 4.11 revisits the map of USL response to upstream 2-speaker and 1-speaker external forcing, with examples correlating the changes in jet mean cross-sectional structure to the response of the USL under associated forcing conditions. Observations highlighted with figure insets show that the relationship of USL lock-in response and its influence on jet structural changes is more complex than "is the upstream shear layer locked-in or not?" to the external forcing. Upstream speaker operation which did not result in lock-in, R U f_f = 1900 Hz with amplitude pressure perturbation P'= 0.15 Pa, resulted in dramatic structural changes in the jet cross-section, which were of similar character to the 1:1 locked-in USL cases under the same forcing frequency and amplitude. All upstream region forcing conditions which resulted in 1:1 lock-in of the USL produced altered cross sections, as compared to the unforced case, with the extent of symmetrization and the resultant far field shape varied. Additionally, if the USL velocity power spectra exhibited quasiperiodic behavior in response to forcing, structural changes to the transverse jet cross section may occur (as in Figure 4.8 (e), (d), and (f)) or may not occur, as shown in the inset figure where f_f = 875 Hz with amplitude P'=0.025 Pa, under L U forcing.

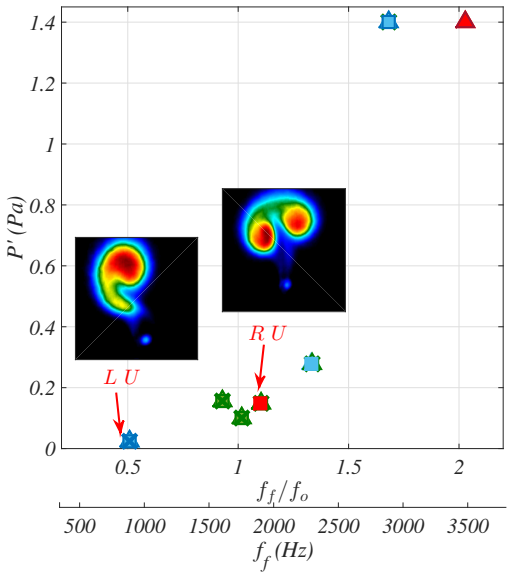

Figure 4.11: Map of USL response to upstream speaker external forcing, as shown in Figure 3.9, with inset of sample jet mean cross-sectional PLIF images taken at downstream location x/D=10.5. Green colored symbols represent 1:1 lock-in of the USL, blue symbols represent quasiperiodic behavior of the USL power spectra, and red symbols represent no lock-in of the USL to external forcing.

Asymmetric forcing of the transverse jet in the downstream region was also shown to influence the $J = 61$ jet cross-sectional structure. Figure 4.12 shows the jet structures produced as a result of downstream forcing at $f_f = 875$ Hz and amplitude P'= 0.225 Pa. The minimal changes observed here from downstream forcing, as opposed to the dramatic changes of full azimuthal 4-speaker forcing with the same frequency and amplitude seen in Figure 4.4 (e) and (f), are unsurprising since the USL was not locked-in to these downstream forcing conditions, per Figure 3.8 (a). The smallest degree of symmetrization occurred for the R D forcing, which was consistent with the fact R D forcing under these conditions elicited the lowest amplitude response in the USL at f_f. Conversely, CW D and CCW D forcing resulted in the highest and second highest amplitude responses at f_f in the USL velocity power spectra, and also produced nearly identical structures along the transverse jet cross-section. An unexpected result was that the L D forcing produced a very symmetric cross-section at $x/D = 10.5$, despite a lower amplitude response in the USL velocity

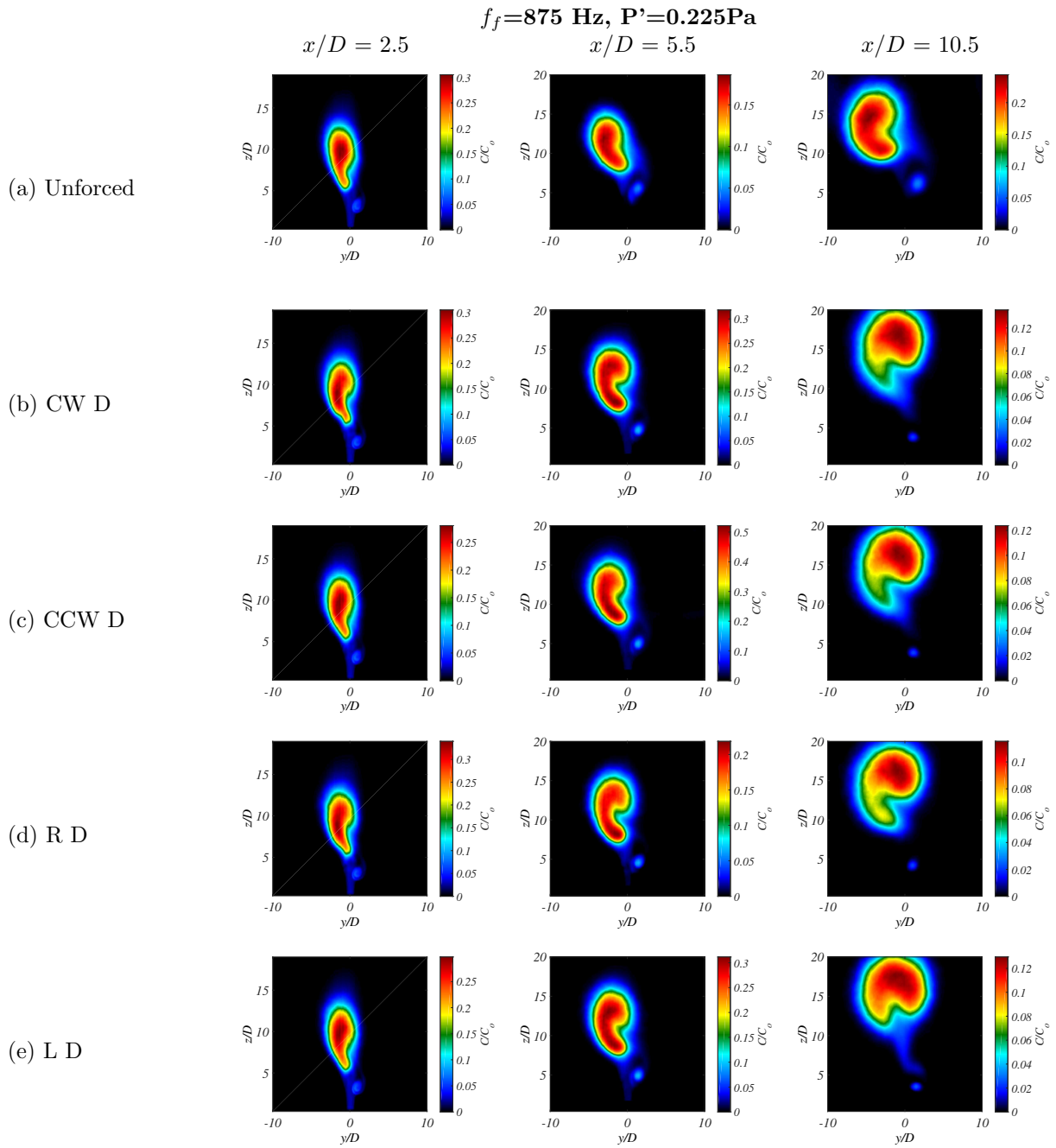

Figure 4.12: Mean PLIF images in the cross-sectional y/D-z/D plane for the J=61 JICF with natural frequency is the range of f_o=1600-1900 Hz. f_f=875 H, pressure perturbation P'=0.225 Pa, and downstream speaker operational orientation as shown.

power spectra at f_f, as compared to CW D and CCW D.

Figure 4.13 shows PLIF jet cross-sectional images for the $J = 61$ transverse jet subject to downstream asymmetric forcing at $f_f = 1900$ Hz and amplitude P'= 0.15 Pa. All speaker operation strategies corresponded to USL lock-in per Figure 3.8 (c). Notable here, it was observed that L D forcing produced the most clearly organized CVP with two lobes in the far-field at $x/D = 10.5$, however this forcing strategy was not the condition which resulted in the greatest amplitude lock-in to f_f of the USL for $f_f = 1900$ Hz downstream forcing. These pieces of information, combined with the observations of Figure 4.12 (e), suggest that the wake region is also important in the formation of the transverse jet far field structure, and perhaps the left side (port) wake region may be particularly susceptible to external forcing, at least, for the specific natural asymmetric cross-sectional shape associated with the unforced JICF explored here. This would agree with the numerical sensitivity study by Regan (2018) which finds for the $R = 4$ ($J = 16$) equidensity JICF, which has a convectively unstable shear layer, a wavemaker region, associated with the mode with the greatest growth rate, exists downstream of the jet, with a bias towards the port side of the symmetry plane.

The USL response map for downstream localized forcing studies is shown again in Figure 4.14. All cases in which the USL was locked-in to the downstream asymmetric forcing produced a jet cross-section which was more symmetric as compared to the unforced case. Highlighted in the figure insets are three CW D forcing cases subject to the same excitation frequency $f_f = 875$ Hz but at different amplitudes; neither case had an USL which was locked-in to the forcing. The jet forced with an amplitude P'= 0.025 Pa did not exhibit any changes to the jet cross-sectional structure which is a result expected for an USL that is not locked-in. However when the amplitude of forcing was increased to P'= 0.225, small changes in the evolution of the jet cross section were observed. This result provides additional evidence that perturbing the wake region influences the convectively unstable transverse structure and that characterization of the USL alone may not provide a comprehensive representation of the flow field instabilities.

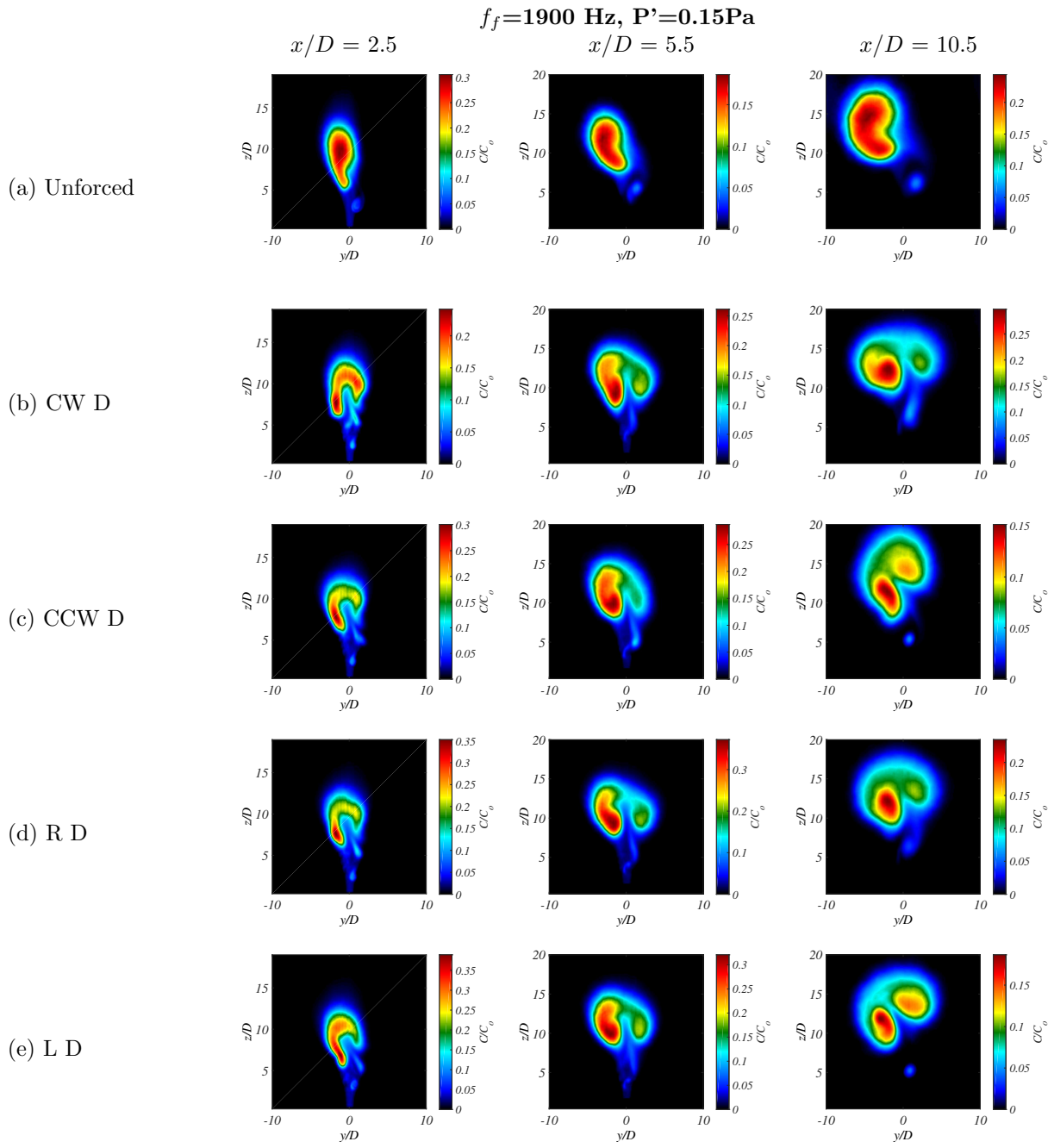

Figure 4.13: P'=0.15 Pa Mean PLIF images in the cross-sectional y/D-z/D plane for the J=61 JICF with natural frequency is the range of f_o=1600-1900 Hz. f_f=1900 Hz for different pressure perturbation P'=0.15 Pa and downstream speaker operational orientation as shown.

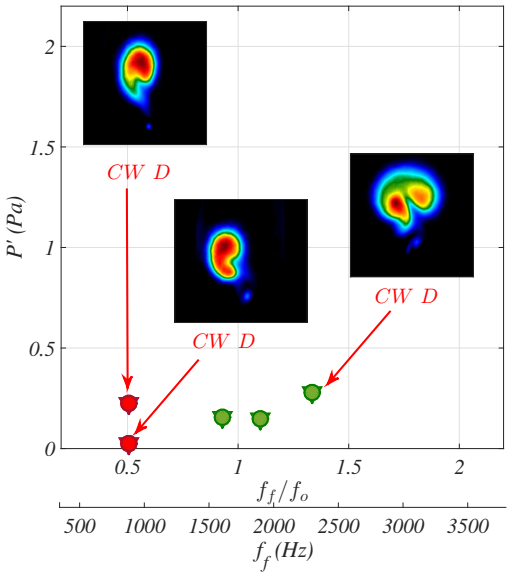

Figure 4.14: Map of USL response to downstream speaker external forcing, as shown in Figure 3.9, with inset of sample jet mean cross-sectional PLIF images taken at downstream location x/D=10.5. Green colored symbols represent 1:1 lock-in of the USL, blue symbols represent quasiperiodic behavior of the USL power spectra, and red symbols represent no lock-in of the USL to external forcing.

4.3 Localized Forcing of $J = 6$ and $J = 24$ Transverse Jets

A limited study was conducted on transverse jets at lower momentum flux ratios, $J = 24$ and $J = 6$, whose upstream shear layers are convectively unstable and absolutely unstable, respectively, as seen in Figure 3.2 (c)-(f). Here the effects of localized 2-speaker and 1-speaker external forcing in the upstream region on the jet structure was explored. As seen in Figure 4.15 (a), the unforced $J = 24$ jet in general had a naturally symmetric cross-section throughout its spatial evolution, especially in the downstream at $x/D = 10.5$; this generally symmetric cross-sectional shape was consistent with earlier results for the JICF shown in Getsinger et al. (2014) . Asymmetric forcing was applied in the region upstream of the jet exit, at $f_f = 1900$ Hz, where f_f was taken as the mean of the USL fundamental range $f_o \approx$ 1750-2050 Hz. Excitation was applied at P'= 0.15 Pa, the same amplitude used in the $J =$ 61 localized forcing studies. All speaker operation strategies (CW U, CCW U, R U, L U,

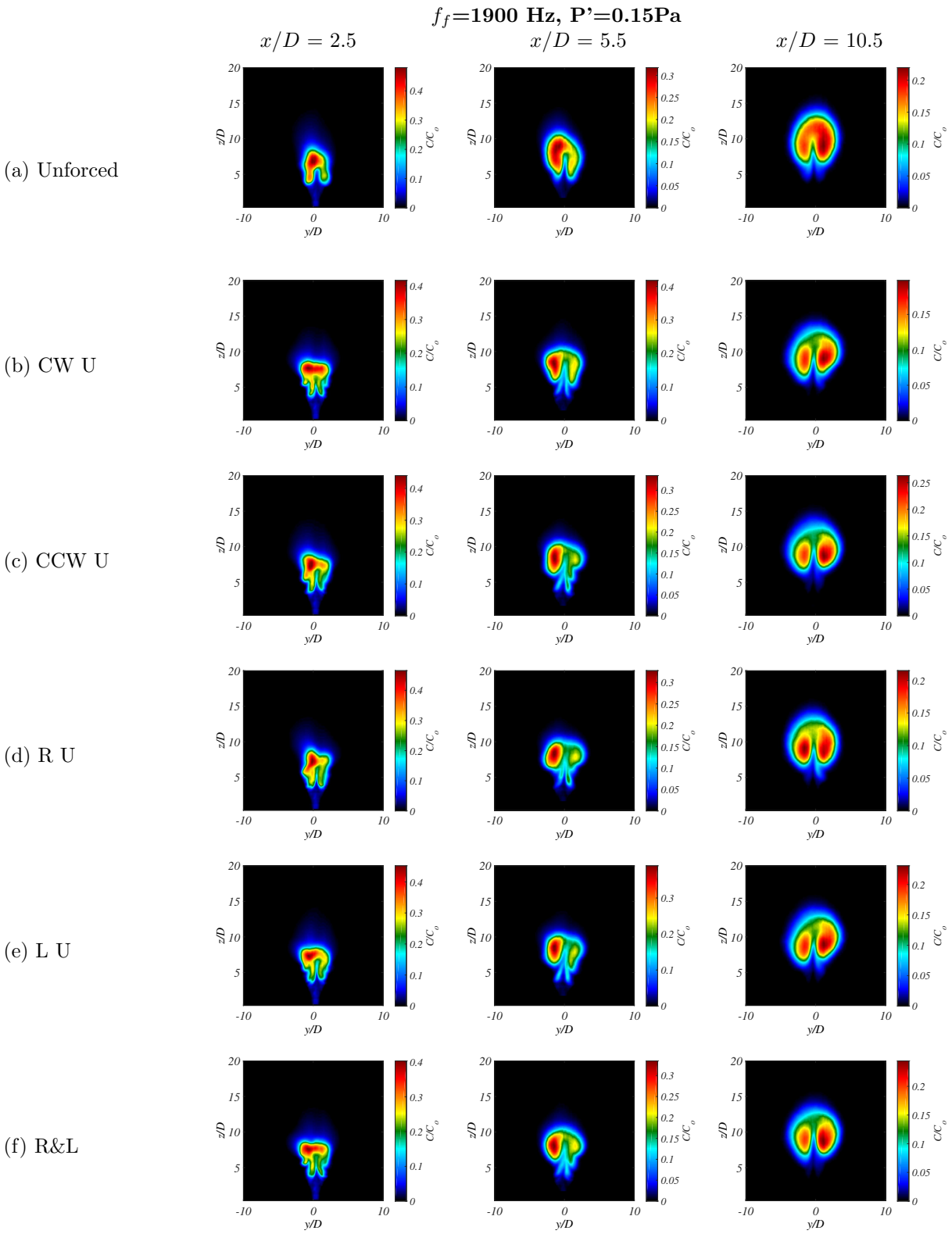

Figure 4.15: Mean PLIF images in the cross-sectional y/D-z/D plane for the J=24 JICF with natural frequency in the range of f_o=1750-2050 Hz. Unforced case is shown in (a), and excitation at f_f=1900 Hz with pressure perturbation amplitude P'= 0.15 Pa for various upstream speaker operation strategies are shown in (b)-(f).

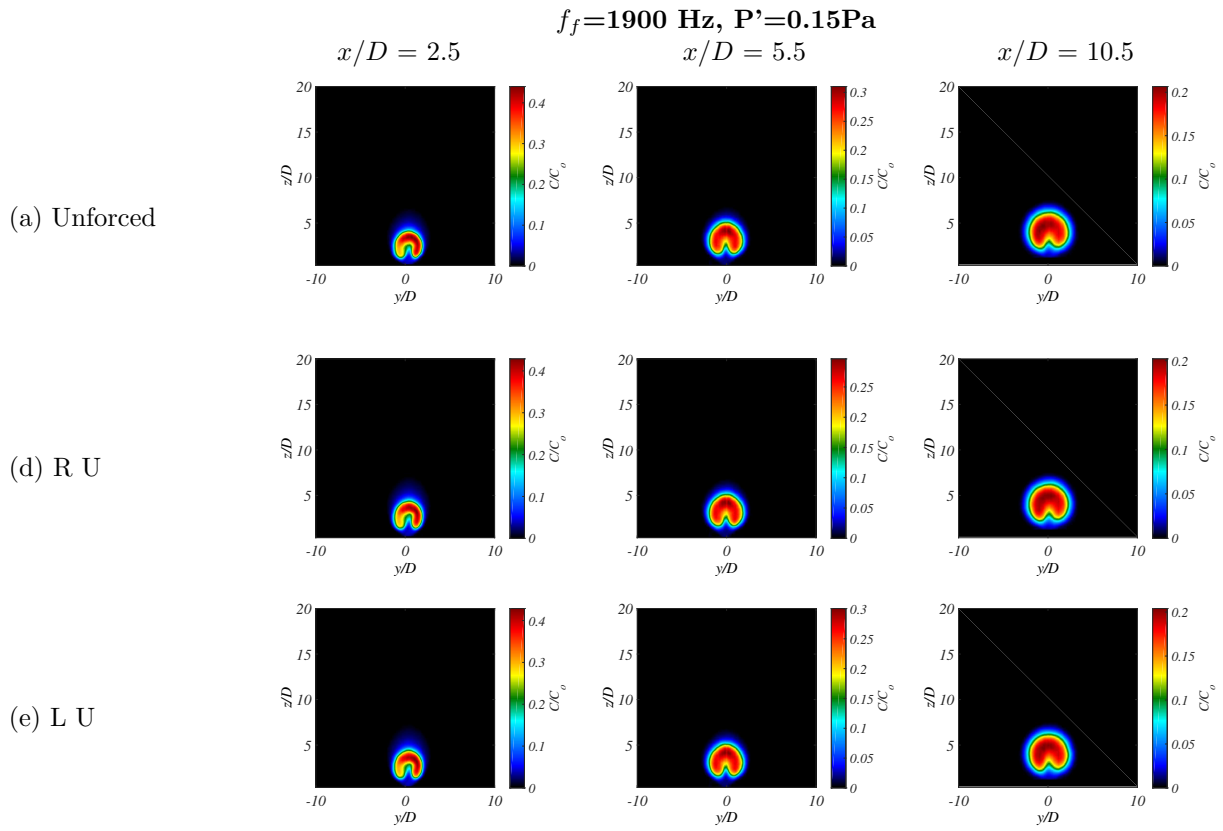

Figure 4.16: Mean PLIF images in the cross-sectional y/D-z/D plane for the J=6 JICF with natural frequency of f_o=1900 Hz. Unforced case is shown in (a), and excitation at f_f=1900 Hz for pressure perturbation P'= 0.15 Pa for (b) right and (c) left upstream speaker operation are shown.

and R&L) produced a cross-section with clear and distinct CVP lobes, in contrast to the unforced $J = 24$ transverse jet whose symmetric cross-section was of fairly uniform concentration throughout the overall shape. Interestingly, R U maintained the most symmetric overall shape and evenly distributed concentration across the two CVP lobes at $x/D = 10.5$, while the other forced cases skewed slightly to the right, with the right CVP lobe retaining higher point concentration than the left. This may suggest that the $J = 24$ transverse jet's USL was least responsive to R U forcing at $f_f = 1900$ Hz, similar to the $J = 61$ jet's response to R U forcing for $f_f > f_o$, or that the USL velocity spectra for R U could be of different character than other speaker operation strategies illustrated in Figure 4.15.

The $J = 6$ JICF has a globally unstable upstream shear layer and previous studies have

demonstrated that low level axisymmetric sinusoidal excitation has a lesser effect on jet structure (Davitian et al., 2010b; Shoji, 2017; Shoji et al., 2019a), requiring higher amplitude perturbations to produce changes. Figure 4.16 shows the results of asymmetric upstream excitation on the $J = 6$ equidensity transverse jet at $f_o = f_f = 1900$ Hz at amplitude P'= 0.15 Pa. Unsurprisingly, it was observed that the very low level forcing had no effect on the jet structure, since for an absolutely unstable JICF the USL already has strong periodic vortex rollup close to the jet exit, and this vorticity interacts with the incoming flow in forming the CVP early in the jet cross-sectional evolution. Also, for an absolutely unstable USL, the dominant disturbance is self-excited, extremely pure-toned, and remains so far downstream along the jet USL trajectory coordinate s, which makes the USL less susceptible to energy transfer induced by external forcing.

The results of this chapter demonstrate that the upstream shear layer instabilities are related to and in some cases can predict the nature of jet structure. Variation in structure observed in Figures 4.3-4.15 suggest there would be associated variation in mixing characteristics. Since in general, a JICF with an absolutely unstable USL and with a naturally symmetric cross section tends to be a better mixer, does this trend apply to the forced cases? If applied external forcing to a naturally asymmetric jet causes the structure to become more symmetrized, is mixing enhanced? These issues will be explored in detail in the next chapter

CHAPTER 5

Mixing and Dynamical Characteristics Extracted from Scalar Concentration Fields

5.1 Effects of Asymmetric Forcing on JICF Mixing

This section discusses the effect of external asymmetric sine wave forcing on the transverse jet mixing. In addition to visually observing the changes in cross-sectional jet structure induced by various external asymmetric forcing schemes, PLIF imaging of the scalar concentration field enabled quantitative evaluation of jet mixing with the crossflow. As noted by Gevorkyan et al. (2016), the transport processes of the low Reynolds number flow field are mainly diffusion limited, therefore mixing metrics discussed here focus on molecular mixing. The Unmixedness (U) metric, which represents the second moment of the scalar field (Danckwerts, 1952; Smith et al., 1997; Kukukova et al., 2009), was used here to quantify mixing:

$$U = \frac{1}{L_y L_z} \int \int \frac{(C/C_0 - \bar{C}/C_0)^2}{\bar{C}/C_0(1 - \bar{C}/C_0)} dydz \tag{5.1}$$

where C/C_0 is the local normalized value of scalar (acetone) concentration at a pixel element at (y,z), $\bar{C}/C_0$ is the spatial average over the domain, C_o is the concentration at the jet exit, and L_y and L_z are the length scales of the local jet interrogation area over which data are quantified. The local U can be evaluated in both cross-sectional and centerplane views, with a matching of the mean concentration $\bar{C}$ at all locations and flow conditions achieved by altering the local interrogation area (e.g., $L_y L_z$) by adding or subtracting zero-valued

pixels, thus enabling comparison of molecular mixing for different cases. The Unmixedness calculation is applied to each scaled instantaneous image at each location and then averaged over the entire data set, typically consisting of 500 images (Gevorkyan et al., 2016; Gevorkyan, 2015). Note that the cross-section based Unmixedness could not be calculated for a few cases when a given mean cross-sectional image could not be appropriately scaled in comparison with the corresponding mean centerplane image, typically due to rather extreme asymmetries as discussed in Chapter 2. Hence, the data points for these cases were omitted from this section. Unmixedness is quantified on a scale of 0-100%, a low value of Unmixedness corresponds to a more homogeneous, or well mixed field, while higher U means greater segregation of fluids and a lesser degree of molecular mixing.

5.1.1 4-Speaker Study, Mixing Characteristics

The influence of asymmetric forcing on structural characteristics of the transverse jet was investigated in Chapter 4, and it was found that in general, when the upstream shear layer of the naturally convectively unstable $J = 61$ jet was locked-in to the excitation, the jet cross-section became more symmetrized. Prior studies have shown that a JICF with an absolutely unstable USL and with a naturally symmetric cross section tends to have a lower Unmixedness (Gevorkyan et al., 2016) for both the centerplane and cross-sectional views. Figure 5.1 shows select results of centerplane Unmixedness $U_{c,xz}$, based on 7 pixel width sections (in the x-direction) and matched mean concentrations evaluated in the local $x - z$ plane as described in Gevorkyan et al. (2016). Additional results are shown in Appendix D. Both clockwise and counterclockwise forcing results utilizing all 4 speakers are shown, with comparison to unforced Unmixedness for the $J = 61$ equidensity transverse jet. In all cases shown in Figure 5.1, forcing created 1:1 lock-in of the USL per Figure 3.9 (a). All forcing conditions improved the molecular mixing over that of the unforced jet, especially far downstream of the jet exit. In general, there were noticeable differences in the reduction of Unmixedness between the clockwise and counterclockwise directional application of forcing for a fixed frequency f_f, implying that cross-sectional alterations observed in Chapter 4

(Figures 4.3-4.6, D.30-31) had an effect on centerplane structure and mixing.

In general, at forcing frequencies which were below the fundamental, ($f_f < f_o$ as shown in 5.1 (a)), counterclockwise excitation at a given frequency and amplitude resulted in significantly greater mixing enhancement (lower U) than equivalent forcing in the clockwise direction, and that enhancement grew as the flow evolved downstream. An exception to this trend was for $f_f = 1000$ Hz excitation, where superior mixing was similar for both excitation orientations. Examination of the USL velocity power spectra (Chapter 3) for the asymmetric forcing conditions shown in Figure 5.1 (a), showed that excitation at $f_f = 1600$ Hz resulted in nearly identical amplitudes of response in the USL at f_f for both clockwise and counterclockwise directions, as seen in Figure 3.4 (b). This was also true for $f_f = 875$ Hz (Figure B.1 (a)). However, as shown in Figure 3.4 (a), for $f_f = 1000$ Hz with amplitude P'= 0.19 Pa, the clockwise direction produced a disturbance at f_f which was approximately an order of magnitude greater than response for the counterclockwise forcing. In this particular case the USL may be more receptive to clockwise forcing at this frequency, perhaps compensating for a general tendency of CCW 4 to be better mixed than CW 4, in the centerplane view, for a given forcing strategy when $f_f \leq f_o$.

When excitation was applied at frequencies above the fundamental ($f_f > f_o$ in Figure 5.1 (b)), it was observed that in general, clockwise excitation at a given frequency and amplitude resulted in greater mixing enhancement (in the centerplane) over the counterclockwise direction, in contrast to the lower frequency forcing trends in Figure 5.1 (a), with a significant enhancement of mixing (lower U) in the near-field for $f_f = 1900$ Hz. Examination of the USL velocity power spectra for the asymmetric forcing conditions of Figure 5.1 (b), showed that when forcing at $f_f = 2300$ Hz and $f_f = 2600$ Hz, the amplitude of response of the USL at f_f to clockwise and counterclockwise forcing was nearly identical for each case (per Figure B.1 (c) and (e)). However, the USL spectral character of $f_f = 1900$ Hz with amplitude P'= 0.15 Pa (Figure 3.4 (c)) showed that clockwise directional forcing saw the emergence of disturbances at the subharmonic of forcing $1/2f_f$, and combinations of the subharmonic with f_f and higher harmonics, while the counterclockwise directional forcing did not. There was

(a) f_f = 875-1600 Hz

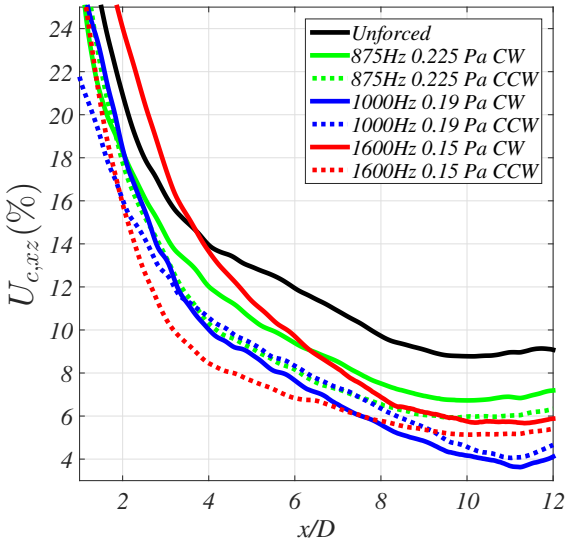

(b) f_f = 1900-2600 Hz

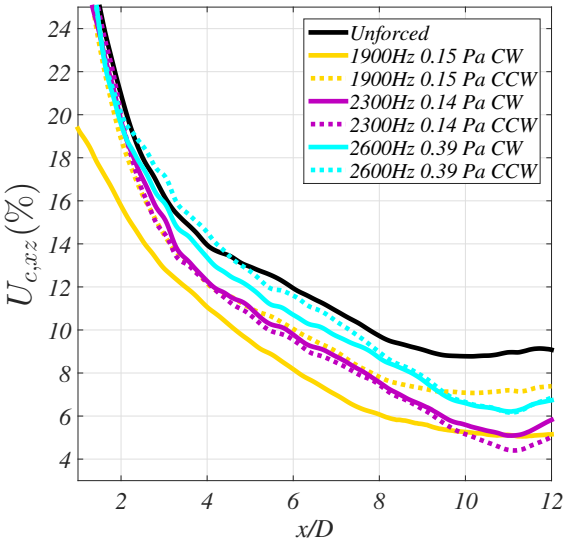

Figure 5.1: Centerplane based mean Unmixedness in the $x-z$ plane, with clockwise and counter-clockwise excitation of all 4 speakers at (a) f_f = 875 Hz, 1000 Hz, and 1600 Hz and (b) f_f = 1900 Hz, 2300 Hz, and 2600 Hz for $J = 61$. The fundamental frequency of the unforced JICF was f_o = 1725 Hz.

also a greater reduction in the spectral peak at the natural frequency f_o with CW forcing as compared with CCW forcing, suggesting the former had a more significant influence in creating lock-in and affecting the USL. These observations in the USL power spectra suggest the possibility of greater shear layer vorticity rollup and merger for the CW case, which would subsequently result in enhanced molecular mixing under this forcing condition, supporting the case for superior mixing of f_f = 1900 CW in Figure 5.1 (b).

Overall, the mixing enhancement provided by external helical forcing was accomplished here at a much lower perturbation amplitude, up to two orders of magnitude lower, than that which is required for axisymmetric sinusoidal forcing of the $J = 61$ transverse jet (Shoji, 2017; Shoji et al., 2019a).

The cross-section views of the jet provides the ability to calculate molecular mixing for cross-sectional slices of the full jet. While centerplane views could be misaligned with respect to the bulk of the jet itself, especially when asymmetric structures occurred, they did enable

(a) f_f = 875-1600 Hz

(b) f_f = 1900-2600 Hz

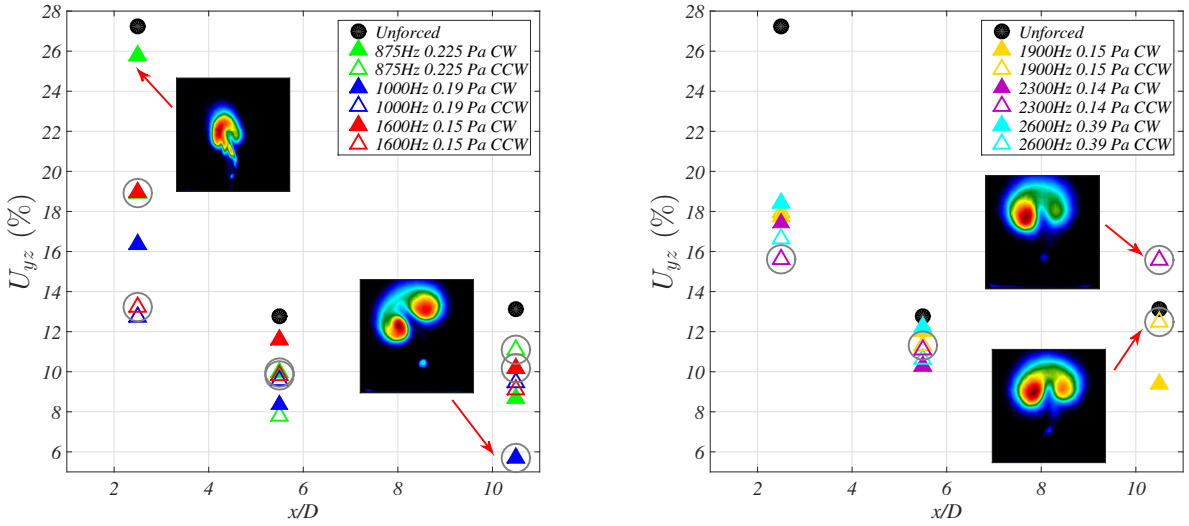

Figure 5.2: Clockwise and counterclockwise cross-section based mean Unmixedness in terms of $y-z$ plane, with clockwise and counterclockwise excitation at (a) f_f = 875 Hz, 1000 Hz, 1600 Hz and (b) f_f = 1900 Hz, 2300 Hz, 2600 Hz for J = 61. Circles represent forcing cases with the most symmetric cross section. Select mean jet cross sectional PLIF images are inset.

study of the spatial evolution of mixing. Figure 5.2 examines the mean Unmixedness in the cross-sectional $(y-z)$ plane of the jet subject to asymmetric forcing, at discrete downstream locations of x/D = 2.5, 5.5, and 10.5. Circled points correspond to cross-sections that had the most symmetric structure as seen in mean PLIF images shown in Chapter 4. It is of note that forcing which resulted in the most symmetric cross-sections (circled points in Figure 5.2) were not always the best mixed cases at a given downstream location or even forcing frequency. Shown in Figure 5.2 (a) inset, clockwise forcing at f_f = 1000 Hz resulted in the most symmetric, best mixed condition for x/D = 10.5, yet clockwise forcing at f_f = 1600 Hz, which also resulted in a symmetric cross-section at x/D = 2.5 and 10.5, did not produce as well mixed conditions. An example of a case which was not symmetric, and was not well mixed was f_f = 875 Hz at location x/D = 2.5, shown if Figure 5.2 (a) inset.

In this cross-sectional view of the jet, with the exception of a single point in Figure 5.2 (b), all forcing conditions improved the molecular mixing over that of the unforced jet. Forcing at or below the fundamental frequency, $f_f \leq f_o$, enhanced the mixing significantly,

particularly the case $f_f = 1000$ Hz, well below the fundamental range of $f_o \approx 1600$-1900 Hz. In general for $f_f < f_o$, as in Figure 5.2 (a), CCW 4 forcing resulted in superior mixing enhancement as compared to the CW 4 direction for a given forcing frequency and amplitude. For asymmetric forcing above the fundamental range, $f_f > f_o$ as in Figure 5.2 (b), a preferential direction for mixing enhancement was not as clearly identified. Differences in mixing metric evaluation between centerplane (Figure 5.1) and cross-sectional (Figure 5.2) views may be due to asymmetries and CVP structures in the jet that are off the centerline, which are inherently not captured by the thin laser sheet orientation required for centerplane flow visualization. Results of the cross-section based Unmixedness suggested that clockwise forcing at all frequencies shown would be appropriate for applications where enhanced mixing is desired, and that a more symmetric cross-section could be associated with improved mixing but may not always be the best mixed case. In general, for 4-speaker directional forcing, all forcing conditions in which 1:1 lock-in of the USL occurred, mixing was enhanced in both the centerplane and cross-sectional views. Moreover, the comprehensive results in this study show that in general, all 4-speaker clockwise and counterclockwise forcing cases considered enhance mixing to some degree, even when the USL was known to exhibit quasiperiodic behavior or was not locked-in to the asymmetric forcing. Furthermore, cases where the USL was locked-in to the forcing provided better mixing enhancement (lower Unmixedness) than cases where the USL exhibited quasiperiodic behavior in the USL in response spectra, or cases which were neither locked-in or quasiperiodic. This indicates that for superior mixing enhancement via asymmetric forcing, the USL should be locked-in to the external excitation.

5.1.2 2-Speaker and 1-Speaker Mixing Characteristics

The influence of localized upstream and downstream external asymmetric forcing on jet mixing enhancement, and relationships to structure symmetry and USL velocity spectra character was studied. For localized forcing, it was seen that the correlation of structure symmetry and 1:1 lock-in of the USL was not always straightforward. However, it appears that for localized forcing, jet cross-sectional structure symmetry and superior mixing were

more closely correlated. Figure 5.3 (a) and (b) show the centerplane based Unmixedness $U_{c,xz}$ and cross-section based Unmixedness U_{yz} for upstream speaker forcing at f_f = 875 Hz with amplitude P'= 0.025 Pa, which corresponded to quasiperiodic behavior of the USL power spectra. In the centerplane view, although the enhancement in mixing was slight, R&L forcing of the upstream speakers produced the best mixed jet. The lower Unmixedness of R&L as compared to the other forcing strategies agreed well with USL spectral measurements of Figure 3.7 (a), in which R&L responded with the greatest amplitude disturbance at f_f. Best mixing when employing R&L forcing also agreed with the observation of R&L to have a symmetric cross-section at $x/D = 10.5$. At $x/D = 10.5$, as highlighted in Figure 5.3 (b), R U was also symmetric in the cross-section for f_f = 875 Hz, and R U was also the best mixer at this downstream location. Also notable in Figure 5.3 (b) was that L U forcing did not result in mixing enhancement, which would be expected since L U produced no changes in structure of the jet cross-section (Figure 4.8 (e)).

Figure 5.3 (c) and (d) show the centerplane based Unmixedness $U_{c,xz}$ and cross-section based Unmixedness U_{yz} for upstream speaker forcing at f_f = 1600 Hz with amplitude P'= 0.15 Pa, which corresponded to 1:1 lock-in of the USL for all speaker operation strategies. Observation showed that again, in the centerplane view, R&L forcing was the best mixer, which in this case significantly enhanced mixing of the jet far-field. R&L forcing here produced slightly less mixing enhancement than cases with 4 speaker operation, and this result could be generalized to all forcing conditions, in that localized 2 or 1 speaker forcing (either upstream or downstream) were not as well mixed as the corresponding cases with all speakers on. Although all upstream speaker forcing cases at f_f = 1600 Hz were locked-in, the R&L case had the most pure-tone response in the USL disturbance at f_f per Figure 3.7 (b). Additionally, although all upstream speaker asymmetric forcing at f_f = 1600 Hz led to various degrees of symmetrization of the jet structure, R&L was very symmetric at x/D = 10.5, as highlighted in Figure 5.3 (d). The far field structure for R&L had a more uniform, symmetric kidney-shaped structure as opposed to a clear CVP with two distinct lobes (as in L U for example), and this uniform structure was most well mixed.

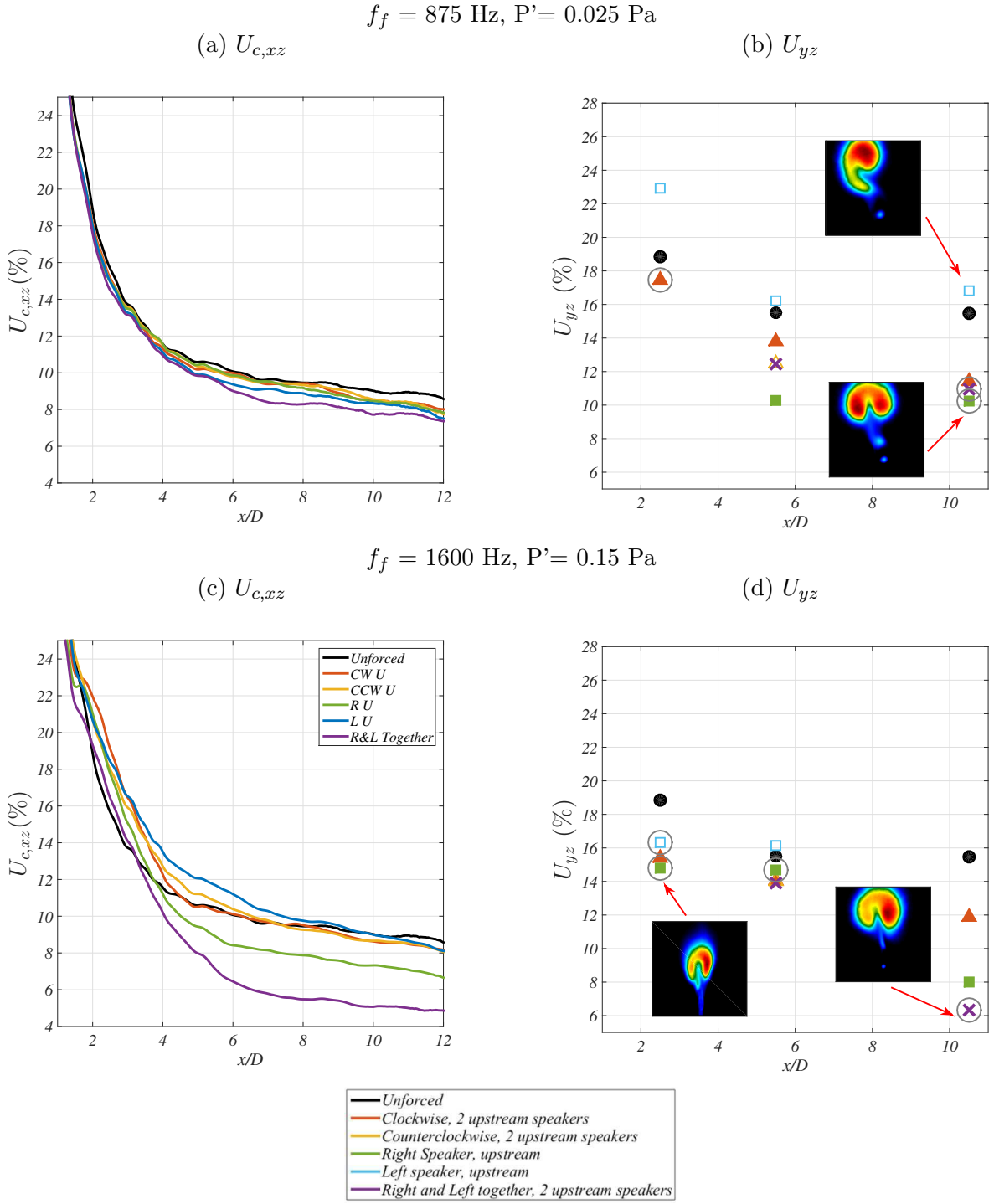

Figure 5.3: Centerplane based mean Unmixedness in the $x-z$ plane for upstream speaker forcing of the $J = 61$ JICF at (a) $f_f = 875$ Hz and (c) $f_f = 1600$ Hz, and cross-section based mean Unmixedness in terms of $y-z$ plane for upstream speaker forcing at (b) $f_f = 875$ Hz and (d) $f_f = 1600$ Hz. Circles represent forcing cases with the most symmetric cross section. Select mean jet cross sectional PLIF images are inset.

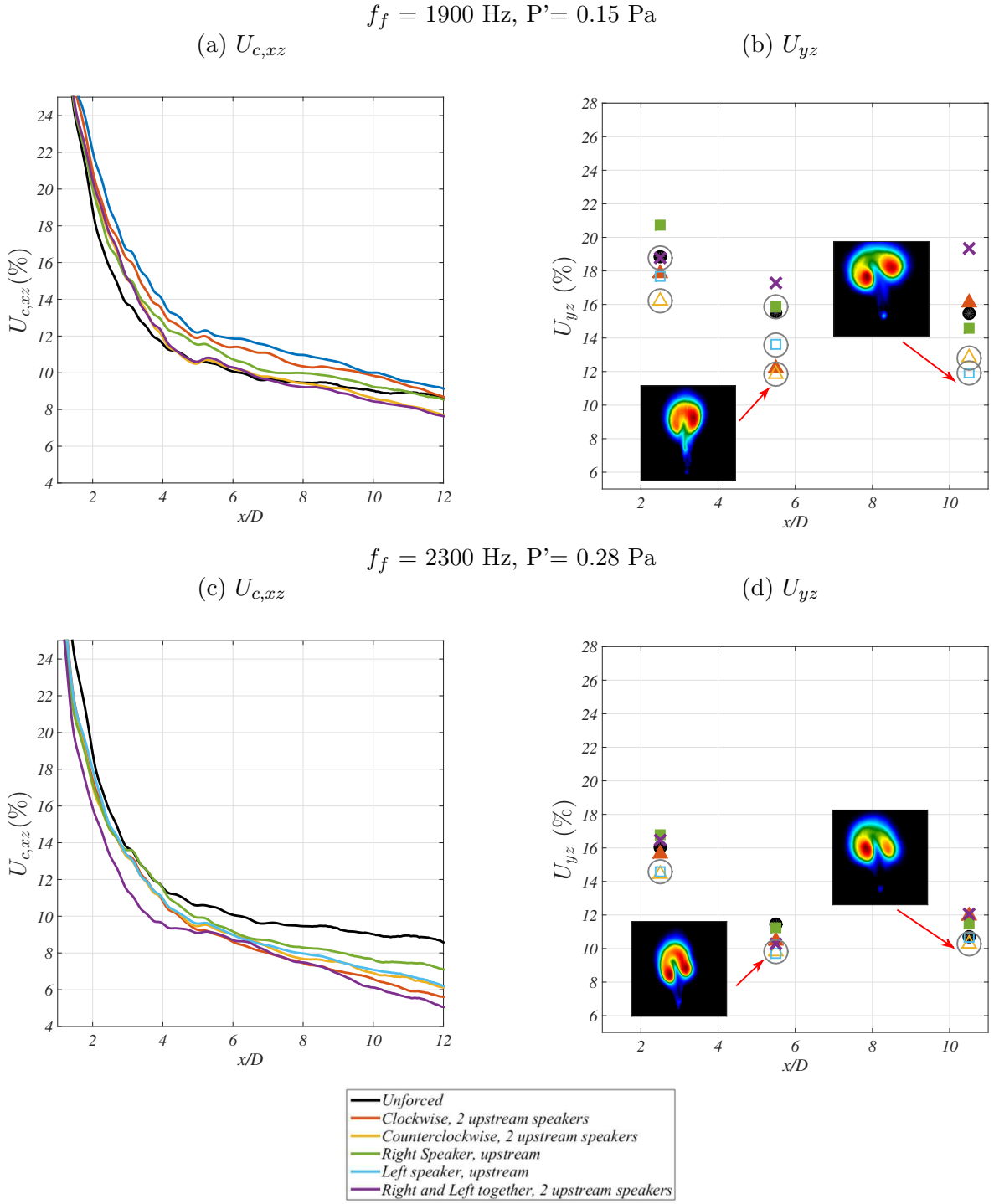

Figure 5.4: Centerplane based mean Unmixedness in the $x-z$ plane for upstream speaker forcing of the $J = 61$ JICF at (a) $f_f = 1900$ Hz and (c) $f_f = 2300$ Hz, and cross-section based mean Unmixedness in terms of $y-z$ plane for upstream speaker forcing at (b) $f_f = 1900$ Hz and (d) $f_f = 2300$ Hz. Circles represent forcing cases with the most symmetric cross section. Select mean jet cross sectional PLIF images are inset.

Similar to the results of the USL velocity power spectra study and jet structure study, the influence of upstream speaker asymmetric forcing at $f_f = 1900$ Hz was found to have interesting results which suggest complex interactions within the flow field. Figure 5.4 (a) and (b) show the centerplane based Unmixedness $U_{c,xz}$ and cross-section based Unmixedness U_{yz} for upstream speaker forcing at $f_f = 1900$ Hz and amplitude P'= 0.15 Pa. All forcing strategies corresponded to lock-in of the USL, with the exception of R U whose USL was not locked-in per Figure 3.7 (c). Molecular mixing quantified by the centerplane mixing metric $U_{c,xz}$, showed that interestingly all forcing conditions slightly decreased mixing as compared to the unforced case, until very far downstream at approximately $x/D \approx 9$, where R&L and CCW U began to enhance mixing. In addition to these two cases exhibiting similar trends in mixing, the USL power spectra of CCW U and R&L had very similar pure-tone responses in the USL disturbance at $f_f = 1900$ Hz, as compared to other speaker operation strategies. As previously observed, all forcing strategies for upstream speaker excitation at $f_f = 1900$ Hz produced symmetric cross-sections (highlighted Figure 5.4 (b)) with clear CVP lobed structure. However, molecular mixing quantification did not show a significant enhancement for this frequency as compared to the unforced case. This may suggest that the CVP shape segregates scalar concentration within the vortex structure, and in some cases may suppress mixing.

Upstream speaker forcing at $f_f = 1900$ Hz with amplitude P'= 0.15 Pa showed that even though the USL velocity spectra exhibited differing types of behavioral response for different speaker operation strategies, the resulting impacts on structure and mixing were similar for all forcing cases. However, Centerplane based Unmixedness $U_{c,xz}$ for upstream speaker forcing $f_f = 2300$ Hz at perturbation amplitude P'= 0.28 Pa (Figure 5.4 (c)) demonstrated slightly more varied mixing results for cases which had different nature of the USL response to excitation. R U, whose USL exhibited fairly weak quasiperiodic behavior in response to this forcing case, provided the least mixing enhancement as compared to the other speaker operation strategies, which were either locked-in (CCW U, L U, R&L), or strongly quasiperiodic (CW U). Yet it is noted that R U had improved mixing as compared to the unforced

case. Figure 5.4 shows the cross-section based Unmixedness U_{yz}, and in this view there were minimal differences in molecular mixing between all forcing cases, which would agree with the acetone PLIF scalar concentration images (Figure C.37), which showed that all forcing conditions produced symmetric cross sections of similar appearance. The differences in quantified mixing results between the centerplane and cross-section are most likely due to the majority of bulk concentration lying off-center throughout the jet evolution. Also notable is again, while the jet structure had been symmetrized by all asymmetric forcing directions, clear CVP double-lobed structures were produced, and the enhancements in mixing here were minimal as compared the unforced case. This again suggests that the formation of a clear CVP structure may not always enhance molecular mixing.

Asymmetric forcing of the $J = 61$ JICF in the downstream region also revealed correlations between jet USL character, structure, and mixing, depending on the frequency of excitation. Figure 5.5 (a) and (b) show the Unmixedness quantification for transverse jet with downstream forcing at $f_f = 875$ Hz at perturbation amplitude P'= 0.225 Pa, which corresponded to no lock-in of the USL, and which produced minimal symmetrization to the jet's cross-section from that of the naturally asymmetric unforced $J = 61$ jet. As could be expected, this forcing condition had minimal influence the centerplane based Unmixedness $U_{c,xz}$. Mixing evaluation of the cross-section planes, U_{yz}, showed qualitatively similar trends to those of the centerplane, such as slightly poorer mixing of the CW D and L D forcing cases as compared to the unforced case at $x/D = 5.5$, and that at $x/D = 2.5$ CCW D is slightly better mixed than other conditions. However, quantitative comparison of the Unmixedness values did not necessarily agree, especially in the jet near and mid-field.

The effects on mixing of a downstream forcing condition which did result in 1:1 lock-in of the USL velocity spectra are shown in Figure 5.5 (c) and (d), where $f_f = 1900$ Hz at amplitude P'= 0.15 Pa. The speaker operation condition that resulted in the greatest mixing enhancement of centerplane based Unmixedness $U_{c,xz}$ was CW D. Interestingly, upon examination of the USL power spectra per Figure 3.8 (c), the CW D forcing condition

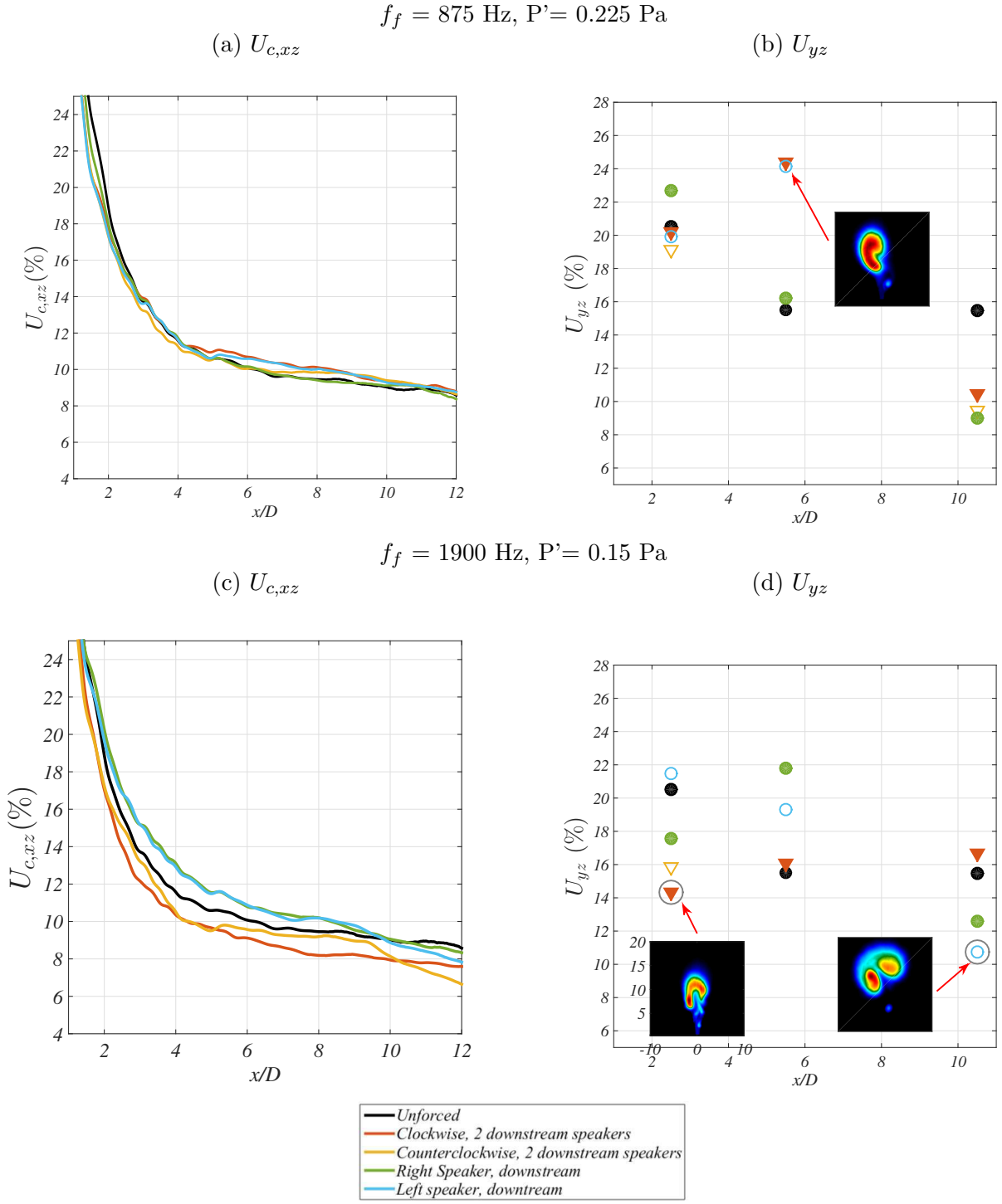

Figure 5.5: Centerplane based mean Unmixedness in the $x-z$ plane for downstream speaker forcing of the $J = 61$ JICF at (a) $f_f = 875$ Hz and (c) $f_f = 1900$ Hz, and cross-section based mean Unmixedness in terms of $y-z$ plane for upstream speaker forcing at (b) $f_f = 875$ Hz and (d) $f_f = 1900$ Hz. Circles represent forcing cases with the most symmetric cross section. Select mean jet cross sectional PLIF images are inset.

uniquely resulted in appearance of the forcing subharmonic $1/2f_f$, and combinations of the subharmonic with f_f, while this behavior was not observed in the other speaker operation strategies. Again this suggests the likelihood of greater shear layer rollup and merer for CW directional forcing, and that this condition improves mixing. The cross-sectional based Unmixedness U_{yz} in Figure 5.5 (d) showed, in general, qualitatively similar trends to the centerplane Unmixedness, and highlights that the most symmetric jet cross-sectional structure resulted in the best mixed cases.

Molecular mixing quantification of the limited localized forcing studies for the $J = 24$ and $J = 6$ transverse jets are shown in Figure 5.6 and Figure 5.7, respectively. Forcing at the fundamental frequency for $J = 24$, $f_o = 1900$ Hz with amplitude P'= 0.15 Pa, was shown to significantly enhance mixing in the centerplane based metric $U_{c,xz}$, and the enhancement was similar for all upstream speaker operation strategies. Cross-sectional based U_{yz} however, showed that mixing of the $J = 24$ jet was not significantly altered by the forcing. The cross-sectional based observations align with previous studies that a jet with a symmetric cross-section has better molecular mixing (Gevorkyan et al., 2016; Shoji, 2017; Shoji et al., 2019a), therefore since the external forcing does not further symmetrize the naturally symmetric $J = 24$ jet, mixing is not significantly impacted. The naturally unforced $J = 24$ jet is symmetric with a cross section whose concentration is fairly evenly disturbed at $x/D = 10.5$. Localized upstream forcing has the effect of segregating the scalar concentration into two distinct CVP lobes therefore the centerplane laser sheet would image a slice of quite different concentration for the forced jet as compared to the unforced case. Such a slice would capture the region bisecting the CVP for the forced case, appearing seemingly better mixed in the centerplane based metric $U_{c,xz}$.

Quantification of molecular mixing of the $J = 6$ transverse jet, for both unforced and asymmetrically forced in the JICF upstream region at conditions $f_o = 1900$ Hz with amplitude P'= 0.15 Pa, is shown in Figure 5.7, for both the centerplane based Unmixedness $U_{c,xz}$ and cross-section based Unmixedness U_{yz}. As previously discussed, the $J = 6$ jet has an absolutely unstable USL which is readily rolled up and remains resistant to low level

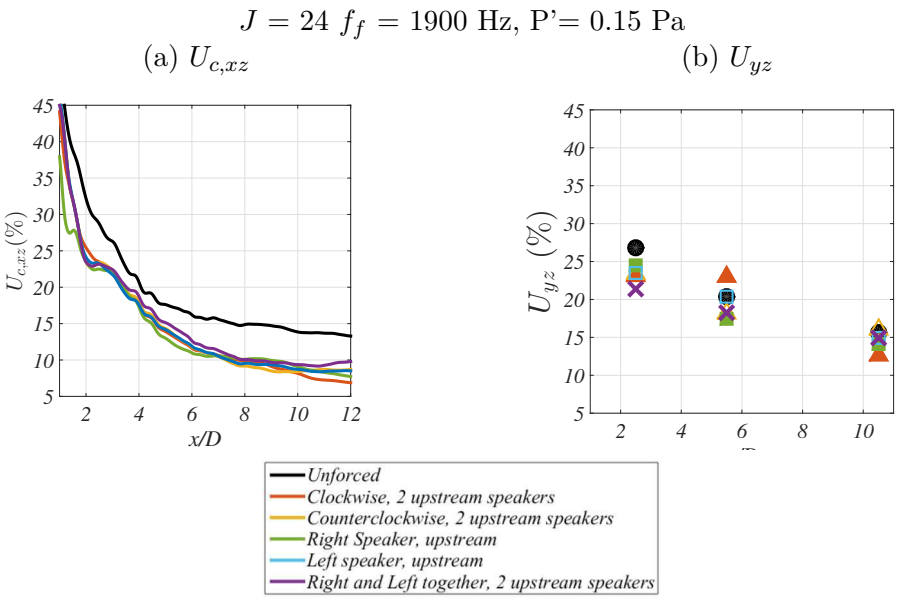

Figure 5.6: Centerplane based mean Unmixedness in the (a) $x-z$ plane and (b) cross-section based mean Unmixedness in terms of $y-z$ plane for speaker forcing of the $J = 24$ JICF at $f_f = 1900$ Hz with amplitude P'= 0.15 Pa.

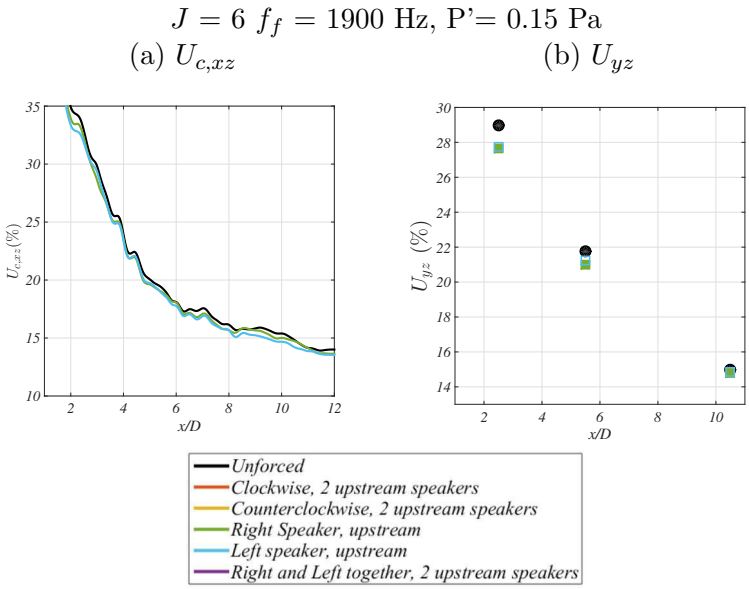

Figure 5.7: Centerplane based mean Unmixedness in the (a) $x-z$ plane and (b) cross-section based mean Unmixedness in terms of $y-z$ plane for speaker forcing of the $J = 6$ JICF at $f_f = 1900$ Hz with amplitude P'= 0.15 Pa.

perturbations. Therefore, unsurprisingly, the very low level external forcing had no effect on jet mixing.

Similar to previous studies on axisymmetric sinusoidal forcing (M'Closkey et al., 2002; Shapiro et al., 2006; Davitian et al., 2010b; Shoji, 2017), this study found that the characteristics of the $J = 61$ JICF, whose natural upstream shear layer is convectively unstable, are easily affected by very low level external sine wave forcing. Using the molecular mixing metric of the local Unmixedness (an instantaneous measure averaged over 500 realizations), asymmetric jet excitation produced similar trends between jet cross-sectional symmetrization and improved jet mixing. Centerplane-based Unmixedness produced generally similar trends to that of Unmixedness based on cross-sectional jet imaging, but there was not always a one-to-one correspondence in conditions producing optimal mixing. This was due at least in part to the fact that the centerplane-based laser sheet, aligned with the $y = 0$ plane, did not capture JICF asymmetric cross-sectional structures in the same way as cross-sectional slices of the jet, and hence mixing statistics could naturally have differing trends. The amplitudes of pressure perturbation were very low as compared to previous axisymmetric forcing studies by Shoji et al. (2019a), in many cases by at least an order of magnitude, yet the enhancements in molecular mixing are comparable to axisymmetric forcing, suggesting practical benefits for the present asymmetric excitation approach.

5.2 POD Analysis

Proper orthogonal decomposition (POD) has most commonly been used in the analysis of turbulent flow to extract coherent structures, which are organized spatial features that repeatedly occur, often times in flows dominated by local shear (Berkooz et al., 1996). POD analysis can reveal important flowfield features by extracting the dominant modes and ordering the modes in terms of fluctuation energy content. Snapshot POD (Sirovich, 1987) can be applied to snapshots, or instantaneous images of the flowfield and hence used to analyze experimental data, typically the velocity field obtained from PIV measurements. Snapshot POD analysis has also been applied to scalar fields (Gurka et al., 2006) as in the study by

Gevorkyan et al. (2018), in which concentration POD mode structures were extracted from the PLIF portion of simultaneous PLIF/PIV snapshots, for the unforced JICF of various flow conditions.

POD analysis has also been performed on flow fields subject to excitation or modulation. In the study by Vernet et al. (2009), POD modes were extracted from PIV measurements of a $R = 1$ square JICF, for both the unforced case and for the jet subject to $f_f = 1$ Hz axisymmetric sine wave forcing. Through the POD analysis, a distinction between natural modes of the unforced jet and forced modes was observed. The numerical study by Gross and Fasel (2007) investigated, among other things, a pulsed low pressure turbine blade. Their findings show that harmonic forcing of the blade causes the flow to become periodic, with the coefficients of the POD modes appearing in pairs of equal magnitude. In addition to the POD modes appearing in pairs, forcing can greatly increase the amplitude (energy fluctuation content) of the first few mode pairs, indicating that the flow dynamics are governed by large energetic, coherent structures. For example, in the study by Bidan et al. (2013) of an inclined transverse get subject to square-wave forcing, it was noted that the cumulative kinetic energy captured by the first two POD modes corresponded to more than 65% of the total energy. Along with gaining energy, evidence of the POD modes influenced by excitation is the emergence of periodicity between them. Lardeau et al. (2010) sees that when pulsing the flow separation point of flow over hill with a slitted synthetic jet, the first POD mode 1, previously lacking any periodicity, adapts a periodic behavior at a frequency roughly half of modes 2 and 3.

Snapshot proper orthogonal decomposition was performed on the acetone PLIF scalar concentration images, typically 500 instantaneous images for each forcing condition. Note that these images were of higher spatial resolution than the PLIF images in Gevorkyan et al. (2018). The modes were extracted, with each mode mode scaled by its own norm and the mean jet velocity at the jet exit U_j, and thus each snapshot could be reconstructed or recovered by a weighted basis of modes. Figure 5.8 provides examples of the two dominant mode structures for (a) the unforced $J = 61$ JICF, and (b) jet subject to forcing condition

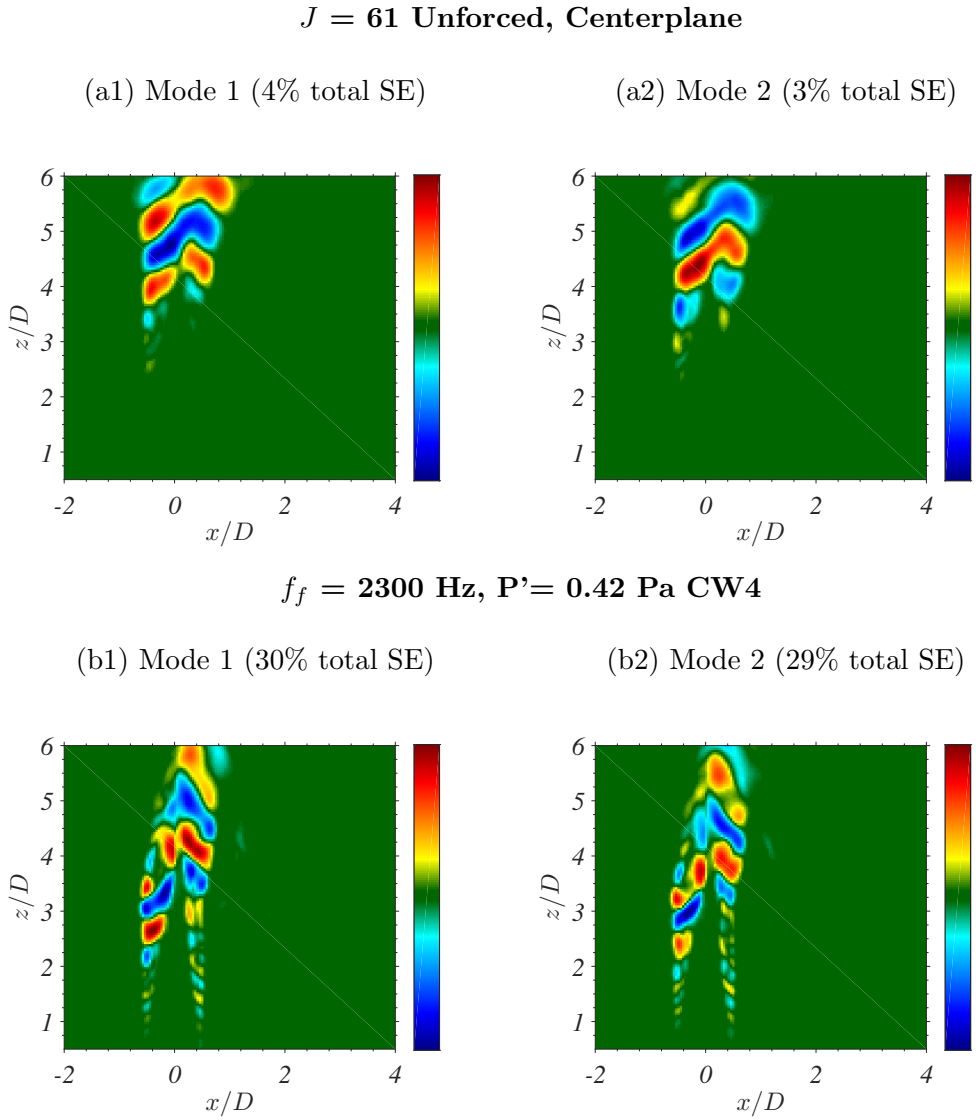

Figure 5.8: PLIF POD mode structures from instantaneous centerplane images of the $J = 61$ JICF for (a) unforced and (b) subject to external asymmetric forcing at $f_f = 2300$ Hz with amplitude P'= 0.42 Pa. Percentage of total scalar fluctuation energy (SE) by each mode is indicated.

$f_f = 2300$ Hz with amplitude P'= 0.42 Pa, in the full azimuthal clockwise direction, which corresponded to lock-in of the USL. The percentages of scalar energy (SE) shown are those contained for the specific POD mode when compared to all other POD modes for the same forcing condition. For the unforced case in Figure 5.8 (a), the dominant mode structures represent the upstream shear layer, forming in locations consistent with the initiation of USL

vortical structures. In the asymmetrically forced case shown in Figure 5.8 (b), shear layer structures again dominate the flow field, with both upstream and downstream shear layer roll up initiating closer to the plane of jet injection, similar to the modes of a JICF with an absolutely unstable USL (Gevorkyan et al., 2018). Here, the fluctuating scalar energy content for the first two modes became paired and had notably increased magnitudes, accounting for 69% of the total energy, similar to trends seen by other groups.

Figure 5.9 shows the first POD mode pair structure for asymmetric forcing at f_f = 1000 Hz with pressure perturbation amplitude P'= 0.65 Pa, in both the clockwise and counterclockwise directions using all 4 speakers. The upstream and downstream shear layers again dominate the flow field, yet differences between the clockwise and counterclockwise speaker operation strategies were observed. In the CW4 direction in Figure 5.9 (a), somewhat sinuous structures are observed in the shear layer modes. Unlike the dominant modes seen in Figure 5.8 (b), which are nearly identical in structure with inverted magnitudes, Modes 1 and 2 for CW4 forcing at $f_f = 1000$ Hz do not appear as similar in structure. The fluctuation energy content of Mode 1 has significantly increased from that of the unforced case, yet the energy content magnitudes of Mode 1 (28% SE) and Mode 2 (19% SE) indicate these two modes may not be paired. However, forcing in the CCW resulted in pairing of the first two modes, based on fluctuation scalar energy content and appearance, and additionally the emergence of wake-like structures are observed (Figure 5.9 (b)).

POD analysis can be extended to the cross-sectional plane of view, capturing the dominant structures in the evolution of the jet and CVP. Figures 5.10-5.12 show example mode structures for the unforced jet and jet subject to asymmetric forcing in the x/D = 2.5, 5.5, and 10.5 cross-section planes. Additional images are found in Appendix D. Figure 5.10 (a) shows the unforced $J = 61$ JICF at downstream location $x/D = 2.5$. The dominant POD mode structures are asymmetric and left-leaning, consistent with the orientation of the unforced jet's mean acetone concentration image (Figure 4.3(a)). The crossflow has deflected the jet, and some USL structures may be visible as an alternating pattern at the top of Mode 2. As the unforced jet evolves downstream, cross-sectional views of the first POD mode pair

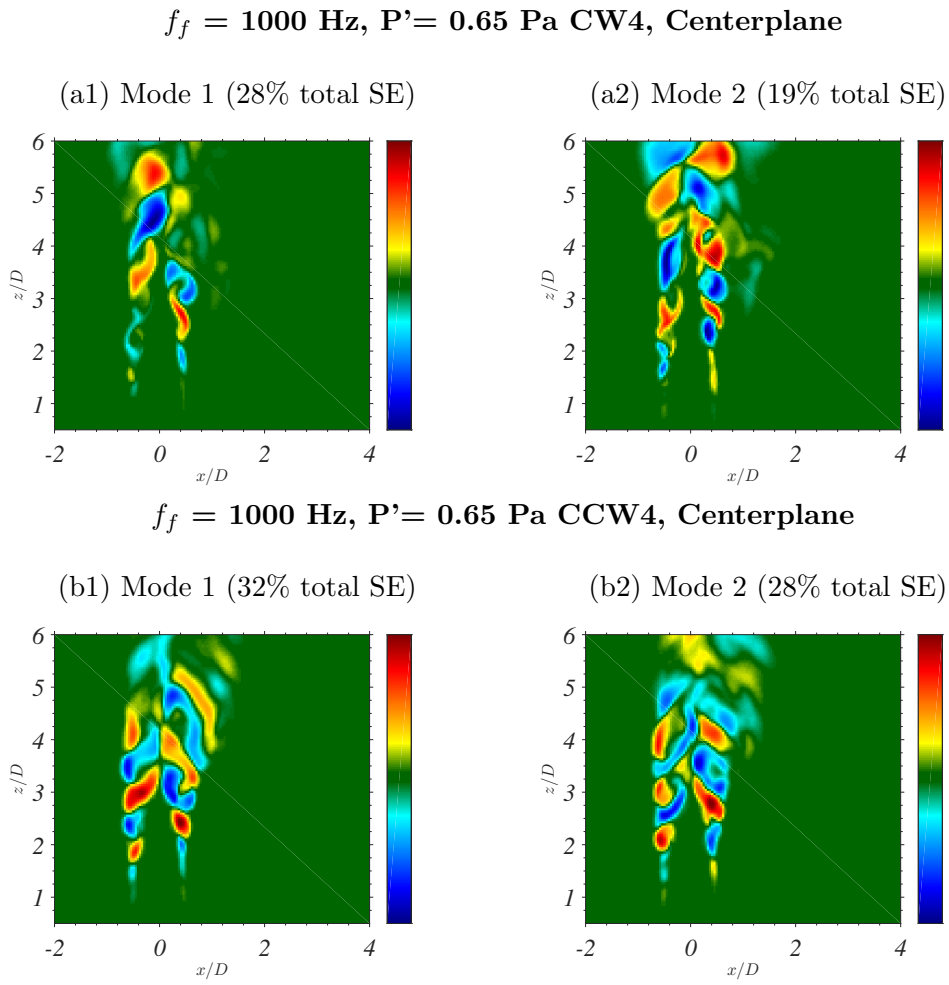

Figure 5.9: PLIF POD mode structures from instantaneous centerplane images of the $J = 61$ JICF subject to external asymmetric forcing at $f_f = 1000$ Hz with amplitude P'= 0.65 Pa with (a) clockwise and (b) counterclockwise 4 speaker operation strategy. Percentage of total scalar fluctuation energy (SE) by each mode is indicated.

structures at $x/D = 5.5$ (Figure 5.11 (a)) and at $x/D = 10.5$ (Figure 5.12 (a)) show that the dominant modes maintain their basic character, growing larger as the jet spreads and twisting as the asymmetry in the mean jet cross-section structure becomes increasingly amplified.

The changes in dominant mode structures of the cross-sectional views for the jet subject to asymmetric forcing can be quite dramatic and interesting. Figure 5.10 (c1) shows a very symmetric cross-sectional structure in POD Mode1, with lobes of opposite magnitude,

x/D **= 2.5**

J = 61, Unforced

(a1) Mode 1 (8% total SE) (a2) Mode 2 (6% total SE)

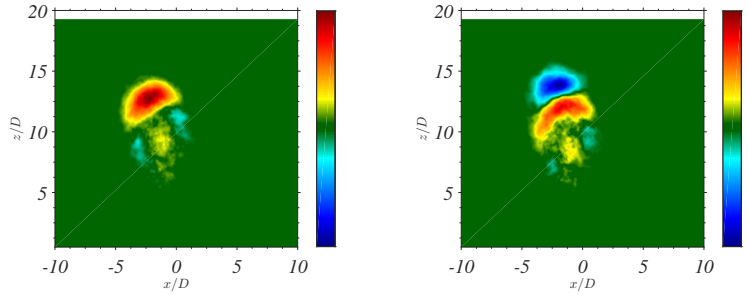

f_f = 875 Hz, P'= 0.225 Pa CW4

(b1) Mode 1 (11% total SE) (b2) Mode 2 (7% total SE)

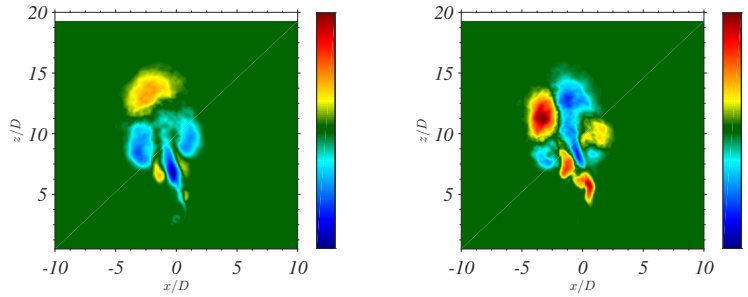

f_f = 875 Hz, P'= 0.225 Pa CCW4

(c1) Mode 1 (21% total SE) (c2) Mode 2 (9% total SE)

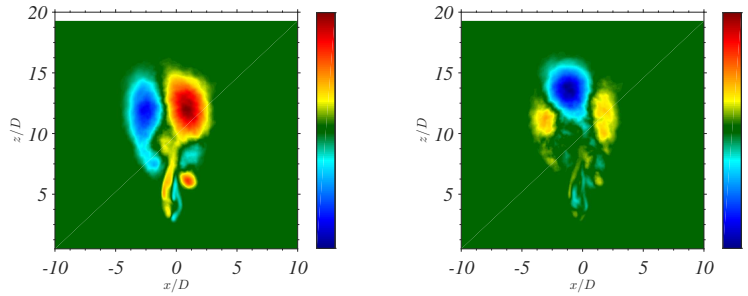

Figure 5.10: PLIF POD mode structures from instantaneous cross-sectional view images at x/D = 2.5, of the J = 61 JICF (a) unforced and (b-c) subject to external asymmetric forcing with all four speakers at f_f = 875 Hz with amplitude P'= 0.225 Pa. Percentage of total scalar fluctuation energy (SE) by each mode is indicated.

x/D **= 5.5**

J = 61, Unforced

(a1) Mode 1 (10% total SE) (a2) Mode 2 (2% total SE)

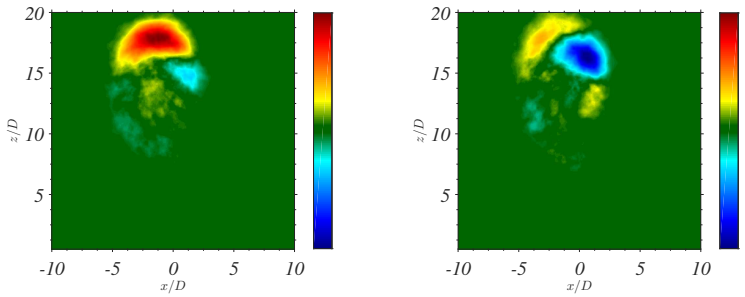

f_f = 1600 Hz, P'= 0.15 Pa CW4

(b1) Mode 1 (6% total SE) (b2) Mode 2 (5% total SE)

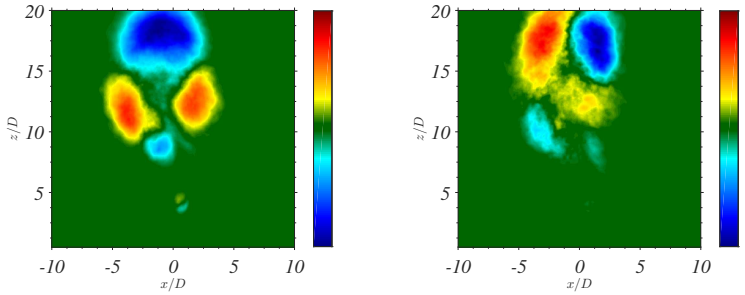

f_f = 1600 Hz, P'= 0.15 Pa CCW4

(c1) Mode 1 (8% total SE) (c2) Mode 2 (6% total SE)

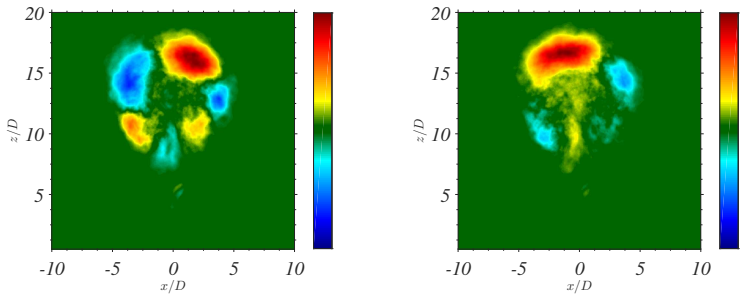

Figure 5.11: PLIF POD mode structures from instantaneous cross-sectional view images at x/D = 5.5, of the J = 61 JICF (a) unforced and (b-c) subject to external asymmetric forcing with all four speakers at f_f = 1600 Hz with amplitude P'= 0.15 Pa. Percentage of total scalar fluctuation energy (SE) by each mode is indicated.

x/D **= 10.5**

J = 61, Unforced

(a1) Mode 1 (10% total SE) (a2) Mode 2 (7% total SE)

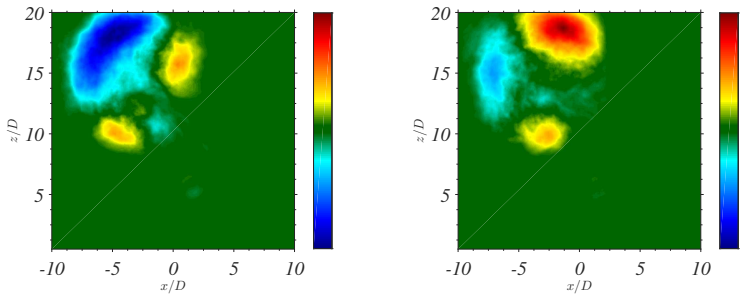

f_f = 875 Hz, P'= 0.225 Pa CW4

(b1) Mode 1 (10% total SE) (b2) Mode 2 (7% total SE)

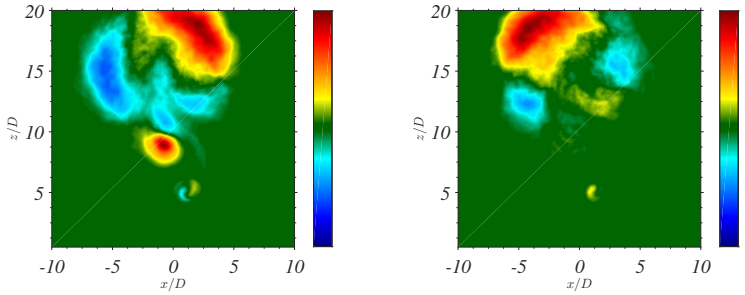

f_f = 875 Hz, P'= 0.225 Pa CCW4

(c1) Mode 1 (11% total SE) (c2) Mode 2 (6% total SE)

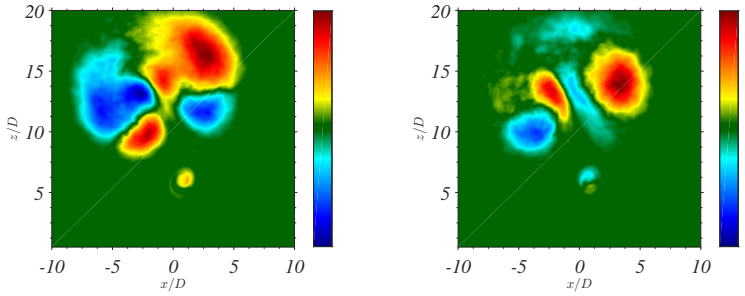

Figure 5.12: PLIF POD mode structures from instantaneous cross-sectional view images at x/D = 10.5, of the J = 61 JICF (a) unforced and (b-c) subject to external asymmetric forcing with all four speakers at f_f = 875 Hz with amplitude P'= 0.225 Pa. Percentage of total scalar fluctuation energy (SE) by each mode is indicated.

which cross paths while extending downward toward the tertiary vortex. This structure corresponds to mean cross-sectional scalar concentration images which is symmetrized and of relatively uniform concentration distribution (Figure 4.4 (f)). At downstream location $x/D = 5.5$, Mode 1 of Figure 5.11 (c1) also corresponds to a symmetric mean cross-section of uniform distribution (Figure 4.3 (e)), and here mode structures of alternating fluctuation energy magnitude form a ring around the edge of the jet structure, with a hollow center. The mode structures for a symmetrized cross section which produced a strikingly clear CVP in the far field (Figure 4.4 (f)), are seen in Figure 5.12 (c), which contain patterns of alternating fluctuation energy magnitude and an overall symmetric nature. Future studies may explore in further detail the flow phenomenon these cross-section mode structures correspond to.

5.3 POD Mode Coefficient Phase Space Plots

Periodicity of the modes can be demonstrated by plotting the POD mode coefficients for each snapshot. The shapes formed in these phase portraits can reveal behaviors of the flowfield. For example, a 2D circular pattern indicates a cyclic behavior of the two modes, such as a traveling wave. Gevorkyan et al. (2018) found that for a JICF with an absolutely unstable USL, indeed a closed circle was formed by the first two extracted POD mode coefficients due to the presence of strong periodic USL vortex rollup. However for a JICF with a convectively unstable USL, which has a weaker and more broadband instability, the PLIF extracted POD coefficients for the dominant mode structures formed a more random pattern. In the case of a periodically forced flow, a recovered circular shape indicates that both modes interact together, operating at the same frequency (such as $1/2f_f$, f_f, $2f_f$, etc.) and with almost equal influence (Vernet et al., 2009; Bidan et al., 2013). Following this analysis, for each asymmetric forcing condition the snapshot POD coefficients of the first two modes pairs were investigated, as well as the 3D phase space formed from the three most dominant POD mode coefficients. Here, consideration of the second mode pair could perhaps reveal secondary periodicity in the flowfield.

POD analysis evaluates a system as a series of differential equations, therefore phase

portrait mapping of the mode coefficients represents the solution space to the equations, where the dominant modes represent the least unstable solutions. In this sense, phase portrait mapping of the POD mode coefficients is perhaps analogous to Poincaré's analysis of the solution curves defined by differential equations (Poincare, 1881), where if there are several unstable solutions in the steady state, a time signal will oscillate around the least unstable solution(s).

Phase plots of select cases for the asymmetrically forced $J = 61$ transverse jet are shown in Figures 5.13 - 5.20. Black symbols represent the mode coefficients of the unforced jet, green colored symbols represent conditions where prior hotwire studies in Chapter 3 indicated 1:1 lock-in of the USL, blue symbols represent quasiperiodic behavior of the USL power spectra, and red symbols represent conditions where no lock-in of the USL to external forcing was found via hotwire spectral measurements. Yellow symbols indicate that the nature of the USL for the forcing condition has not been specifically measured, or its character can not be directly inferred from other spectral measurements, such as forcing with an amplitude above a condition where the USL is known to be locked-in, or below a condition in which the USL was not locked-in to forcing. However, the specific cases presented in this section which have yellow colored symbols are likely to be locked-in to the forcing, due to the emergence of patterns in the phase plots. As Gevorkyan et al. (2018) saw a circular pattern in the plot of the a_1 and a_2 POD coefficients for an unforced $J = 5$ jet, which has an absolutely unstable USL, Bidan et al. (2013) saw the emergence of a circular pattern in the POD coefficients for the forced jet portions of their study, while their unforced jet's coefficients had no such organization in the phase space. In the study by Vernet et al. (2009), they conclude that absolute instabilities must dominate the pulsed transverse jet. The appearance of formed patterns in the POD coefficients would align with evidence of jets with convectively unstable USL, whose instabilities are weak and broadband, becoming locked-in to external forcing, in which the pure tone of f_f dominates the USL disturbance.

Figures 5.13 - 5.15 plot the POD modes for select forcing cases of the 4-speaker study, and compare them to the unforced J= 61 jet. The specific cases are shown here to demonstrate

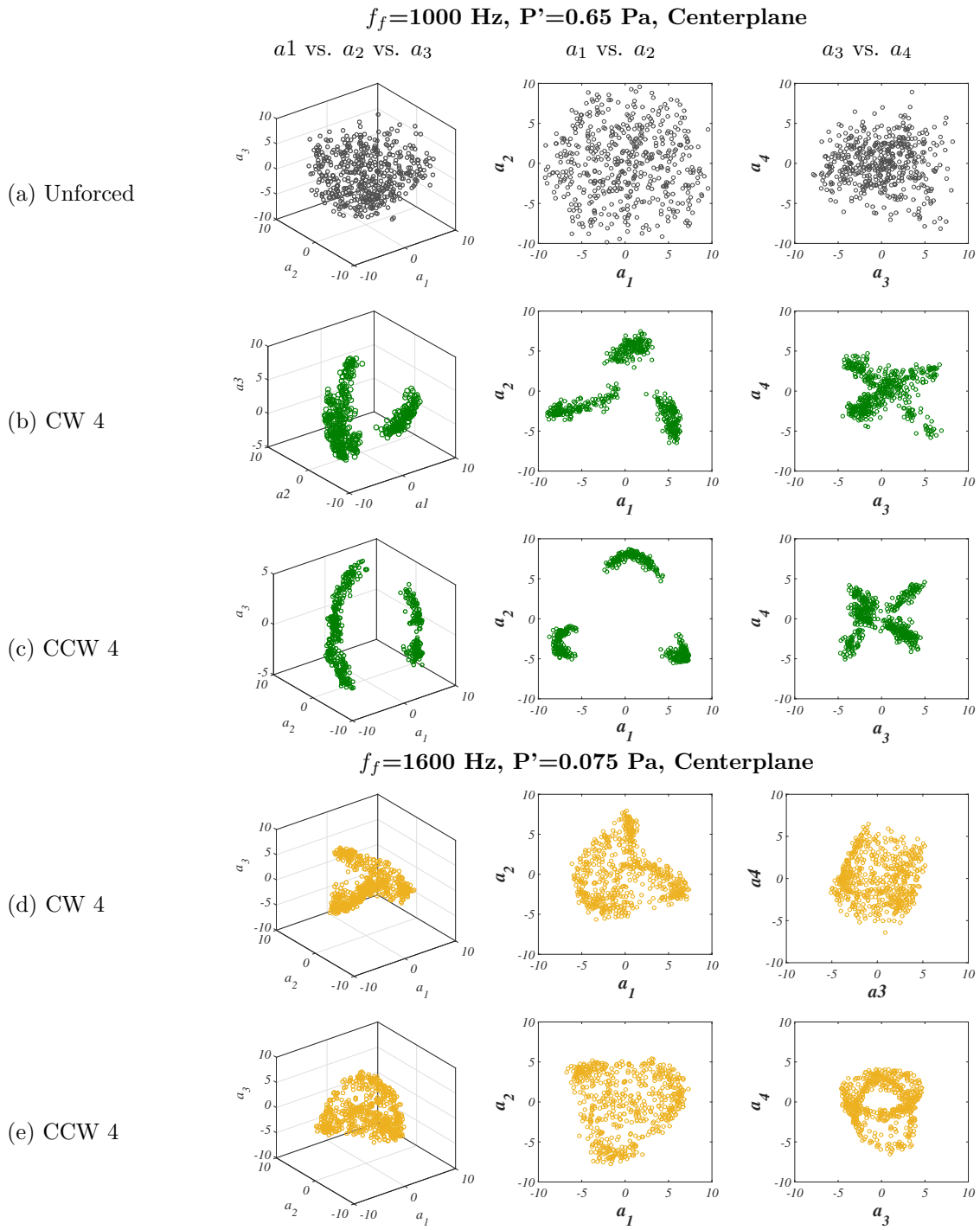

Figure 5.13: PLIF POD coefficients for the first 4 modes plotted against each other, extracted from instantaneous centerplane images of the $J = 61$ JICF, (a) unforced, (b-c) subject to $f_f = 1000$ Hz, and (d-e) $f_f = 1600$ Hz CW and CCW forcing. Black symbols represent the unforced condition, green colored symbols represent 1:1 lock-in of the USL, and yellow symbols indicate the nature of the USL response spectra cannot be inferred from direct measurements.

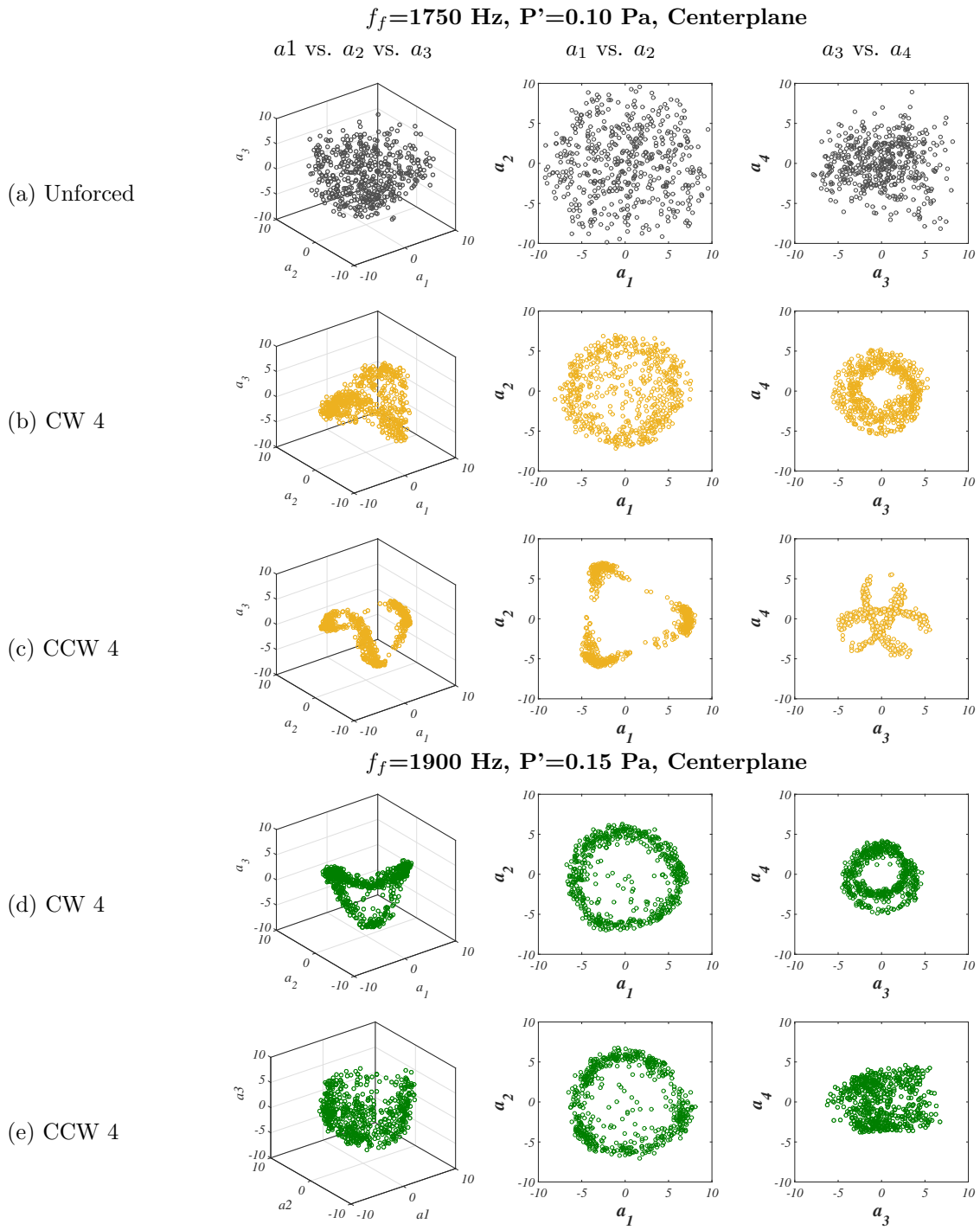

Figure 5.14: PLIF POD coefficients for the first 4 modes plotted against each other, extracted from instantaneous centerplane images of the $J = 61$ JICF, (a) unforced, (b-c) subject to $f_f = 1750$ Hz, and (d-e) $f_f = 1900$ Hz CW and CCW forcing. Black symbols represent the unforced condition, green colored symbols represent 1:1 lock-in of the USL, and yellow symbols indicate the nature of the USL response spectra cannot be inferred from direct measurements.

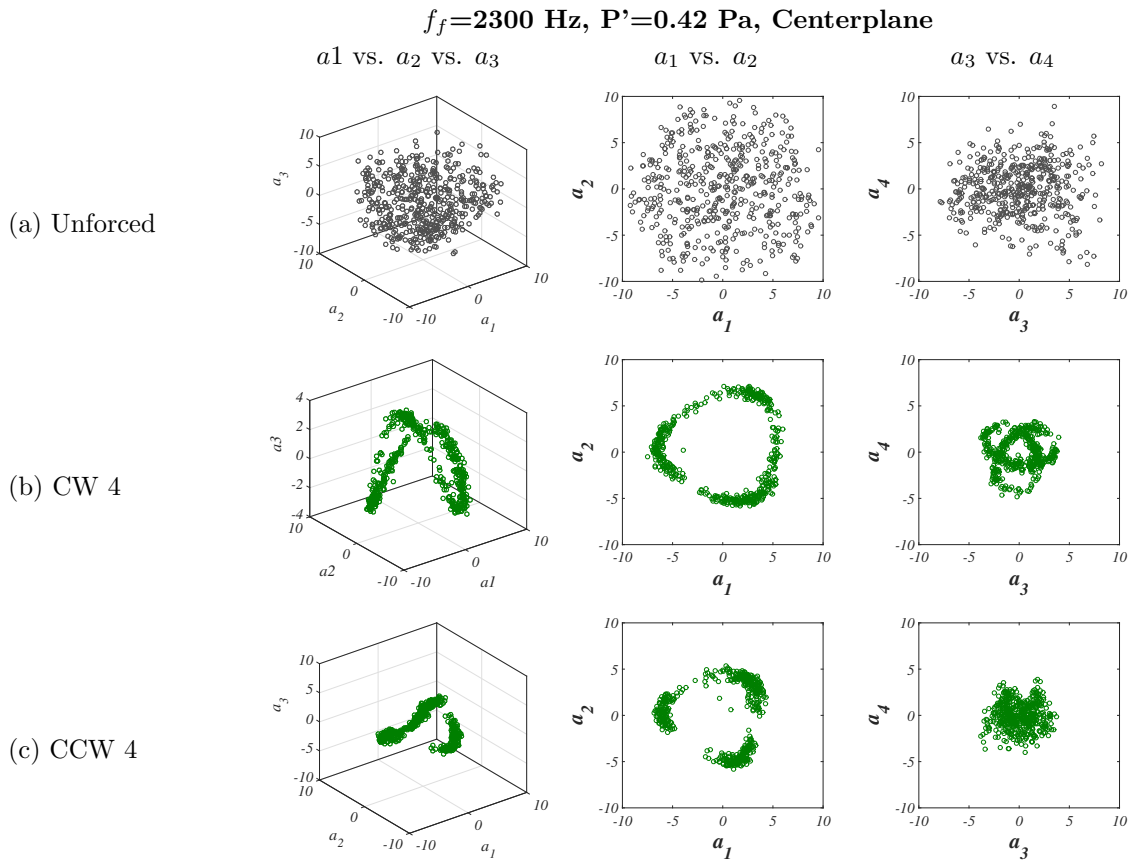

Figure 5.15: PLIF POD coefficients for the first 4 modes plotted against each other, extracted from instantaneous centerplane images of the $J = 61$ JICF, (a) unforced, and (b-c) subject to $f_f = 2300$ Hz CW and CCW forcing. Black symbols represent the unforced condition, green colored symbols represent 1:1 lock-in of the USL.

particular trends in the phase space, and should not imply that all asymmetric forcing cases resulted in the emergence of patterns in the coefficients of the dominant modes. The unforced case did not produce periodicity in the POD coefficients, as expected; these are shown for reference in the POD coefficient plots. When forcing well below the fundamental frequency at $f_f = 875$ Hz or $f_f = 1000$ Hz, if the USL was locked-in to the clockwise or counterclockwise directional forcing, the 3D representation of the first three coefficients always produced a 3-pronged like structure which often twisted as it developed in the third dimension, as seen in Figure 5.13 (b) and (c). Tripled patterns or nodes emerged from the first two modes, which perhaps suggests 3 different preferred combinations of paired dominant modes over the ensemble of 500 images. A few forcing cases whose USL exhibited 1:1 lock-in to forcing

at $f_f = 875$ Hz or 1000 Hz also saw the emergence of patterns in the coefficients of the second mode pair, a_3 and a_4, as seen in Figure 5.13 (c) and (d), suggesting a secondary recurring relationship in the flowfield. Other studies have also observed 2D phase plots in which the POD coefficients were clustered into nodes or preferred locations. For example the study by Bidan et al. (2013) observed that over a time resolved trajectory, the first pair of POD coefficient assumed a starlike shape in the energy distribution, which only appeared under certain forcing conditions.

Asymmetric forcing at $f_f = 1600$ Hz always produced a coherent three-dimensional phase representation of the POD coefficients. This was true for every amplitude and every speaker forcing strategy for which PLIF data was available; including 4-speaker azimuthal in Figure 5.13 (d-e), upstream speaker operation in Figure 5.16, and downstream speaker operation in Figure 5.19. For $f_f = 1600$ Hz, the first three POD modes manifested themselves as a closed or partially closed "bent" circles of varying orientations in the 3D phase space. Modes 1 and 2 mapped together formed either a semi-triangular shape, yet with smoothed corners, as in Figure 5.19 (d), or a partial circle, as in Figure 5.16 (c) for example. Note the fundamental frequency range for $J = 61$ spans $f_o \approx$ 1600-1900 Hz, and as seen in the studies of USL velocity power spectra, jet cross-sectional structure, and molecular mixing quantification, as the frequency moved above the fundamental it became more difficult to elicit a response from asymmetric forcing with the low amplitude perturbations employed in the current study. Therefore, the propensity of the jet to form coherent structures in POD phase space when subject to external forcing at $f_f = 1600$ Hz (at the bottom end of the fundamental range), is an additional piece of evidence for preference of the jet to be susceptible to lower frequency excitation, along with the symmetrized cross-sectional structure and enhanced mixing produced by $f_f = 1600$ Hz.

The POD coefficients of the upstream forcing strategies for $f_f = 2300$ Hz with perturbation amplitude P'= 0.28 Pa are shown in Figure 5.18 to demonstrate two observations. First, shown in (b) and (d) are representative phase space plots for forcing conditions which resulted in quasiperiodicity in the USL power spectra, and overall it was observed that

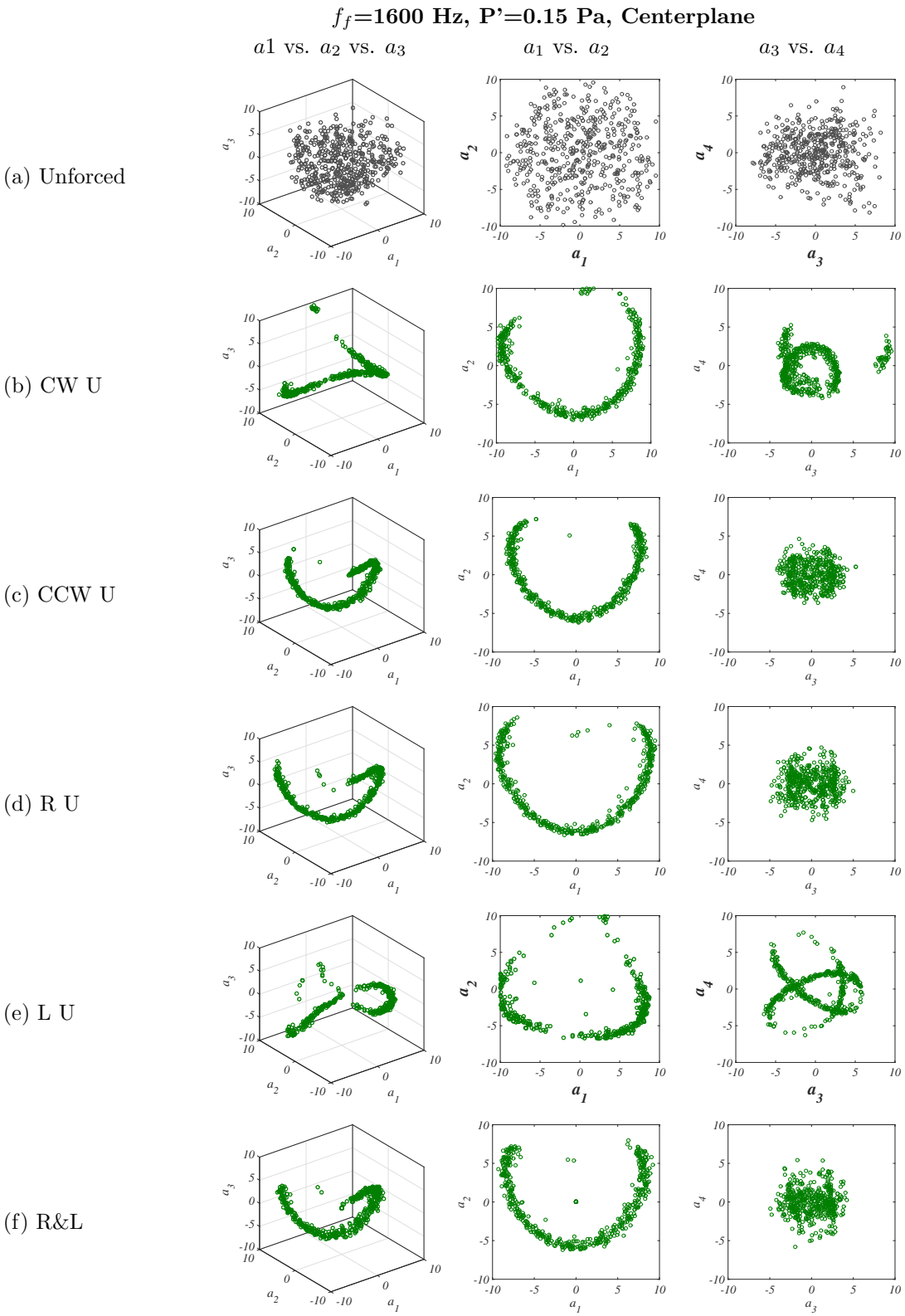

Figure 5.16: PLIF POD coefficients for the first 4 modes plotted against each other, extracted from instantaneous centerplane images of the $J = 61$ JICF, (a) unforced, and (b-f) subject to $f_f = 1600$ Hz upstream region forcing. Black symbols represent the unforced condition, green colored symbols represent 1:1 lock-in of the USL.

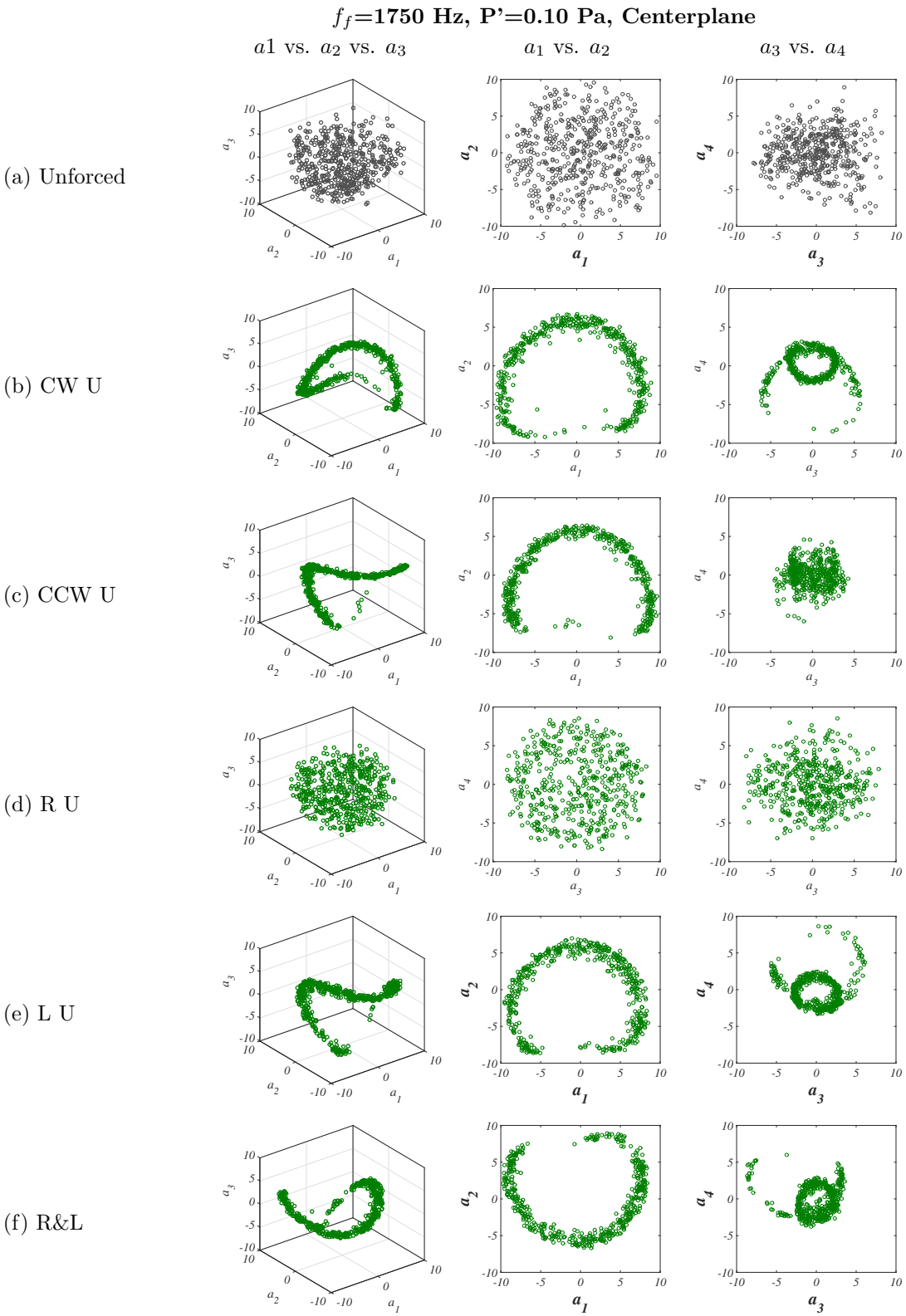

Figure 5.17: PLIF POD coefficients for the first 4 modes plotted against each other, extracted from instantaneous centerplane images of the $J = 61$ JICF, (a) unforced, and (b-f) subject to $f_f = 1750$ Hz upstream region forcing. Black symbols represent the unforced condition, green colored symbols represent 1:1 lock-in of the USL.

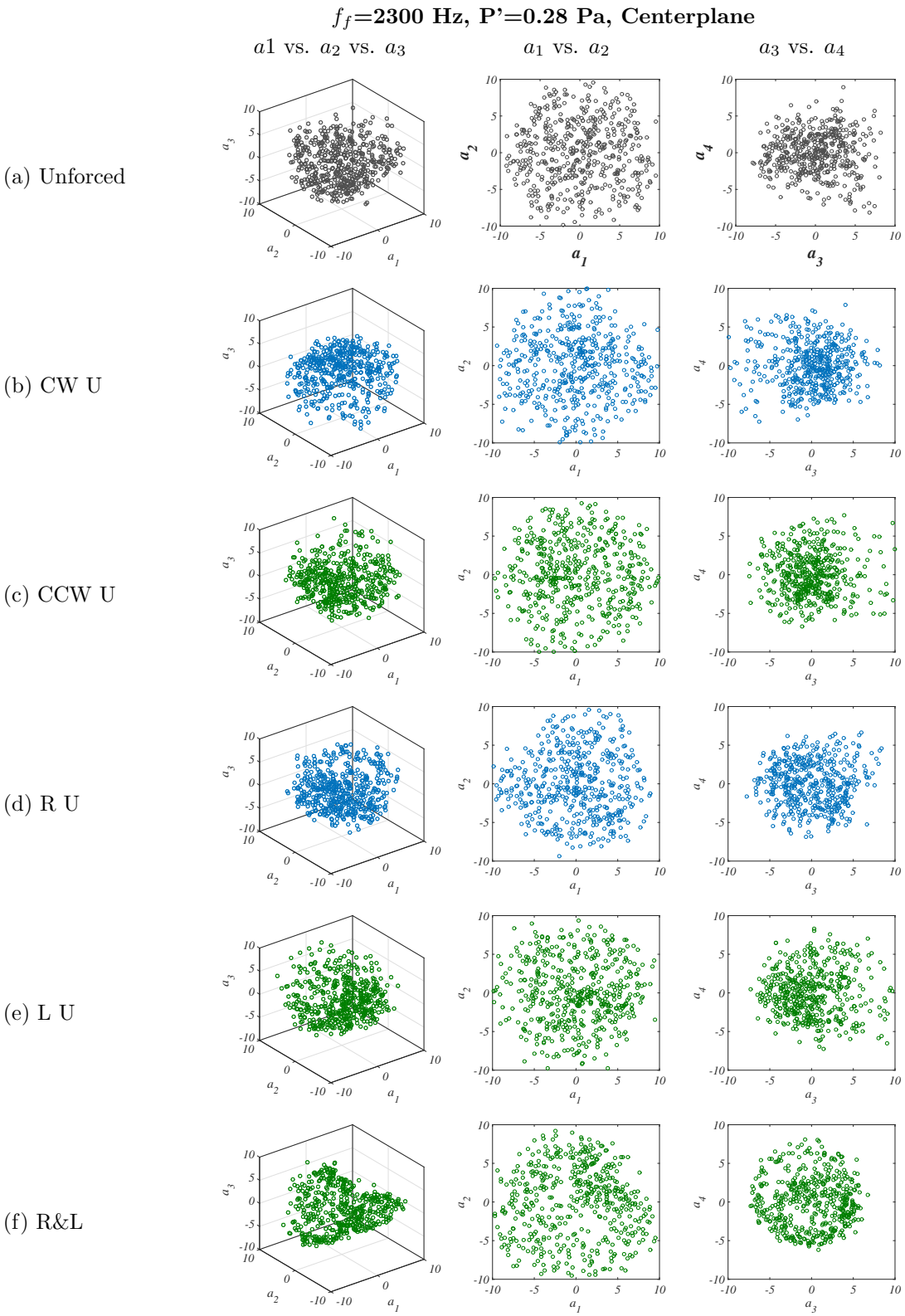

Figure 5.18: PLIF POD coefficients for the first 4 modes plotted against each other, extracted from instantaneous centerplane images of the $J = 61$ JICF, (a) unforced, and (b-e) subject to f_f = 2300 Hz upstream region forcing. Black symbols represent the unforced condition, green colored symbols represent 1:1 lock-in of the USL, and blue symbols represent quasiperiodic behavior of the USL power spectra.

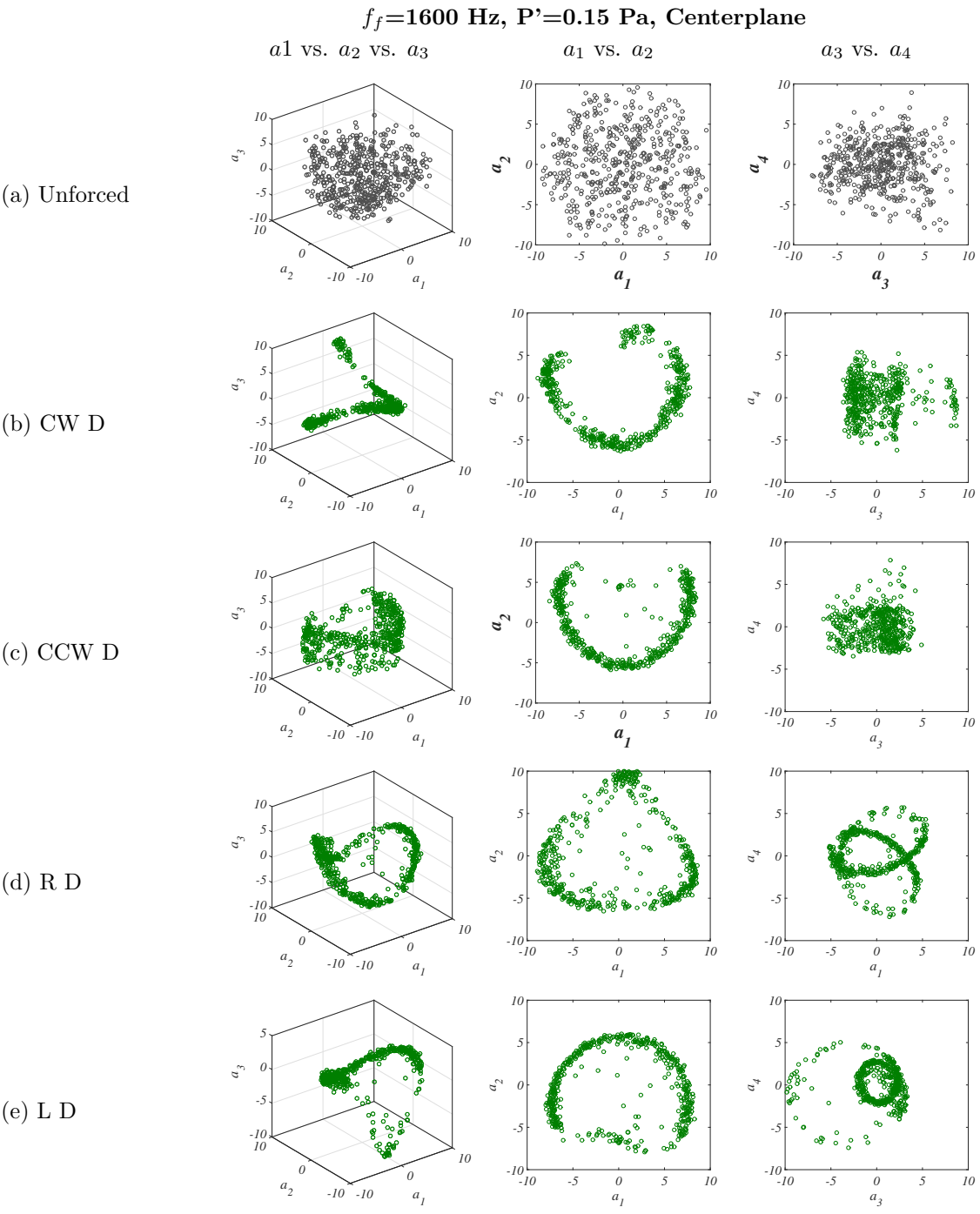

Figure 5.19: PLIF POD coefficients for the first 4 modes plotted against each other, extracted from instantaneous centerplane images of the $J = 61$ JICF, (a) unforced, and (b-e) subject to $f_f =$ 1600 Hz downstream region forcing. Black symbols represent the unforced condition, green colored symbols represent 1:1 lock-in of the USL.

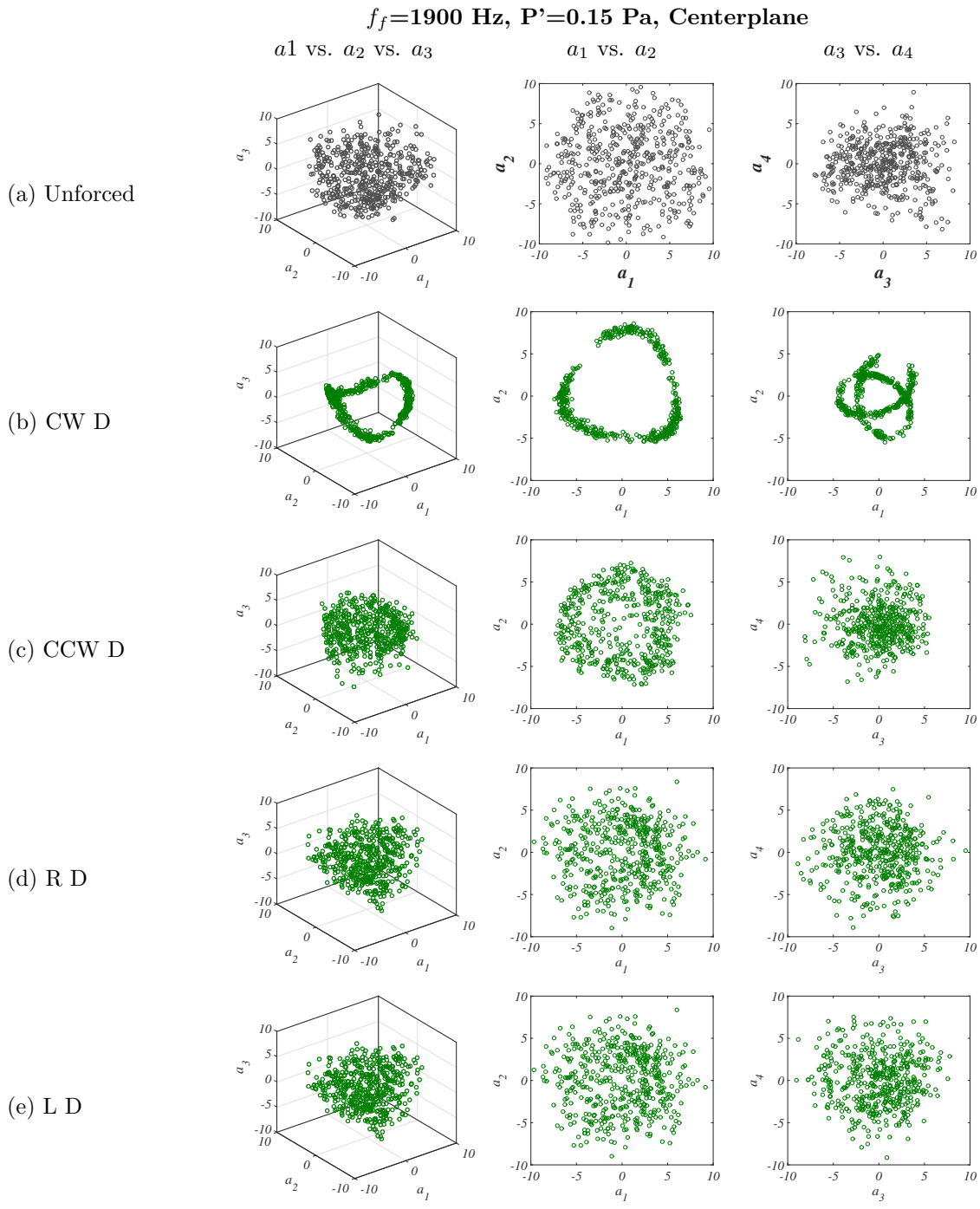

Figure 5.20: PLIF POD coefficients for the first 4 modes plotted against each other, extracted from instantaneous centerplane images of the $J = 61$ JICF, (a) unforced, and (b-e) subject to $f_f =$ 1900 Hz downstream region forcing. Black symbols represent the unforced condition, green colored symbols represent 1:1 lock-in of the USL.

no coherent structures were formed in any cases which exhibited quasiperiodic behavior. Secondly, Figure 5.18 illustrates that in general, forcing frequencies above the $J = 61$ fundamental range of $f_o \cong$ 1600-1900 Hz were less likely to produce coherent phase maps of POD coefficients extracted from the PLIF images. As the forcing frequency was applied farther above the fundamental, likelihood of randomness in the phase space increased. In the 4-speaker study, external forcing at $f_f = 2300$ Hz, but with a significantly increased the pressure perturbation amplitude of P'= 0.42 Pa, did give rise to the formation of patters in the POD mode coefficients as shown in Figure 5.15. However, no frequency of forcing above $f_f = 2300$ Hz demonstrated any signs of periodicity in the phase space, despite employing very high perturbation amplitudes for this asymmetric forcing study.

Study of the POD coefficients showed that in general, for forcing cases near the fundamental range in which the USL velocity power spectra saw the emergence of the forcing subharmonic $1/2f_f$, and pairings of the subharmonic with the fundamental and higher modes ($3/2f_f$, $5/2f_f$, etc.), tended to produce phase maps in which the coefficients of the second mode pair a_3 and a_4 formed coherent structures. Similar behavior was observed for cases where excitation of only one or two speakers was applied. For example, Figure 5.20 (b) shows that for $f_f = 1900$ Hz subject to CW D asymmetric forcing, cyclic or recurring behavior emerged from the phase plots of the first two mode pairs. Upon examination of the USL power spectra for this set of forcing conditions at $f_f = 1900$ Hz in Figure 3.8 (c), only the CW D condition showed peaks in the USL response spectra at $1/2f_f$ and higher combinations. This may suggest that the coherence in the second mode pair is an artifact of this secondary set of harmonic frequencies present within the flowfield, however it is noted that not all forcing conditions in which the subharmonics were present in the USL power spectra resulted in pattern formation in the coefficient plots of a_3 vs. a_4.

Figure 5.21 shows the PLIF extracted POD coefficient phase space for the $J = 6$ JICF, which has an absolutely unstable USL in the unforced state (a). In agreement with the findings of Gevorkyan et al. (2018), for the unforced jet the first two mode coefficients formed a circle or ring, indicating strong periodicity generated from the upstream sear layer

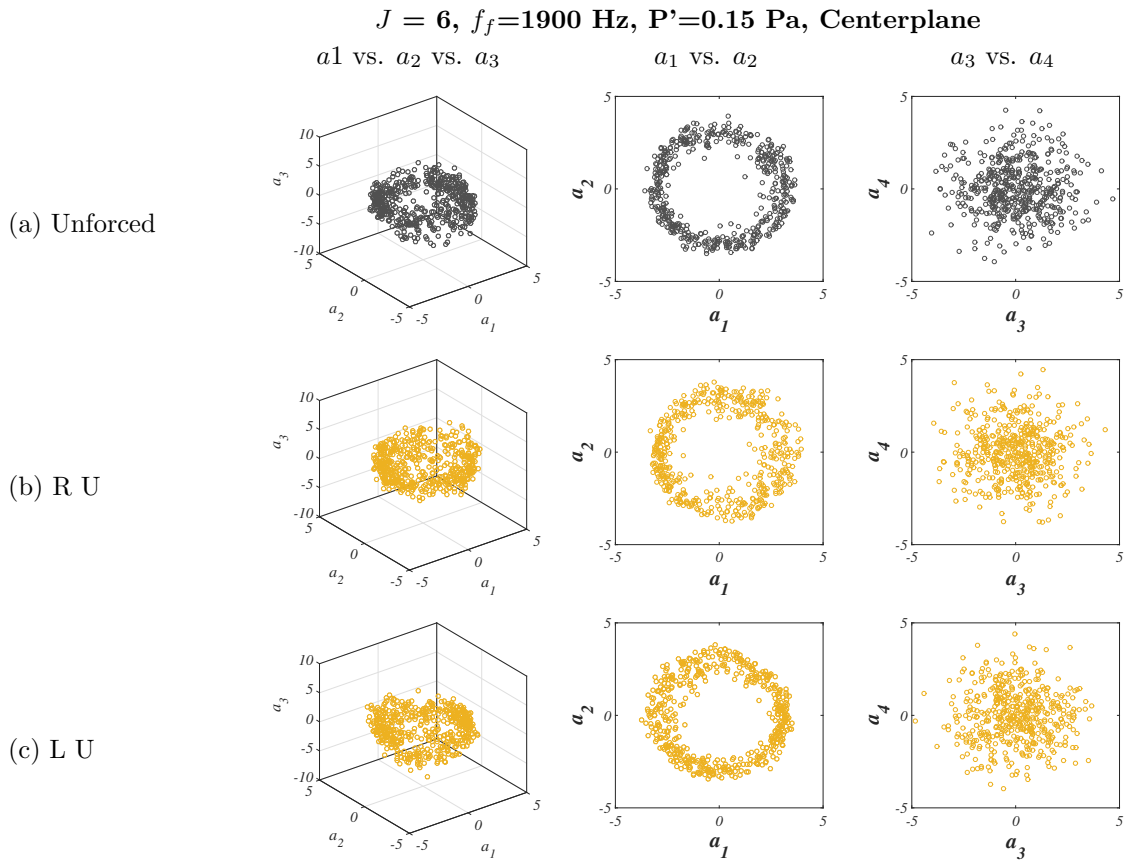

Figure 5.21: PLIF POD coefficients for the first 4 modes plotted against each other, extracted from instantaneous centerplane images of the $J = 6$ JICF subject to $f_f = 1900$ Hz upstream forcing. Black symbols represent the unforced condition, and yellow symbols indicate the nature of the USL response spectra can not be inferred from direct measurements.

vortex roll up. The $J = 6$ jet was subject to localized upstream region forcing at the USL fundamental frequency $f_o = f_f = 1900$ Hz, and POD coefficient maps are for these cases are shown in Figure 5.21 (b) and (c), where no discernible differences were observed between the forced and unforced conditions. These findings are consistent with previously discussed results of $J = 6$ structure and mixing studies, in that an absolutely unstable JICF already has a strong periodic vortex rollup, which makes the USL less susceptible to external forcing at low amplitudes.

Quite interestingly, coherent structures in the phase plots of the POD coefficients in general formed, or partially formed, a number of unusual shapes, some of which have been discussed. Specifically, those coherent shapes strongly resemble those of strange attractors

(Ruelle, 1980). An attractor is a set of values in phase space in which the system tends to evolve, and a strange attractor is one that has a long-term pattern but is not a simple periodic oscillation; time resolved trajectories within a strange attractor appear to skip around randomly. Since for the current study, the instantaneous PLIF images from which the POD mode coefficients were extracted are not time resolved, the emergence of a general orbit may have been easier to identify without noisy path traces. Moreover, the identification of such shapes is generally only enabled when one or both of the second most energetic mode pair coefficients a_3 and/or a_4 were considered. For example, plots of a_3 vs. a_4 strongly resemble a Smale-Williams attractor in Figure 5.19 (e), or a trefoil knot (also known as a 2-3 torus knot) as in Figure 5.15 (b). In 3D phase space, Rössler-like attractors are sometimes observed to emerge as in Figure 5.19 (d). Other coherent shapes formed from the mapping of snapshot POD mode coefficients resemble structures such as Lorenz, Henon, Pliny, Feigenbaum, and possibly the Duffing and Ikeda strange attractors.

Strange attractors have been associated with fluid dynamics since Edward Lorenz (Lorenz, 1963) developed a model for atmospheric convection in 1963, whose solutions where highly sensitive to initial conditions. Ruelle and Takens (1971) suggested that turbulence might be a manifestation in physical space of a strange attractor in phase space, and that a strange attractor would appear at the third bifurcation in the Landau sequence, for a system subject to steady action such as pumping or forcing (Berkooz et al., 1996; Miles, 1984). In the solution space, at most two incommensurate frequencies (or modes in the current study) could appear before the appearance of the strange attractor and subsequent transition to chaotic flow.

Indeed this study, as in Li and Juniper (2013c), observed such evidence of incommensurate frequencies in quasiperiodic power spectra in which the two frequencies were f_o and f_f. Additionally, in the study by Li and Juniper (2013c) Poincaré maps are used to analyze the response character of the low density free jet to subject to external forcing. In general, a Poincaré section is slice through an attractor, plotting the points where the trajectory crosses the plane, thereby reducing the attractor to one less dimension. If a system is

quasiperiodic, the trajectory wold be a non-repeating orbit around a torus attractor, and torus birth bifurcation could be visualized in the Poincaré map. But if the system is chaotic, the trajectory is a non-repeating orbit around one or more strange attractors (Strogatz, 1994).

Guan et al. (2018) note the emergence of strange attractors during transition to chaos in for a periodic acoustically forced laminar flame, when forcing at amplitudes above the lock-in threshold. The transition is also characterized by the appears of a third incommensurate frequency in the PSD, due to the emergence of a second natural mode of the system. In the current study, for cases in which strange attractors appeared in the POD phase space, three incommensurate frequencies were not observed in the USL power spectra. As previously discussed, in some instances the subharmonic $1/2f_f$ and combination of the subharmonic with f_f were observed in the PSD, but these frequencies are not incommensurate with one another. However, the existence of additional frequencies cannot be ruled out. The USL spectra for the forced conditions are measured at a fixed location, $s/D = 2.0$, so perhaps additional frequencies appear elsewhere along the trajectory. Additionally, the current measurement of the USL spectra is for the vertical component of velocity, and may not be detecting frequencies of any $m = \pm 1$ helical modes traveling azimuthally around the jet periphery. In a free jet subject to axisymmetric forcing, Bonetti and Boon (1989) identified that in the transitional region where the helical mode is amplitude saturated, the instability can be described by a low-dimensional chaotic attractor. So perhaps similarly in the current study, the appearance of strange attractors may be associated with the saturation of the helical modes. Therefore the emergence of strange attractors in the phase space of PLIF extracted POD coefficients may indicate onset of turbulence/chaos, or some other transition in the fluid dynamics, and bears further study.

CHAPTER 6

Simultaneous Scalar and Velocity Field Characteristics for the Asymmetrically Forced JICF

Chapters 4 and 5 have discussed the influence of external asymmetric acoustic forcing on the transverse jet scalar concentration field, specifically examining the alterations in jet cross-sectional structure and molecular mixing induced by the different directional and localized excitation strategies. This chapter investigates the influence of asymmetric forcing on the transverse jet velocity field, interactions between the velocity field and scalar field, and seeks to extract flow parameters that are relevant to reactive and mixing processes. Simultaneous PLIF/PIV measurements were acquired for the jet centerplane view, as well as cross-sectional views of planes $x/D = 0$ (at nozzle orifice) and x/D = -0.4 (slightly upstream of jet exit), for the $J = 41$ JICF.

6.1 Simultaneous PLIF/PIV Flow and Imaging

Prior results in the current study have presented stability characteristics and scalar concentration images for the $J = 61$, $S = 1$ transverse jet with acetone mole fraction $\Psi = 0.218$ with $Re = 2300$. These jet flow condition corresponded to that of other studies by our group, which were based on acetone PLIF imaging (Getsinger et al., 2014; Gevorkyan et al., 2016; Shoji et al., 2019c,a). Results from this section were produced from flow conditions corresponding to that of previous work by our group, which analyzed simultaneous PLIF/PIV measurements (Gevorkyan et al., 2018). In order to better characterize the USL instability for the newly presented flow condition, similar to the power spectra results of Figure 3.2,

(a) $J = 41$ (b) $J = 41$

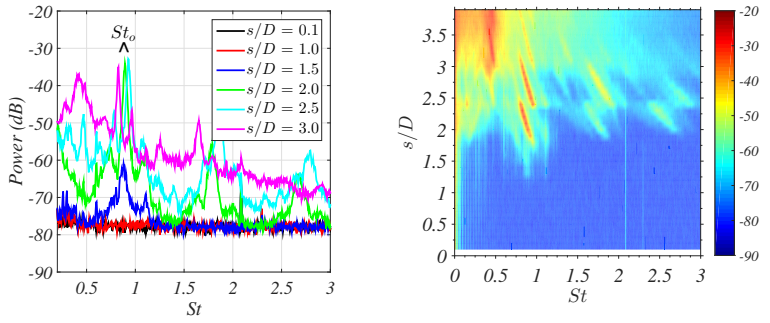

Figure 6.1: Power spectra of vertical velocity disturbances along the USL coordinate s for the unforced $Re_j = 1900$ and acetone mole fraction $\Psi = 0.112$ JICF for (a,b) $J = 41$. Left column represents power spectra at discrete s/D USL trajectory locations. Right column represents spectral contour maps with 0.1 s/D spatial resolution with color bar indicating disturbance amplitude in dB.

the evolution of the USL spectral character was measured for the unforced $J = 41$ JICF with $\Psi = 0.112$ via hotwire anemometry, with methods as described in Chapter 3.

Figure 6.1 (a) represents the magnitude of the local velocity perturbation in dB as a function of upstream shear layer (USL) trajectory locations s/D and $St = \frac{fD}{U_j}$, or normalized frequency, where D is the jet diameter (4.04 mm) and U_j is the velocity of the jet. For the spectra shown here, the jet fluid was seeded with acetone at a mole fraction of $\psi = 0.112$ and mole fractions of helium of $\psi = 0.102$ and nitrogen of $\psi = 0.785$, corresponding to simultaneous PLIF and PIV experiments discussed here. These conditions produced a jet density that was approximately equal to that of air, such that $S = 1$, with a jet Reynolds number of $Re = 1900$. Figure 6.1 (b), is a more finely resolved spectral magnitude contour plot, in trajectory increments of $s/D = 0.1$, where the color bar corresponds to the disturbance magnitude. Similar to Figure 3.2 (b), the $J = 41$ transverse jet showed frequency hopping or shifting of the dominant disturbance along the shear layer, where here the dominant frequency range was $f_o \approx$ 1350-1600 Hz. The fundamental frequency of the instability, St_o or f_o, was estimated as the mean of this broadband frequency shifting range to be $f_o = 1475$ Hz. Farther downstream along the s coordinate, for $J = 41$, a subharmonic

of this fundamental mode developed, $f_{1/2}$, indicating the onset of energy transfer from the fundamental frequency to the subharmonic, corresponding to vortex pairing of the upstream shear layer instability structures. These spectral features are characteristic of a convectively unstable shear layer (Megerian et al., 2007; Davitian et al., 2010a; Getsinger et al., 2012). Furthermore, the USL power spectra for the $J = 41$ JICF was quite similar in character to that of the USL for $J = 61$, for which asymmetric forcing results have been presented in previous chapters. Similarly, it has been previously noted that the dominant instabilities frequencies differ for jets comprised of helium, nitrogen, and acetone as compared with the pure nitrogen but with the same density (Shoji, 2017), yet the spectral characteristics are similar for the same J values.

Figures 6.2 through 6.5 show sample scaled vorticity and scaled jet fluid scalar concentration plots, where spanwise vorticity (ω_y in the centerplane view and ω_x in the cross section views) was extracted from the PIV velocity field and scaled by jet mean velocity and jet diameter (U_j/D), and the jet acetone concentration was scaled by the concentration of the jet potential core C_o. This chapter primarily presents results for the $J = 41$ transverse jet subject to asymmetric forcing at $f_f = 1600$ Hz, at pressure perturbation amplitude P'= 0.15 Pa, and comparative results for the unforced case. The $f_f = 1600$ Hz forcing cases generally resulted in the most interesting results, as $f_f \approx$ 1600 Hz is at the top of the USL fundamental frequency range f_o = 1350-1600 Hz. Sample results for additional forcing conditions are shown in Appendix E. As discussed in Chapter 2, the PLIF portion of the simultaneous PLIF/PIV imaging is captured with a camera of lower resolution than what is utilized for PLIF-only experiments, and without a signal intensifier. Additionally, small variations in the crossflow seeding density over the duration of the experiment affect instantaneous laser energy absorption, while shot-to-shot laser energy normalization was not performed post-processing since instantaneous relative magnitude energy measurements are not obtained for such experiments. These combined factors contribute to generally noisier PLIF images whose scalar concentration values are less accurate, thus cannot be used for certain calculations such as mixing quantification.

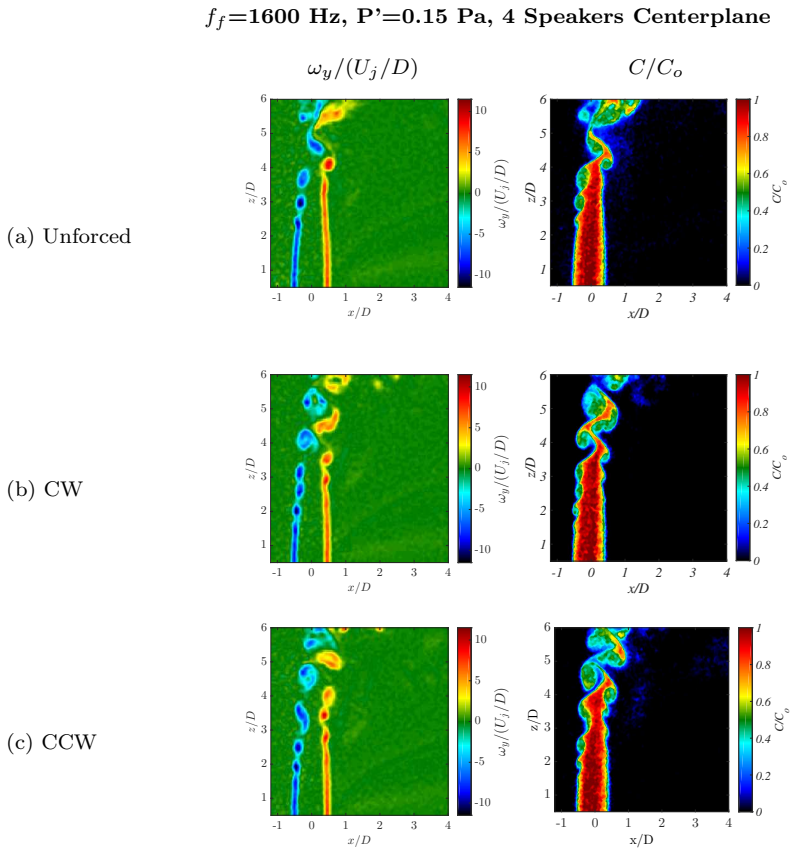

Figure 6.2: Instantaneous simultaneous PLIF/PIV imaging of the $J = 41$ JICF. Data shown for scaled vorticity $\omega_y/(U_j/D)$ and scaled jet fluid concentration C/C_o in the centerplane view for the (a) unforced case and (b-c) subject to directional forcing with excitation $f_f = 1600$ Hz and P'= 0.15 Pa.

As shown by Gevorkyan et al. (2018), the transport of vorticity and the passive scalar show remarkable correspondence in jet centerplane images for the unforced JICF of varying flow conditions and nozzle configurations. Similarly, the asymmetrically forced jet demonstrated close correspondence between the instantaneous vorticity field and scalar concentration images. In Chapter 4, in the centerplane view high resolution PLIF imaging results, asymmetric forcing was previously observed to initiate the USL roll-up closer to the jet exit, and indeed this was observed PIV vorticity images as vortex cores in the upstream shear layer in Figures 6.2 and 6.4. It is noted that the crossflow as well as the jet fluid are seeded in PIV experiments, and hence additional information on the crossflow deflection as well as wake structures can be obtained in these experiments.

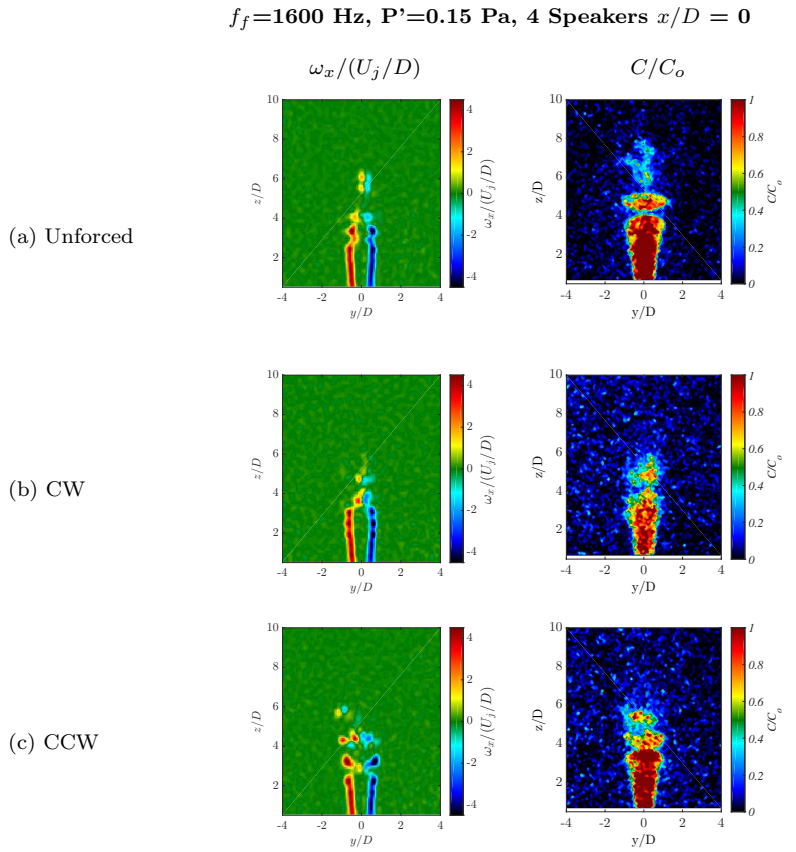

Figure 6.3: Instantaneous simultaneous PLIF/PIV imaging of the $J = 41$ JICF. Data shown for scaled vorticity $\omega_x/(U_j/D)$ and scaled jet fluid concentration C/C_o for the $x/D = 0$ cross-sectional view (a) unforced case, and (b-c) jet subject to clockwise and counterclockwise directional forcing with excitation $f_f = 1600$ Hz and P'= 0.15 Pa.

Cross-sectional PIV is a new capability to our group, enabling quantification of the jet bulk velocity field in slices over the evolution of the JICF. At this time, cross-sectional PIV far downstream of the jet, such as $x/D = 10.5$, was not implemented in part due to the very large out-of-plane component of velocity (U_x) in the jet at such locations. Figure 6.3 (a-c) shows instantaneous images of simultaneous PIV and PLIF extracted data in the cross sectional view of the jet exit, $x/D = 0$. As seen in the scaled vorticity images, the jet potential core region is captured as symmetric continuous vortex regions on either side of the jet until $z/D \approx$ 2-3 where USL roll-up was evidenced as vortex cores. Figure 6.3 (b), where asymmetric forcing in the clockwise direction utilizing all 4 speakers was applied at $f_f = 1600$ Hz, clearly captured the USL roll-up instability forming closer to the jet exit.

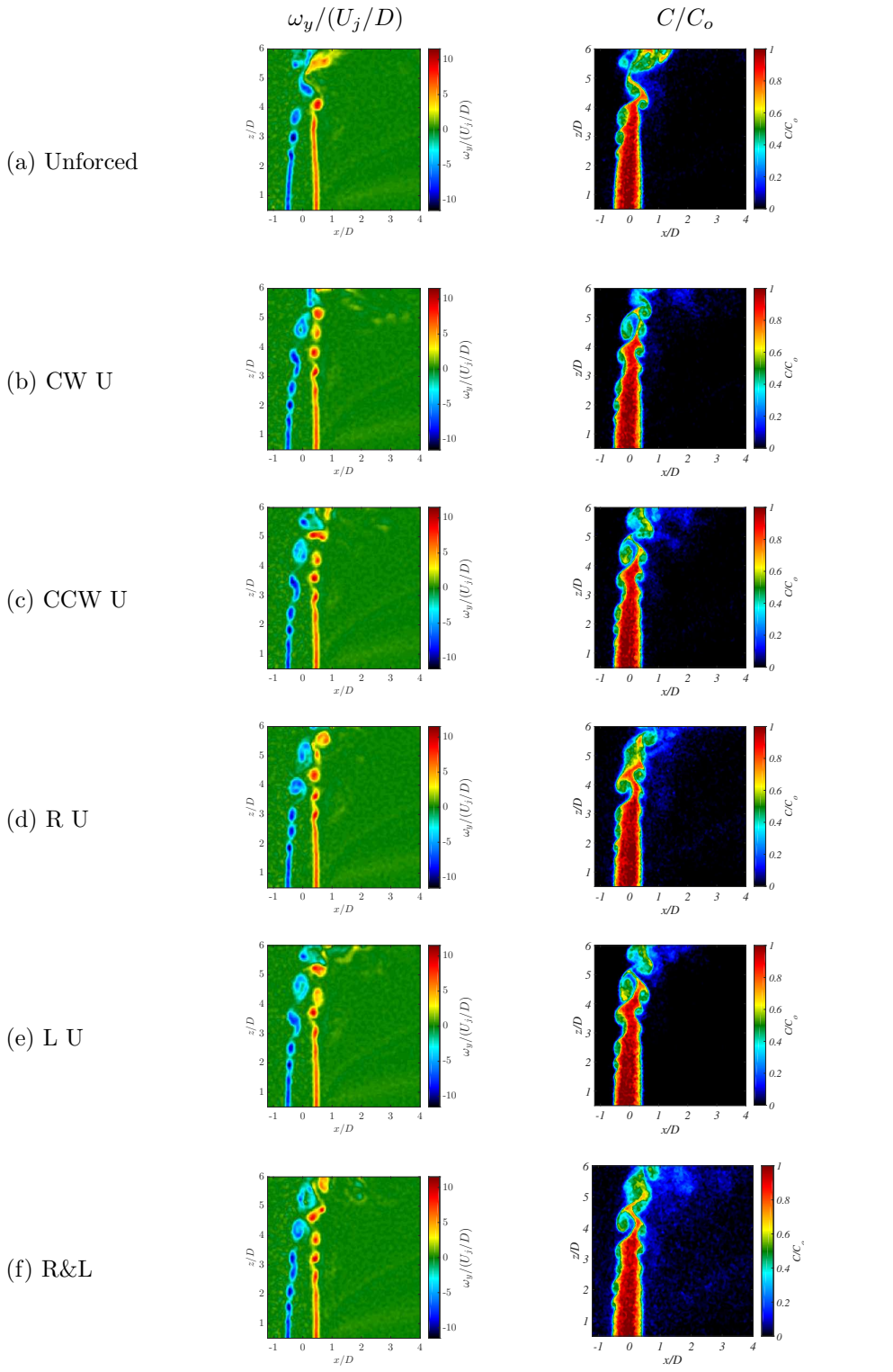

Figure 6.4: Instantaneous centerplane simultaneous PLIF/PIV imaging of the $J = 41$ JICF. Data shown for scaled vorticity $\omega_y/(U_j/D)$ and scaled jet fluid concentration C/C_o for the (a) unforced jet, and jet subject to upstream directional forcing with excitation (b-f) f_f = 1600 Hz and P'= 0.15 Pa.

Farther away from the exit, portions of jet the as it was deflected by the crossflow were seen as more diffuse regions of vorticity, such as for the unforced case in Figure 6.3 (a) at $z/D \approx 6$. Similar features of the flowfield were captured in simultaneous PLIF/PIV jet cross-sectional images just upstream of the jet exit, at x/D = -0.4, shown in Figure 6.5 for the unforced and forced conditions. The location of x/D = -0.4 corresponds with the upstream edge of the nozzle orifice, where the laser sheet would be likely to capture a portion of the USL for the $J = 41$ transverse jet.

In the instantaneous cross-sectional images of jet scalar concentration and vorticity fields, some asymmetries were observed, as in 6.5 (d) for example. It is known that the mean cross-section downstream of the $J = 61$ JICF is highly asymmetric, therefore the mean near-field vorticity and scalar images were examined for origin of such asymmetries, shown in Figure 6.6. At the edge of the jet orifice, in the upstream region where the USL is formed, clear asymmetries were apparent in the mean vorticity and concentration images at x/D = -0.4, in Figure 6.6 (a). The right hand side vorticity region (a1) was bent inwards toward the jet center, and a slight trail of diffuse vorticity veered to the left as the jet evolved vertically in this cross-sectional view. In the mean concentration image (a2) the asymmetry presented itself much more dramatically, again with a diffuse trail veering to the left as the jet evolves vertically. These images suggest that asymmetries exist in the most upstream portion of the jet, that the initial vortex roll-up of the USL is asymmetric in nature. At the jet exit cross-sectional plane $x/D = 0$, in Figure 6.6 (b), the asymmetries were less apparent in the mean vorticity and mean concentration images. This view primarily captured the jet potential core, whose structural symmetry has not been characterized yet at this time, but slight asymmetries were seen in both mean vorticity (b1) and mean concentration (b2) at the top portion of the jet, where the jet begins to bend over and the USL is presented in the plane of view. These results suggest that the origin of the jet asymmetries reside in the USL and form in the jet windward side.

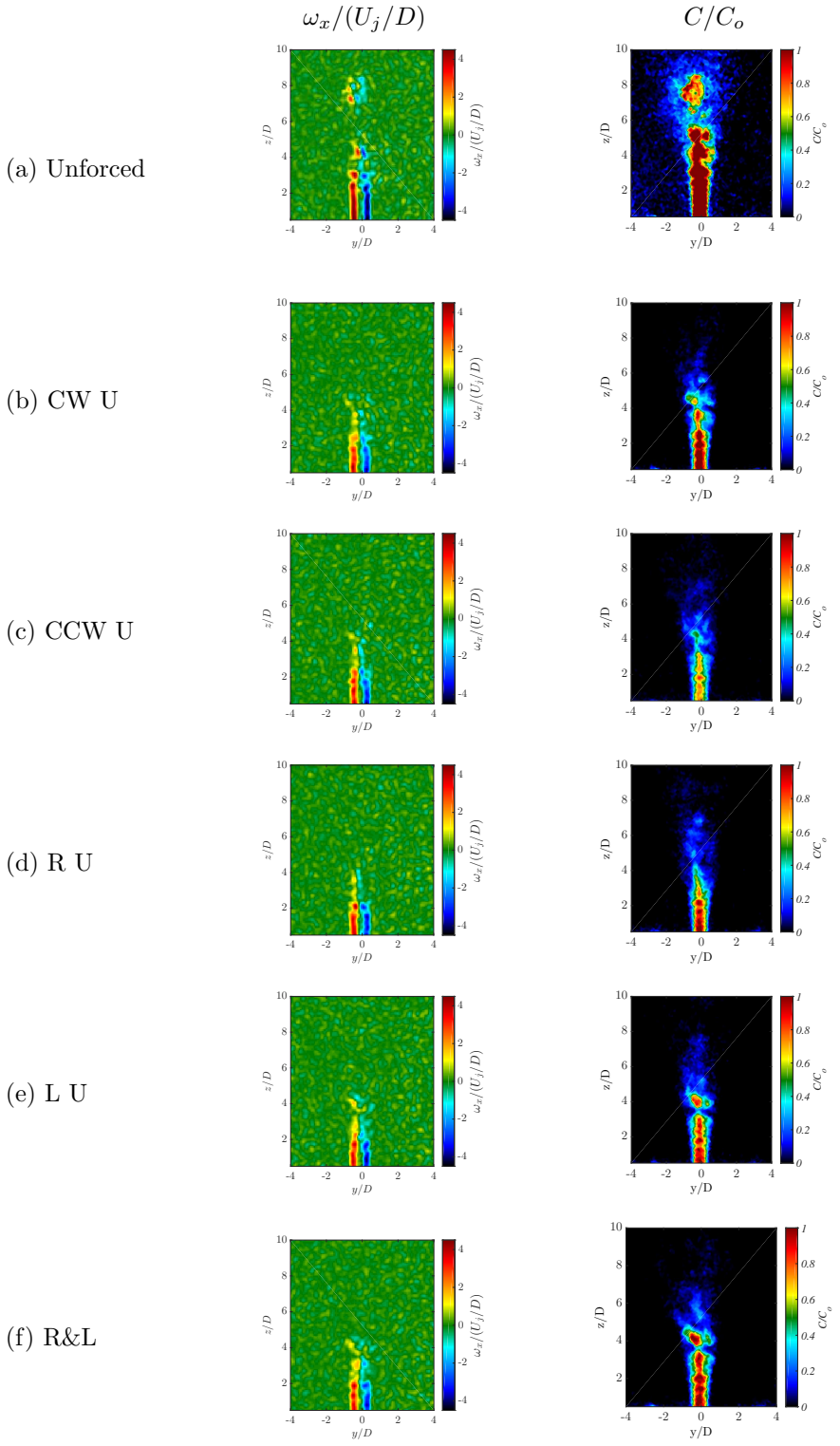

Figure 6.5: Instantaneous cross-section view at x/D = -0.4 simultaneous PLIF/PIV imaging of the $J = 41$ JICF. Data shown for scaled vorticity $\omega_x/(U_j/D)$ and scaled jet fluid concentration C/C_o for the (a) unforced jet, and jet subject to upstream directional forcing with excitation (b-f) f_f = 1600 Hz and P'= 0.15 Pa.

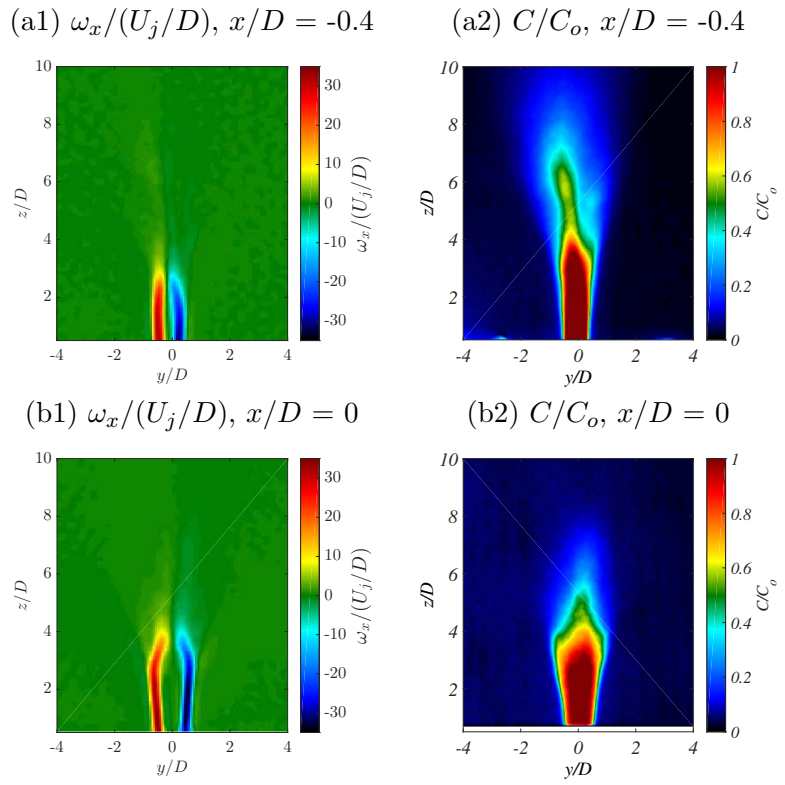

Figure 6.6: Mean scaled vorticity $\omega_x/(U_j/D)$ and jet concentration C/C_o for the unforced $J = 41$ jet in the cross-section view at (a) x/D = -0.4 and (b) $x/D = 0$.

6.2 POD Analysis for Simultaneous PLIF and PIV

Snapshot POD analysis was applied to the instantaneous images of the simultaneous PLIF/PIV asymmetric excitation velocity field and scalar concentration data. Figure 6.7 shows the first two velocity and scalar mode structures and their corresponding portions of fluctuating kinetic energy (KE, extracted from PIV) or scalar energy (SE, extracted from PLIF) content. As expected, for the unforced jet in the centerplane view, Figure 6.7 (a-b), the first two PIV and PLIF POD mode structures and proportional energy contributions aligned well with the results reported by Gevorkyan et al. (2018) for the flush nozzle-generate equidensity $J = 41$ JICF. The first two PIV and PLIF POD modes in the cross-sectional plane of the jet orifice upstream edge (x/D = -0.4) are shown in 6.7 (c-d). The first PIV mode (c1) indicates the dominant kinetic energy fluctuating structure may represent the crossflow bending around

the jet, as indicated by the in-plane velocity arrows outside of the jet. Interestingly, the pattern of crossflow motion showed a definite clockwise directional preference above $z/D \approx 3$, which corresponds to the location of USL roll up initiation. This may suggest that the formation of the USL is asymmetric, resulting in asymmetric entrainment of the cross-flow. Some evidence of the clockwise preferential velocity persists in the second PIV POD mode structure (d1), which had a relatively low percentage fluctuation energy contribution as compared to mode 1, though this mode was dominated by alternating patterns of in-plane and out-of-plane velocity components which correspond the USL vortical structures. For the jet upstream edge location x/D = -0.4, the PLIF-based POD mode structures offered less insight to the flowfield, but showed that the USL structures did not dominate the scalar field here. However, for the $J = 41$ unforced jet at the cross-sectional plane of jet injection, $x/D = 0$, the first two POD mode structures extracted from PIV and PLIF data clearly represent the jet USL vortical roll-up structures.

Figures 6.8 through 6.10 show sample POD mode structures for the asymmetrically forced jet, with $f_f = 1600$ Hz and pressure perturbation amplitude P'= 0.15 Pa for clockwise and counterclockwise 4 speaker operation. In the centerplane view of the asymmetrically forced jet (6.8), the fluctuation energy content of the first two POD modes significantly increased for both the PIV and PLIF based analysis. These first two modes also appeared paired, in both the energy content and in structure character. In this view, significant effects on the centerplane POD mode structures as a result of asymmetric forcing can be observed. Evident in both the PIV-based POD and PLIF-based POD structures, the initiation of the upstream shear layer-roll up moved closer to the jet exit, which is consistent with the scalar concentration images in Chapter 4 of the $J = 61$ jet. Interestingly, in the PIV mode structures (Figure 6.8, column 1), evidence of cross-flow entrainment is observed as structures of alternating magnitude appear upstream of the jet USL. No discernible differences between clockwise and counterclockwise directional forcing were observed in the dominant POD mode structures.

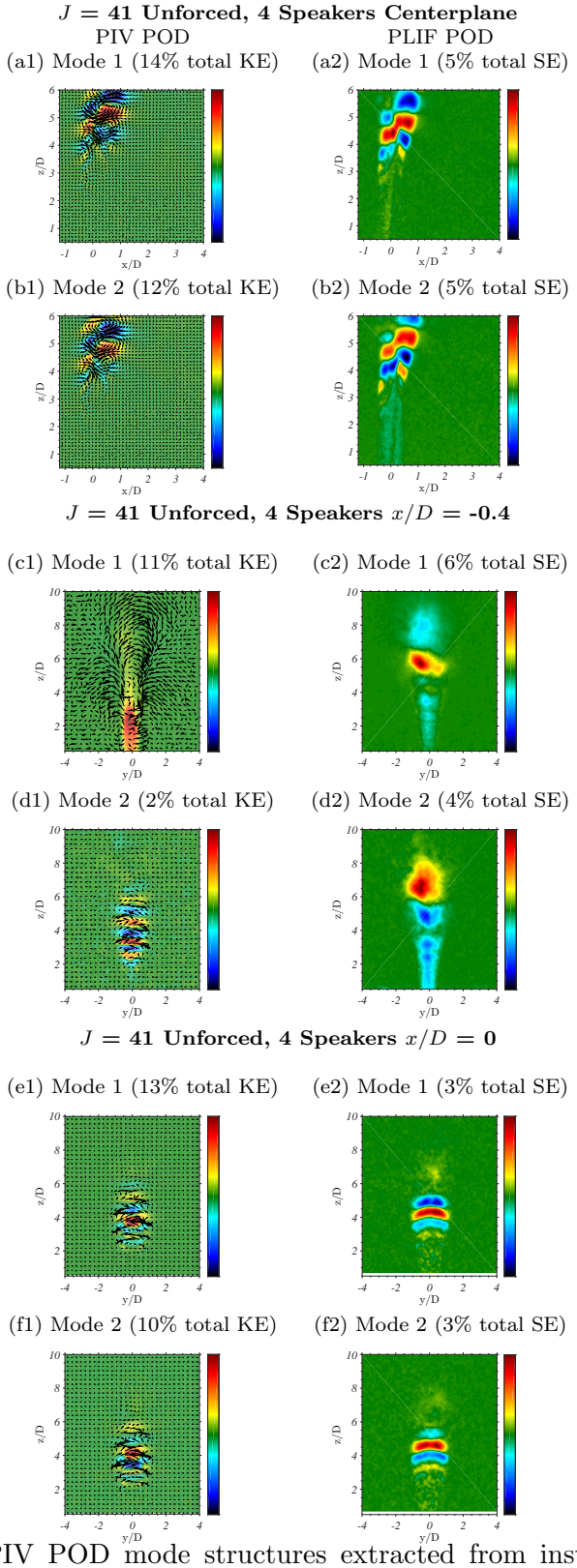

Figure 6.7: PLIF and PIV POD mode structures extracted from instantaneous images of the unforced $J = 41$ JICF in (a-b) centerplane view, (c-d) upstream cross-sectional view at x/D = -0.4, (e-f) jet center cross-sectional view at $x/D = 0$. Percentage of total kinetic energy (KE) or scalar fluctuation energy (SE) contributed by each mode is indicated.

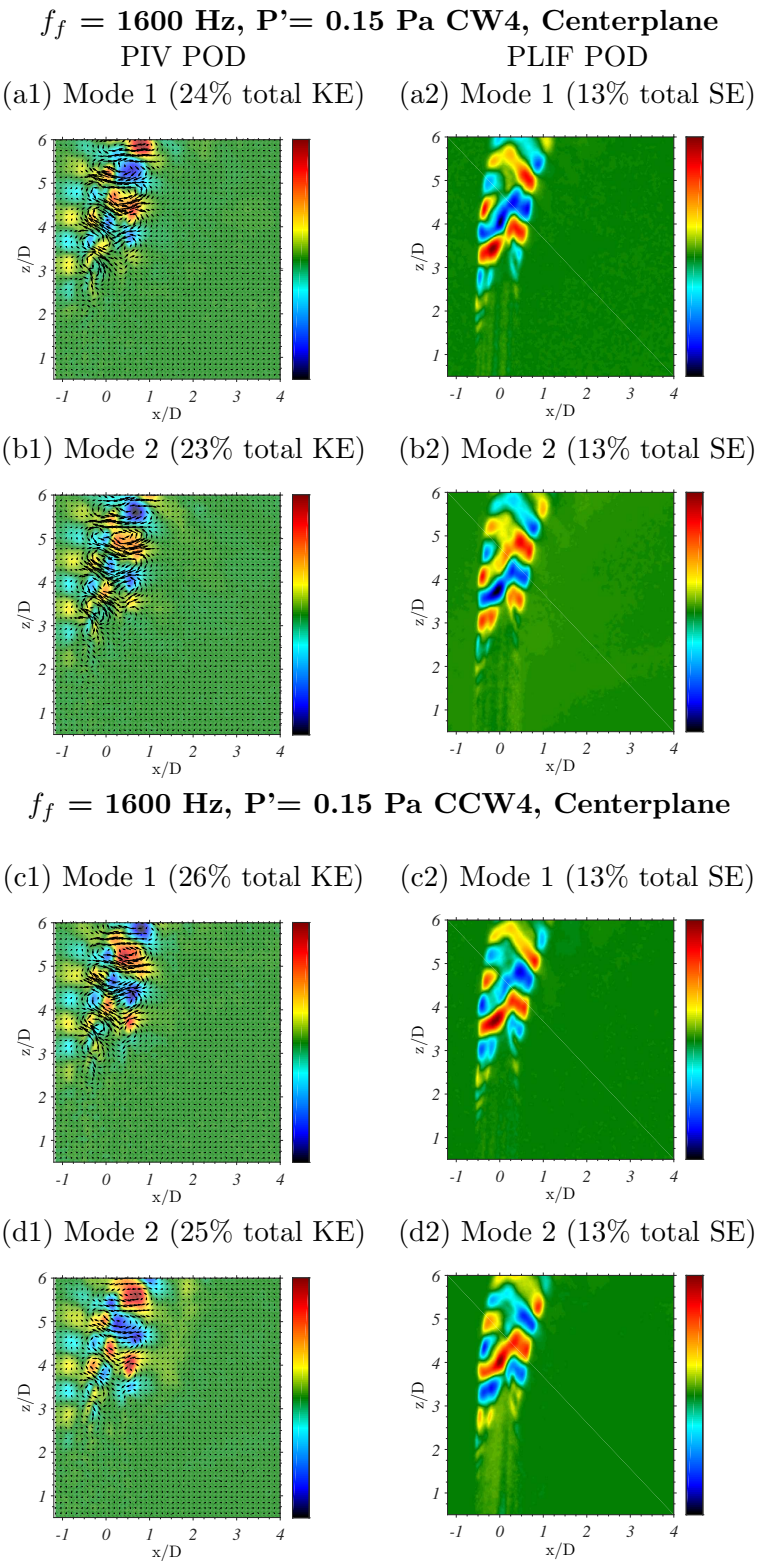

Figure 6.8: PLIF and PIV POD mode structures from instantaneous centerplane images of the J = 41 JICF subject to external asymmetric forcing at f_f = 1600 Hz with amplitude P'= 0.15 Pa in the (a-b) clockwise and (c-d) counterclockwise directions for 4 speaker operation. Percentage of total kinetic energy (KE) or scalar fluctuation energy (SE) contributed by each mode is indicated.

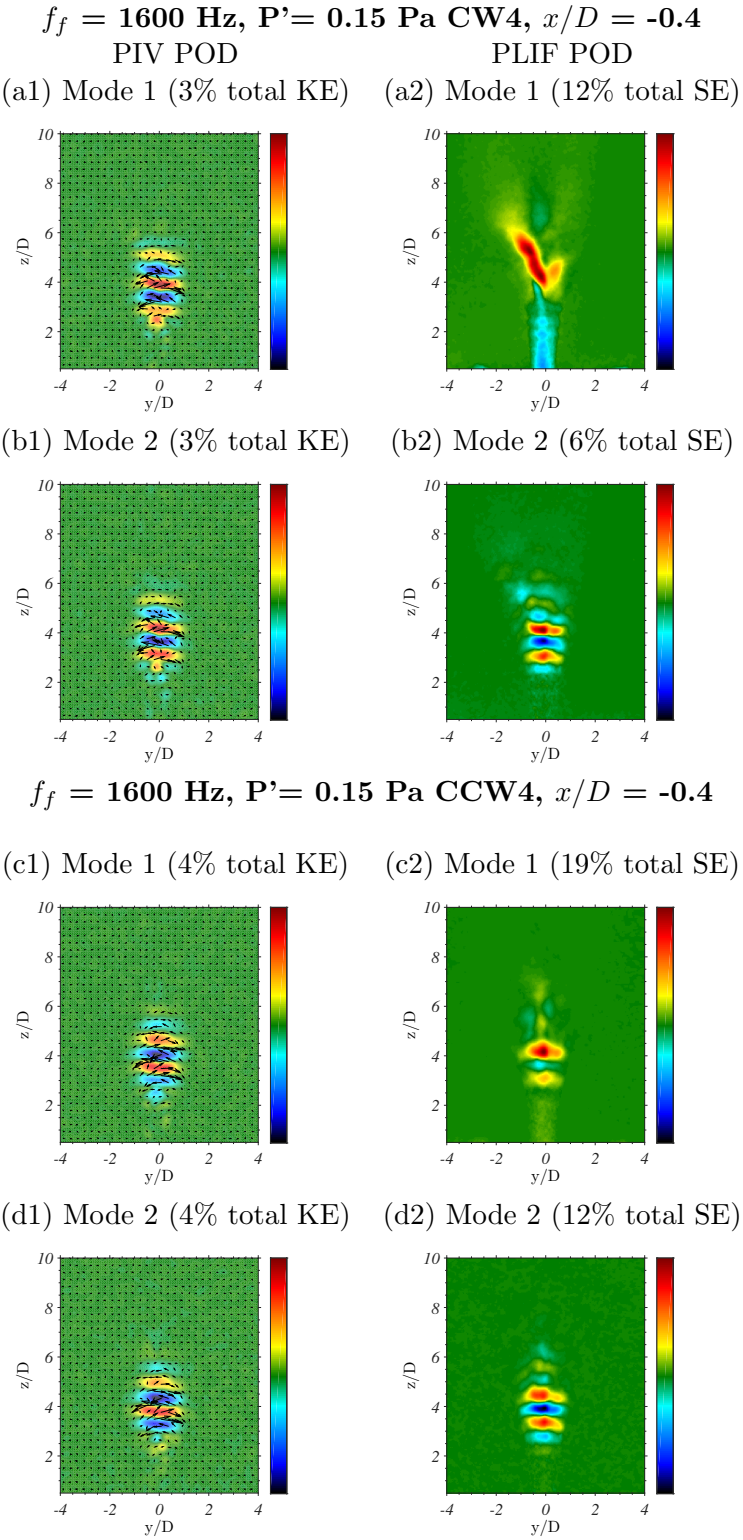

Figure 6.9: PLIF and PIV POD mode structures from instantaneous x/D = -0.4 cross-sectional plane images of the J = 41 JICF subject to external asymmetric forcing at f_f = 1600 Hz with amplitude P'= 0.15 Pa in the (a-b) clockwise and (c-d) counterclockwise directions, utilizing all 4 speakers. Percentage of total kinetic energy (KE) or scalar fluctuation energy (SE) contributed by each mode is indicated.

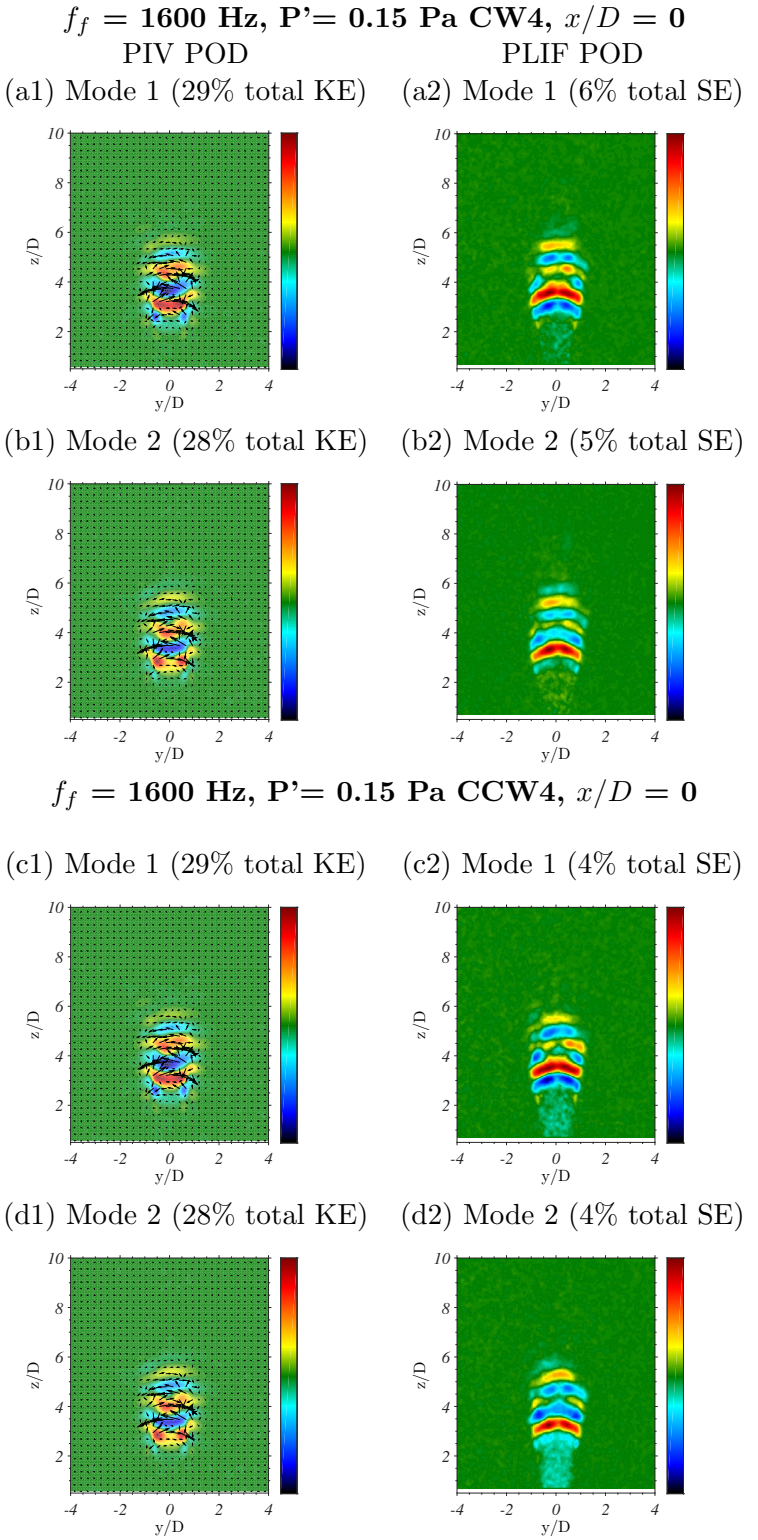

Figure 6.10: PLIF and PIV POD mode structures from instantaneous $x/D = 0$ cross-sectional plane images of the $J = 41$ JICF subject to external asymmetric forcing at $f_f = 1600$ Hz with amplitude P'= 0.15 Pa in the (a-b) clockwise and (c-d) counterclockwise directions for 4 speaker operation. Percentage of total kinetic energy (KE) or scalar fluctuation energy (SE) contributed by each mode is indicated.

In the cross-sectional views of the jet in Figures 6.9 and 6.10, the USL generally dominated the PIV and PLIF extracted POD modes. An exception can be seen in Figure 6.9, where the first PLIF POD mode structures in both the clockwise (a2) and counterclockwise (b2) forcing directions at the jet upstream edge (x/D = -0.4) showed structures that were more uniform and did not imply scalar field oscillations, similar to what was seen in the unforced case (Figure 6.7 (c2) and (d2)). Interestingly, at the jet upstream edge, the forcing resulted in increased energy content in the PLIF-based POD modes 1 and 2, but unexpectedly the fluctuation energy content of the PIV-based POD modes had not been significantly increased. Although asymmetric forcing has previously been shown to initiate the USL roll up somewhat closer to the jet exit, the initiation had likely not yet occurred in this view of the upstream region. However, in the plane of the nozzle center at $x/D = 0$ in Figure 6.10, the energy content of the first two PIV mode pair structures had increased significantly and appeared in pairs, agreeing with the trends of the centerplane view.

6.3 Mode Coefficient Phase Space Plots

Since the energy content of the first two PIV POD modes for the asymmetrically forced jet was observed to significantly increase over that of the unforced case, and the modes appeared in energy pairs, as in the analysis for high resolution PLIF POD in Chapter 5, PLIF and PIV-based POD mode coefficients were examined for relationships of periodicity. Although the flowfield in this study was slightly different than in the previous sections, some of the phase mapping results are quite similar to those of Chapter 5. POD mode coefficients examined here were extracted from PIV velocity fields and PLIF scalar fields, and in general the PIV-based mapping produced more coherent, well-defined shapes than the corresponding simultaneous PLIF POD coefficient map. Again, specific cases are shown here to demonstrate particular trends in the phase space, and should not imply that all asymmetric forcing cases resulted in the emergence of patterns in the coefficients of the dominant modes.

Asymmetric forcing at $f_f = 1600$ Hz always produced a coherent three dimensional phase representation of the PIV based POD coefficient, which manifested themselves as a closed

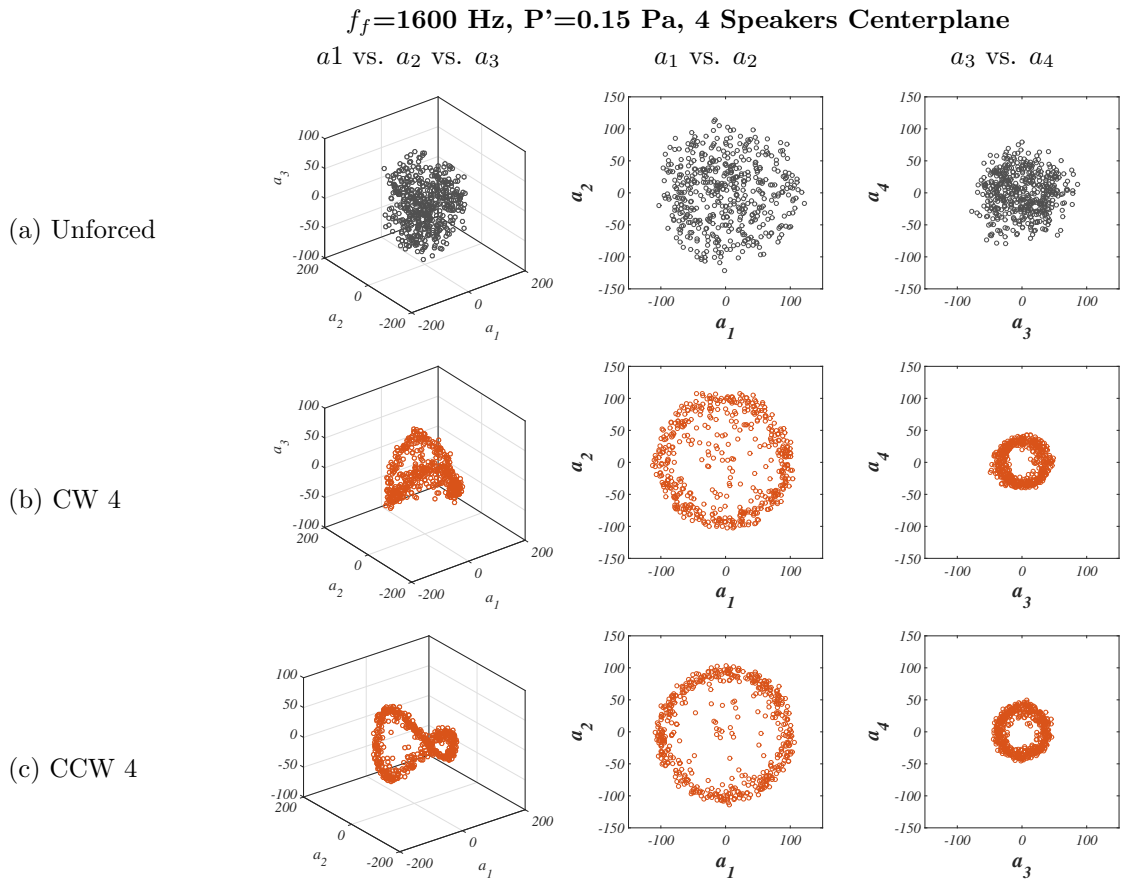

Figure 6.11: PIV POD coefficients for the first 4 modes plotted against each other, extracted from instantaneous centerplane images of the $J = 41$ JICF, (a) unforced, and (b-c) subject to 4 speaker clockwise and counterclockwise directional forcing, where $f_f = 1600$ Hz. Black symbols represent the unforced condition, orange symbols represent the jet subject to asymmetric forcing.

or partially closed "bent" circles of varying orientations in the 3D phase space; hence $f_f = 1600$ Hz is exclusively discussed in this section for brevity. Figure 6.11 shows the coefficient maps for 4 speaker clockwise and counterclockwise asymmetric forcing. For this forcing frequency and speaker operation, a_1 and a_2 were clearly periodic with each other, forming a closed circle. Interestingly, PIV mode coefficients a_3 and a_4 also formed a circle indicating cyclic behavior, but with a circle of approximately 1/2 the radius of the circle formed by coefficients a_1 vs. a_2, which may indicate periodicity of a higher frequency. This result aligns with the velocity power spectra of a transverse with an absolutely unstable USL, where strong, pure-tone higher harmonics of f_o are present and persist along far downstream of the shear layer trajectory coordinate. The corresponding centerplane view-based PLIF

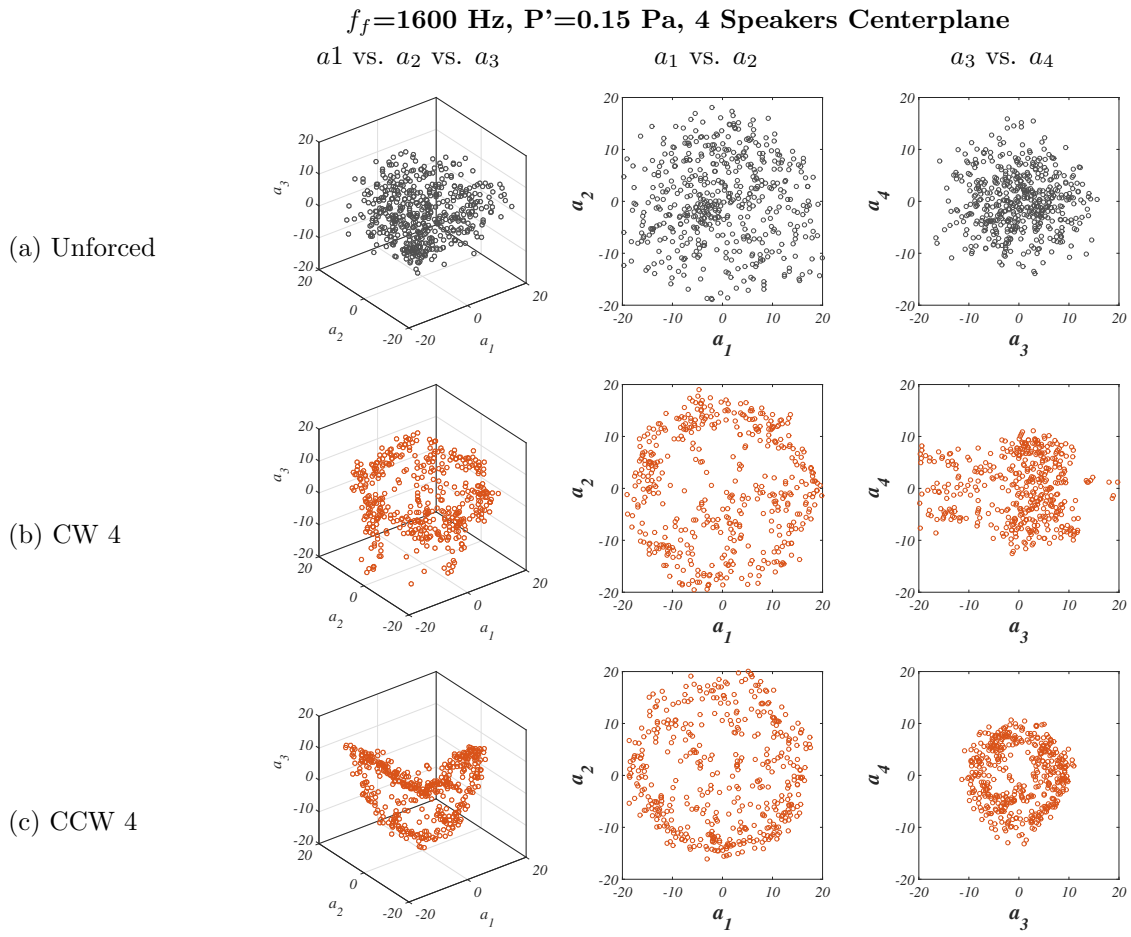

Figure 6.12: PLIF POD coefficients for the first 4 modes plotted against each other, extracted from instantaneous centerplane images of the $J = 41$ JICF, (a) unforced, and (b-c) subject to 4 speaker clockwise and counterclockwise directional forcing, where $f_f = 1600$ Hz. Black symbols represent the unforced condition, orange symbols represent the jet subject to asymmetric forcing.

POD mode coefficient mapping for the forcing condition $f_f = 1600$ Hz, utilizing all 4 speakers is shown in Figure 6.12. The overall shapes bear resemblance to the associated PIV coefficient phase space, however there is significantly more noise in the map, likely an artifact of the PLIF portion of simultaneous PLIF/PIV imaging and processing limitations previously discussed.

In the plane of the jet orifice leading edge, at x/D = -0.4 in Figure 6.13, the 2-D phase space of the first two mode POD coefficients for the unforced case was considerably irregular, perhaps due to the somewhat unique structure and high energy content of PLIF-extracted

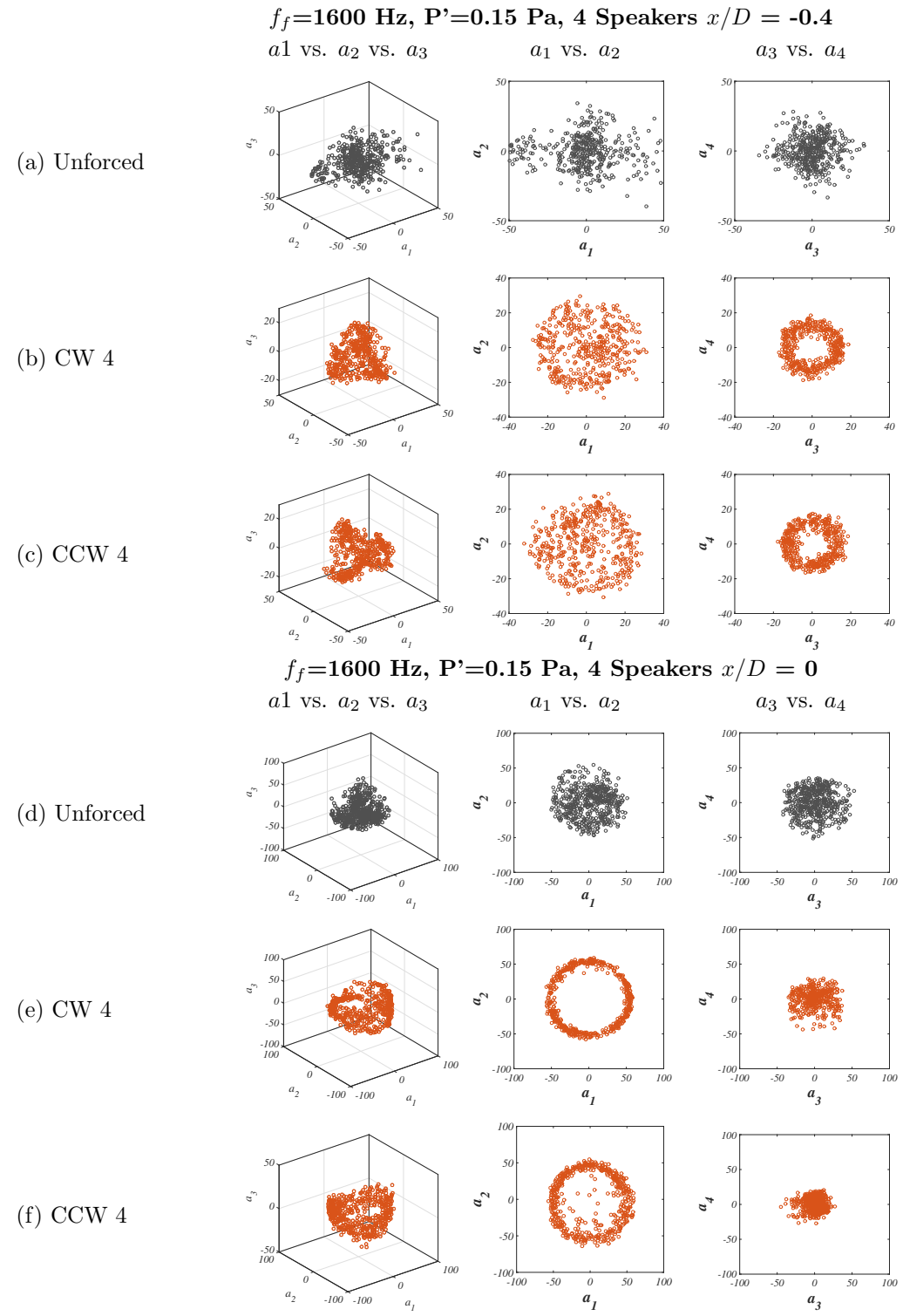

Figure 6.13: PIV POD coefficients for the first 4 modes plotted against each other, extracted from instantaneous cross-sectional plane images of the $J = 41$ JICF, for the unforced jet at (a) x/D = -0.4 and (d) $x/D = 0$, and subject to CW4 and CCW4 excitation in the (b-c) x/D = -0.4 plane and the (e-f) $x/D = 0$ plane, where $f_f = 1600$ Hz. Black symbols represent the unforced condition, orange symbols represent the jet subject to asymmetric forcing.

POD mode 1, shown in Figure 6.7 (c1) and previously discussed. External asymmetric forcing regularizes the random associations of a_1 vs. a_2, such that the phase space resembles that of a_1 vs. a_2 for the centerplane view of the unforced jet (Figure 6.11 (a)). Interestingly, the second mode pair coefficients a_3 and a_4 demonstrated a tight ring of periodicity, despite the first mode pair not exhibiting cyclic behavior. Slightly farther downstream at $x/D = 0$, periodicity had developed in the first mode pair coefficients for the forced transverse jet, while the periodicity of the second mode pair was no longer evident.

In the centerplane view, localized forcing in the jet upstream region with $f_f = 1600$ Hz produced quite coherent, well defined structures in the three dimensional phase space of the PIV extracted POD mode coefficients, as seen in Figure 6.14. The phase space of PLIF extracted POD mode coefficients for this forcing case are seen in Figure 6.15, where the character of the formed structures are of very similar nature to the PIV coefficient phase space, yet significant noise is apparent. However, in the phase space of the PIV mode coefficients (Figure 6.14), examination of the second most energetic mode pair coefficients revealed the emergence of shapes resembling strange attractors. In these localized upstream asymmetric forcing cases, plots of a_3 vs a_4 strongly resembled a form of the Smale-Williams strange attractor, similar to the results of CW4 forcing at $f_f = 1900$ Hz for the $J = 61$ jet shown in Figure 3.14 (d). It is notable to emphasize the similarity of the coherent structures produced in the phase space for these forcing conditions. The fundamental frequency range of the USL for the $J = 61$ JICF is $f_o \approx$ 1600-1900 Hz, while the fundamental frequency range of the USL for the $J = 41$ JICF studied in this chapter is $f_o \approx$ 1350-1600 Hz, and it is interesting that both forcing conditions at the upper bound of the fundamental range in their respective flowfield produced similar results in the POD coefficient phase space. And likewise, the emergence of a strange attractor in the phase space of PIV extracted POD mode coefficients may indicate the onset of of turbulence or other complex aspects of the fluid dynamics.

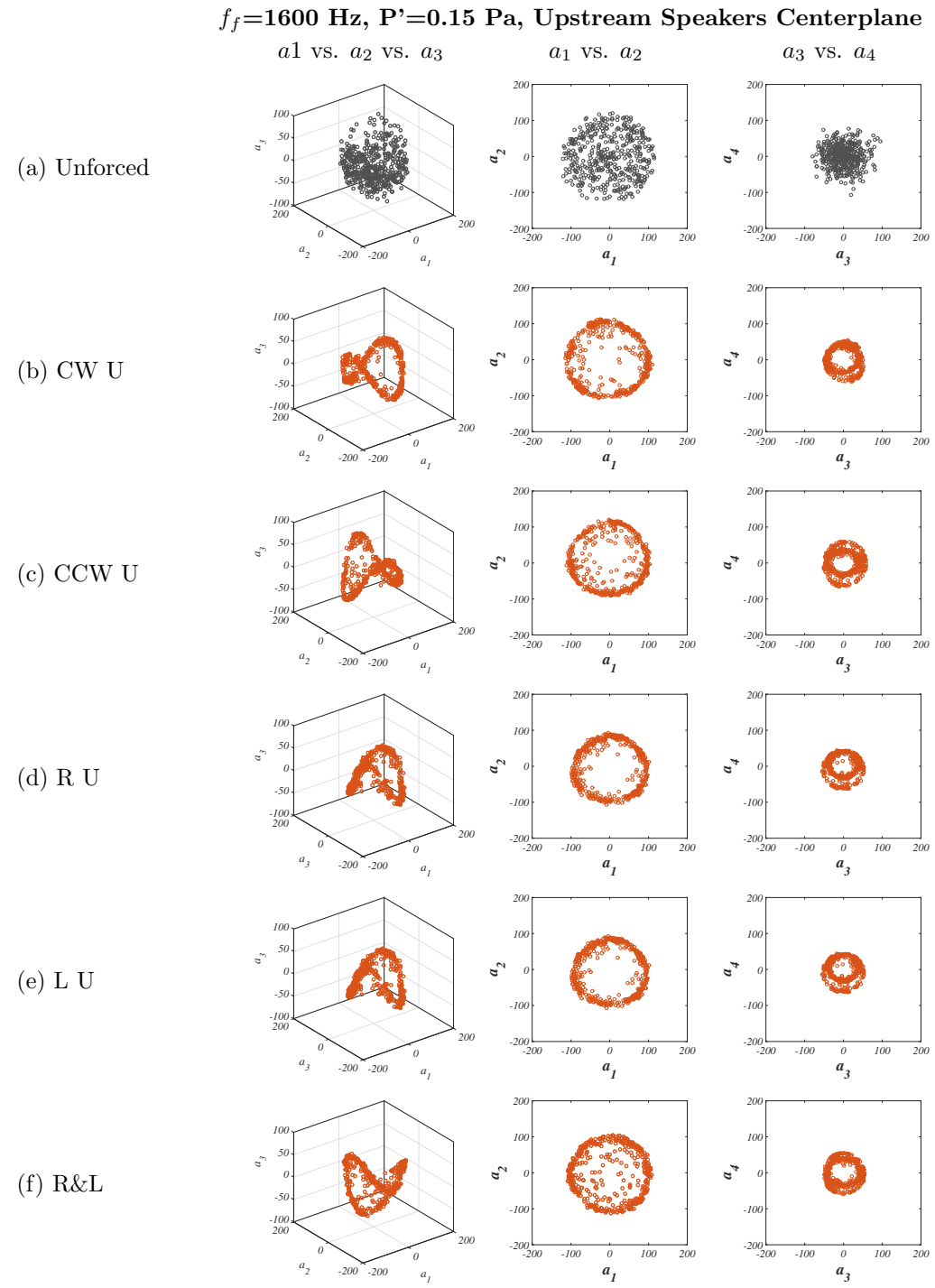

Figure 6.14: PIV POD coefficients for the first 4 modes plotted against each other, extracted from instantaneous centerplane images of the $J = 41$ JICF, (a) unforced, and (b-f) subject to $f_f = 1600$ Hz upstream region forcing. Black symbols represent the unforced condition, orange symbols represent the jet subject to asymmetric forcing.

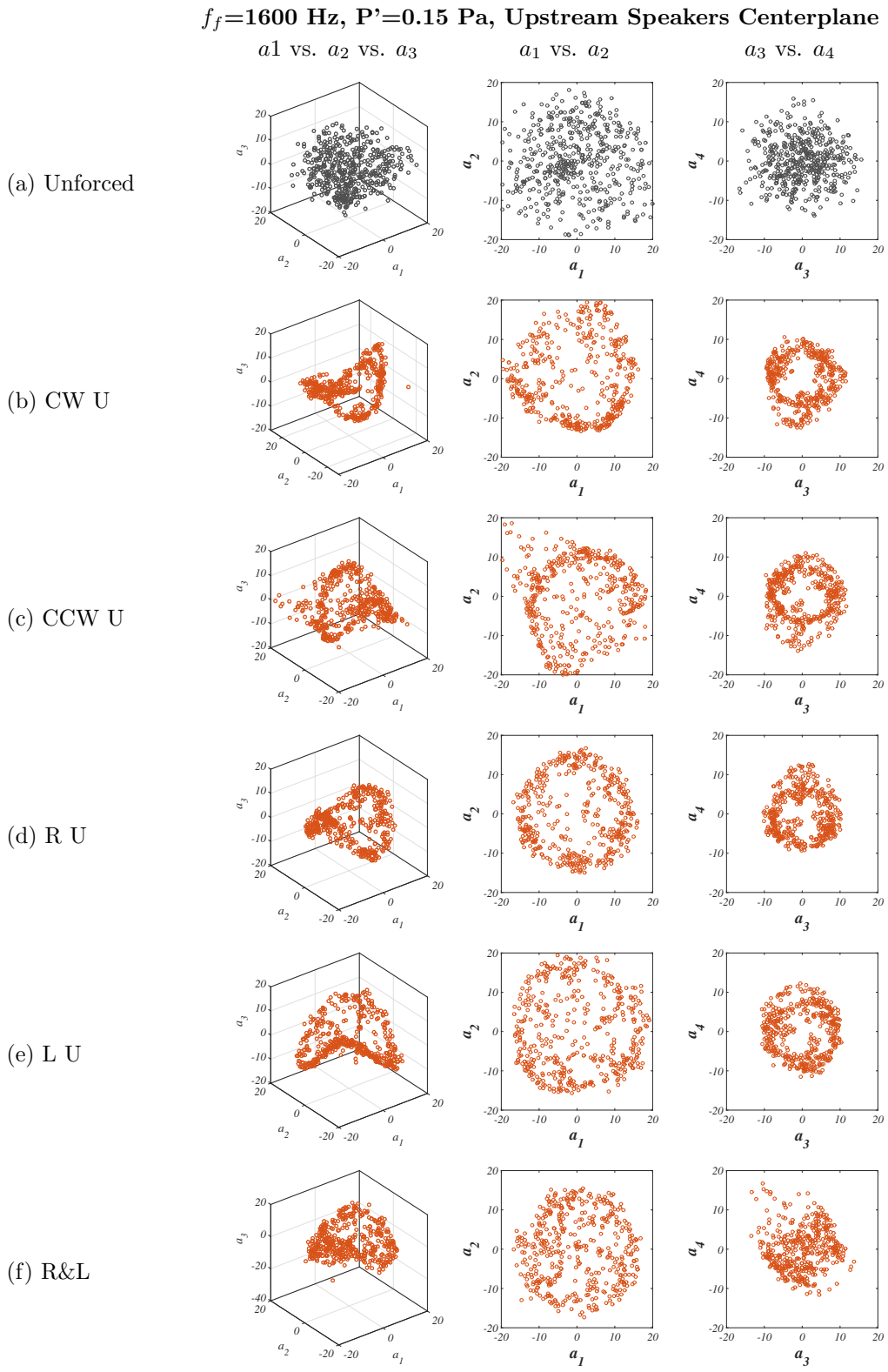

Figure 6.15: PLIF POD coefficients for the first 4 modes plotted against each other, extracted from instantaneous centerplane images of the $J = 41$ JICF, (a) unforced, and (b-f) subject to $f_f =$ 1600 Hz upstream region forcing. Black symbols represent the unforced condition, orange symbols represent the jet subject to asymmetric forcing.

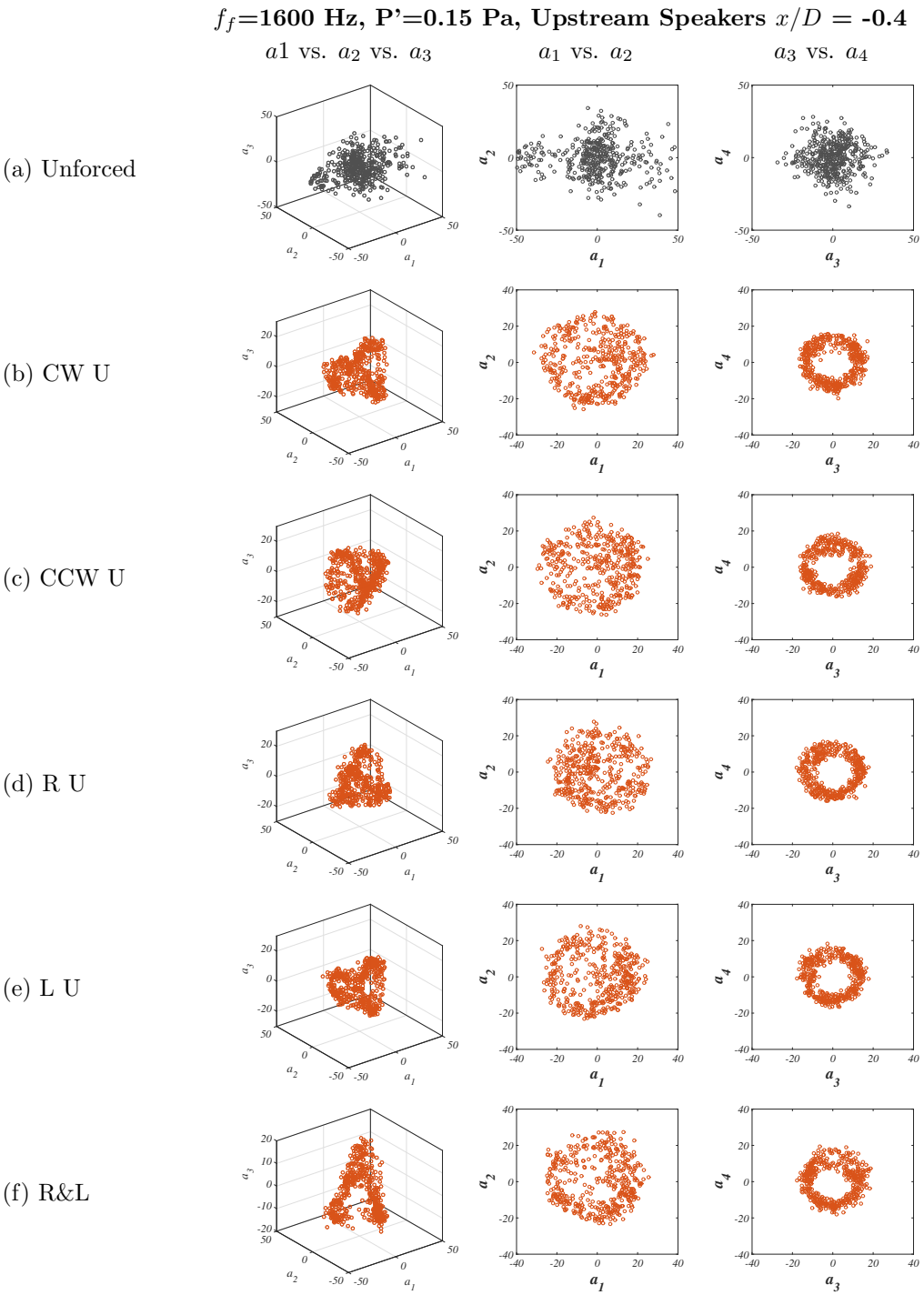

Figure 6.16: PIV POD coefficients for the first 4 modes plotted against each other, extracted from instantaneous cross-sectional plane images of the $J = 41$ JICF, for the (a) unforced, and (b-f) subject to upstream speaker excitation in the x/D = -0.4 plane where $f_f = 1600$ Hz. Black symbols represent the unforced condition, orange symbols represent the jet subject to asymmetric forcing.

6.4 Strain Rate and Scalar Dissipation Rate

Following the analysis of Gevorkyan et al. (2018), the interplay between the strain field ϵ acting along the transverse jet USL, and the local scalar field dissipation rate χ was examined for the $J = 41$ JICF, and the influence external asymmetric forcing had on this relationship was investigated. The relationships between enhanced molecular mixing of the transverse jet, symmetry of the cross-sectional CVP structure, character of the USL velocity power spectra, and the influence asymmetric forcing had on these features of the flowfield have been discussed extensively in the current study. The PIV-obtained data enabled additional insights into the velocity field to add to the evidence for relationships of these flowfield components.

The transport processes of the low Reynolds number flow field are mainly diffusion limited (Gevorkyan et al., 2016), which is dependent on the magnitude of the concentration gradient. Also contributing to the scalar mixing process is the underlying strain rate, where the strain rate is the symmetric portion of the velocity gradient tensor defined:

$$\epsilon_{ij} = \frac{1}{2}\left(\frac{\partial u_i}{\partial x_j} + \frac{\partial u_j}{\partial x_i}\right) \tag{6.1}$$

Variations in strain cause variations in the scalar dissipation rate χ and hence scalar variance, or Unmixedness. Scalar dissipation rate is defined:

$$\chi = \hat{D}\left(\frac{\partial \zeta}{\partial x_i}\right)\left(\frac{\partial \zeta}{\partial x_i}\right) \tag{6.2}$$

where ζ is the mixture fraction, a conserved scalar, and $\hat{D}$ is the mass diffusivity of the jet mixture into air. Hence the strain field was extracted from instantaneous PIV images, while scalar dissipation rate was extracted from corresponding instantaneous acetone PLIF images. To minimize shot-to-shot variations, all calculated gradient quantiles were averaged over each set of images. The maximum scalar dissipation rate and shear layer-normal strain rate were evaluated in the jet centerplane view, and as described in Gevorkyan et al. (2018), local

extensive strain (negative strain) rate values were neglected in the set average, since a quasi-steady state solution to the advection-diffusion equation of the conserved scalar requires that in the scalar gradient direction, molecular diffusion is balanced by compressive strain (Bish and Dahm, 1995). A minimum of 200 data points were required at each location in the upstream mixing layer along the jet centerline trajectory (s_c/D) to produce statistically converged local averages of scalar dissipation rate $\bar{\chi}$ and layer-normal strain rate $\bar{\epsilon}$.

Figure 6.17 compares the trends for upstream mixing layer average scalar dissipation rates $\bar{\chi}$ and average layer-normal strain rates $\bar{\epsilon}$ for the unforced $J = 41$ transverse jet and the jet subject to 4 speaker directional asymmetric forcing, where $f_f = 1600$ Hz and pressure perturbation amplitude P'= 0.15 Pa. Here, the unforced case 6.17 (a) showed that the trends in spatial evolution of scalar dissipation rate corresponded well with the evolution of the strain rate, and those trends were quite similar to the results of Gevorkyan et al. (2018) for the flush nozzle-injected equidensity $J = 41$ JICF. In Figure 6.17 (a), the average strain rate and scalar dissipation rate were particularly well correlated in the region of the initial USL vortex roll up, $s_c/D \approx 2.75$, where local increases in the strain and scalar dissipation rate would naturally occur.

Trends in the spatial evolution of $\bar{\chi}$ and $\bar{\epsilon}$ for the asymmetric forcing at $f_f = 1600$Hz for different speaker operation strategies are shown in Figure 6.17 (a-b) for 4 speaker directional forcing and Figure 6.18 for external excitation in the jet upstream region. Here, the average PIV-extracted strain rate and average PLIF-extracted scalar dissipation rate trends correlate quite closely with one another. In the forced cases, three main peaks were observed in the local $\bar{\chi}$ and $\bar{\epsilon}$, occurring at $s_c/D \approx 2$, $s_c/D \approx 3.25$, and $s_c/D \approx 4.5$, as seen in 6.17 (b), for example. Examination of the jet centerplane instantaneous vorticity and concentration fields for these forcing conditions, seen in Figures 6.2-6.4, revealed that these locations of increased scalar dissipation rate and strain rate were coincident with changes in the USL vortex roll-up.

When subject to $f_f = 1600$ Hz, the USL vortex roll up for the $J = 41$ jet was observed to initiate at $z/D \approx 2$, which corresponded with the first sharp increase in the local strain

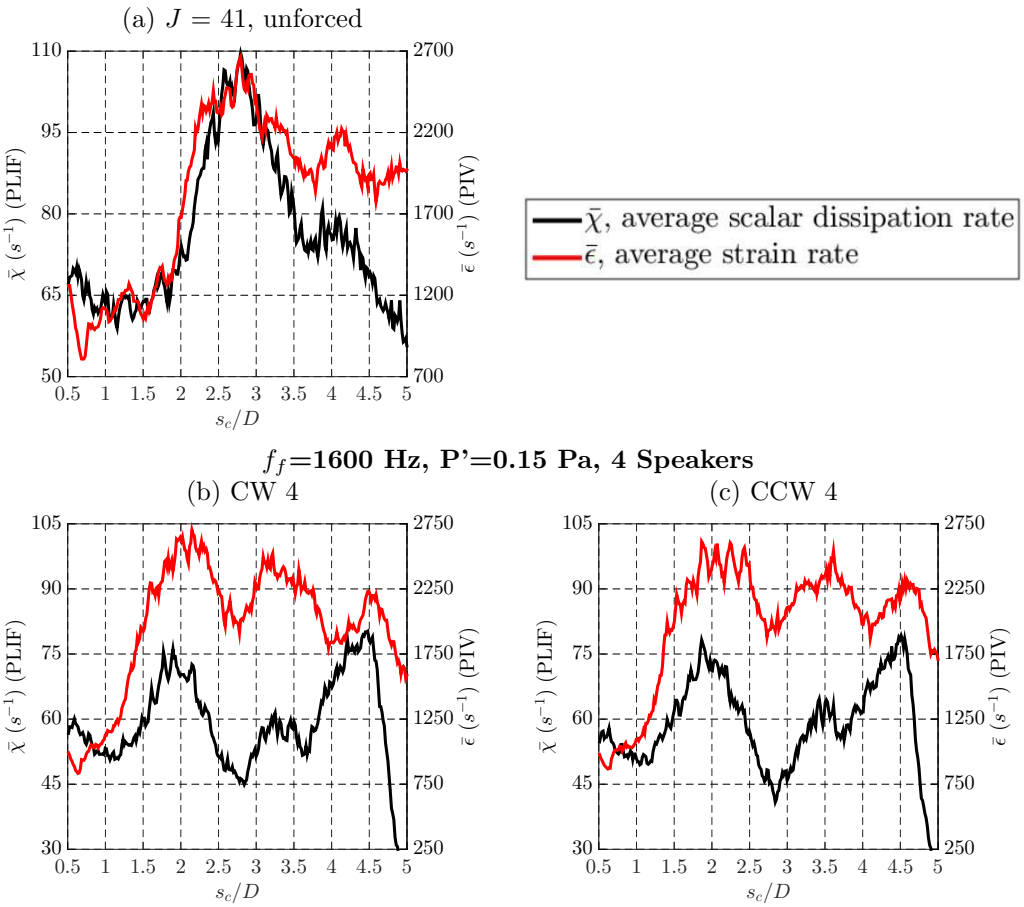

Figure 6.17: Upstream mixing layer average maximum scalar dissipation rate, $\bar{\chi}$ and average strain rate normal to the scalar gradient direction, $\bar{\epsilon}$ for the (a) $J = 41$ unforced JICF, and subject to (b) clockwise and (c) counterclockwise directional forcing with all 4 speakers at $f_f = 1600$ Hz and amplitude P'= 0.15 Pa. Data points with extensive strain in the scalar gradient direction are removed from the averaging process.

and scalar dissipation rates seen in Figures 6.17-6.18. Note that for transverse jets with high momentum flux ratios, such as $J = 41$ or $J = 61$, the crossflow does not strongly deflect the jet, thus in the field of view of the analysis in this Chapter, $s_c/D \approx z/D$. The second local peak in the trends of $\bar{\epsilon}$ and $\bar{\chi}$ for the $f_f = 1600$ Hz occurred at $s_c/D \approx 3.25$, which corresponded to the appearance of larger vortex cores in the vorticity field, such as in Figure 6.4 (e), first column, which are likely associated with energy transfer from the fundamental frequency to the subharmonic, corresponding to vortex pairing of the upstream shear layer instability structures. The 3rd peak observed in Figure 6.17 (b-c) occurred at $s_c/D \approx 4.5$.

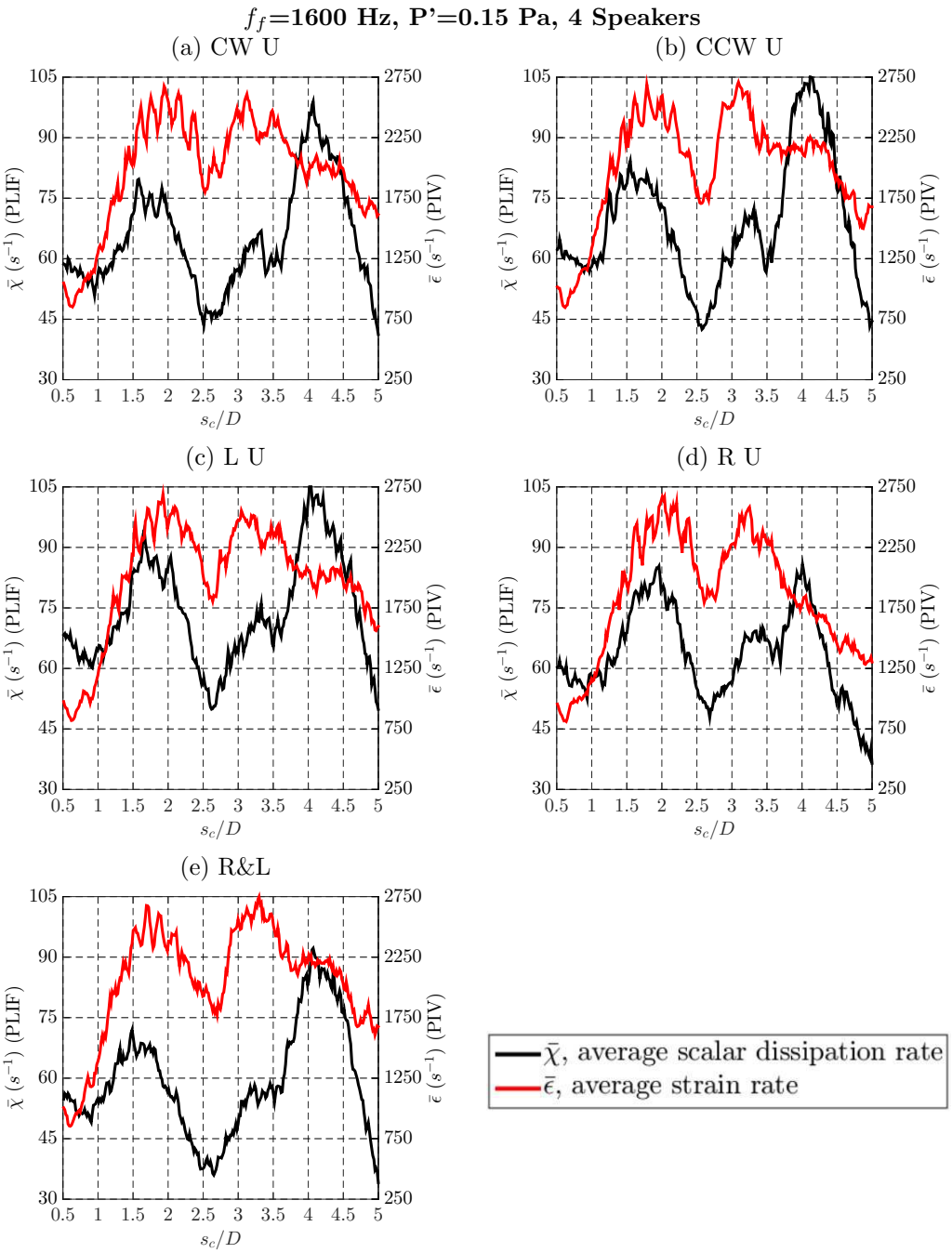

Figure 6.18: Upstream mixing layer average maximum scalar dissipation rate, $\bar{\chi}$ and average strain rate normal to the scalar gradient direction, $\bar{\epsilon}$ for the $J = 41$ JICF subject to asymmetric forcing in the upstream region with $f_f = 1600$ Hz and amplitude P'= 0.15 Pa. Data points with extensive strain in the scalar gradient direction are removed from the averaging process.

Examination of the scalar concentration images and vorticity fields at this jet trajectory location, such as in Figure 6.4 (c), leads to the observation that this location corresponded to the end of the jet potential core, and the shedding of larger vortex structures. Notably, the trends in scalar dissipation rate and layer normal strain rate for the asymmetrically forced case did not resemble the trends for the $J = 5$ JICF with a naturally absolutely unstable shear layer, such as was seen by Gevorkyan et al. (2018).

The simultaneous PLIF and PIV results of this chapter for the $J = 41$ JICF demonstrate that external asymmetric forcing can have an impact on velocity components of the flowfield, and that characteristic trends of the velocity field alterations induced by the excitation generally correspond to similar changes in the scalar concentration field. Proper orthogonal decomposition analysis was performed, and interestingly the phase space for certain forcing cases of the PIV-based mode coefficients saw the emergence of coherent structures resembling strange attractors, similar to results of high resolution PLIF imaging analysis in Chapter 5. Flow parameters $\bar{\chi}$ and $\bar{\epsilon}$, which are relevant to reactive and mixing processes, were evaluated for asymmetrically forced transverse jets and results showed that the interaction between the scalar and velocity fields were in general related and concurrent. However, unlike what has been observed thus far for the asymmetrically forced JICF whole USL is locked-in to the external forcing, which generally result in symmetrization of the jet cross-sectional structure, and superior mixing enhancement, the results of this chapter do not demonstrate that the average strain rate and average scalar dissipation rate of an asymmetrically forced jet mimic the trends expected for the transverse jet with an absolutely unstable USL.

CHAPTER 7

Conclusions and Future Work

Experimental results shown in this study demonstrate the influence of external asymmetric forcing on transverse jets with convectively unstable upstream shear layers. The amplitudes of pressure perturbation were very low as compared to previous axisymmetric forcing studies by Shoji et al. (2019a,b), in many cases by at least an order of magnitude. The effects of varying forcing amplitude, forcing frequency, forcing direction/location, and to some extent momentum flux ratio, on the upstream shear layer instability, jet structure, mixing properties, and simultaneous velocity/scalar fields were studied. Hotwire-based velocity power spectra, acetone-PLIF imaging, and PIV measurements suggest a strong correlation between the nature of the USL disturbances and alterations to the flowfield in response to asymmetric forcing, with an attendant influence on molecular mixing.

The upstream shear layer behavior of the $J = 61$ equidensity JICF with acetone mole fraction $\psi = 0.218$, subject to external asymmetric forcing was investigated. Forcing f_f within the fundamental range of the jet USL instability, where f_o = 1600-1900 Hz, was generally observed to strongly lock-in the USL. Forcing within or below the fundamental range, $f_f \leq 1900$ Hz, sometimes produced a response in the USL at subharmonic $1/2 f_f$ and its parings with f_f, predominantly only in response to CW 4, CW U, or CW D forcing. Localized forcing of the jet upstream region revealed that when forcing above the fundamental range, $f_f > 1900$ Hz, the USL responded weakly to the R U forcing location. These results demonstrate that inherent asymmetries of the $J = 61$ JICF are also associated with asymmetric responses of the jet's USL to differently oriented helical/asymmetric external forcing. Differing shear layer responses to asymmetric perturbations are consistent with earlier LSA studies (Alves et al., 2007) suggesting different growth rates between positive and negative helical modes

for the high momentum ratio JICF.

Similar to lock-in studies on the free jet (Li and Juniper, 2013c) and JICF subject to axisymmetric forcing (Shoji et al., 2019b), quasiperiodic behavior on the run-up to lock-in was observed for forcing cases outside the fundamental range, $f_f < 1600$ Hz and $f_f > 1900$ Hz. High above f_o, as f_f approached $2f_o$, the jet USL did not lock-in to the external forcing, even at relatively high pressure perturbation amplitudes. This suggests that the jet USL may not be able to respond to external forcing at frequencies high above the fundamental and that a lock-in diagram for external asymmetric forcing, centered around f_o, may have a steeper slope of the lock-in boundary for $f_f > f_o$ than for $f_f < f_o$. Such an asymmetric orientation of the lock-in diagram would be the opposite to that observed for axisymmetric excitation of the JICF (Shoji et al., 2019b) but would be similar in the orientation to that for the low density free jet (Li and Juniper, 2013c).

Acetone PLIF imaging showed that this very low amplitude asymmetric forcing at frequencies near the fundamental frequency f_o or below, where $f_f \leq 2300$ Hz, could significantly influence jet cross-sectional structure, in many cases with enhanced symmetrization of the CVP, more typical of jets with an absolutely unstable USL. General jet responsiveness to asymmetric forcing near the fundamental frequency, where the speakers are operated in a temporally sinusoidal mode, appeared to be consistent with traditional lock-in behavior for axisymmetrically forced jets with and without crossflow (Davitian et al., 2010a; Getsinger et al., 2012; Shoji, 2017), and the altered jet structure during excitation above lock-in conditions was consistent with the phenomenon. Asymmetric excitation at frequencies far above the fundamental range ($f_f = 2600$ Hz, 2900 Hz, and 3500 Hz) did not create a very symmetric cross-section, even when the USL corresponded to 1:1 lock-in to the applied forcing. When the USL was not locked-in, such as at $f_f = 3500$ Hz, the jet did not substantially respond to excitation, with the exception of $f_f = 1900$ Hz R U. Additionally, if the USL velocity power spectra exhibited quasiperiodic behavior in response to forcing, structural changes to the transverse jet cross section may occur or may not occur. Differences in the far field cross-sections, produced by varied forcing strategies for a given frequency and pressure per-

turbation, could generally be correlated to differences observed in the associated USL power spectra.

Using the molecular mixing metric of the local Unmixedness, helical jet excitation produced similar trends between jet cross-sectional symmetrization and improved jet mixing. In general, there were noticeable differences in the reduction of Unmixedness between the varied speaker operation forcing strategies for a fixed frequency f_f, implying that cross-sectional structure alterations had an effect on centerplane structure and mixing. In particular, improved cross-sectional symmetry corresponded relatively closely to optimal mixing conditions for a range of forcing conditions, especially in the mid- and far-field of the jet. In the centerplane view, for forcing utilizing all four speakers, at forcing frequencies which were below the fundamental $f_f < f_o$, counterclockwise excitation at a given frequency and amplitude generally resulted in significantly greater mixing enhancement (lower U) than clockwise excitation. Forcing frequencies above the fundamental $f_f > f_o$, the opposite trend was seen in that clockwise excitation at a given frequency and amplitude resulted in greater mixing enhancement, however but higher frequency excitation, well beyond the fundamental range (e.g., at $f_f = 3500$ Hz $= 2f_o$), did not significantly alter jet structure or improve mixing. The separation in the behavior of the JICF in response to asymmetric forcing at $f_f \leq f_o$ vs. $f_f > f_o$ aligns with similar trends seen in the USL power spectra and structure study, indicating the fundamental interplay of these properties.

For all forcing conditions in which 1:1 lock-in of the USL occurred, mixing was generally enhanced in both the centerplane and cross-sectional views. Moreover, results in this study show that in general, asymmetric forcing enhanced mixing to some degree, even in instances when the USL was known to exhibit quasiperiodic behavior or was not locked-in to the asymmetric forcing. Yet cases where the USL was locked-in to the forcing virtually always provided better mixing enhancement (lower Unmixedness) than cases where the USL exhibited quasiperiodic behavior in the USL in response spectra, or cases which were neither locked-in or quasiperiodic.

POD modes extracted from the high resolution $J = 61$ PLIF centerplane instantaneous

images showed that asymmetric forcing induces changes in the dominant modes structures, similar to the shear layer structures typically seen for a JICF, even at lower momentum flux ratios where the USL instabilities can be stronger in the absence of excitation. POD analysis of the cross-sectional acetone-PLIF imaging show that interesting dominant mode structures, which are highly asymmetric for the unforced $J = 61$ transverse jet, can become more symmetrized by the asymmetric forcing, as cross-sectional PLIF imaging itself indicates. Interestingly, it appears that even when the jet cross-section is symmetric per the PLIF imaging, the dominant modes in the cross-section can be of different structure for different excitation conditions, perhaps suggesting that the excitation of different asymmetric modes inherent in the transverse jet's upstream shear layer can produce different growth dynamics, yet that they can still enable formation of a more symmetric CVP via strengthening key USL instabilities.

Phase mapping of the POD coefficients produced extremely interesting results. Prior studies by Gevorkyan et al. (2018) show that a JICF with an AU USL produces a map of a_1 vs. a_2 which form a circle, indicating periodic behavior such as a traveling wave. For the asymmetrically forced $J = 61$ JICF, consideration of the second mode pair coefficients, a_3 and/or a_4, sometimes saw the emergence of coherent shapes in 3D phase space, and in the 2D phase space of the second mode pair. Like other results presented in the current study, for forcing well above the fundamental range ($f_f \geq$ 2600 Hz), the POD phase space was unchanged as compared the the unforced case, even when the USL was locked-in. And forcing at or below the fundamental range, $f_f \leq f_o$ generally resulted in the emergence of coherent shapes when the USL was locked in. Coherent shapes in the POD coefficient phase space were not observed for forcing cases in which the jet USL response was quasiperiodic or not locked-in to the excitation, providing further evidence that to ensure the ability to tailor characteristics of the JICF with a CU USL, the USL should be locked-in to external forcing.

Coherent shapes that emerged from the POD coefficient phase space mapping (which can be analogous to Poincaré time series mapping for velocity disturbances, for example)

strongly resemble strange attractors, representing non-periodic solutions for flow parameters. All forcing cases which produced strange attractor-like structures had a strongly locked-in USL, perhaps indicating the amplitude of forcing was well above the lock-in boundary. It has been theorized that in an externally forced system, strange attractors appear at a third bifurcation associated with onset of turbulence (Ruelle and Takens, 1971; Newhouse et al., 1978), and strange attractors have been observed experimentally for various fluid systems (Bonetti and Boon, 1989; Williams-Stuber and Gharib, 1990; Aref et al., 1987; Guzman and Amon, 1994) at the transition to chaos. Guan et al. (2018), for example, focused their investigation on the behavior of a laminar flame when excited with a single-tone acoustic frequency at amplitudes beyond those known to correspond to the lock-in threshold, and again found evidence for strange attractors in the run-up to chaotic behavior. The present results suggest that the asymmetric forcing cases in which coherent shapes appear in the POD coefficient phase space may be associated with transition of the flow, especially the transverse jet's upstream shear layer.

The present study of the interaction of the transverse jet's velocity field and scalar concentration field in response to asymmetric forcing was explored with simultaneous PLIF/PIV imaging for the $J = 41$ condition. Asymmetric forcing clearly demonstrated influence on the flowfield velocity and associated strain rate, in turn affecting the scalar dissipation rate, an important component in fluid mixing. Cross-sectional PLIF/PIV results show asymmetries in both the vorticity field and mean scalar concentration field at the upstream edge of the jet orifice, reinforcing previous evidence that the natural jet asymmetry is formed very early in the jet evolution, and that perhaps the formation of the shear layer itself is asymmetric. POD analysis was performed on the simultaneous velocity and concentration fields, and again some forcing conditions led to the appearance of coherent structures in the phase mapping of the PLIF-based or PIV-base POD coefficients.

Results of this study suggest that asymmetric forcing can cause a transverse jets at high momentum flux ratios such as $J = 41$ or 61, which have a naturally convectively unstable USL, to behave like a jet whose USL is absolutely unstable, which under unforced conditions

would occur only at lower J values, below around 8-10. Asymmetric forcing can induce effects in the USL of the JICF which can mimic the behavior of an AU transverse jet. For example, with asymmetric excitation, spectra of the USL disturbances can change from a broadband nature characterized by frequency shifting of the dominant instability without forcing, to that with a pure-tone frequency f_f and its harmonics. The jet's cross-sectional structure can become symmetrized, resulting in a better mixed flowfield. POD modes can form into more organized shear layer-specific structures, and the phase plots for a_1 vs. a_2 POD coefficients of the first mode pair can from a tight circle indicating periodicity in modes 1 and 2. At the same time, for other aspects of the flowfield, the high momentum flux ratio JICF subject to asymmetric forcing can differ from that of a jet whose USL is naturally AU. The jet trajectory is at most minimally altered by the asymmetric forcing, therefore no change in jet penetration is observed. Trends in jet strain rate and scalar dissipation rate do not start out at a relatively high values and decrease as the shear layer evolves, as in the AU JICF, but rather form peaks at key roll-up events in the jet USL, similar to the CU transverse jet. This behavior could have implications for excitation of jets in a reactive environment, where enhanced fuel-air mixing is desired but very high strain rates could lead to premature flame extinction. Further, in the POD mode phase space, an unforced AU jet does not result in periodic solutions to the second most dominant mode pair and beyond, but asymmetric forcing does provide evidence of more than one periodic relationship in the flowfield for some forcing conditions whose amplitudes were in excess of the lock-in boundary.

Based on these extensive studies of the effects of external asymmetric excitation of the high momentum ratio transverse jet, there are a number of suggested future studies on asymmetric forcing of the convectively unstable transverse jet, which include:

- Combined axisymmetric forcing and external asymmetric forcing for detailed, tailored control of transverse jet properties, and understanding the relative influence and coupling of axisymmetric and asymmetric perturbations on the flow.
- Investigations into the growth rate measurements along the USL for the Nitrogen free jet for both the axisymmetric and first helical modes have begun at UCLA. Preferred

frequencies of the helical modes may offer insight into the interplay between the axisymmetric $m = 0$ mode and helical modes. A natural extension to this study would be to investigate such growth rates in the transverse jet, perhaps utilizing the removable test section floor to implement additional azimuthal speaker arrangements, such as more speakers to excite the $m = \pm 2$ and higher modes.

- Further exportation of quasiperiodic behavior of the JICF USL in response to asymmetric forcing is warranted, and time series or time resolved data would enable dynamical analysis techniques such as Poincaré mapping and van der Pol modeling.

- Well above the fundamental range f_o of the JICF, the jet is less likely to respond to external forcing, despite in conditions where the USL is locked-in. However, when f_f is well above f_o, the response in the jet USL power spectra may be of greater amplitude at $1/2f_f$ than at f_f. Further study may explore whether these asymmetric forcing conditions correspond to 1:1 lock-in of the USL as seen in Li and Juniper (2013c), or if these are within the family of the more general n:m lock-in. If so, this may change some conclusions of this study on the influence of USL lock-in on jet parameters such as mixing.

- The appearance of structures which resemble strange attractors in the phase space of extracted POD coefficients is particularly intriguing, given the background theory and prior experiments associating the strange attractor to a transitional phase in the fluid dynamics, such as the onset of turbulence. Further investigation into the nature of the coherent structures is warranted. Potentially, Lyapunov exponents can be calculated from experimental data. Although the phase space reconstruction and Poincar sections provide information about the geometric nature of the system, Lyapunov exponents quantify the sensitivity of the dynamical system to initial conditions (Williams-Stuber and Gharib, 1990; Wolf et al., 1985). If the largest exponent is greater than zero, the dynamical system attractor is "strange". However "strange" attractors may be non-chaotic, where the Lyapunov exponents are non-positive, yet the attractor has a non-integer fractal dimension, leading to the term "strange non-chaotic attractor", or SNA

(Guan et al., 2018), which are still associated with the transition to chaos/turbulence.

APPENDIX A

Asymmetric Forcing Control Circuit

The following section details the design and operation of the control circuit designed to enable controlled, relatively uniform, helical-like excitation, where the location of the maximum perturbation amplitude would be at the peak of the forcing sine wave and travel around the transverse jet in time as the out-of phase speakers alternated excitation of the peak at a given frequency. For example, the clockwise forcing (speaker sequence 2-1-4-3) speaker acoustic output signal scheme is shown in Figure A.1.

A.1 Circuit Design

The asymmetric external forcing control circuit, designed by Michael Andonian and Stephen Schein, utilized an arrangement of three basic functional blocks to alter the incoming excitation signal and independently tailor its properties for an individual speaker's desired performance output. The basic concept of the control circuit is shown in Figure A.2, where circuit elements are contained within the gray dash-dotted outline. The control circuit accepted a single sinewave input from the HP 8904A multifunction synthesizer, that signal was then split off into multiple branches for separate control of each speaker. There were various locations where the signal was sampled, buffered, and sent to the dSPACE 1104 DSP data acquisition (DAQ) and controller board, and information of the filtered signal was used for further calibration and control of the circuit.

The three functional sub-blocks in the system architecture consisted of a phase adjustment circuit, an amplitude adjustment circuit, and a signal reducing circuit to deliver appropriate amplitude to a five channel stereo amplifier (Adcom GFA-7300). The signal was

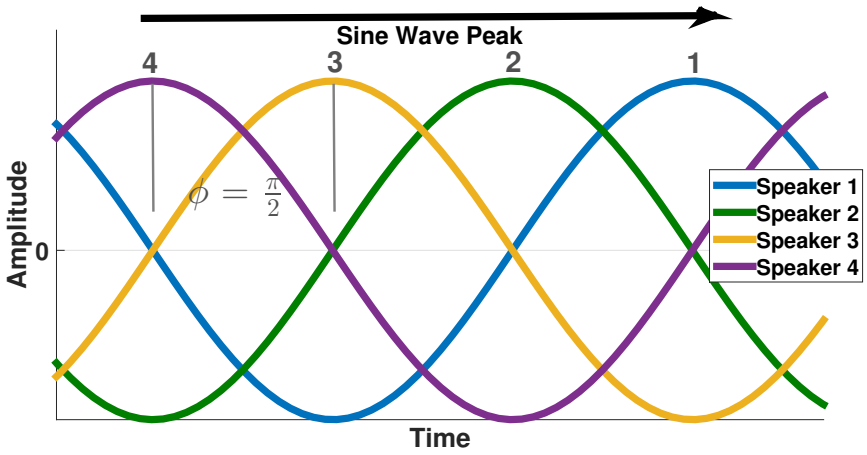

Figure A.1: Jet helical forcing clockwise input signals

first split to a reference branch which was delivered to a master or reference speaker (named speaker 1 here but not correlated with specific speaker numbering in Section 2.4). This leg was not adjustable, as the control process concept was designed to tune the output of each speaker to desired perturbation relative to the reference speaker.

The other 3 branches of the design contained signal control functions. Each of the legs that lead to the remaining speakers had the means to independently adjust the output signal phase and amplitude. The first block on each branch was the phase adjustment block, which contained a sub-block switching inverter and a phase tuner sub-block. The input signal from the function generator fed directly into the switching sub-block for the 2nd speaker branch. The purpose of this function was to invert the input signal from the function generator if necessary to provide nearly 360° range of phase adjustment achievable. There was a physical toggle switch which provided continuity to either a op-amp with unity gain, or an inverting op-amp with gain of -1. Both op-amps utilized 10 kΩ ± 0.1% precision matched resistors. The switch was toggled to the appropriate gain op-amp based on the real-time measured speaker phase and direction (more positive or more negative) required to adjust the phase to desired setting. An additional feature of the switching sub-block was that the op-amps buffered the signal and prevented feedback to the common input from the function generator. After the switching sub-block, the forcing signal reached the 1st phase tuning sub-block.

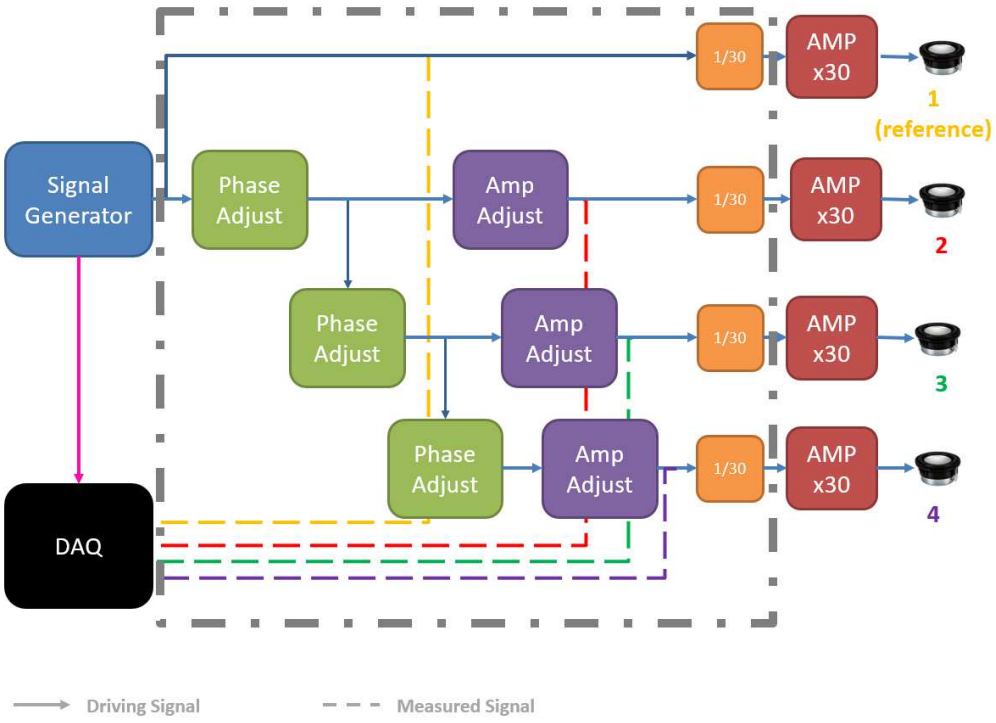

Figure A.2: Functional block diagram of control circuit, contained within gray dash-dotted outline. Functional blocks include phase adjustment, amplitude adjustment, and signal reduction for each independent speaker.

Phase tuning was accomplished via an all-pass filter which passed all frequencies with a gain of unity via precision matched resistors (10 kΩ ± 0.1%), a 33 μF capacitor, and a 10 kΩ adjustable resistance potentiometer. The choices of these components (Smith, 2010) enabled a phase shift:

$$\Delta\phi = 180 - 2\tan^{-1}(2\pi R_{pot} C f_f) \tag{A.1}$$

where C is the capacitance value, and R_{pot} represents the variable resistance potentiometer, whose value was adjusted to alter the forcing signal relative phase. Per equation A.1, the minimum phase shift was 0° and maximum +180°, however if the signal was inverted via the switching sub-block, that range would be from 0° to -180° in an ideal circuit. The combination of phase tuner and switch allowed for nearly 360° full range of phase adjustment capability.

Once the signal had passed through the phase adjustment block on the 2nd speaker, the signal was again split. The branches for the 3rd and 4th speakers were tiled in series from the exit node of the previous branch, and were otherwise duplicates of the 2nd speaker branch as seen in Figure A.2. With this design the subsequent speaker's phase was referenced from the previous speaker. With this design smaller increments of 90° equal spacing could be tuned as opposed to larger increments of 90°- 270°.

The other signal leg split from the node following the phase adjustment block fed to the amplitude adjustment block, with each speaker having an identical adjustment block in a parallel configuration. The amplitude adjustment block seen in Figure A.3 utilized a slightly customized inverting op-amp gain circuit to give a wide range of attainable gain tuning via additional resistors in series and parallel, and a 100 kΩ adjustable resistance potentiometer. The ideal gain would be:

$$Gain = (\frac{R_2}{R_1})\frac{R_3 + R_{pot}}{R_2 + R_3 + R_{pot}} \tag{A.2}$$

where in this control circuit R_1= 13 kΩ, R_2= 50 $k\Omega$, R_3=5 kΩ, and R_{pot} was the setting of the adjustable resistance potentiometer. These resistor values provided for an ideal gain adjustment range from 0.35-2.6.

A.2 Signal Processing and Filtering

In order to determine the phase and amplitude of any acquired sinewave, the signal was digitally modulated and filtered for manipulation in Simulink. Digital filter modulation process decomposed the signal, passed it through a low pass filter, where phase and gain could be isolated.

The block diagram in Figure A.2 shows two separate output signals from the signal generator. One signal was the control circuit input and was in the form of $A\cos(\omega t)$, where ω was the f_f in radians and A was the amplitude in Volts. This signal was sent to the control

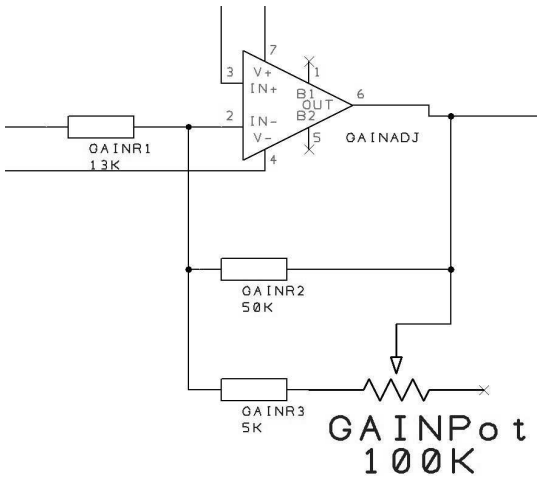

Figure A.3: Electrical schematic for amplitude gain adjustment block, showing the configuration of gain resistors; GAINR1, GAINR2, GAINR3, and adjustable potentiometer GAINPot.

circuit which then passed to the speakers. The second output from the signal generator was a reference signal in the form of $A\sin(\omega t)$. Both signals were sampled at 20kHz and sent through a digital fourth order Butterworth low pass filter to return A. The two signals were then normalized by A to return $\cos(\omega t)$ and $\sin(\omega t)$ reference waves. This dynamic calculation of amplitude was required to get an accurate phase calculation.

The phase and amplitude of any other signal of the same frequency, such as signals sampled from the control circuit or measured via the microphone, could be determined using the $\cos(\omega t)$ and $\sin(\omega t)$ reference waves. The signal of interest was acquired and assumed to be in the form of $B\cos(\omega t+\phi)$, where B was the amplitude and ϕ was the phase offset from the signal generator (circuit input) cosine wave. The signal of interest was then processed by the digital low pass filter as such:

$$B\cos(\omega t+\phi)\times\cos(\omega t)\rightarrow\frac{1}{2}B\cos(\phi) \tag{A.3}$$

$$B\cos(\omega t+\phi)\times\sin(\omega t)\rightarrow\frac{1}{2}B\sin(\phi) \tag{A.4}$$

then B and ϕ could then be easily calculated. The phase and amplitude could actively be monitored while using the control circuit to achieve desired adjustments.

A.2.1 Calibration

The intent of this custom circuit was to control the acoustic waveform phase and amplitude output of each speaker, by means of carefully controlling the signal waveform being input to each speaker. A calibration procedure was developed to determine the waveform settings for each speaker prior to performing a given experiment.

The calibration process graphically shown in Figure A.4 began with measuring the output of the speaker connected to the non-adjustable reference leg of the circuit. The desired forcing frequency f_f and target input amplitude were set via function generator and the signal was sent to the control circuit. Although this leg of the circuit did not have adjustment capability, a coarse adjustment of the amplitude could be made at the function generator if desired. The pressure perturbation amplitude created by acoustic forcing was measured by a free-field piezoelectric microphone/amplifier (PCB Piezotronics 377C01/426B03), whose signal was passed through a conditioner (PCB Piezotronics 484B11) on a gain setting of 100. The piezoelectric microphone was placed at a distance of 1.0 jet diameters directly above the jet exit and the output amplitude and phase were measured and noted. This waveform become the reference waveform. The microphone remained stationary above the jet exit and the next speaker was connected to the first adjustment leg of the control circuit, while the reference speaker was turned off. The output of this speaker was measured and with the control circuit the phase tuned to the desired phase offset relative to the reference speaker output. After the phase adjustment, the amplitude of the output acoustic wave was tuned to match that of the reference speaker. During this process the circuit waveform leading to the speaker input line was sampled and filtered, where the amplitude and phase were dynamically calculated. Once the response output of the speaker under calibration was as desired for forcing, the tuned/adjusted input waveform amplitude and phase were recorded and entered into a lookup table. Since the output of the speakers are repeatable for a given input signal, and the input signals are always accessible for sampling, this lookup table could be used later when the microphone was removed to create desired external excitation schemes.

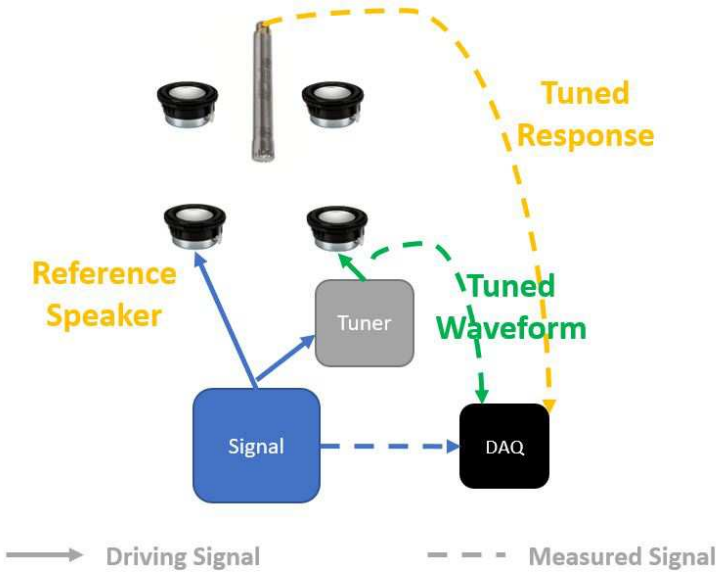

Figure A.4: Illustration of calibration procedure.

APPENDIX B

Asymmetric External Forcing Velocity Power Spectra

The following section provides additional results not shown in Chapter 3 on the study of the transverse jet upstream shear layer response to external asymmetric forcing, as measured by vertical velocity power spectra.

B.1 JICF Velocity Power Spectra, directional forcing study

This section represents power spectra of the hotwire-measured velocity perturbations at the USL trajectory coordinate $s/D = 2.0$, not shown in Chapter 3.

(a) f_f = 875 Hz, P'= 0.225 Pa

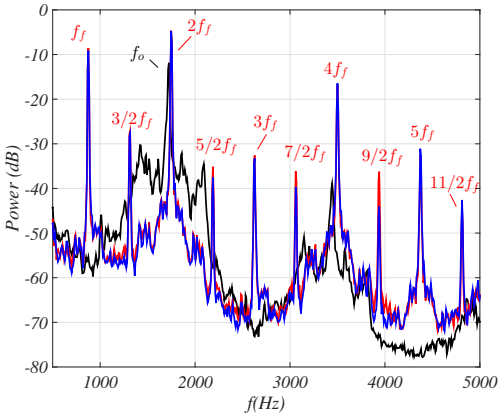

(b) f_f = 1750 Hz, P'= 0.41 Pa

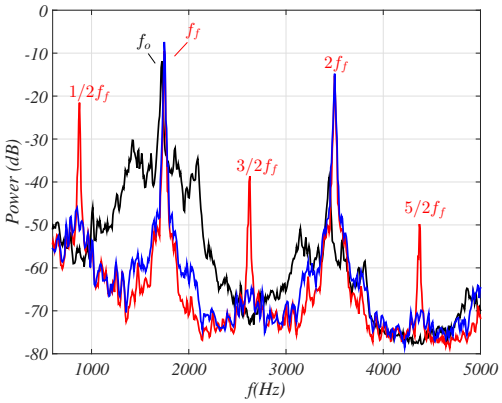

(c) f_f = 2300 Hz, P'= 0.14 Pa

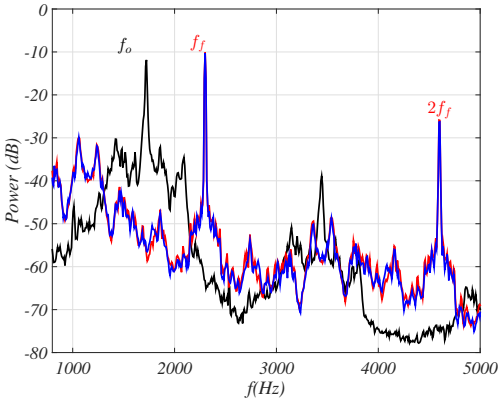

(d) f_f = 2300 Hz, P'=0.28 Pa

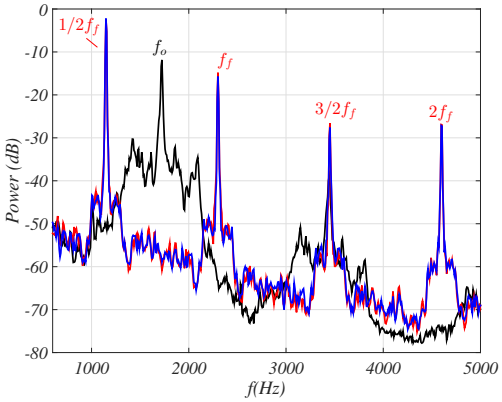

(e) f_f = 2600 Hz, P'= 0.39 Pa

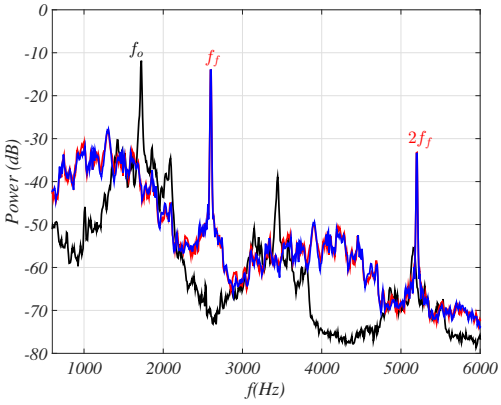

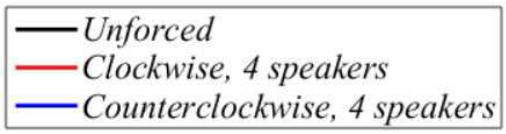

Figure B.1: Power spectra of upstream vertical velocity disturbances, 4 speaker study. All forcing conditions shown exhibit 1:1 lock-in of the USL.

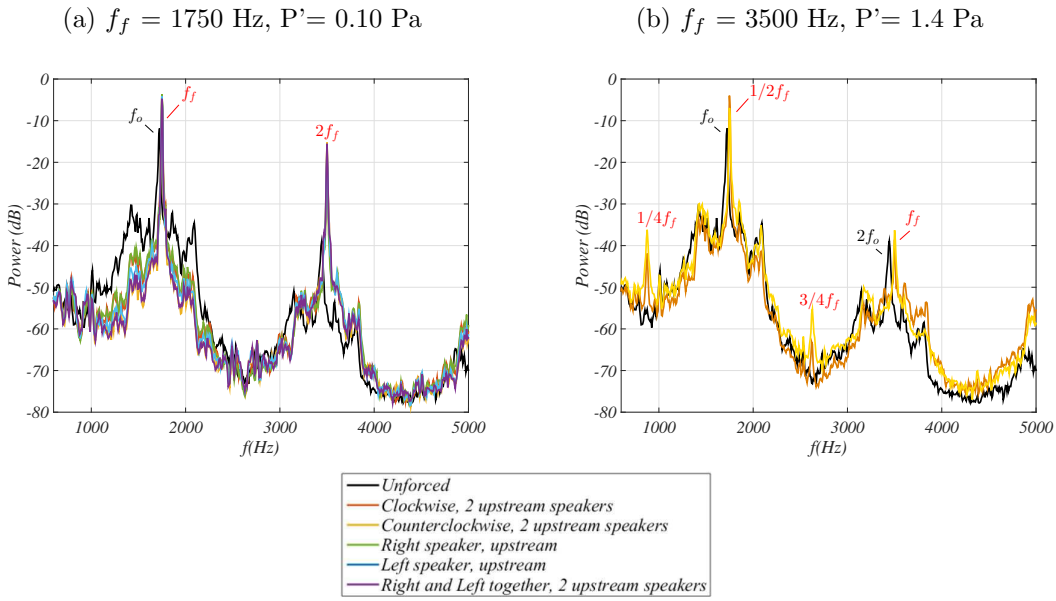

Figure B.2: Power spectra of vertical velocity, upstream speaker study, where 1:1 lock-in of the USL is seen in (a), while no lock-in of the USL was observed in (b).

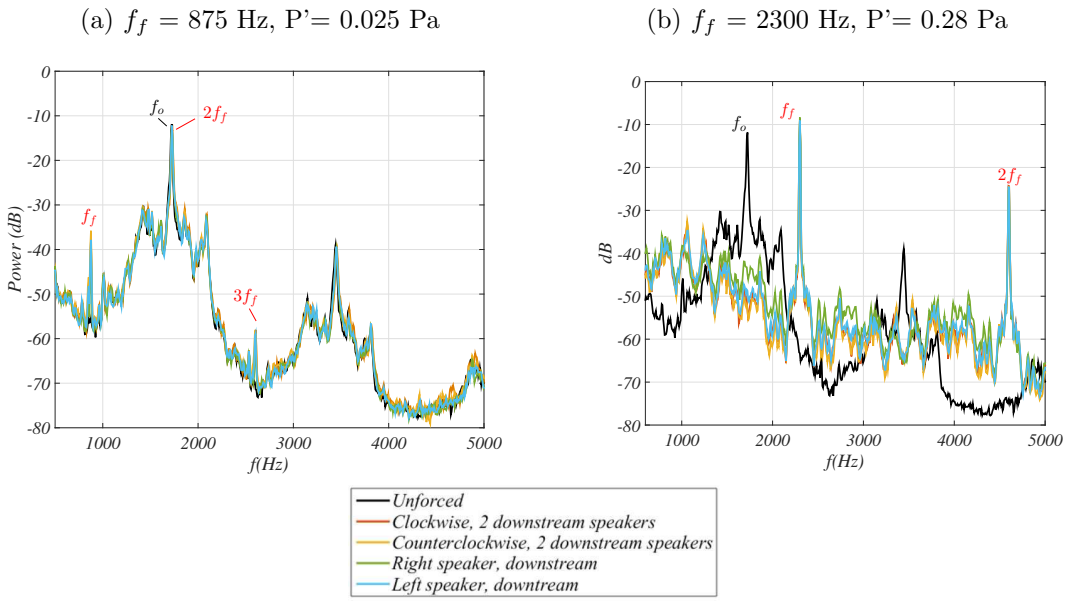

Figure B.3: Power spectra of upstream vertical velocity disturbances, downstream speaker study, where no lock-in of the USL was observed in (a), while 1:1 lock-in of the USL was observed in (b).

APPENDIX C

Asymmetric External Forcing Acetone PLIF Concentration Images

The following section provides additional results associated with the study of asymmetric external forcing structural effects on the transverse jet in Chapter 4.

C.1 Mean Centerplane PLIF Images, 4-Speaker Study

This section represents mean centerplane acetone PLIF images with external asymmetric sinusoidal forcing of the jet, not shown in Chapter 4. Mean images are typically an average of 500 instantaneous images.

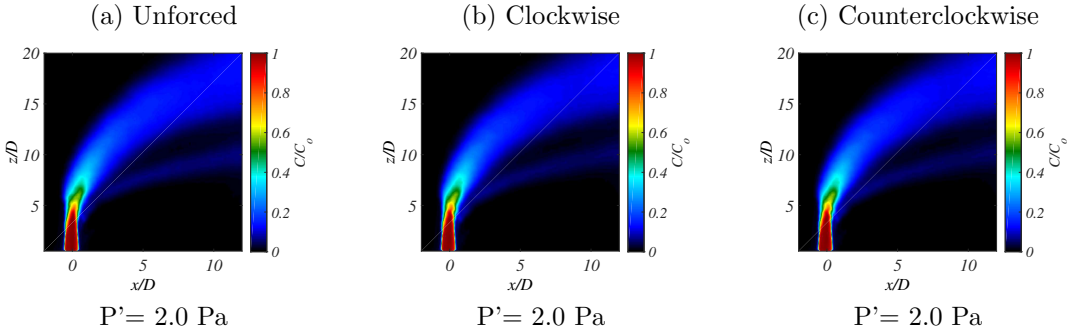

Figure C.1: Mean centerplane acetone concentration images in the regular plane (x/D - z/D) for the equidensity $J = 61$ jet for (a) unforced jet, and (b)-(c) $f_f = 3500$ Hz.

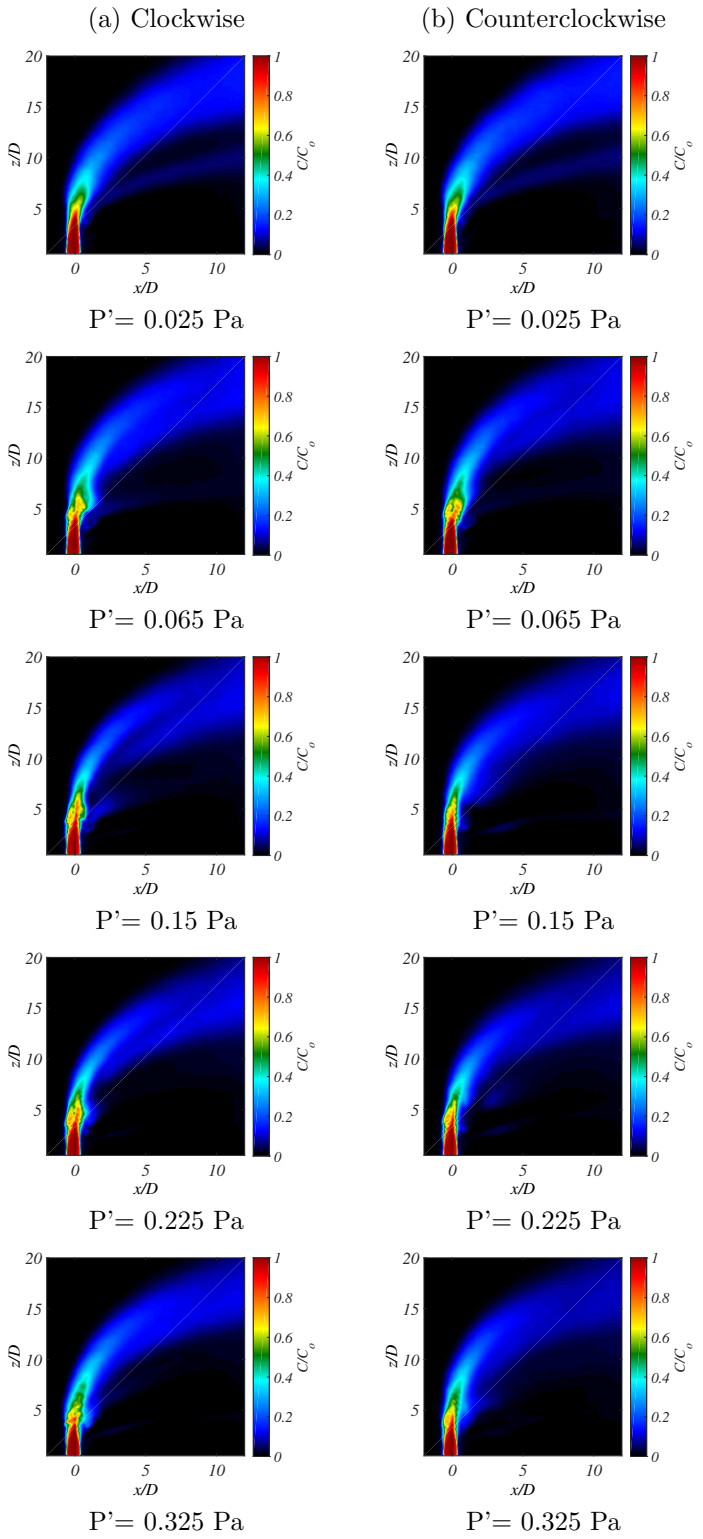

Figure C.2: Mean centerplane acetone concentration images in the regular plane (x/D - z/D) for the equidensity $J = 61$ jet for $f_f = 875$ Hz, with increasing forcing pressure perturbation P'.

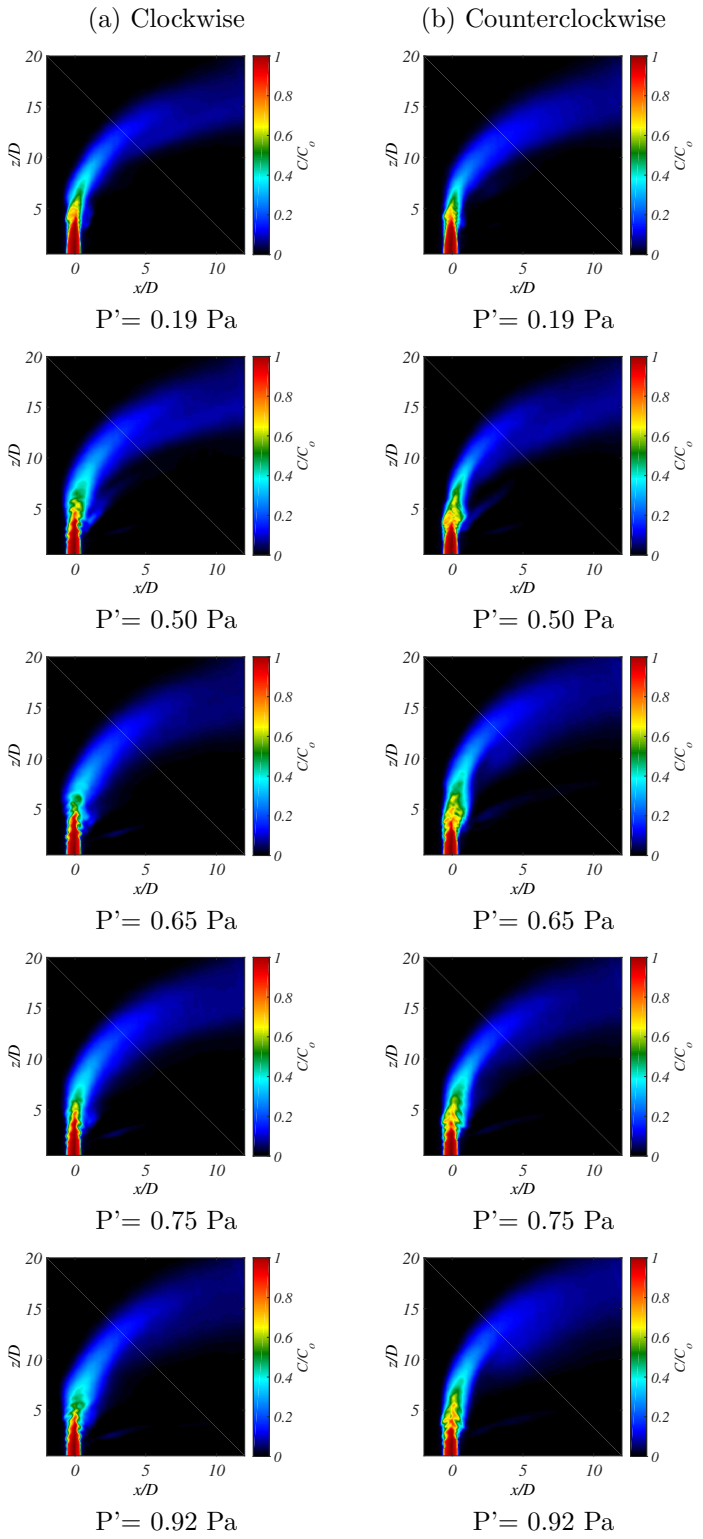

Figure C.3: Mean centerplane acetone concentration images in the regular plane (x/D - z/D) for the equidensity $J = 61$ jet for $f_f = 1000$ Hz, with increasing forcing pressure perturbation P'.

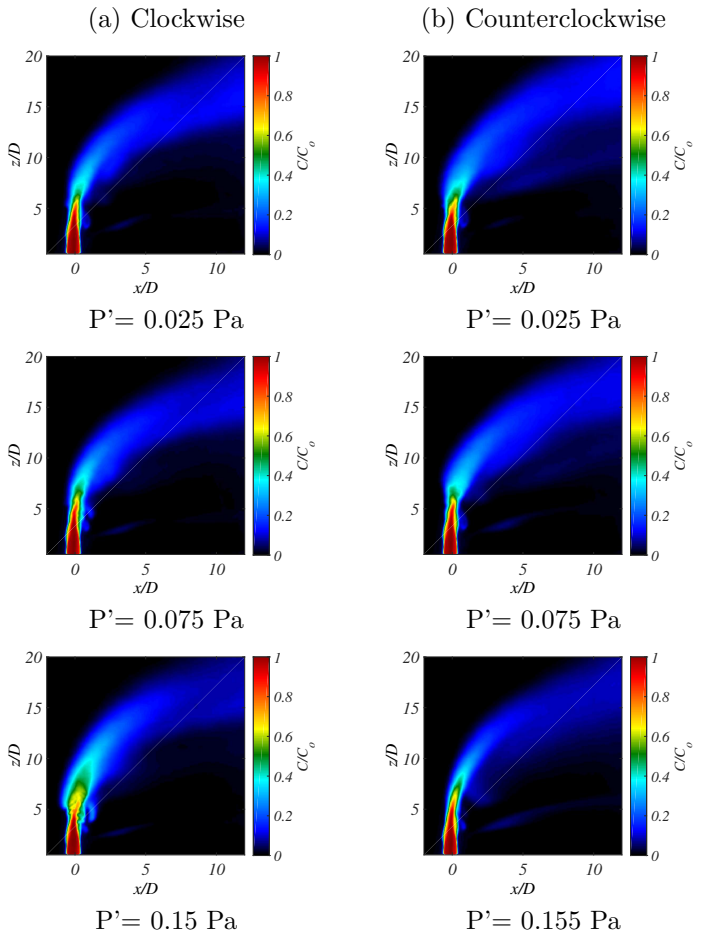

Figure C.4: Mean centerplane acetone concentration images in the regular plane (x/D - z/D) for the equidensity $J = 61$ jet for $f_f = 1600$ Hz, with increasing forcing pressure perturbation P'.

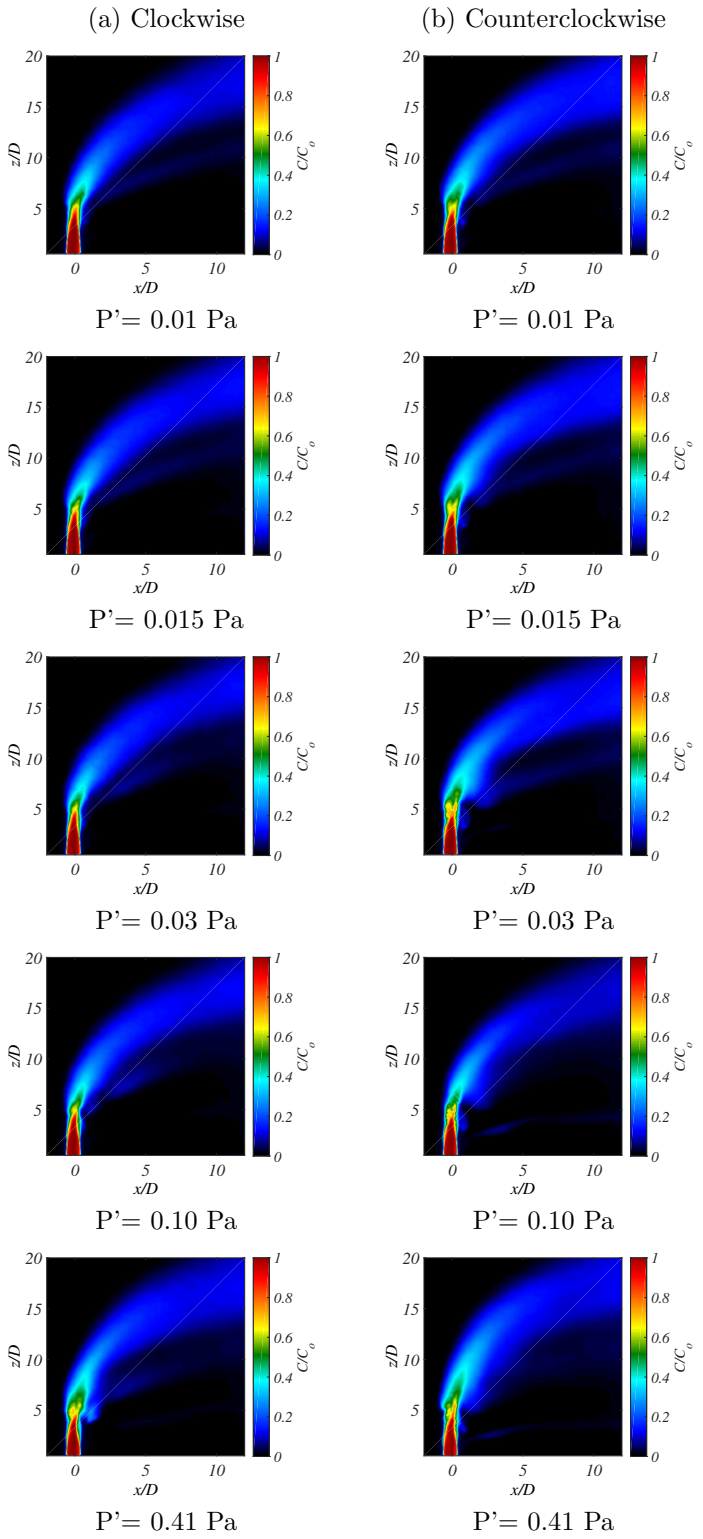

Figure C.5: Mean centerplane acetone concentration images in the regular plane (x/D - z/D) for the equidensity $J = 61$ jet for $f_f = 1750$ Hz, with increasing forcing pressure perturbation P'.

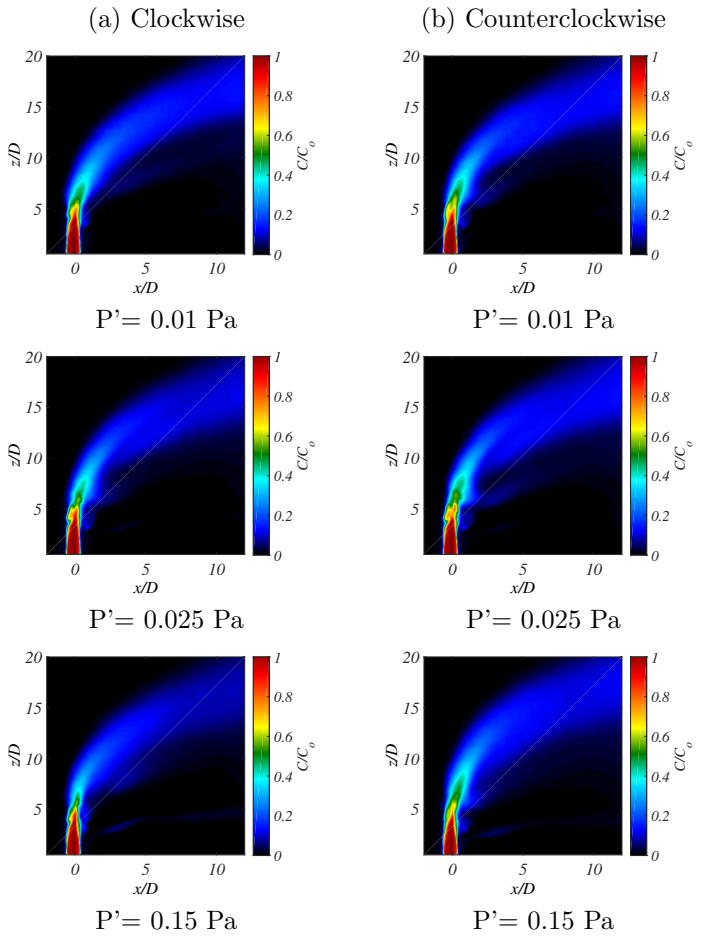

Figure C.6: Mean centerplane acetone concentration images in the regular plane (x/D - z/D) for the equidensity $J = 61$ jet for $f_f = 1900$ Hz, with increasing forcing pressure perturbation P'.

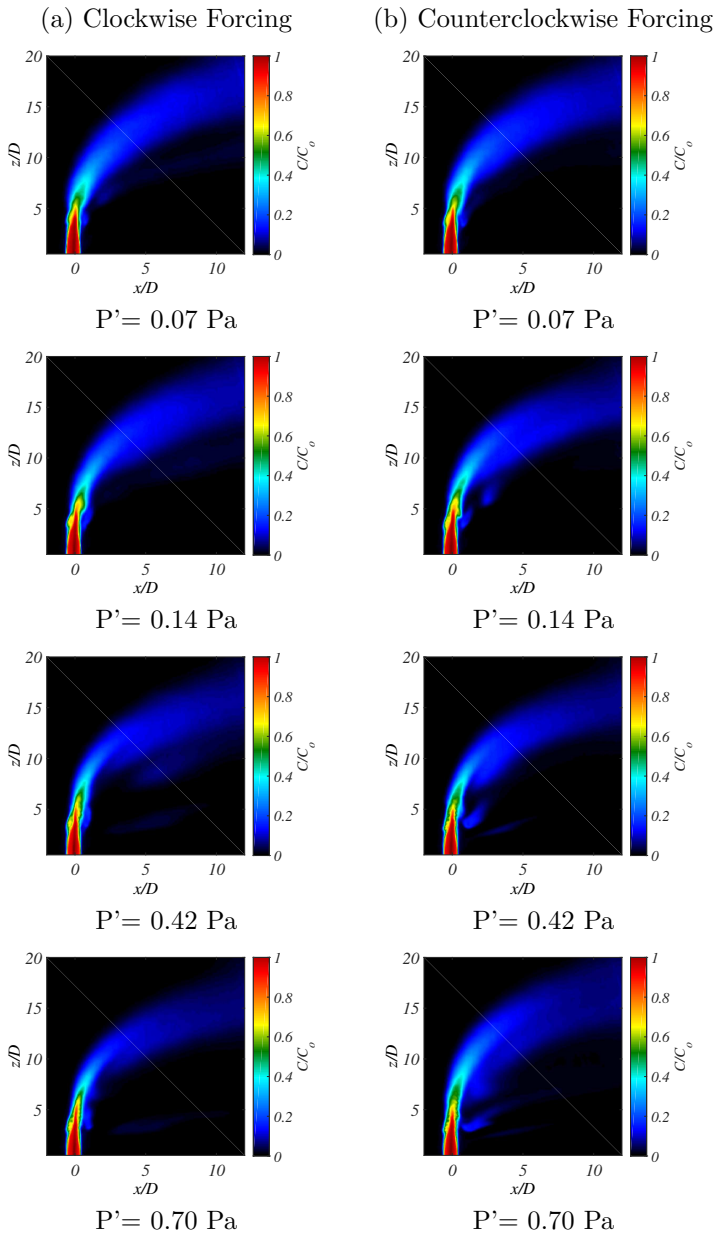

Figure C.7: Mean centerplane acetone concentration images in the regular plane (x/D - z/D) for the equidensity $J = 61$ jet for $f_f = 2300$ Hz, with increasing forcing pressure perturbation P'.

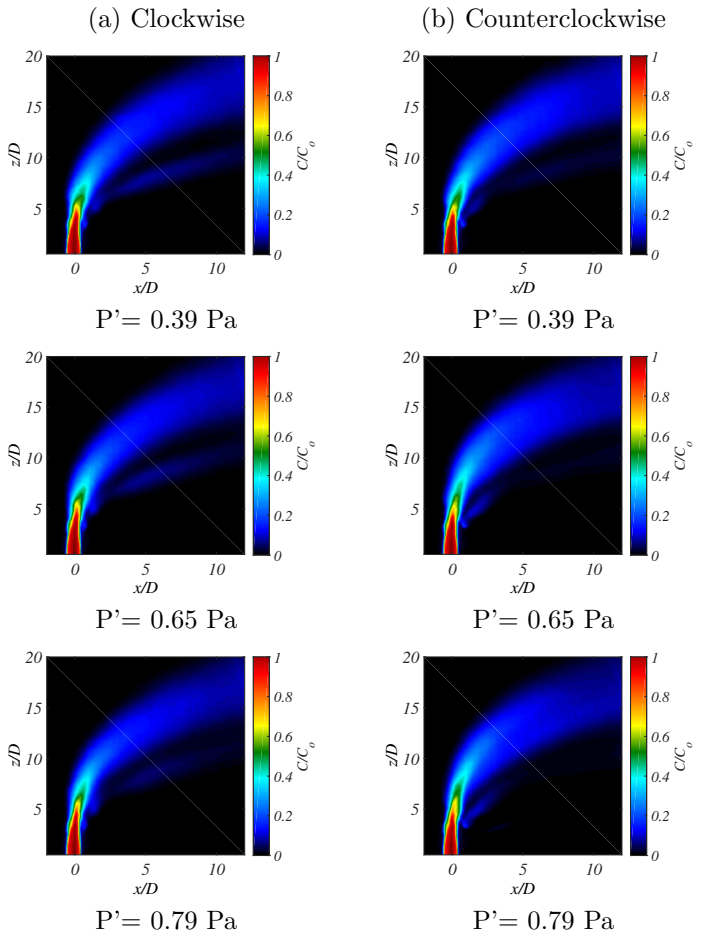

Figure C.8: Mean centerplane acetone concentration images in the regular plane (x/D - z/D) for the equidensity $J = 61$ jet for $f_f = 2600$ Hz, with increasing forcing pressure perturbation P'.

C.2 Mean Centerplane PLIF Images, 2-Speaker and 1-Speaker Study

This section represents mean centerplane acetone PLIF images with external asymmetric sinusoidal forcing of the jet, not shown in Chapter 4. Mean images are typically an average of 500 instantaneous images.

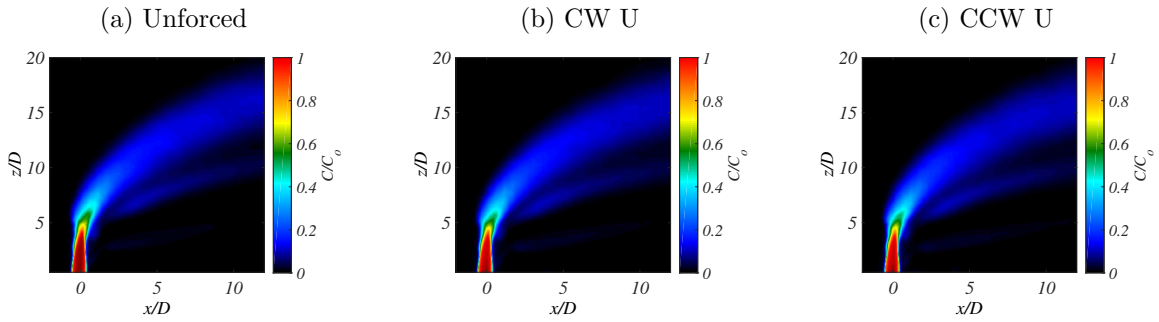

Figure C.9: Mean centerplane acetone concentration images in the regular plane (x/D - z/D) for the equidensity $J = 61$ jet for $f_f = 875$ Hz, with pressure perturbation P'=0.004 Pa.

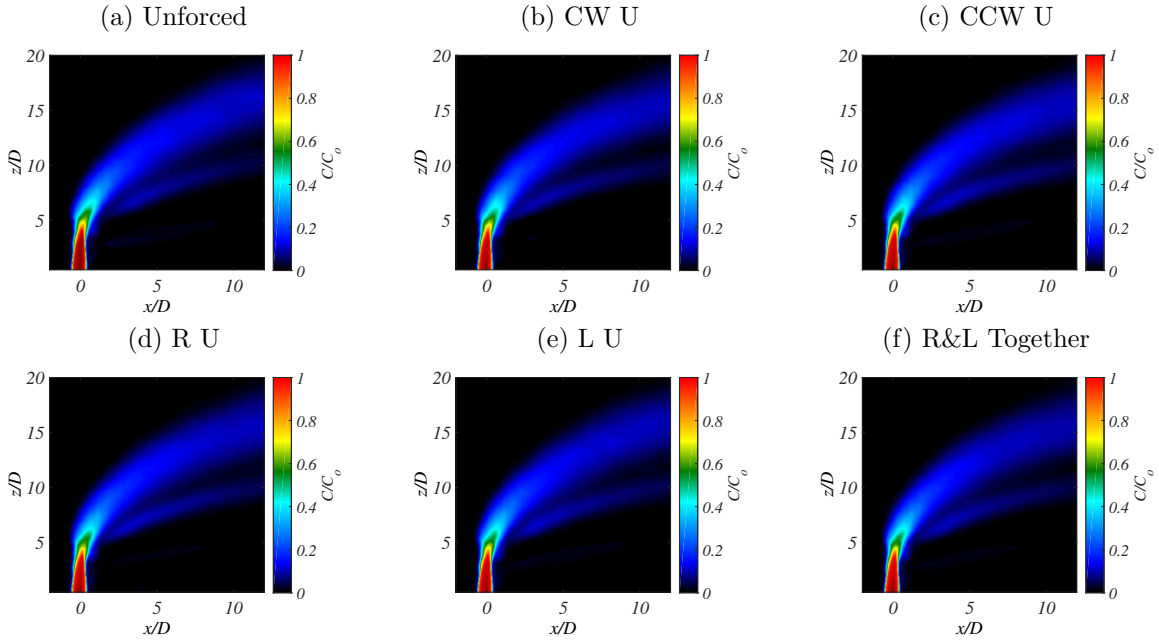

Figure C.10: Mean centerplane acetone concentration images in the regular plane (x/D - z/D) for the equidensity $J = 61$ jet for $f_f = 875$ Hz, with pressure perturbation P'=0.025 Pa.

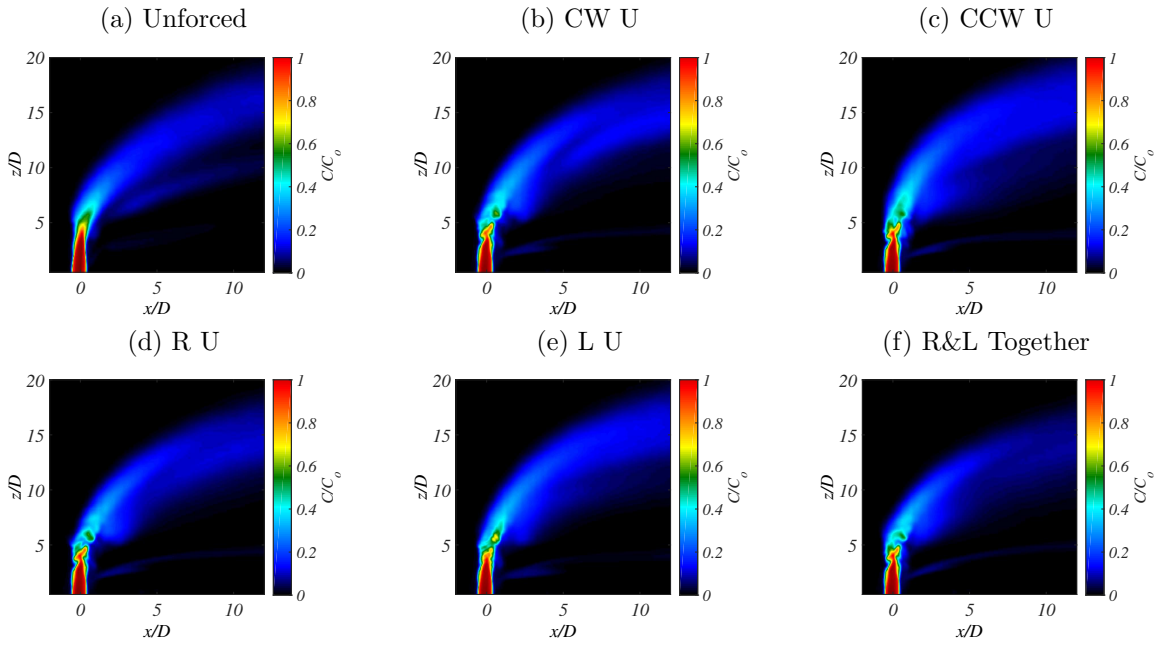

Figure C.11: Mean centerplane acetone concentration images in the regular plane (x/D - z/D) for the equidensity $J = 61$ jet for $f_f = 1600$ Hz, with pressure perturbation P'=0.15 Pa.

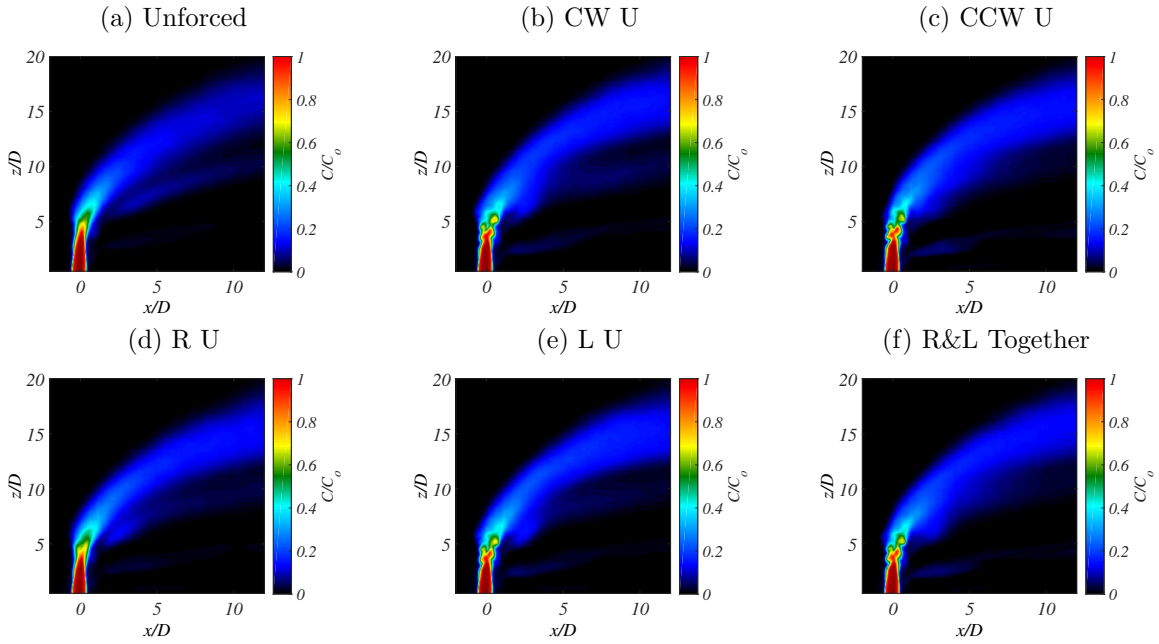

Figure C.12: Mean centerplane acetone concentration images in the regular plane (x/D - z/D) for the equidensity $J = 61$ jet for $f_f = 1750$ Hz, with pressure perturbation P'=0.10 Pa.

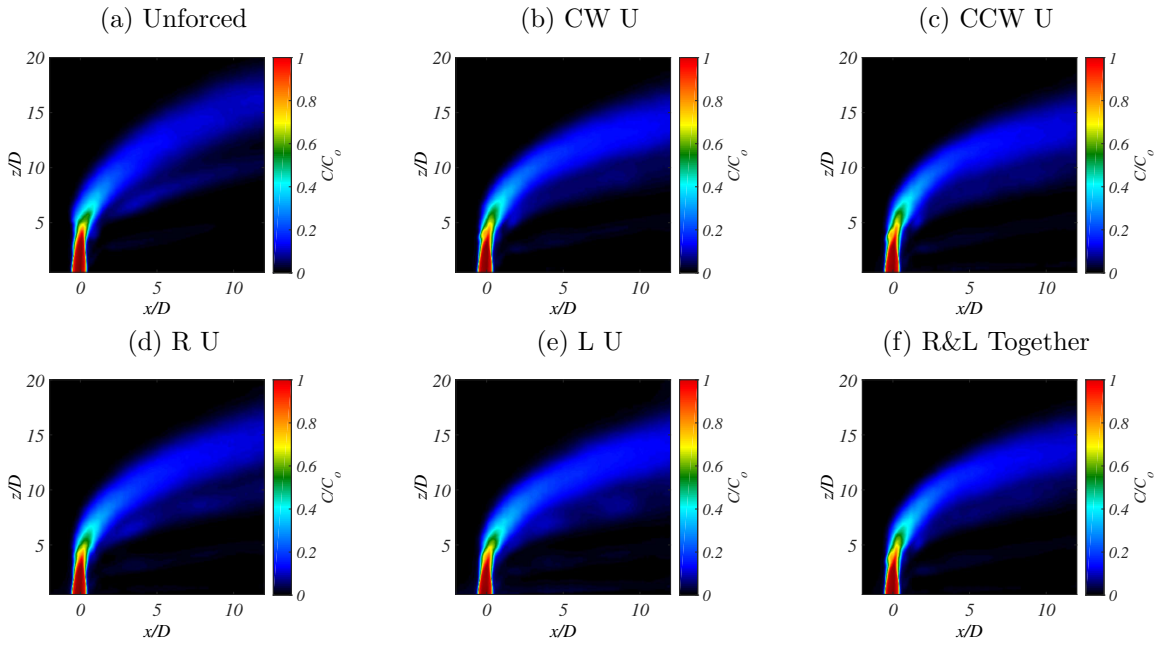

Figure C.13: Mean centerplane acetone concentration images in the regular plane (x/D - z/D) for the equidensity $J = 61$ jet for $f_f = 1900$ Hz, with pressure perturbation P'=0.15 Pa.

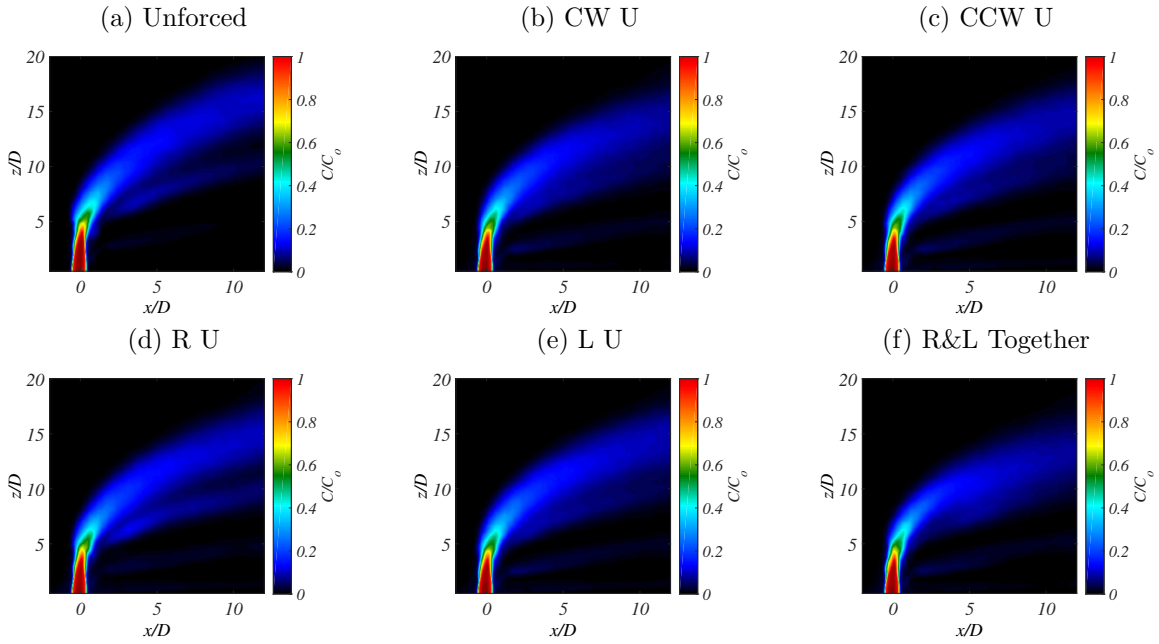

Figure C.14: Mean centerplane acetone concentration images in the regular plane (x/D - z/D) for the equidensity $J = 61$ jet for $f_f = 2300$ Hz, with pressure perturbation P'=0.28 Pa.

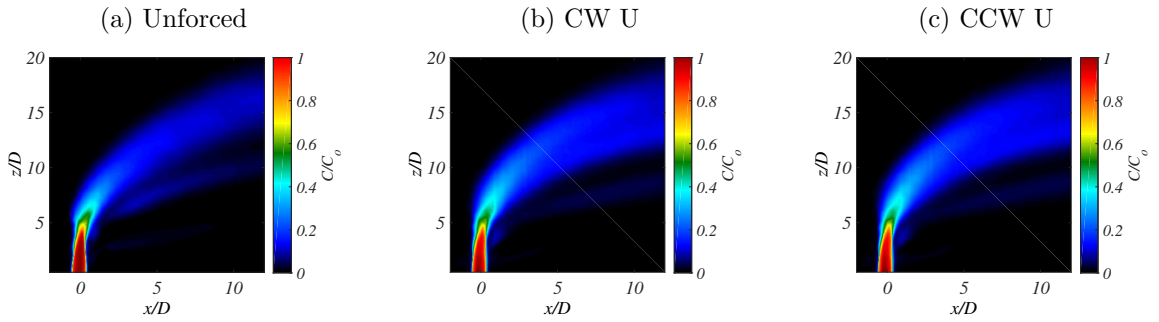

Figure C.15: Mean centerplane acetone concentration images in the regular plane (x/D - z/D) for the equidensity $J = 61$ jet for $f_f = 2900$ Hz, with pressure perturbation P'=0.004 Pa.

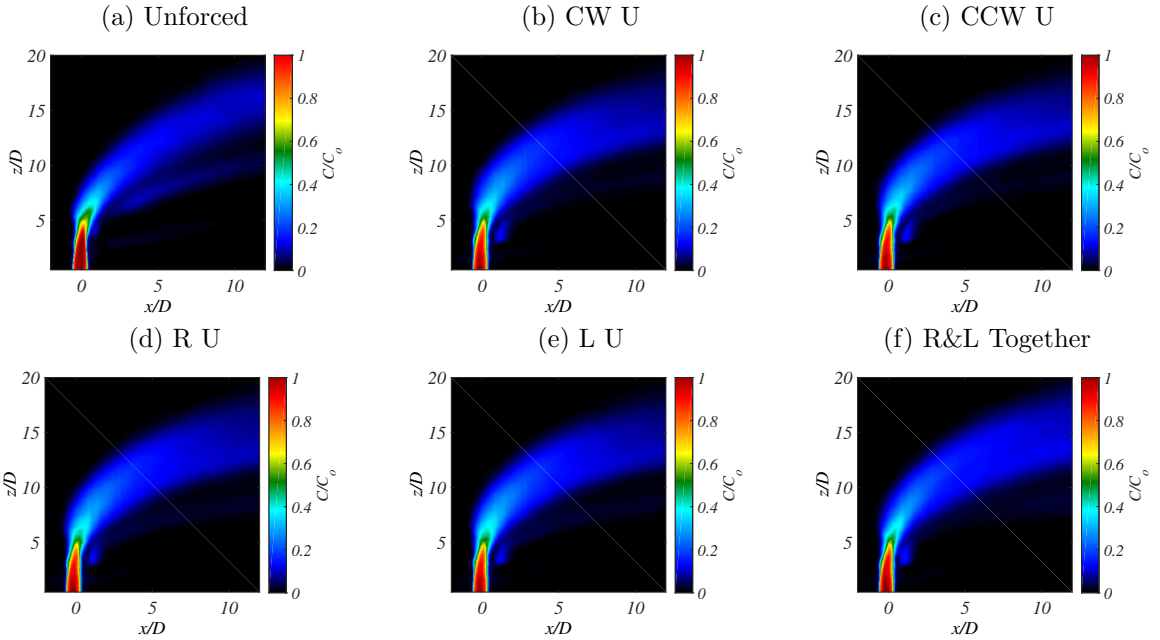

Figure C.16: Mean centerplane acetone concentration images in the regular plane (x/D - z/D) for the equidensity $J = 61$ jet for $f_f = 2900$ Hz, with pressure perturbation P'=1.4 Pa.

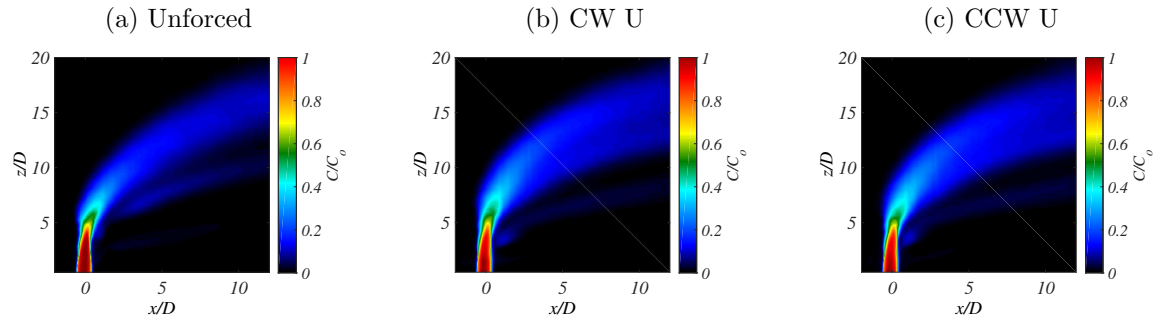

Figure C.17: Mean centerplane acetone concentration images in the regular plane (x/D - z/D) for the equidensity $J = 61$ jet for $f_f = 3500$ Hz, with pressure perturbation P'=1.4 Pa.

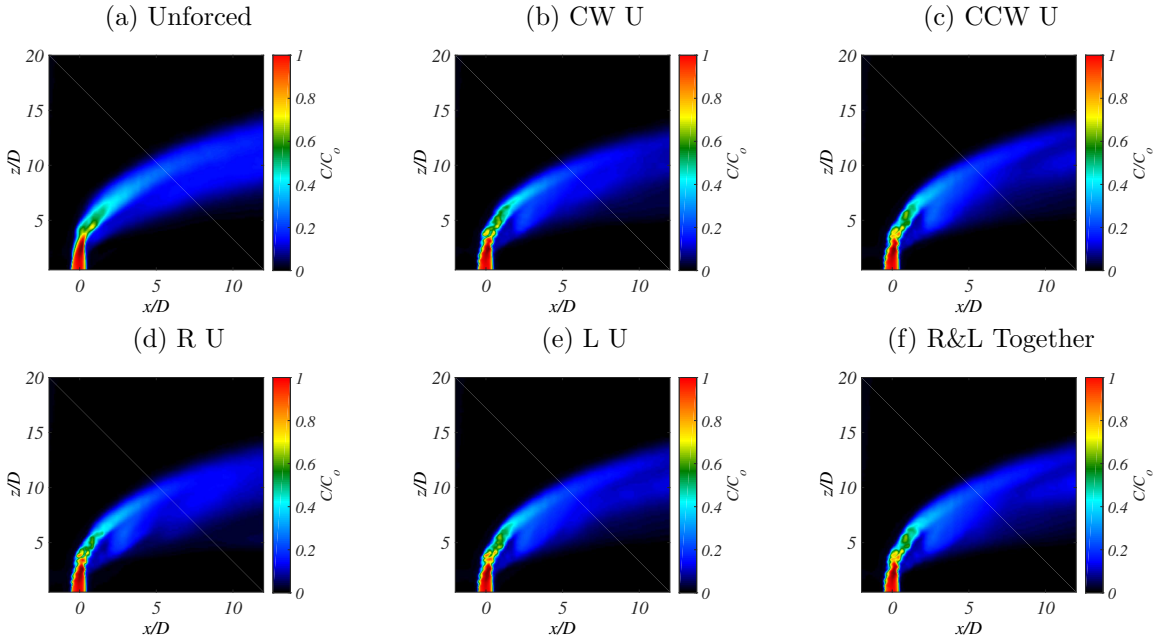

Figure C.18: Mean centerplane acetone concentration images in the regular plane (x/D - z/D) for the equidensity $J = 24$ jet for $f_f = 1900$ Hz, with pressure perturbation P'=0.15 Pa.

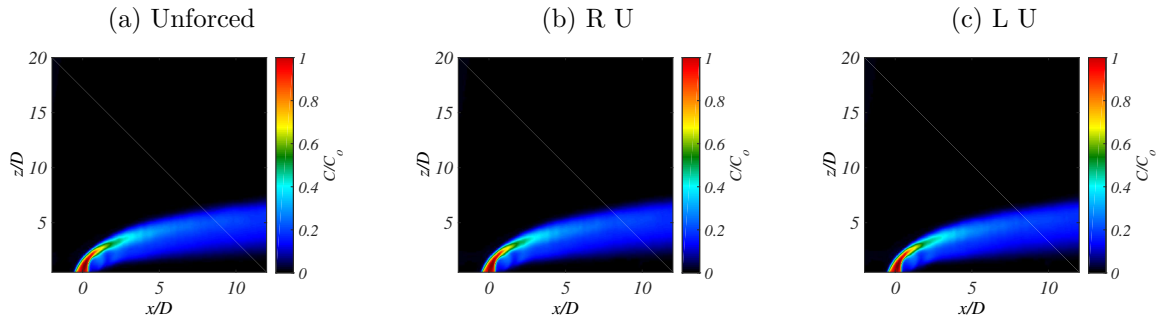

Figure C.19: Mean centerplane acetone concentration images in the regular plane (x/D - z/D) for the equidensity $J = 6$ jet for $f_f = 1900$ Hz, with pressure perturbation P'=0.15 Pa.

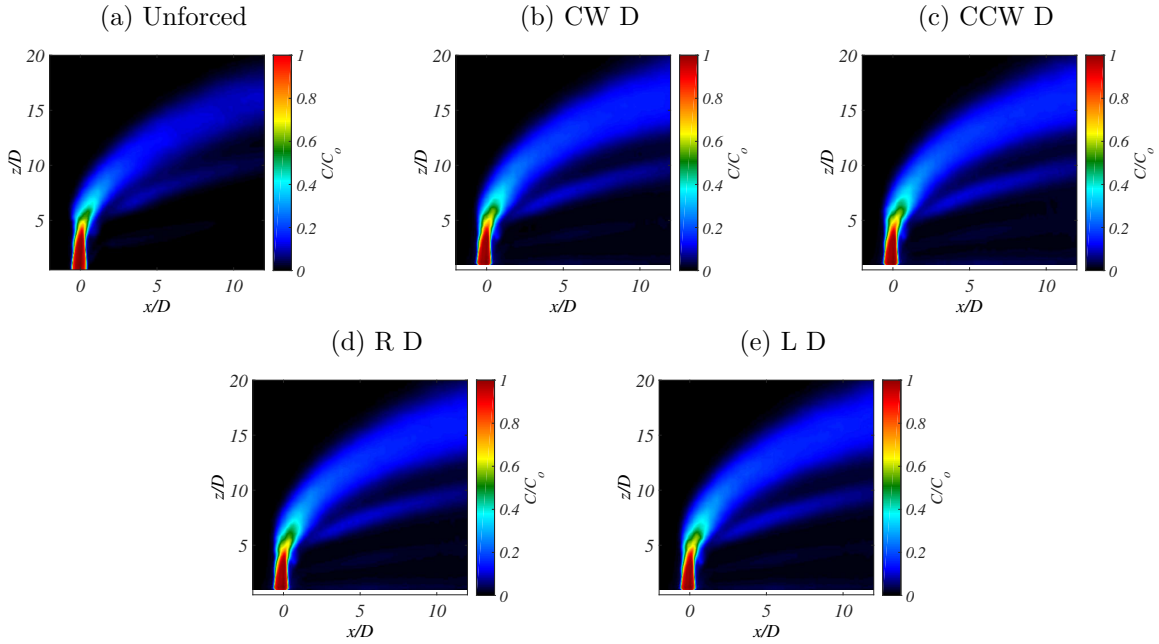

Figure C.20: Mean centerplane acetone concentration images in the regular plane (x/D - z/D) for the equidensity $J = 61$ jet for $f_f = 875$ Hz, with pressure perturbation P'=0.025 Pa.

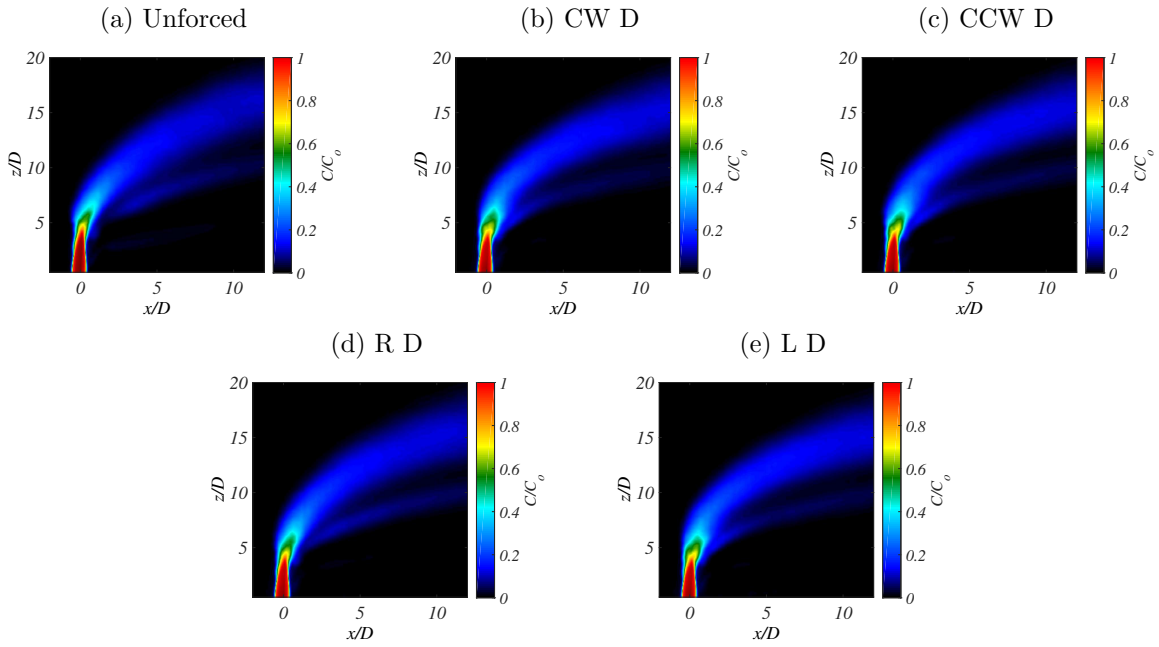

Figure C.21: Mean centerplane acetone concentration images in the regular plane (x/D - z/D) for the equidensity $J = 61$ jet for $f_f = 875$ Hz, with pressure perturbation P'=0.225 Pa.

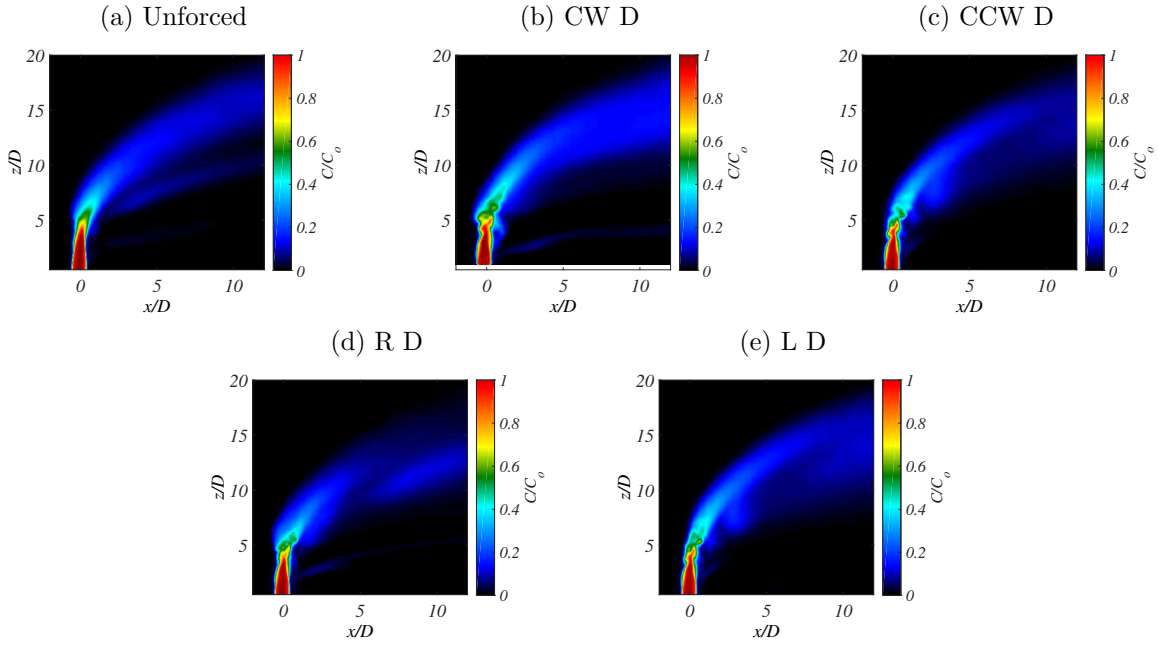

Figure C.22: Mean centerplane acetone concentration images in the regular plane (x/D - z/D) for the equidensity $J = 61$ jet for $f_f = 1600$ Hz, with pressure perturbation P'=0.15 Pa.

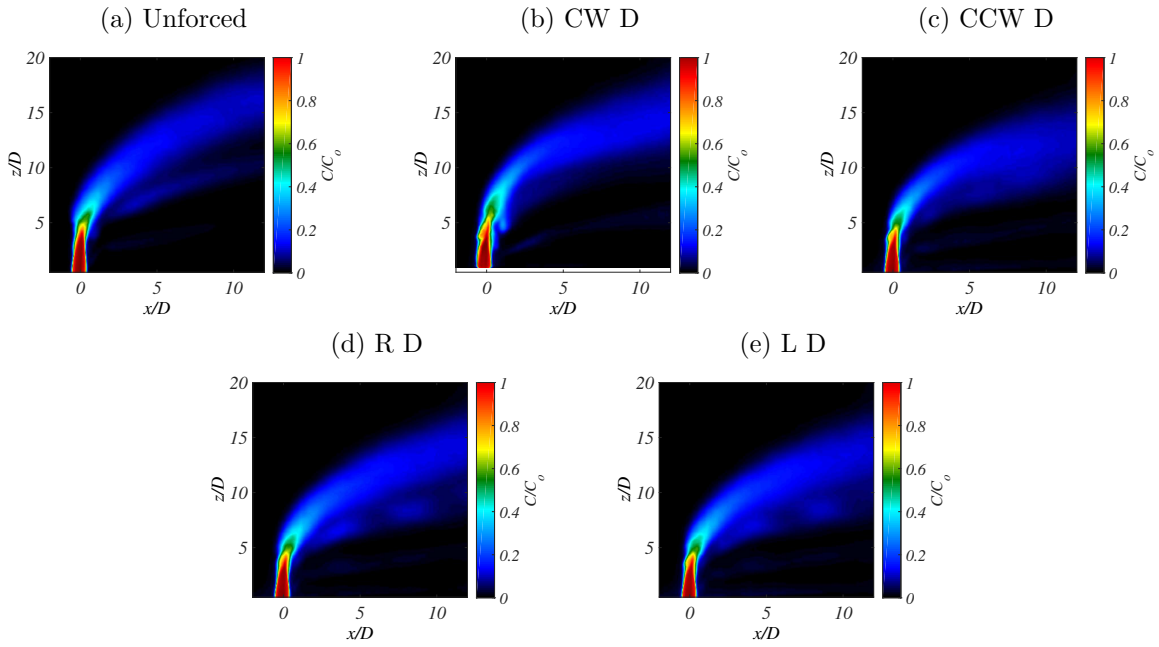

Figure C.23: Mean centerplane acetone concentration images in the regular plane (x/D - z/D) for the equidensity $J = 61$ jet for $f_f = 1900$ Hz, with pressure perturbation P'=0.15 Pa.

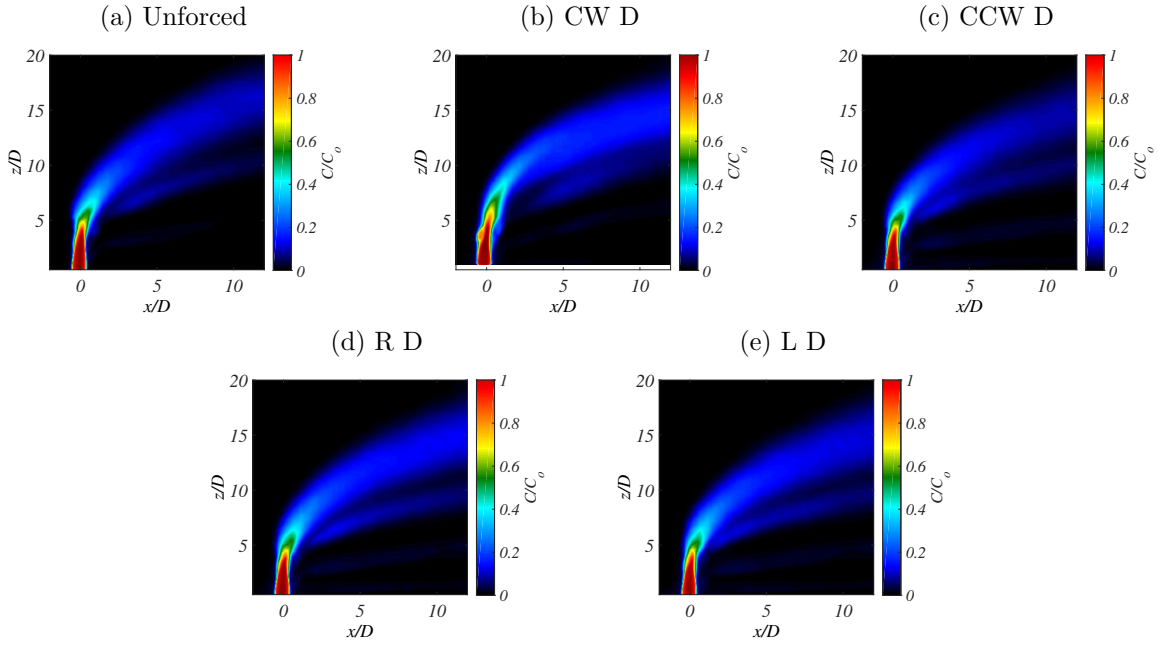

Figure C.24: Mean centerplane acetone concentration images in the regular plane (x/D - z/D) for the equidensity $J = 61$ jet for $f_f = 2300$ Hz, with pressure perturbation P'=0.28 Pa.

C.3 Mean Cross-Sectional PLIF Images, 4-Speaker Study

This section represents mean cross-sectional acetone PLIF images with external asymmetric sinusoidal forcing of the jet, not shown in Chapter 4. Mean images are typically an average of 500 instantaneous images.

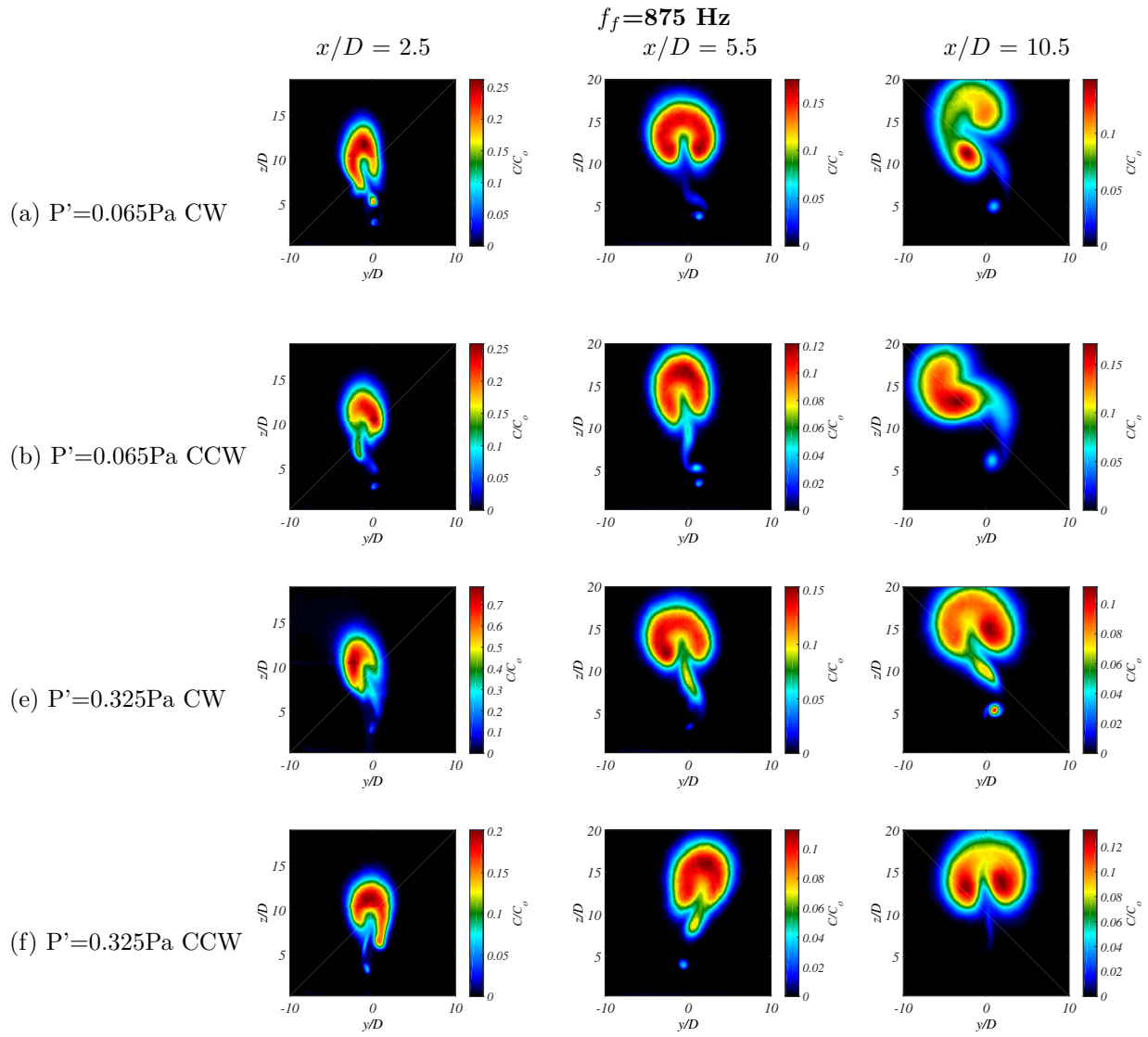

Figure C.25: Mean PLIF images in the cross-sectional y/D-z/D plane for the J=61 JICF with natural frequency in the range of f_o=1600-1900 Hz. f_f=875 Hz for different pressure perturbations P' and speaker operational orientation as shown.

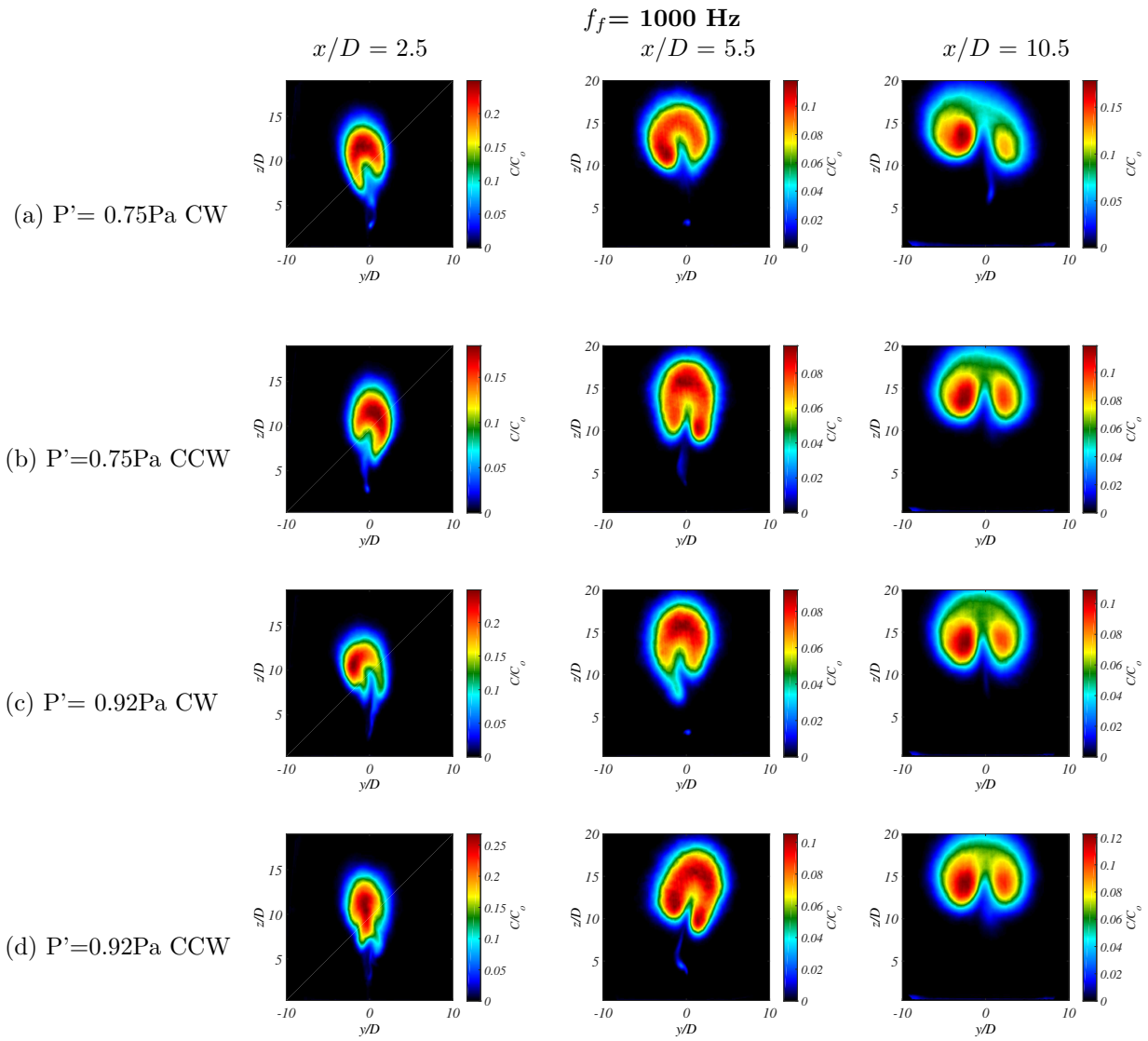

Figure C.26: Mean PLIF images in the cross-sectional y/D-z/D plane for the J=61 JICF with natural frequency in the range of f_o=1600-1900 Hz. f_f=1000 Hz for different pressure perturbations P' and speaker operational orientation as shown.

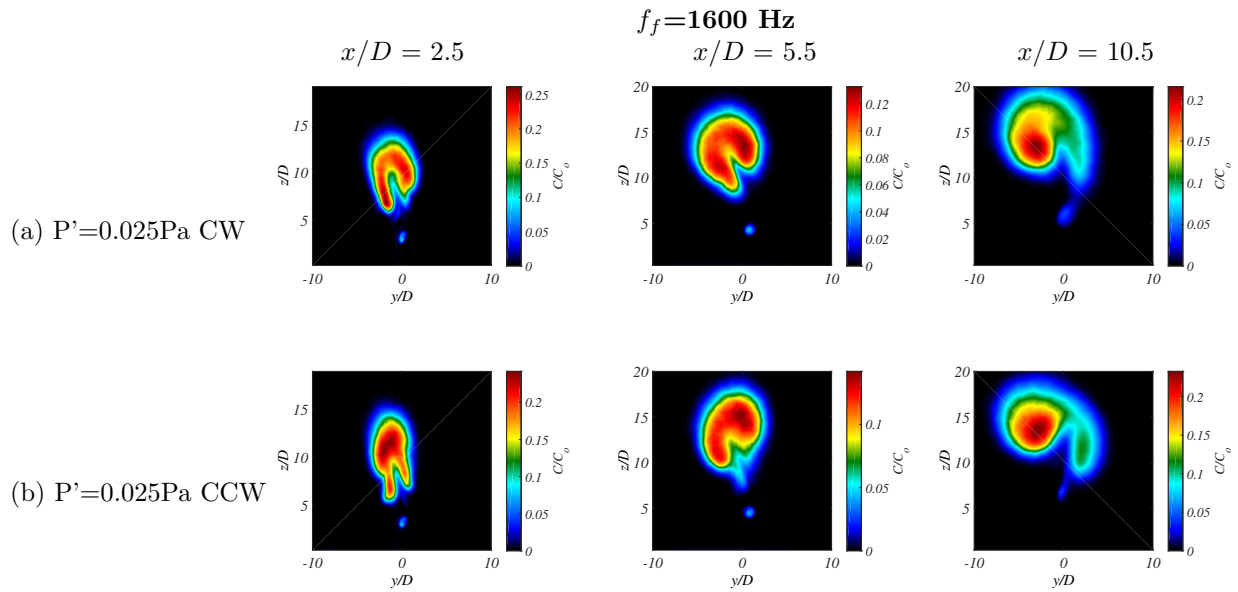

Figure C.27: Mean PLIF images in the cross-sectional y/D-z/D plane for the J=61 JICF with natural frequency in the range of f_o=1600-1900 Hz. f_f=1600Hz for different pressure perturbations P' and speaker operational orientation as shown.

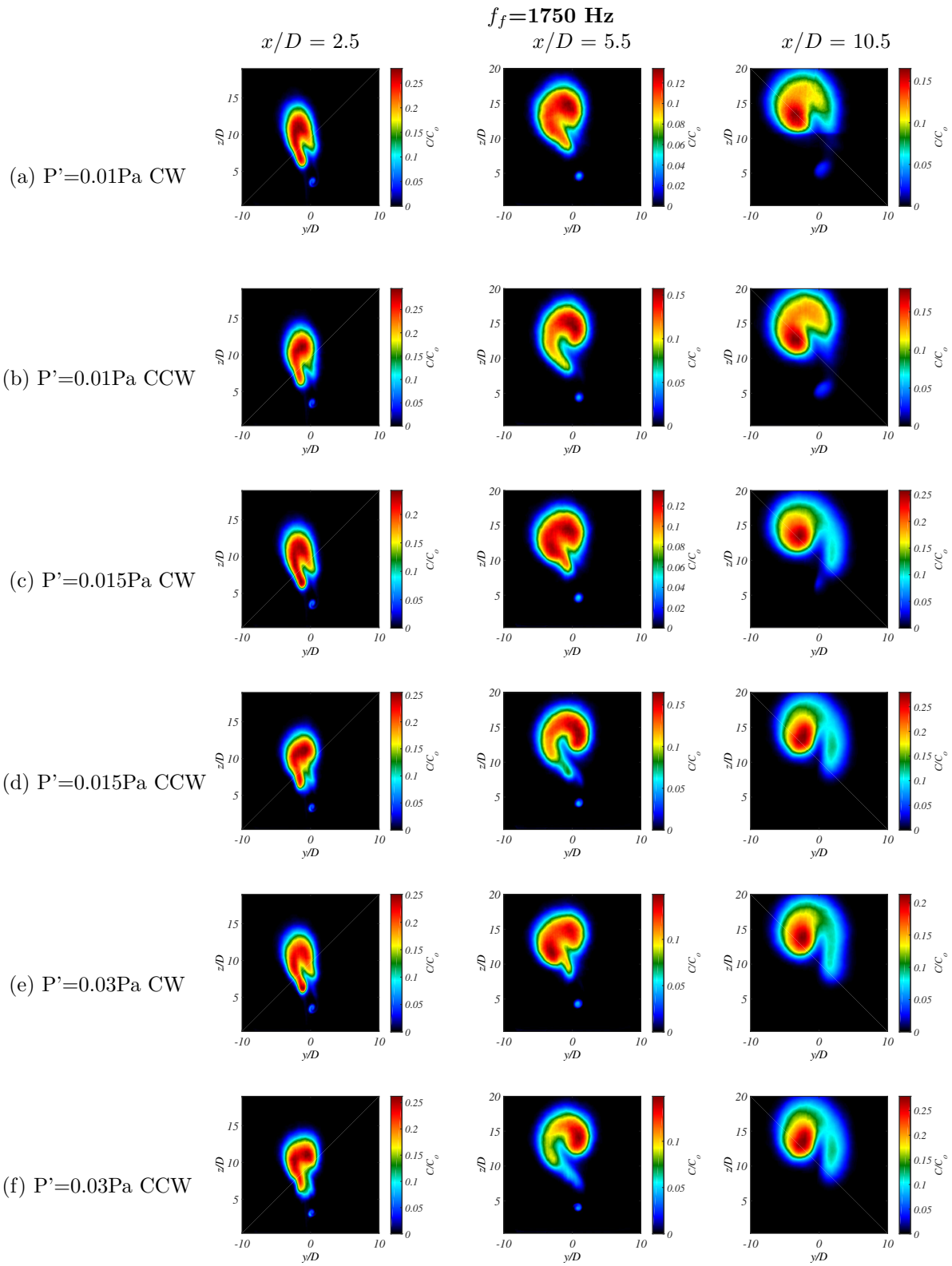

Figure C.28: Mean PLIF images in the cross-sectional y/D-z/D plane for the J=61 JICF with natural frequency in the range of f_o=1600-1900 Hz. f_f=1750 Hz for different pressure perturbations P' and speaker operational orientation as shown.

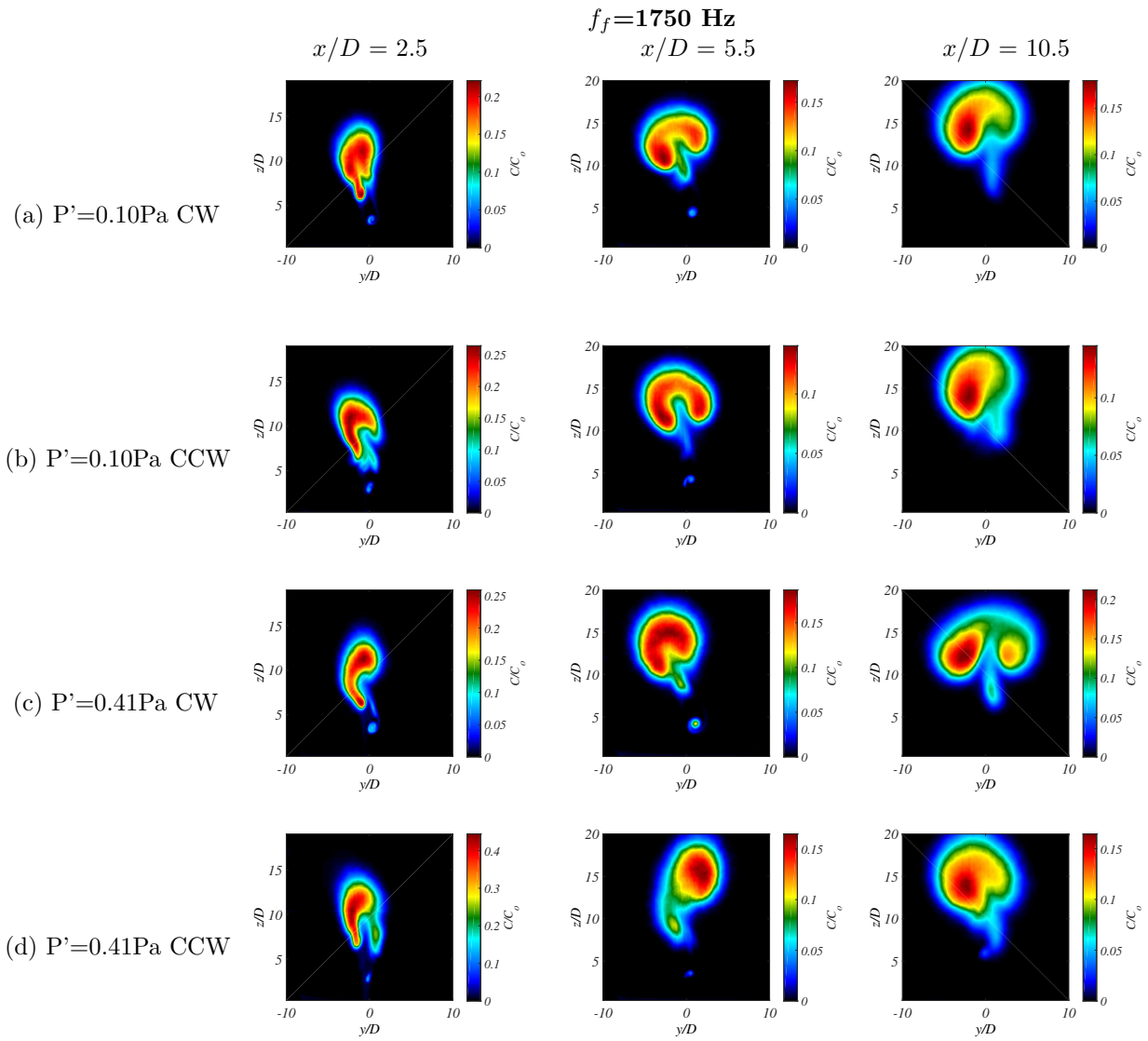

Figure C.29: Mean PLIF images in the cross-sectional y/D-z/D plane for the J=61 JICF with natural frequency in the range of f_o=1600-1900 Hz. f_f=1750 Hz for different pressure perturbations P' and speaker operational orientation as shown.

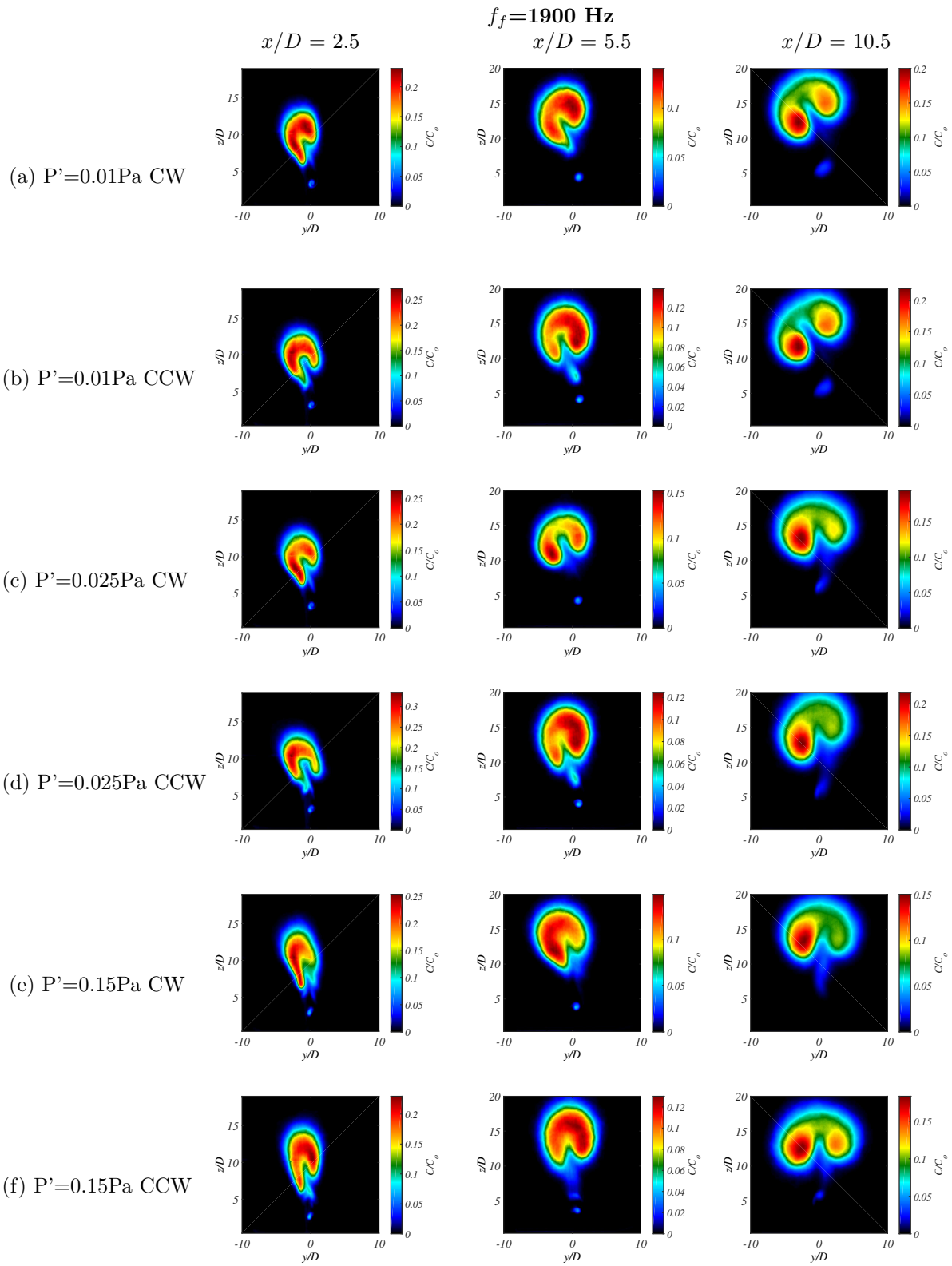

Figure C.30: Mean PLIF images in the cross-sectional y/D-z/D plane for the J=61 JICF with natural frequency in the range of f_o=1600-1900 Hz, f_f=1900Hz for different pressure perturbations P' and speaker operational orientation as shown.

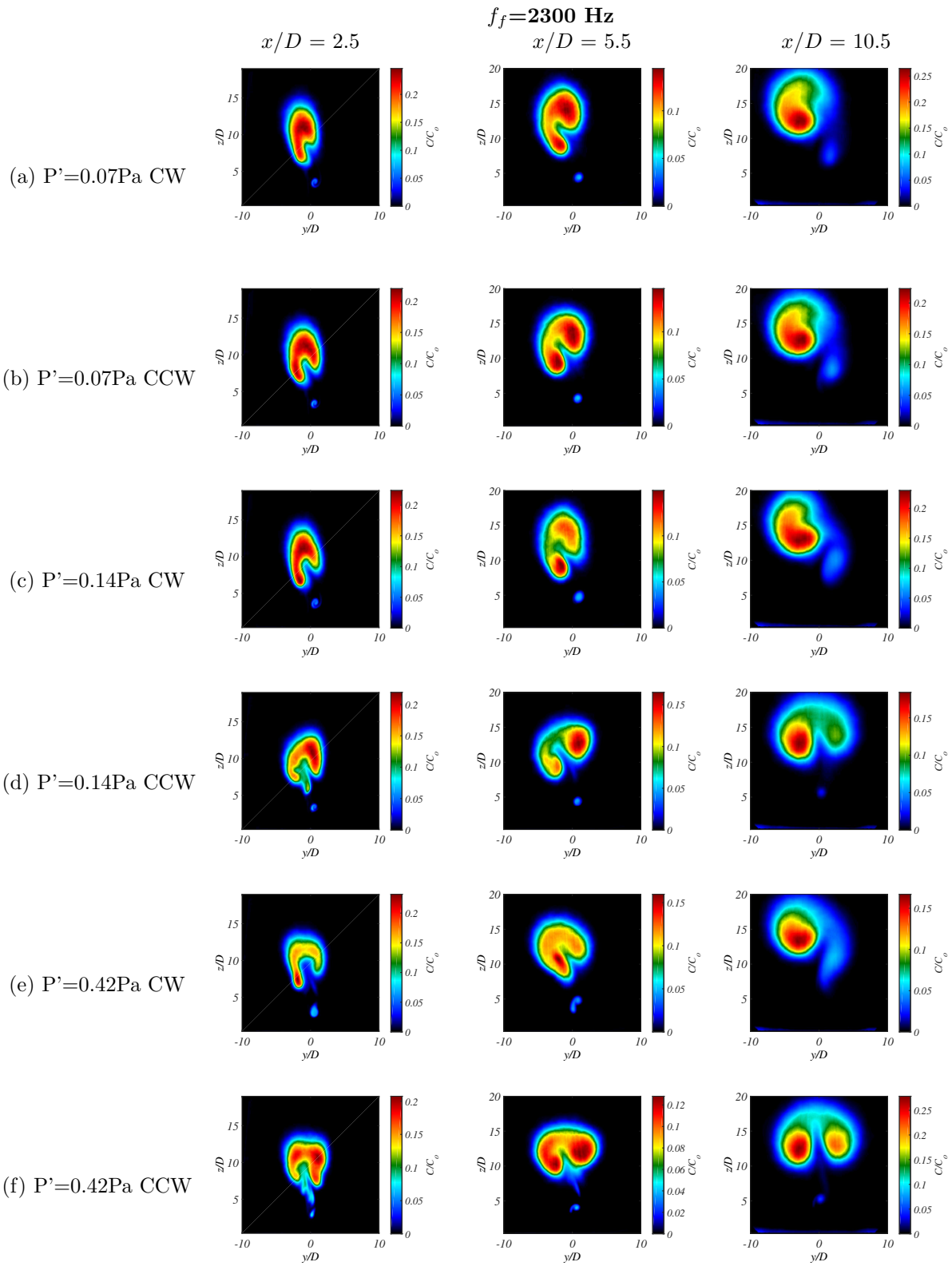

Figure C.31: Mean PLIF images in the cross-sectional y/D-z/D plane for the J=61 JICF with natural frequency in the range of f_o=1600-1900 Hz. f_f=2300 Hz for different pressure perturbations P' and speaker operational orientation as shown.

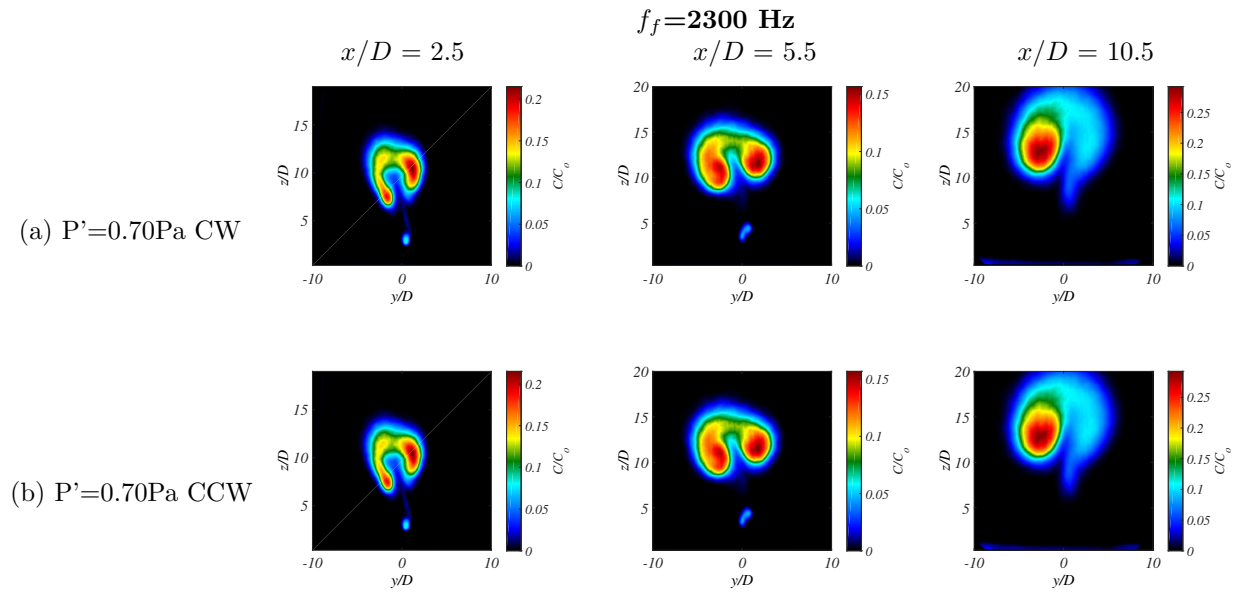

Figure C.32: Mean PLIF images in the cross-sectional y/D-z/D plane for the J=61 JICF with natural frequency in the range of f_o=1600-1900 Hz. f_f=2300 Hz for different pressure perturbations P' and speaker operational orientation as shown.

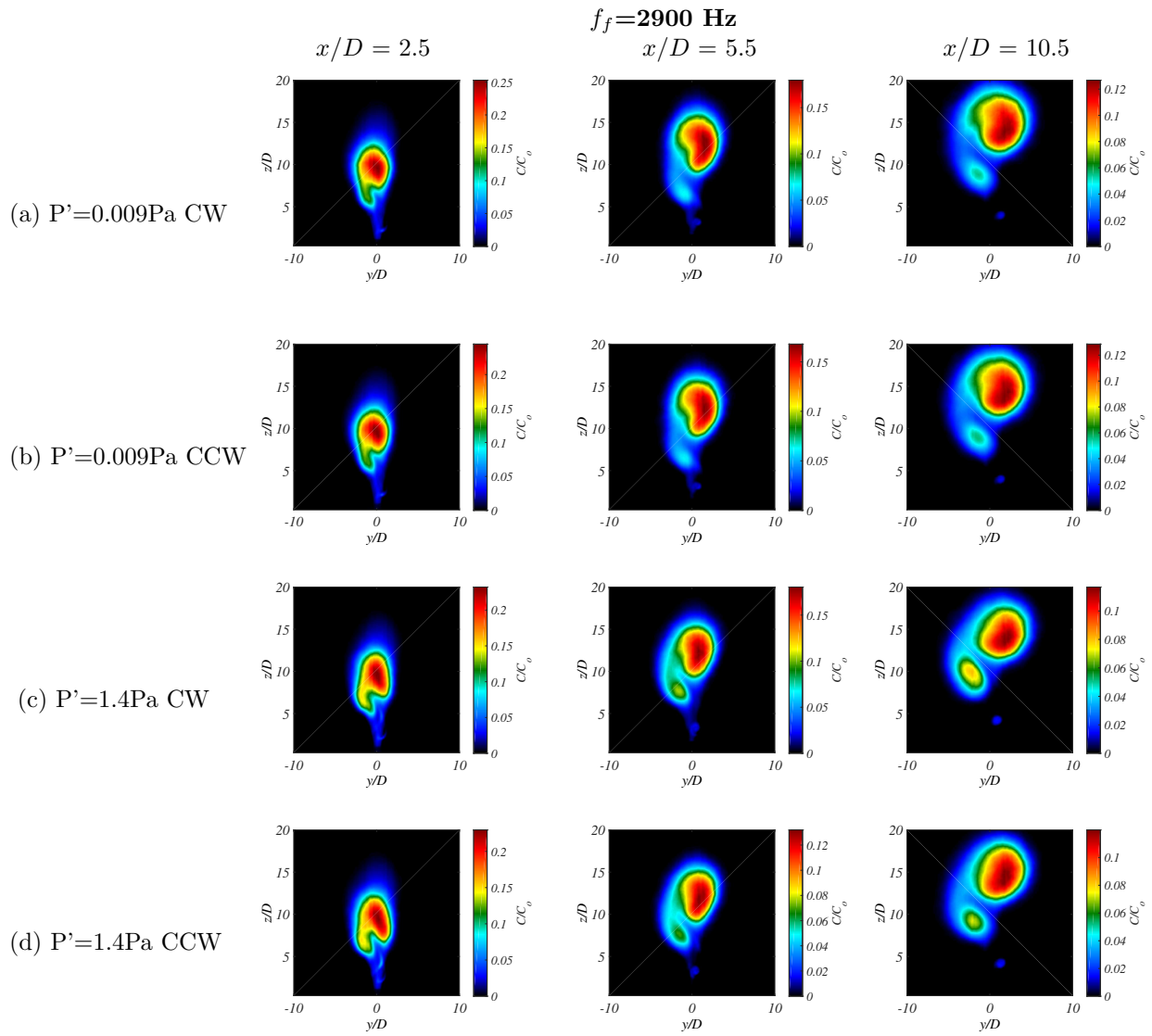

Figure C.33: Mean PLIF images in the cross-sectional y/D-z/D plane for the J=61 JICF with natural frequency in the range of f_o=1600-1900 Hz. f_f=2900 Hz for different pressure perturbations P' and speaker operational orientation as shown.

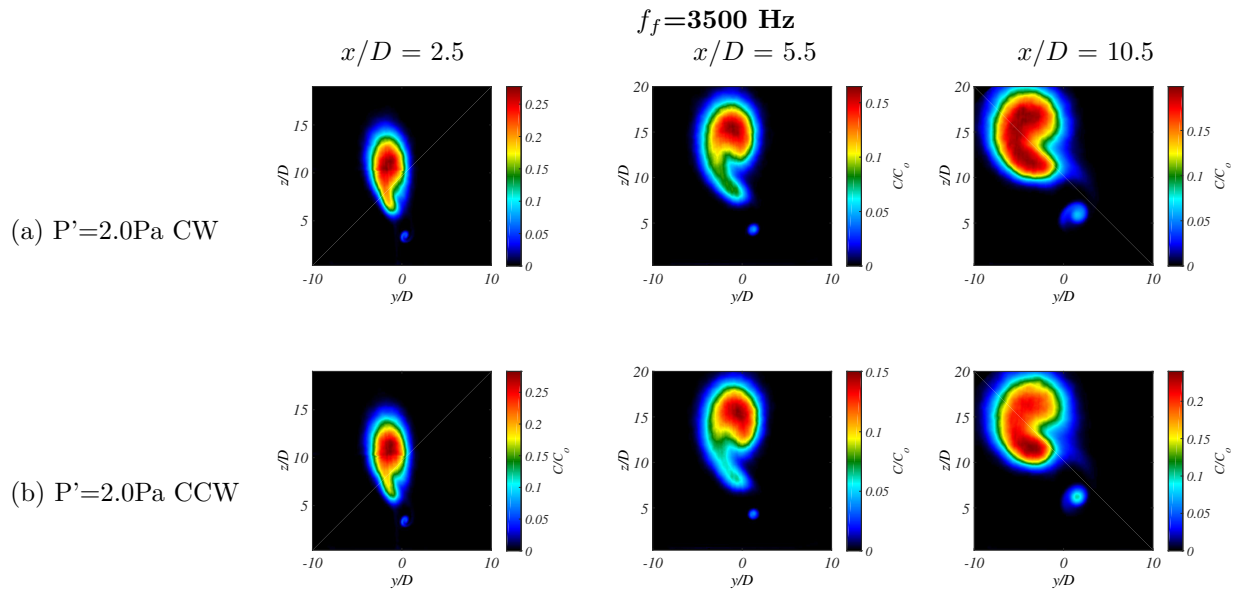

Figure C.34: Mean PLIF images in the cross-sectional y/D-z/D plane for the J=61 JICF with natural frequency in the range of f_o=1600-1900 Hz. f_f=3500 Hz for different pressure perturbations P' and speaker operational orientation as shown.

C.4 Mean Cross-Sectional PLIF Images, 2-Speaker and 1-Speaker Study

This section represents mean cross-sectional acetone PLIF images with external asymmetric sinusoidal forcing of the jet, not shown in Chapter 4. Mean images are typically an average of 500 instantaneous images.

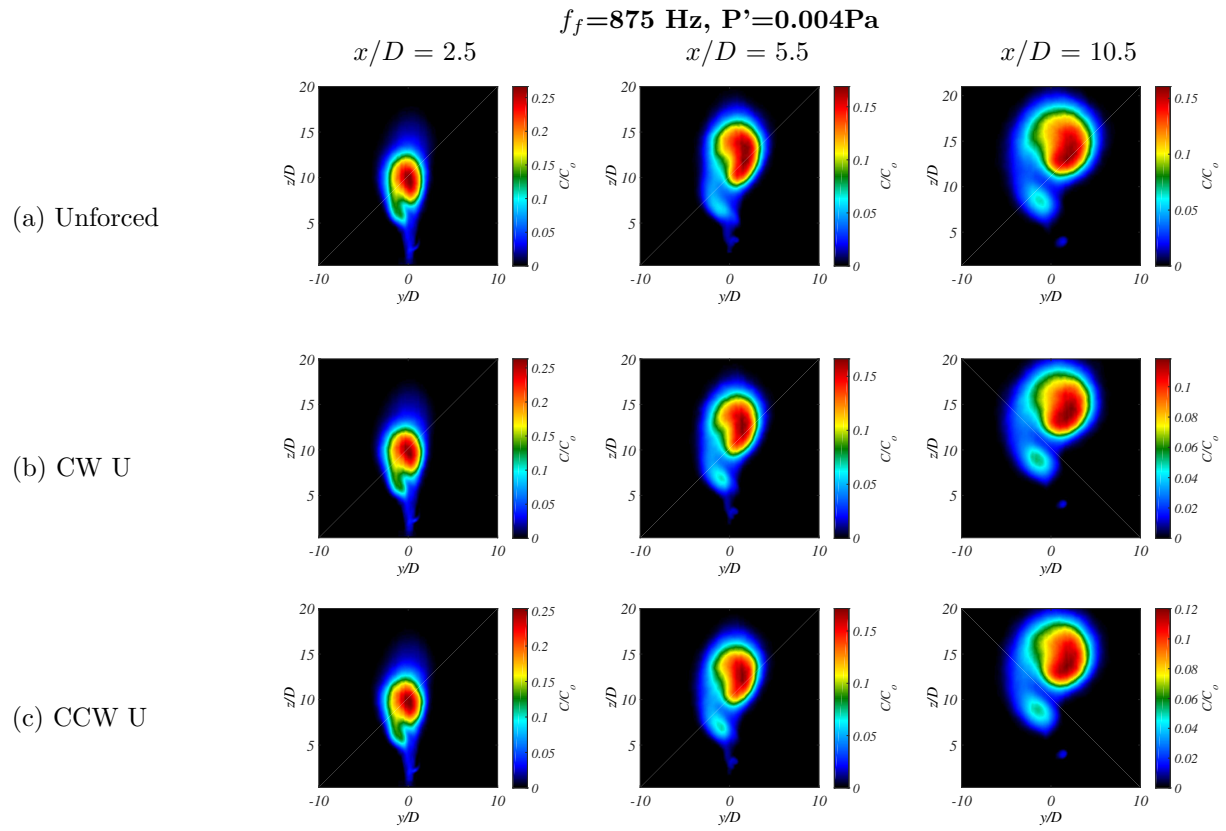

Figure C.35: Mean PLIF images in the cross-sectional y/D-z/D plane for the J=61 JICF with natural frequency in the range of f_o=1600-1900 Hz. f_f=875 Hz for P'=0.004 Pa and upstream speaker operation.

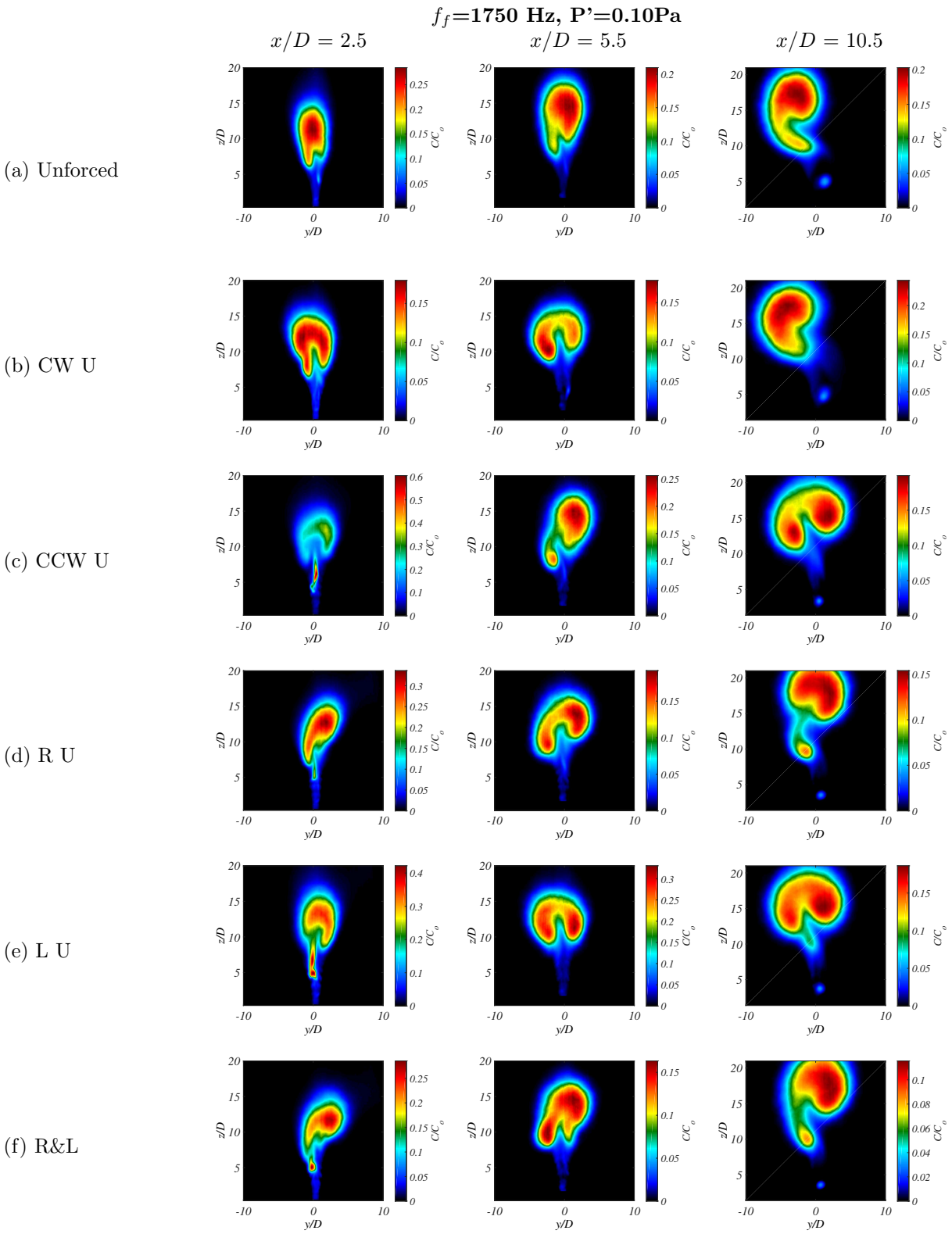

Figure C.36: Mean PLIF images in the cross-sectional y/D-z/D plane for the J=61 JICF with natural frequency in the range of f_o=1600-1900 Hz. f_f=1750 Hz for P'=0.10 Pa upstream speaker operation.

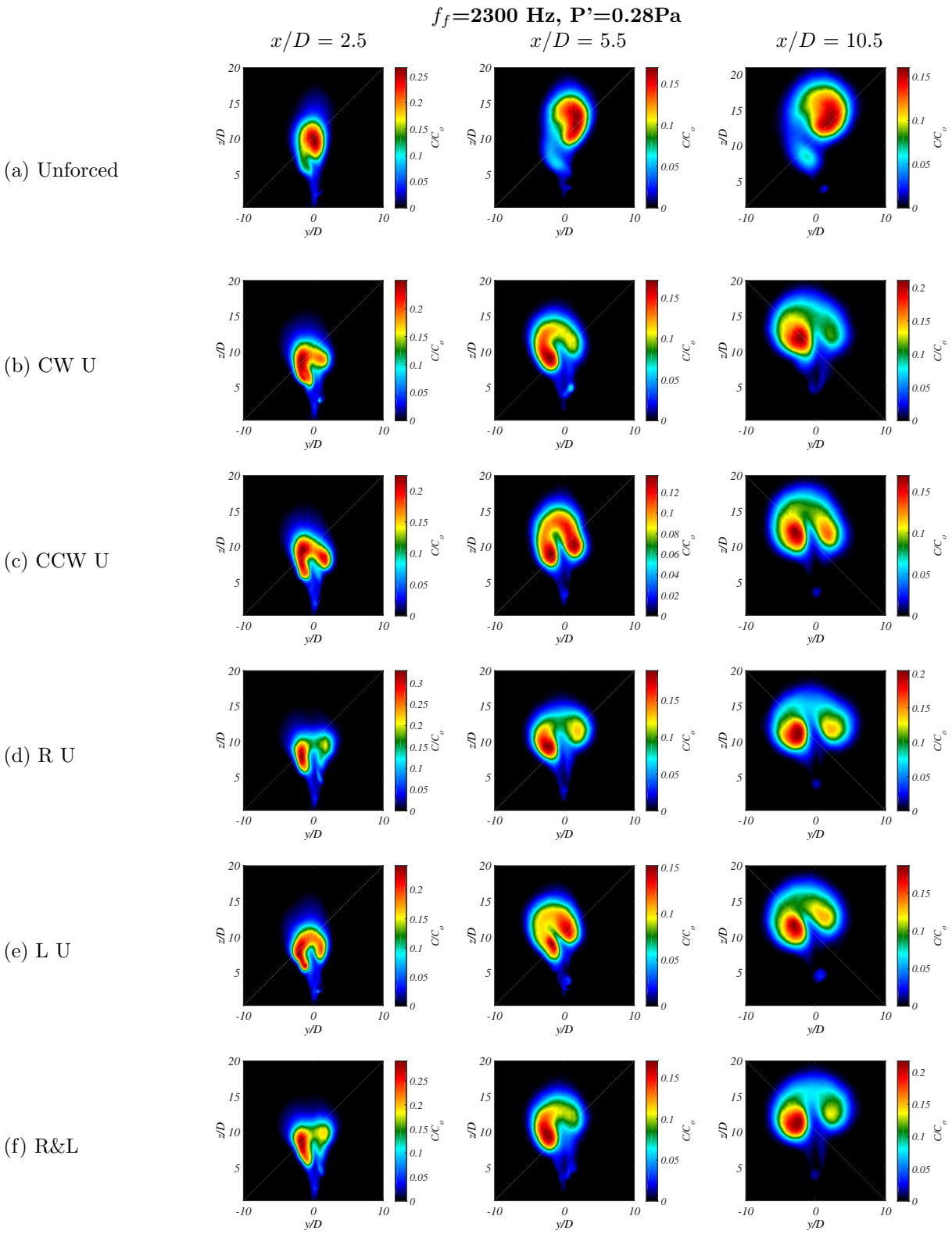

Figure C.37: Mean PLIF images in the cross-sectional y/D-z/D plane for the J=61 JICF with natural frequency in the range of f_o=1600-1900 Hz. f_f=2300 Hz for P'= 0.28 Pa upstream speaker operation.

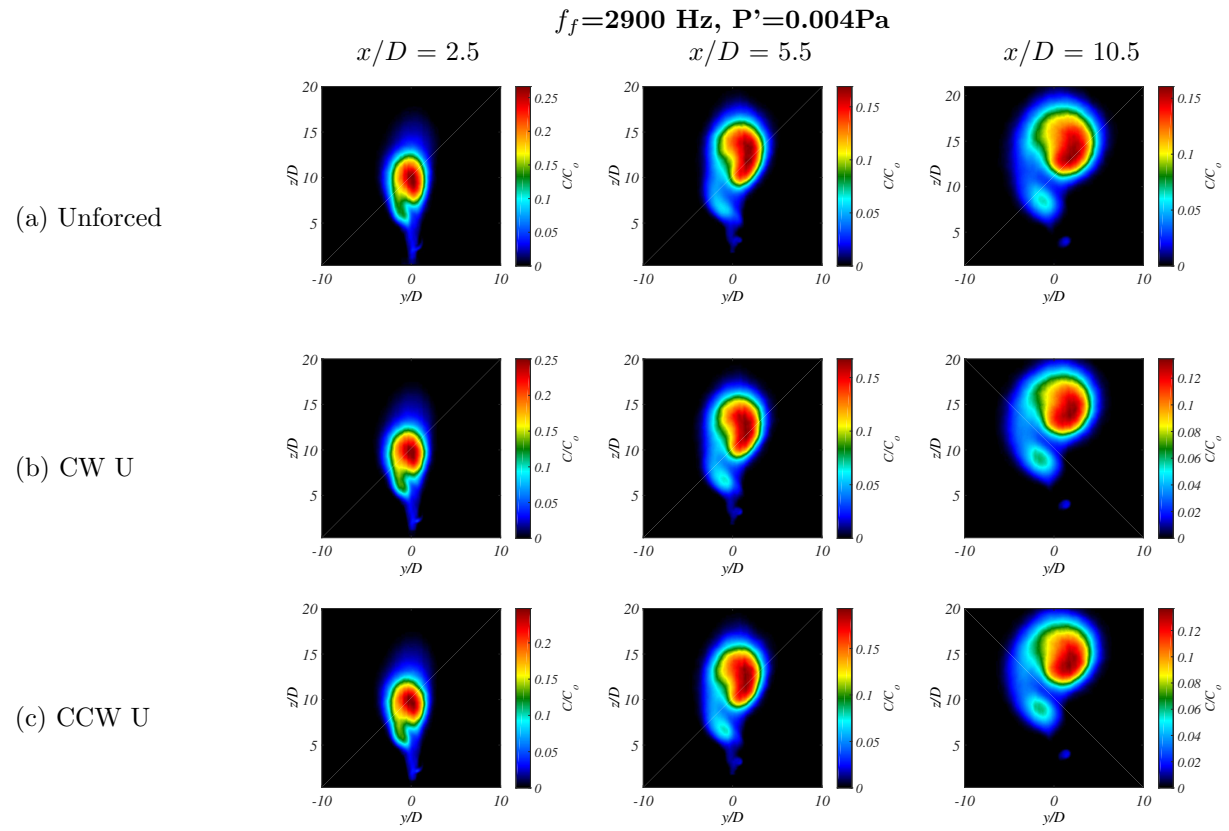

Figure C.38: Mean PLIF images in the cross-sectional y/D-z/D plane for the J=61 JICF with natural frequency in the range of f_o=1600-1900 Hz. f_f=2900 Hz for P'=0.004 Pa upstream speaker operation.

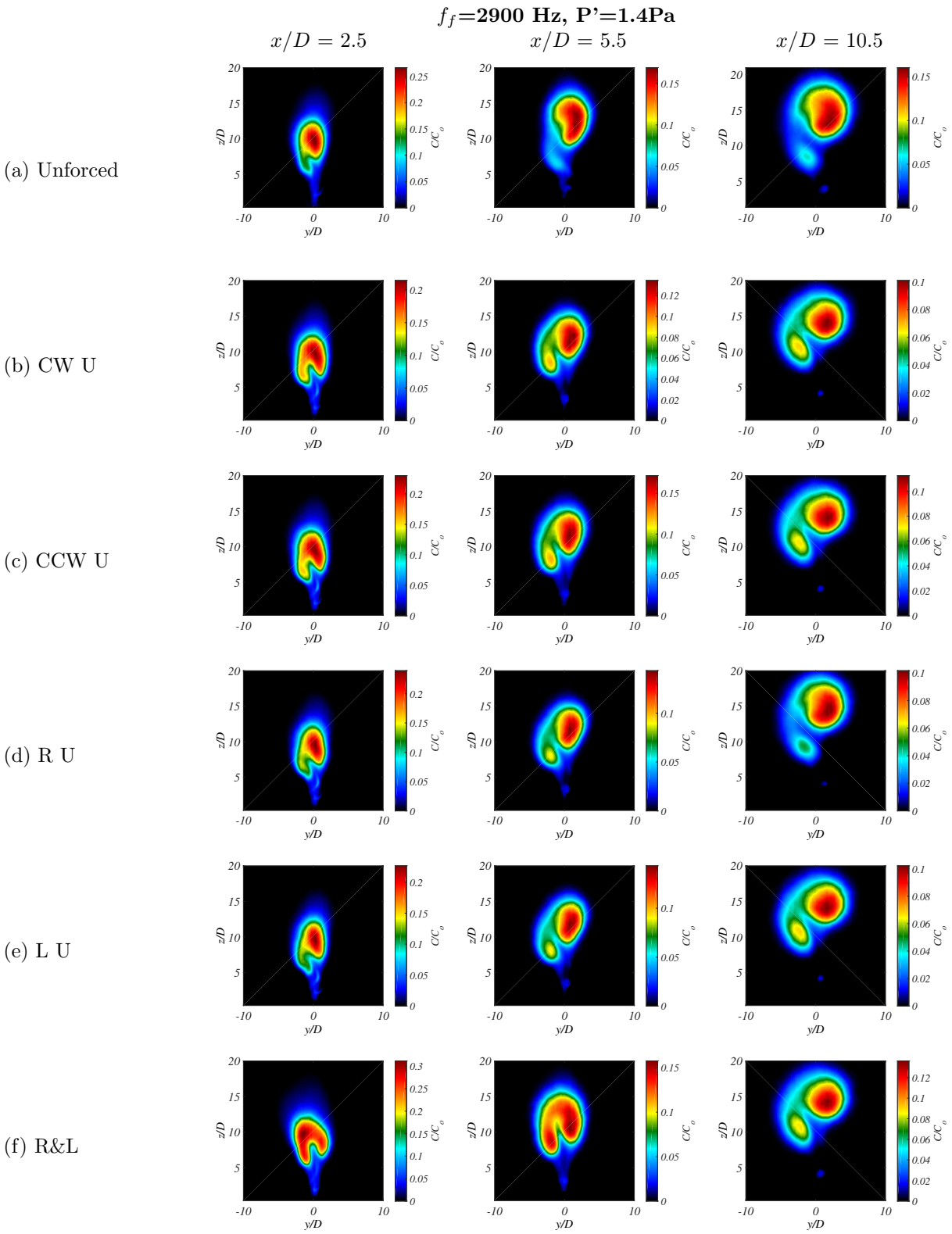

Figure C.39: Mean PLIF images in the cross-sectional y/D-z/D plane for the J=61 JICF with natural frequency in the range of f_o=1600-1900 Hz. f_f=2900 Hz for P'=1.4 Pa upstream speaker operation.

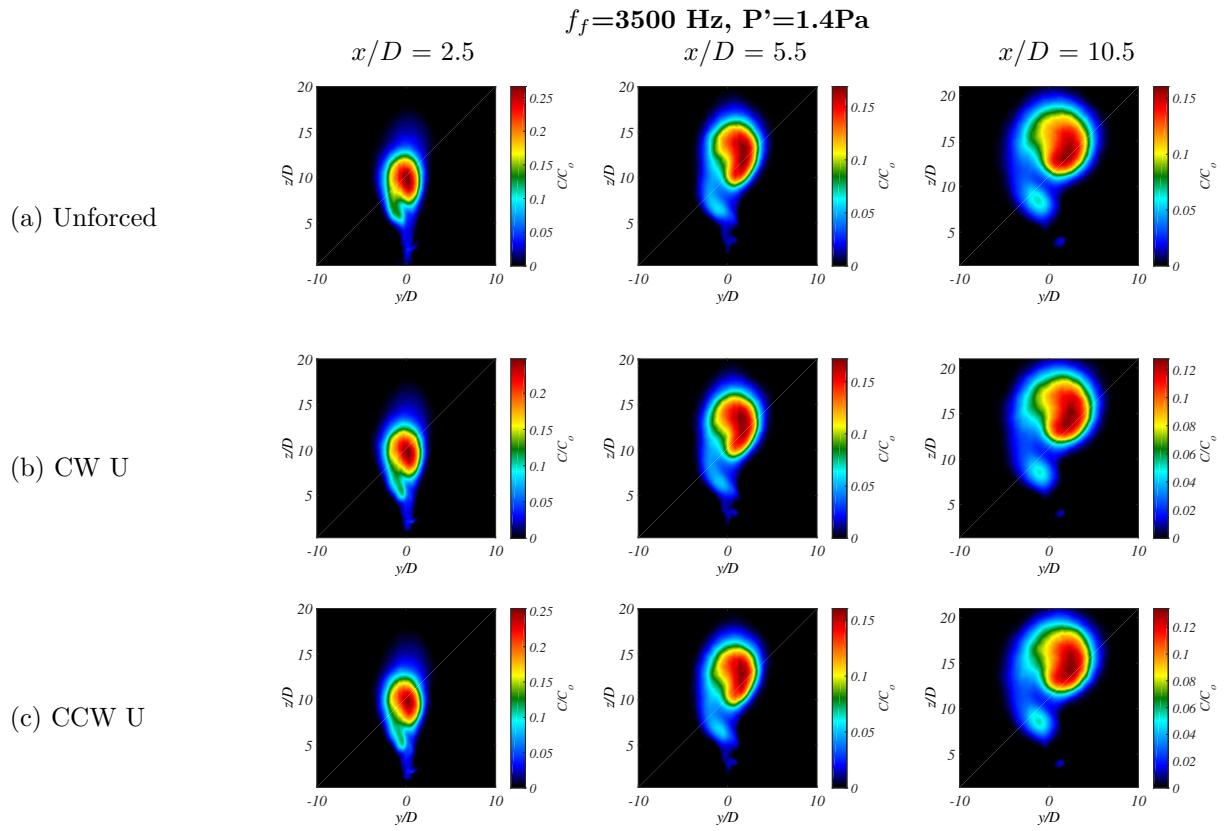

Figure C.40: Mean PLIF images in the cross-sectional y/D-z/D plane for the J=61 JICF with natural frequency in the range of f_o=1600-1900 Hz. f_f=3500 Hz, pressure perturbation P=1.4 Pa, and upstream speaker operational orientation as shown.

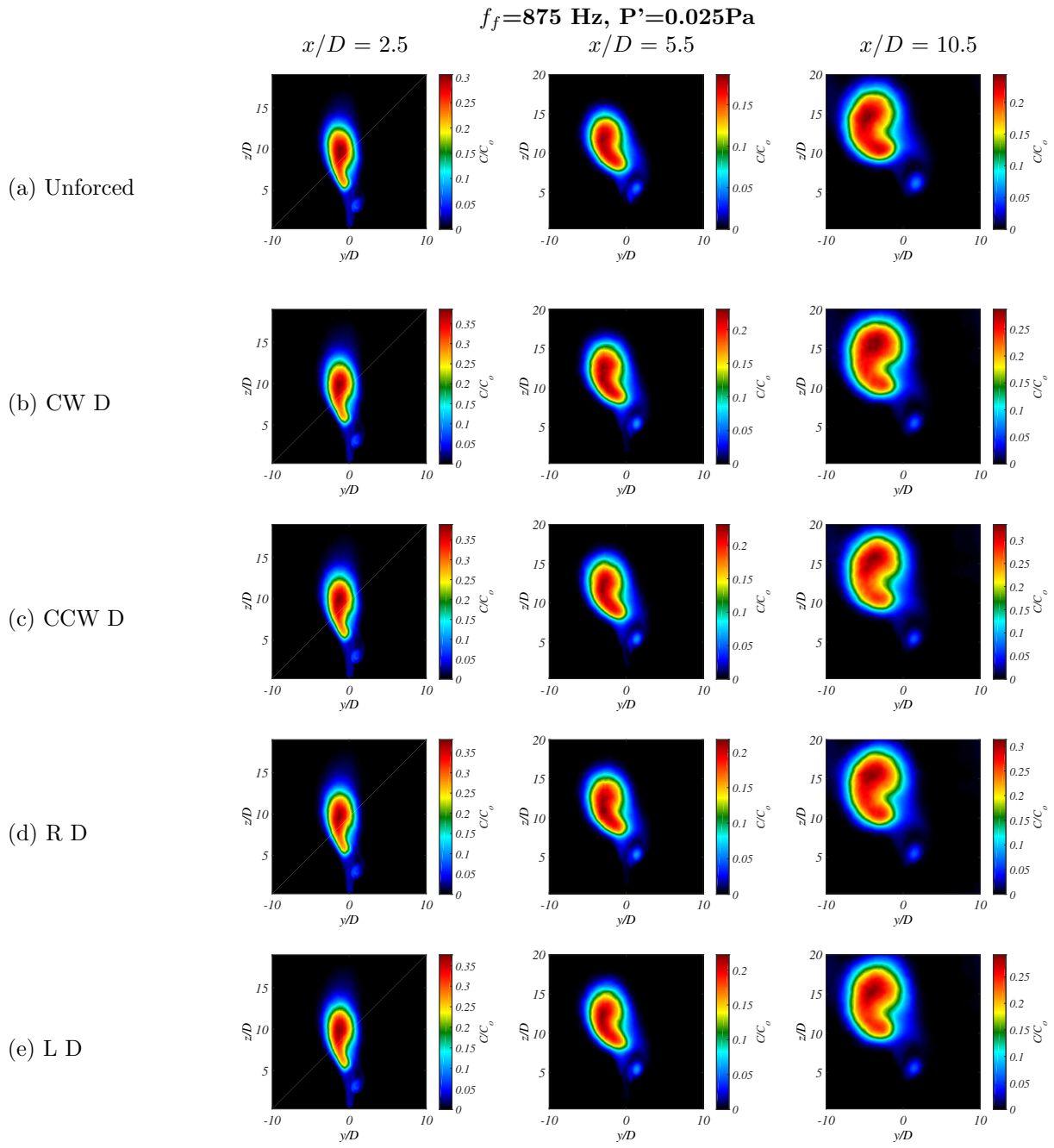

Figure C.41: Mean PLIF images in the cross-sectional y/D-z/D plane for the J=61 JICF with natural frequency in the range of f_o=1600-1900 Hz. f_f=875 H, pressure perturbation P'=0.025 Pa, and downstream speaker operational orientation as shown.

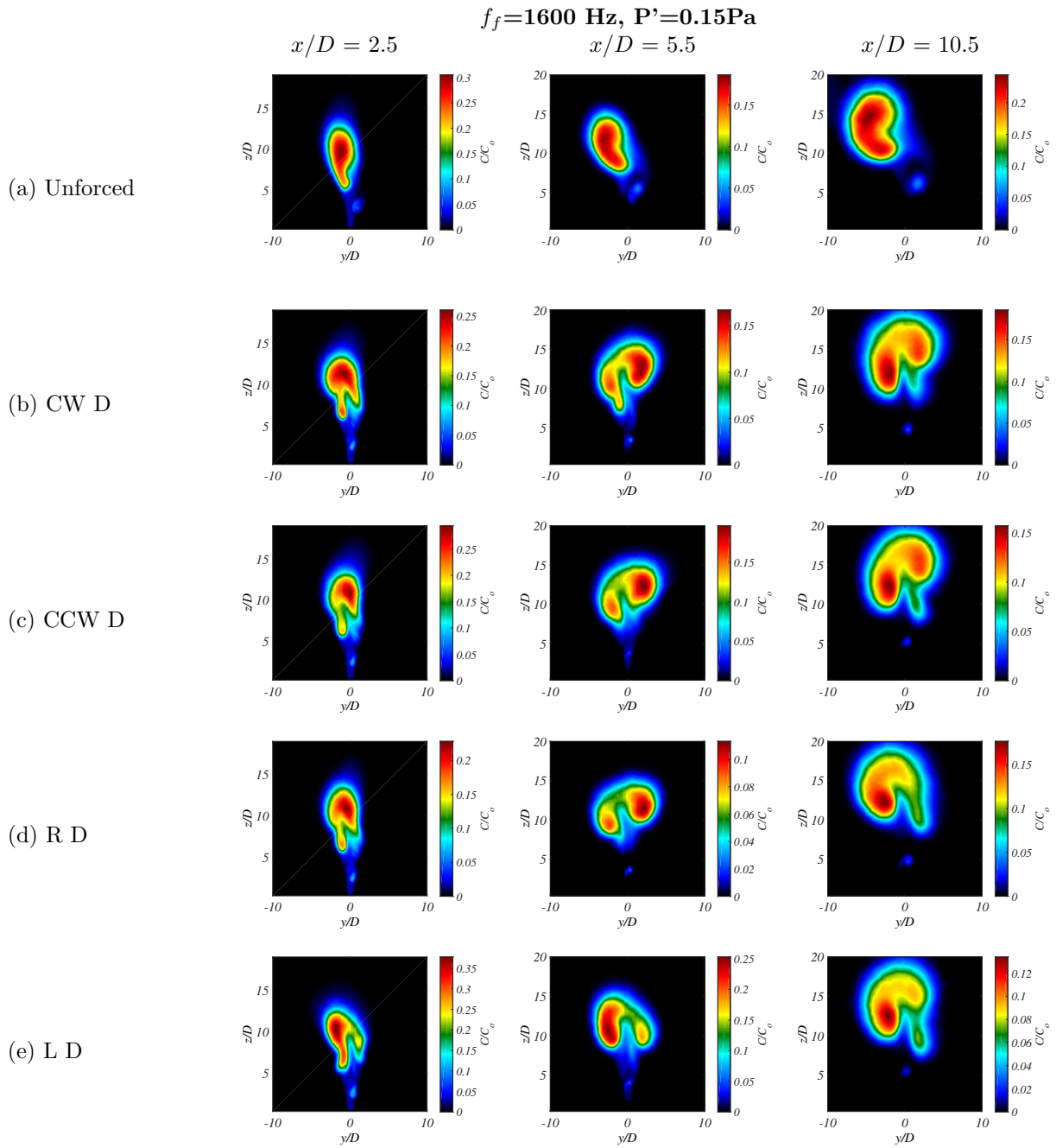

Figure C.42: Mean PLIF images in the cross-sectional y/D-z/D plane for the J=61 JICF with natural frequency in the range of f_o=1600-1900 Hz. f_f=1600 Hz for P'=0.15 Pa downstream speaker operational orientation as shown.

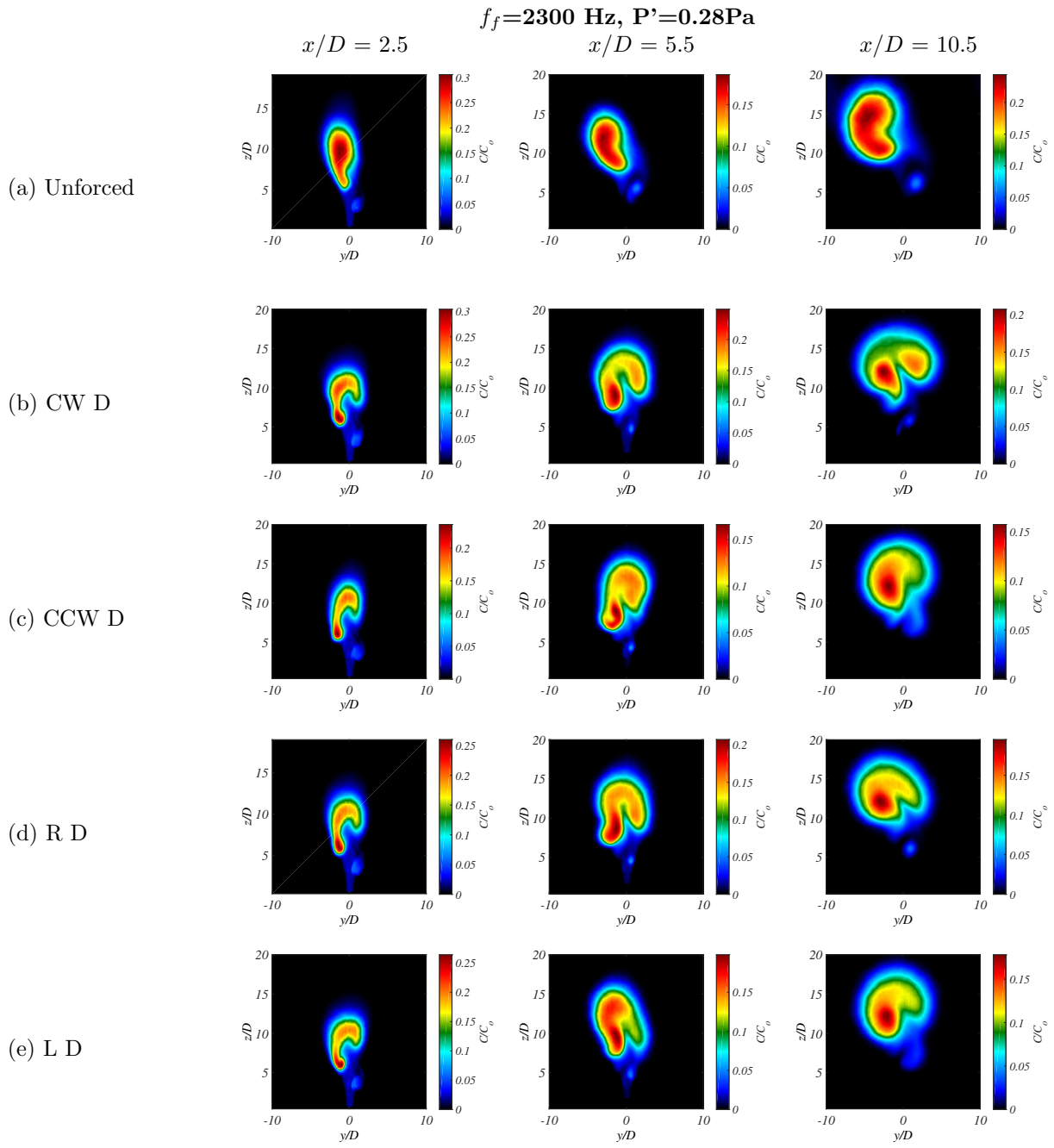

Figure C.43: Mean PLIF images in the cross-sectional y/D-z/D plane for the J=61 JICF with natural frequency in the range of f_o=1600-1900 Hz. f_f=2300 Hz, pressure perturbation P'=0.28 Pa, downstream speaker operation.

APPENDIX D

Asymmetric External Forcing Mixing Quantification

The following section provides additional results associated with the study of asymmetric external forcing effects on mixing of the transverse jet in Chapter 5.

D.1 Centerplane Based Unmixedness, 4-Speaker Study

This section represents centerplane based Unmixedness for the JICF subject to external asymmetric sinusoidal forcing, not shown in Chapter 5.

(a) $f_f = 875$ Hz

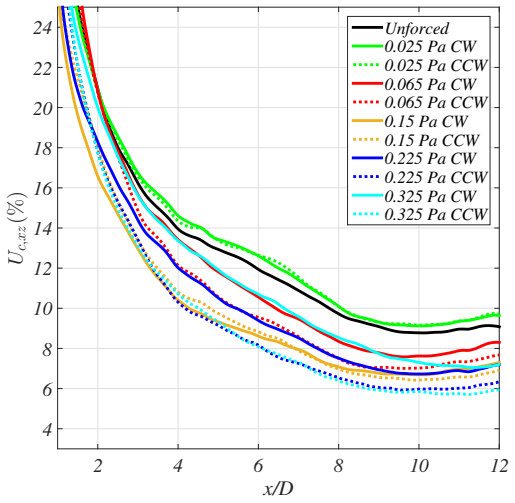

(b) $f_f = 1000$ Hz

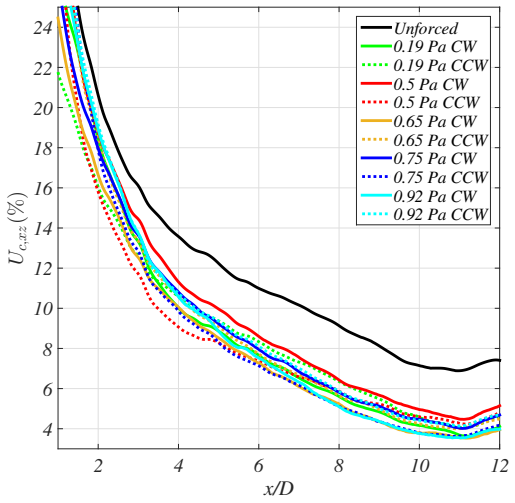

(c) $f_f = 1600$ Hz

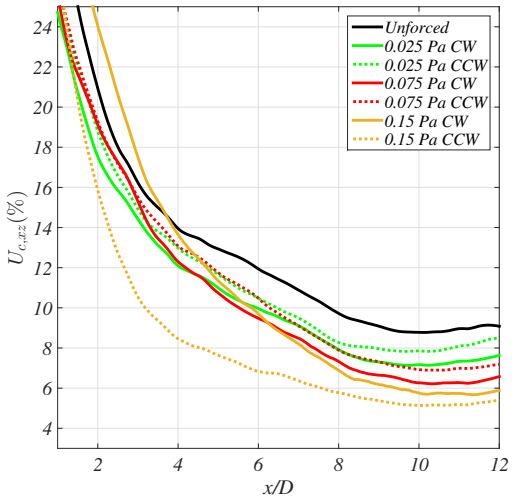

(d) $f_f = 1750$ Hz

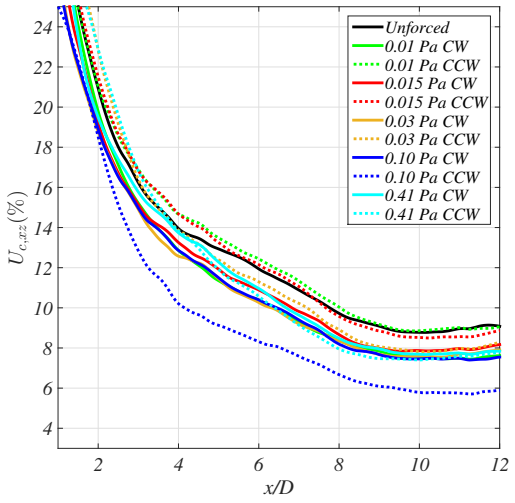

Figure D.1: Centerplane based mean Unmixedness in the $x-z$ plane, with clockwise and counter-clockwise excitation at (a) $f_f = 875$ Hz, (b) $f_f = 1000$ Hz, (c) $f_f = 1600$ Hz, and (d) $f_f = 1750$ Hz for $J = 61$.

(a) $f_f = 1900$ Hz

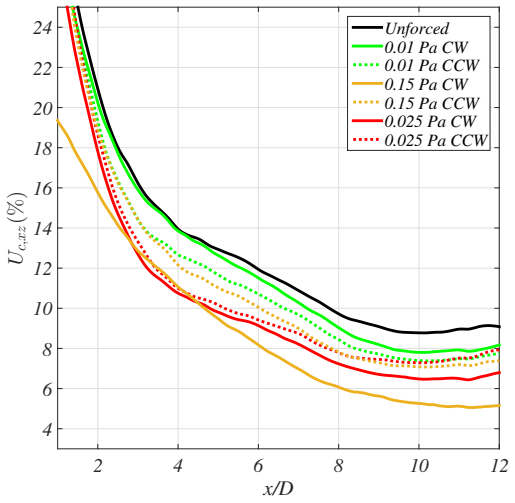

(b) $f_f = 2300$ Hz

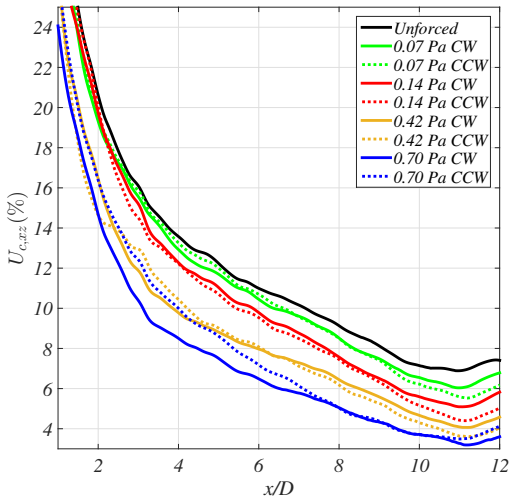

(c) $f_f = 2600$ Hz

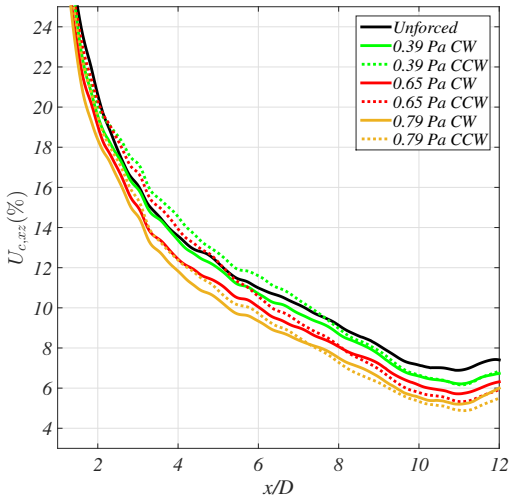

(d) $f_f = 2900$ Hz and 3500 Hz

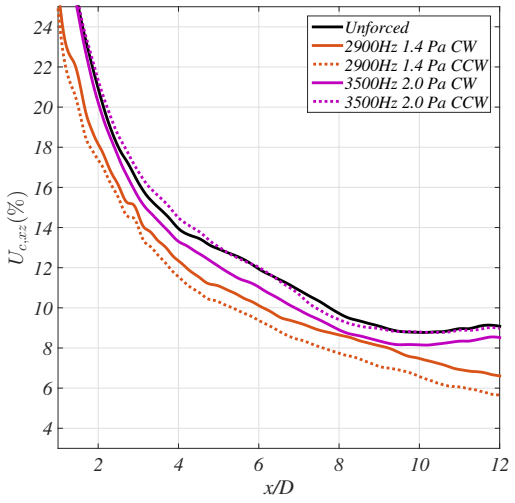

Figure D.2: Centerplane based mean Unmixedness in the $x-z$ plane, with clockwise and counter-clockwise excitation at (a) $f_f = 1900$ Hz, (b) $f_f = 2300$ Hz, (c) $f_f = 2600$ Hz, and (d) $f_f = 2900$ Hz and 3500 Hz for $J = 61$.

D.2 Cross-Sectional Based Unmixedness, 4-Speaker Study

This section represents cross-sectional based Unmixedness for the JICF subject to external asymmetric sinusoidal forcing, not shown in Chapter 5.

(a) $f_f = 875$ Hz

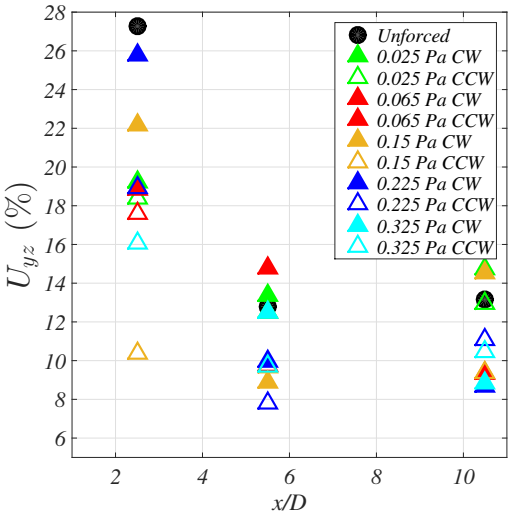

(b) $f_f = 1000$ Hz

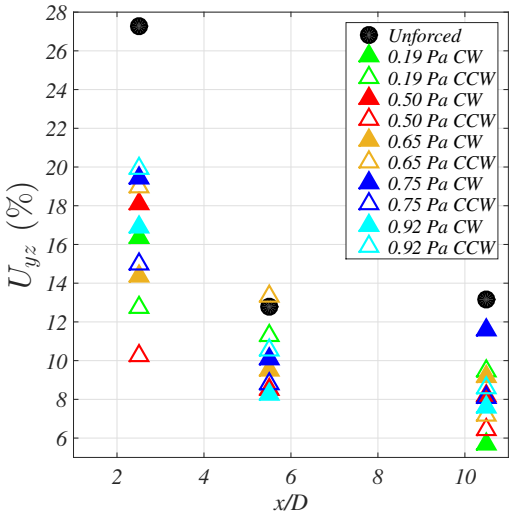

(c) $f_f = 1600$ Hz

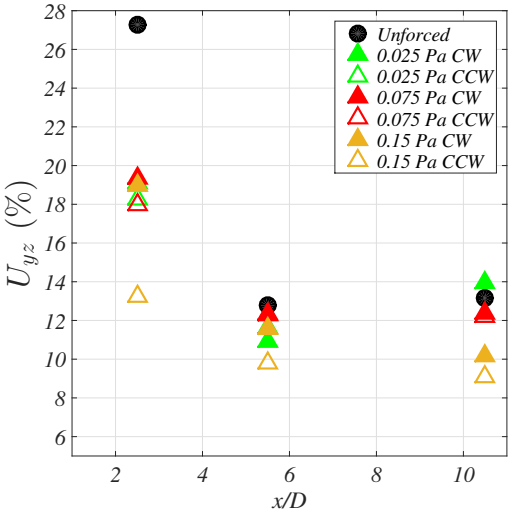

(d) $f_f = 1750$ Hz

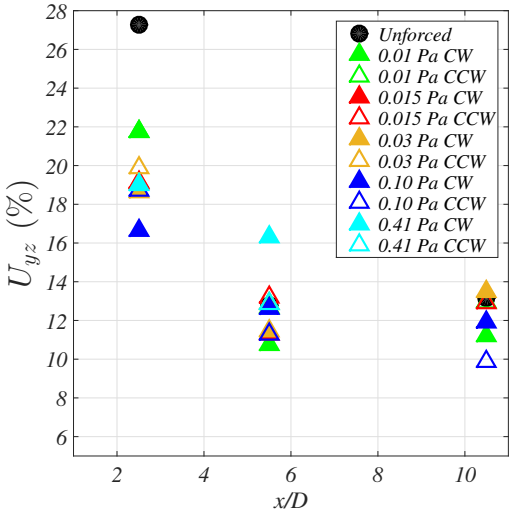

Figure D.3: Clockwise and counterclockwise cross-section based mean Unmixedness in terms of $y-z$ plane, with clockwise and counterclockwise excitation at (a) $f_f = 875$ Hz, (b) $f_f = 1000$ Hz, (c) $f_f = 1600$ Hz, and (d) $f_f = 1750$ Hz for $J = 61$.

(a) $f_f = 1900$ Hz

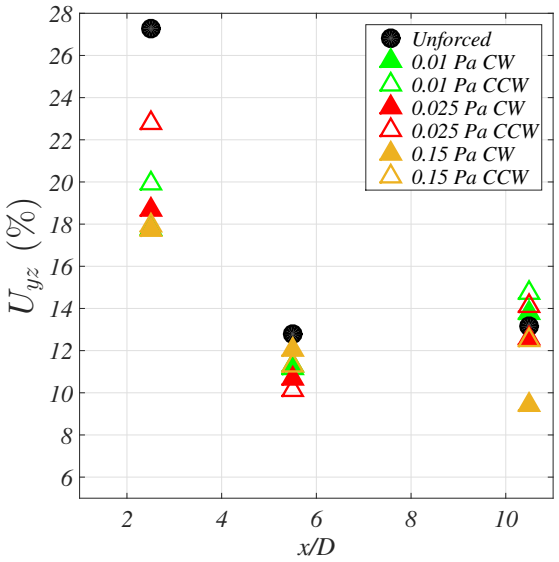

(b) $f_f = 2300$ Hz

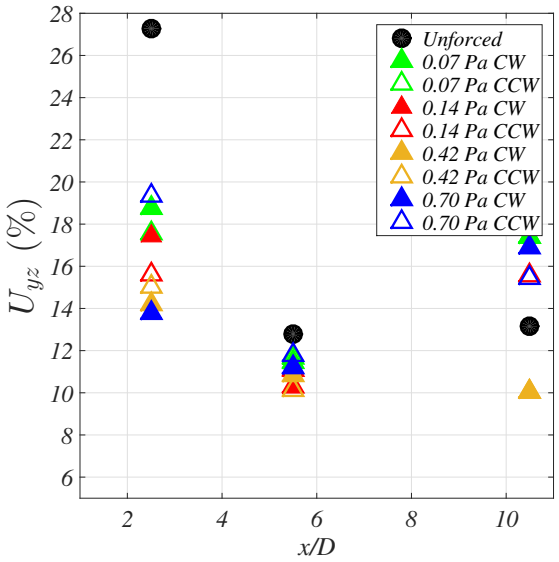

(c) $f_f = 2600$ Hz

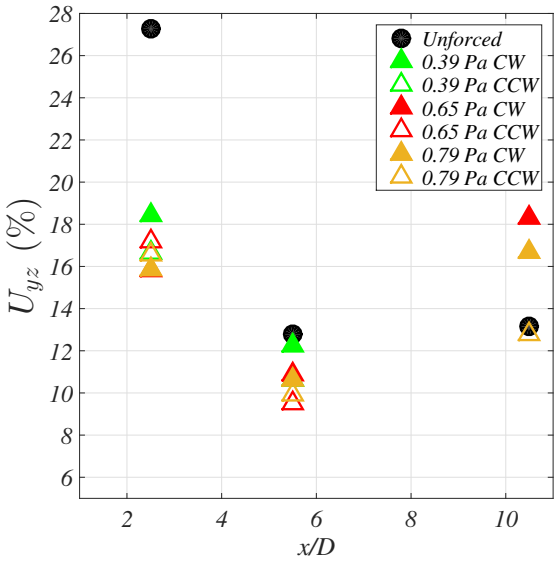

(d) $f_f = 2900$ Hz and 3500 Hz

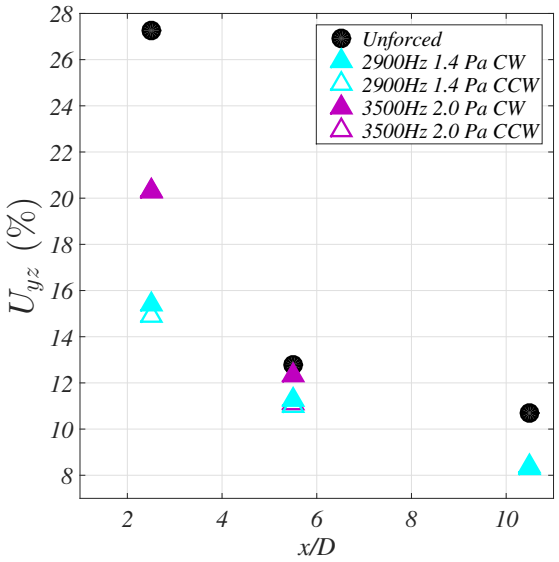

Figure D.4: Clockwise and counterclockwise cross-section based mean Unmixedness in terms of $y-z$ plane, with clockwise and counterclockwise excitation at (a) $f_f = 1900$ Hz, (b) $f_f = 2300$ Hz, (c) $f_f = 2600$ Hz, and (d) $f_f = 2900$ Hz and 3500 Hz for $J = 61$.

D.3 Centerplane Based Unmixedness, 2-Speaker and 1-Speaker Study

This section represents centerplane based Unmixedness for the JICF subject to external asymmetric sinusoidal forcing, not shown in Chapter 5.

(a) f_f = 1750 Hz, P'= 0.10 Pa

(b) f_f = 2900 Hz, P'= 1.4 Pa

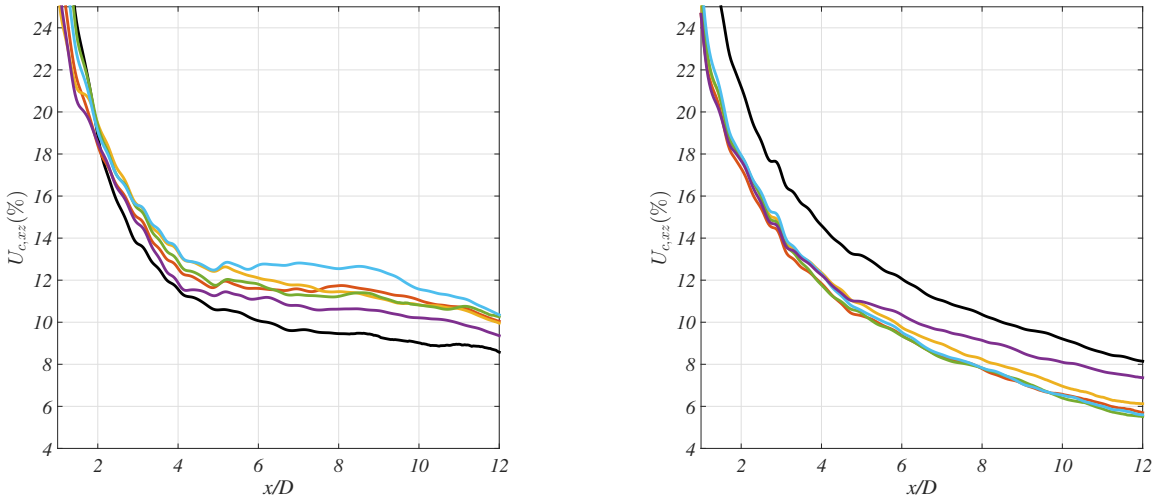

(c) f_f = 3500 Hz, P'= 1.4 Pa

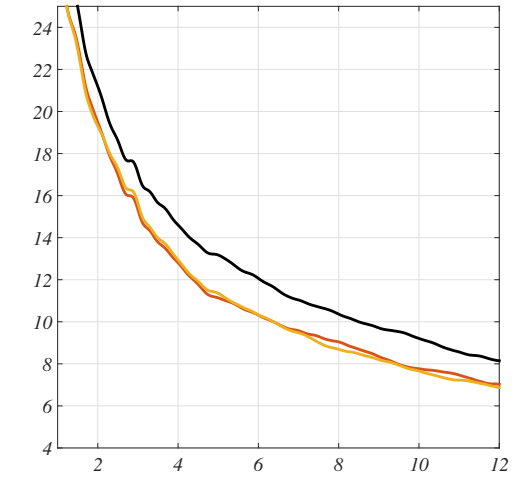

Figure D.5: Centerplane based mean Unmixedness in the $x-z$ plane, with upstream excitation at (a) f_f = 1750 Hz, (b) f_f = 2900 Hz, and (c) f_f = 3500 Hz for $J = 61$.

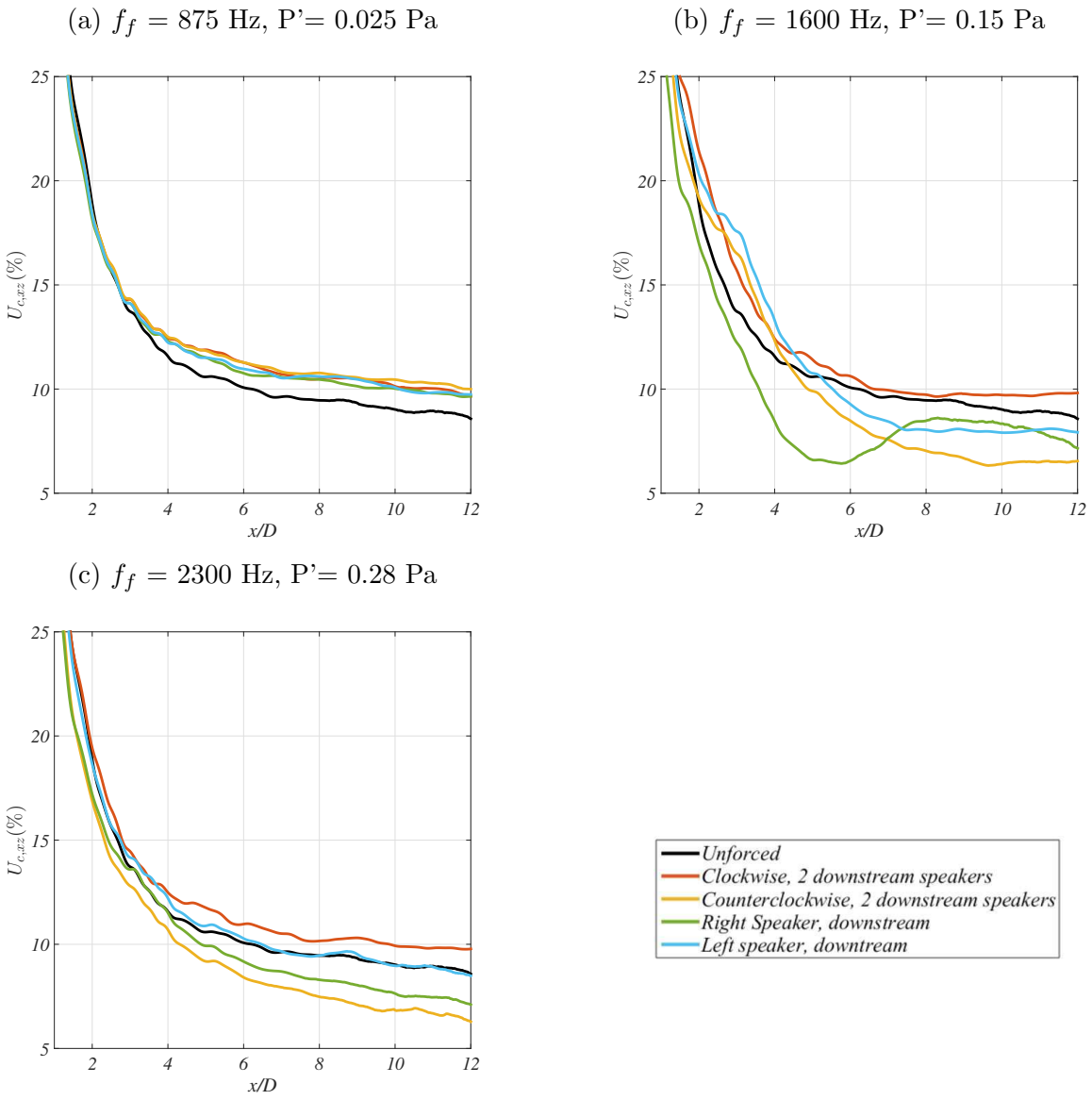

Figure D.6: Centerplane based mean Unmixedness in the $x-z$ plane, with downstream excitation at (a) f_f = 875 Hz, (b) f_f = 1600 Hz, and (c) f_f = 2300 Hz for $J = 61$.

D.4 Cross-Sectional Based Unmixedness, 2-Speaker and 1-Speaker Study

This section represents cross-sectional based Unmixedness for the JICF subject to external asymmetric sinusoidal forcing, not shown in Chapter 5.

(a) f_f = 1750 Hz, P'= 0.10 Pa

(b) f_f = 2900 Hz, P'= 1.4 Pa

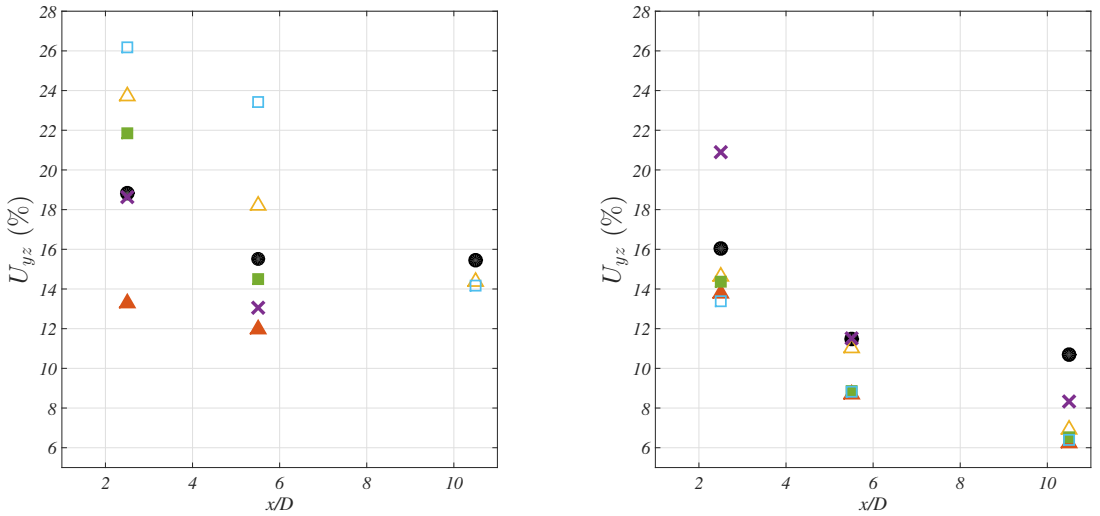

(c) f_f = 3500 Hz, P'= 1.4 Pa

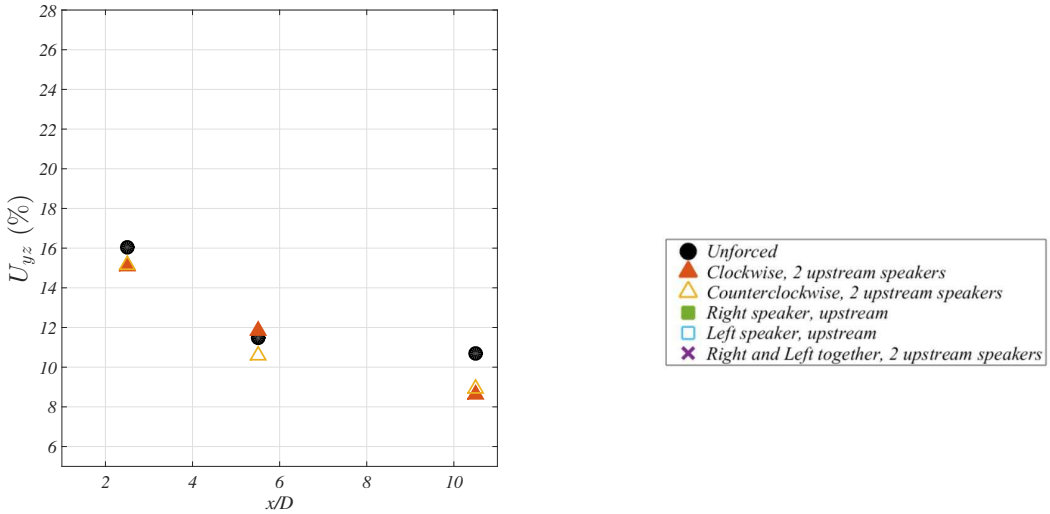

Figure D.7: Cross-section based mean Unmixedness in terms of $y-z$ plane, with upstream excitation at (a) f_f = 1750 Hz, (b) f_f = 2900 Hz, and (d) f_f = 3500 Hz for $J = 61$.

(a) f_f = 875 Hz, P'= 0.025 Pa

(b) f_f = 1600 Hz, P'= 0.15 Pa

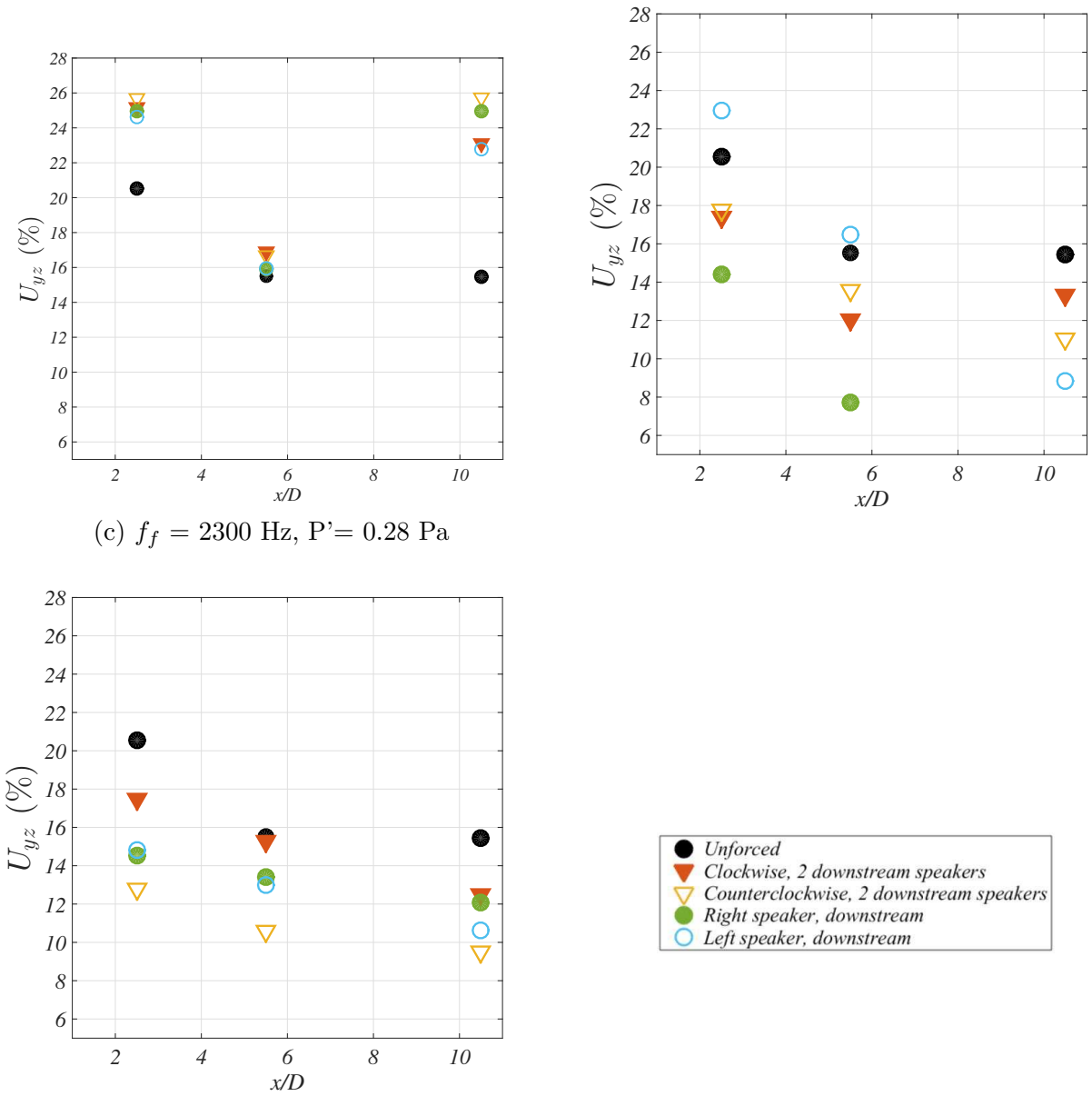

(c) f_f = 2300 Hz, P'= 0.28 Pa

Figure D.8: Cross-section based mean Unmixedness in terms of $y-z$ plane, with downstream excitation at (a) f_f = 875 Hz, (b) f_f = 1600 Hz, and (d) f_f = 2300 Hz for J = 61.

D.5 POD Analysis, 4 Speaker Study

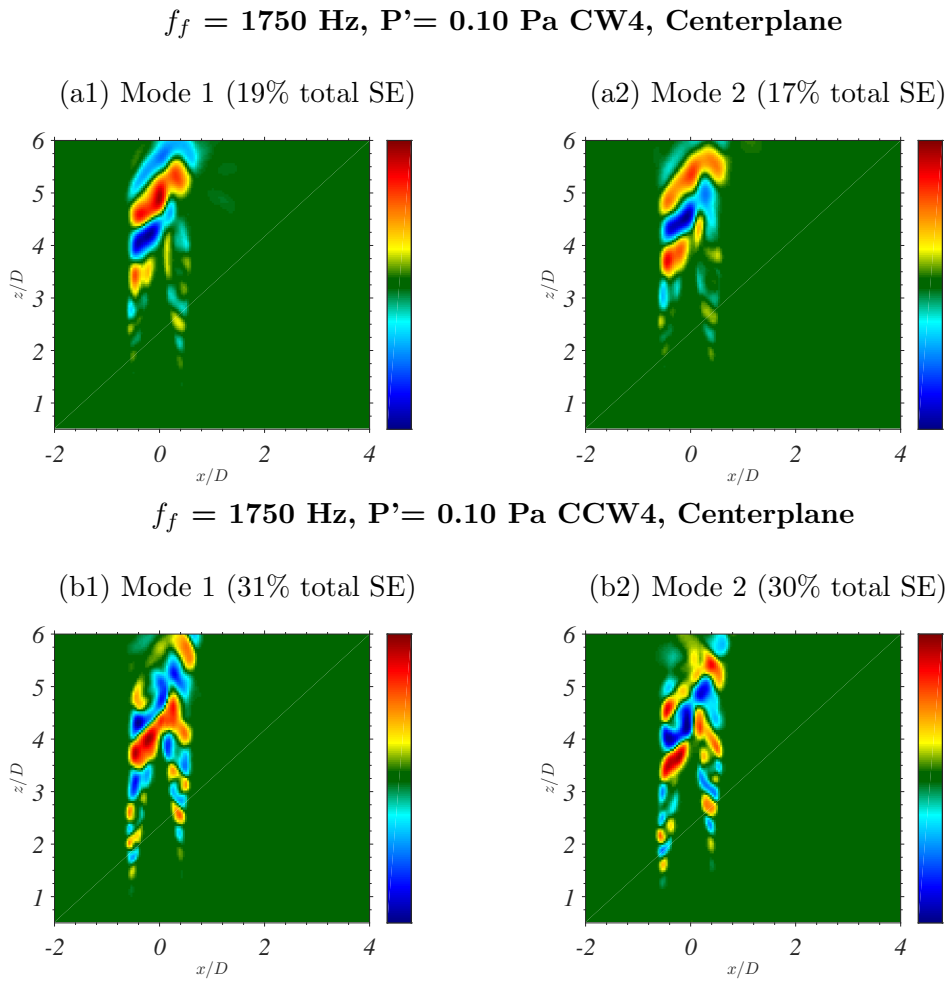

Figure D.9: PLIF POD mode structures from instantaneous centerplane images of the $J = 61$ JICF subject to external asymmetric forcing at $f_f = 1750$ Hz with amplitude P'= 0.10 Pa with (a) clockwise and (b) counterclockwise 4 speaker operation strategy. Percentage of total scalar fluctuation energy (SE) by each mode is indicated.

x/D **= 2.5**

f_f **= 1000 Hz, P'= 0.65 Pa CW**

(a1) Mode 1 (11% total SE) (a2) Mode 2 (6% total SE)

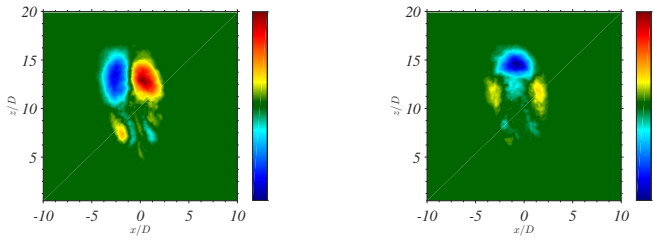

f_f **= 1000 Hz, P'= 0.65 Pa CCW4**

(b1) Mode 1 (13% total SE) (b2) Mode 2 (6% total SE)

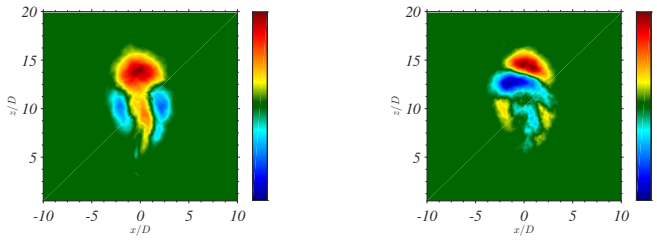

f_f **= 1600 Hz, P'= 0.075 Pa CW4**

(c1) Mode 1 (12% total SE) (c2) Mode 2 (6% total SE)

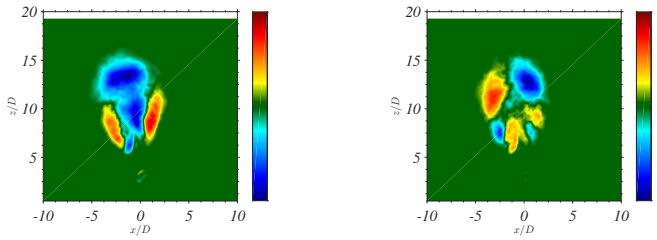

f_f **= 1600 Hz, P'= 0.075 Pa CCW4**

(d1) Mode 1 (10% total SE) (d2) Mode 2 (7% total SE)

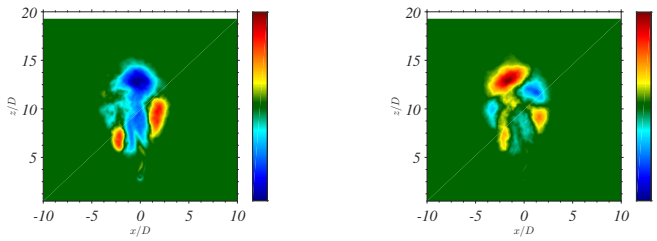

Figure D.10: PLIF POD mode structures from instantaneous cross-sectional view images at x/D = 2.5, of the $J = 61$ JICF (a,b) subject to external asymmetric forcing with all 4 speakers at f_f = 1000 Hz with amplitude P'= 0.65 Pa, and (c,d) asymmetric forcing at $f_f = 1600$ Hz with amplitude P'= 0.075 Pa. Percentage of total scalar fluctuation energy (SE) by each mode is indicated.

x/D **= 2.5**

f_f **= 1600 Hz, P'= 0.15 Pa CW4**

(a1) Mode 1 (20% total SE) (a2) Mode 2 (6% total SE)

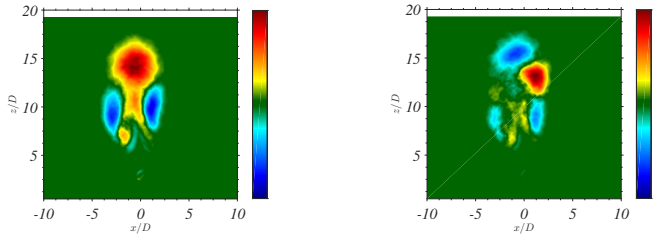

f_f **= 1600 Hz, P'= 0.15 Pa CCW4**

(b1) Mode 1 (7% total SE) (b2) Mode 2 (4% total SE)

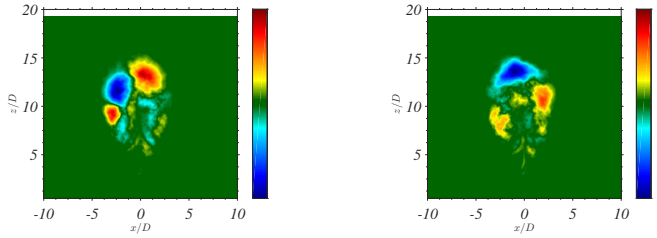

f_f **= 1900 Hz, P'= 0.15 Pa CW4**

(c1) Mode 1 (9% total SE) (c2) Mode 2 (5% total SE)

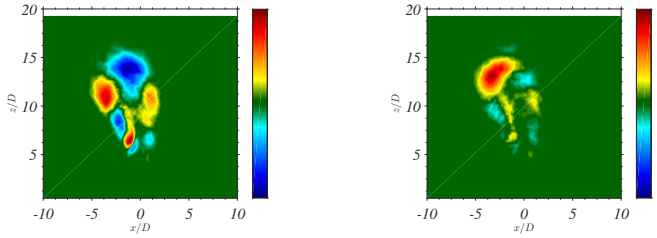

f_f **= 1900 Hz, P'= 0.15 Pa CCW4**

(d1) Mode 1 (11% total SE) (d2) Mode 2 (7% total SE)

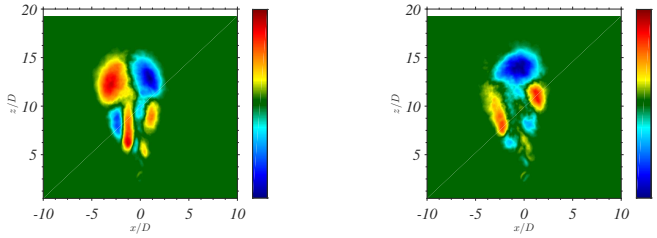

Figure D.11: PLIF POD mode structures from instantaneous cross-sectional view images at x/D = 2.5, of the $J = 61$ JICF (a,b) subject to external asymmetric forcing with all 4 speakers at f_f = 1600 Hz with amplitude P'= 0.15 Pa, and (c,d) asymmetric forcing at $f_f = 1900$ Hz with amplitude P'= 0.15 Pa. Percentage of total scalar fluctuation energy (SE) by each mode is indicated.

x/D **= 2.5**

f_f **= 1750 Hz, P'= 0.10 Pa CW4**

(a1) Mode 1 (8% total SE) (a2) Mode 2 (5% total SE)

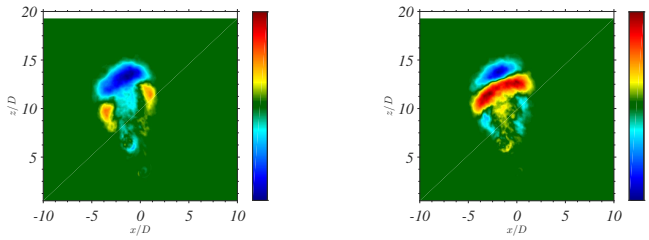

f_f **= 1750 Hz, P'= 0.10 Pa CCW4**

(b1) Mode 1 (6% total SE) (b2) Mode 2 (5% total SE)

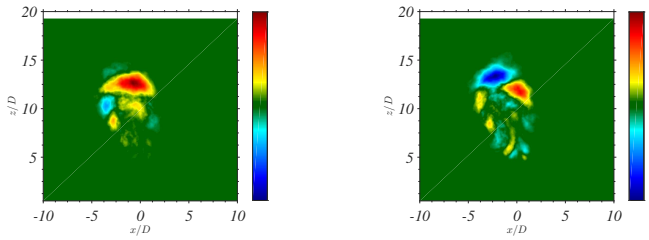

f_f **= 2300 Hz, P'= 0.42 Pa CW4**

(c1) Mode 1 (6% total SE) (c2) Mode 2 (4% total SE)

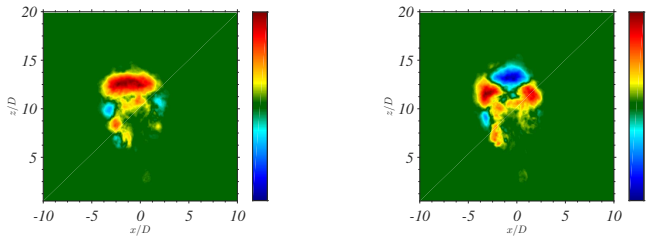

f_f **= 2300 Hz, P'= 0.42 Pa CCW4**

(d1) Mode 1 (7% total SE) (d2) Mode 2 (5% total SE)

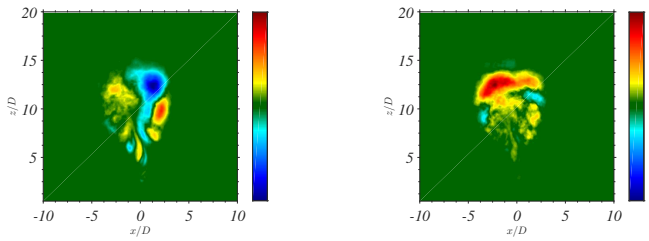

Figure D.12: PLIF POD mode structures from instantaneous cross-sectional view images at x/D = 2.5, of the $J = 61$ JICF (a,b) subject to external asymmetric forcing with all 4 speakers at f_f = 1750 Hz with amplitude P'= 0.10 Pa, and (c,d) asymmetric forcing at $f_f = 2300$ Hz with amplitude P'= 0.42 Pa. Percentage of total scalar fluctuation energy (SE) by each mode is indicated.

x/D **= 5.5**

f_f **= 875 Hz, P'= 0.225 Pa CW4**

(a1) Mode 1 (22% total SE) (a2) Mode 2 (6% total SE)

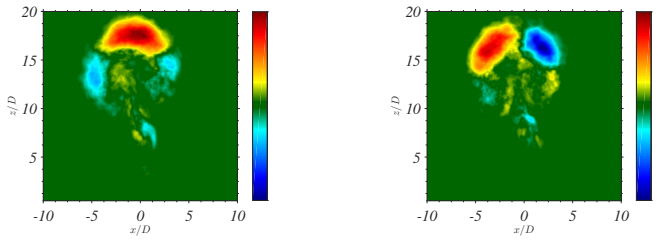

f_f **= 875 Hz, P'= 0.225 Pa CCW4**

(b1) Mode 1 (7% total SE) (b2) Mode 2 (6% total SE)

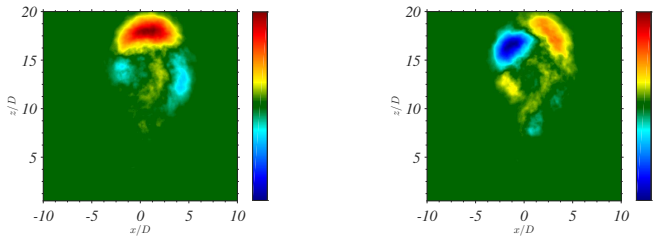

f_f **= 1900 Hz, P'= 0.15 Pa CW4**

(c1) Mode 1 (8% total SE) (c2) Mode 2 (6% total SE)

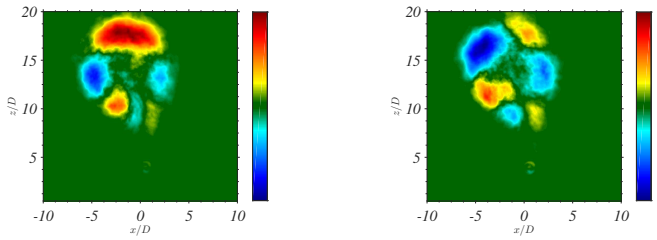

f_f **= 1900 Hz, P'= 0.15 Pa CCW4**

(d1) Mode 1 (10% total SE) (d2) Mode 2 (8% total SE)

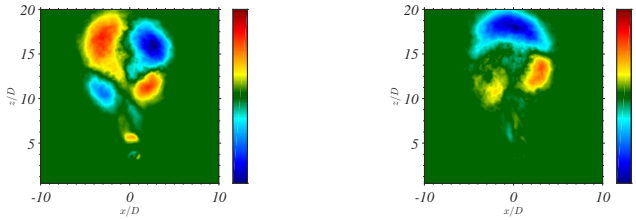

Figure D.13: PLIF POD mode structures from instantaneous cross-sectional view images at x/D = 5.5, of the $J = 61$ JICF (a,b) subject to external asymmetric forcing with all 4 speakers at f_f = 875 Hz with amplitude P'= 0.225 Pa, and (c,d) asymmetric forcing at $f_f = 1900$ Hz with amplitude P'= 0.15 Pa. Percentage of total scalar fluctuation energy (SE) by each mode is indicated.

x/D **= 5.5**

f_f **= 1000 Hz, P'= 0.65 Pa CW4**

(a1) Mode 1 (14% total SE) (a2) Mode 2 (2% total SE)

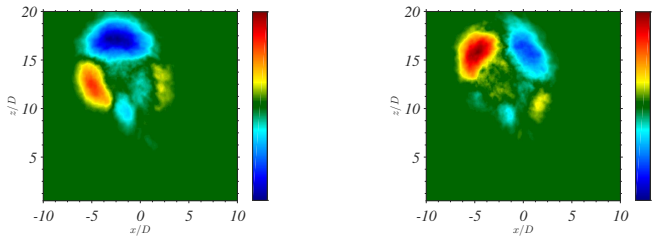

f_f **= 1000 Hz, P'= 0.65 Pa CCW4**

(b1) Mode 1 (7% total SE) (b2) Mode 2 (5% total SE)

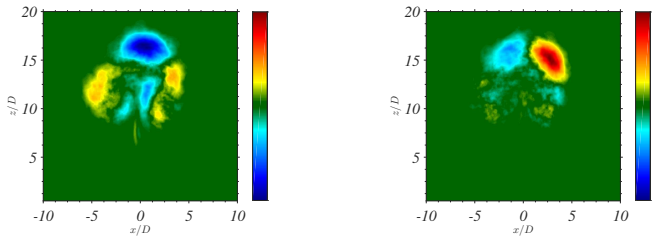

f_f **= 1600 Hz, P'= 0.075 Pa CW4**

(c1) Mode 1 (8% total SE) (c2) Mode 2 (5% total SE)

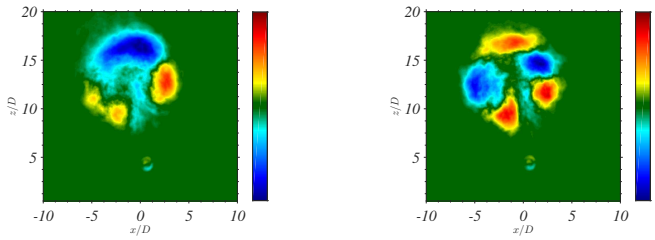

f_f **= 1600 Hz, P'= 0.075 Pa CCW4**

(d1) Mode 1 (7% total SE) (d2) Mode 2 (6% total SE)

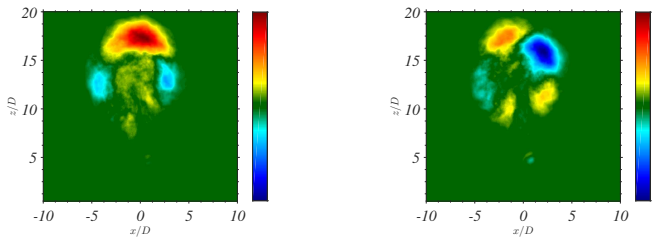

Figure D.14: PLIF POD mode structures from instantaneous cross-sectional view images at x/D = 5.5, of the $J = 61$ JICF (a,b) subject to external asymmetric forcing with all 4 speakers at f_f = 1000 Hz with amplitude P'= 0.65 Pa, and (c,d) asymmetric forcing at $f_f = 1600$ Hz with amplitude P'= 0.075 Pa. Percentage of total scalar fluctuation energy (SE) by each mode is indicated.

x/D **= 5.5**

f_f **= 1750 Hz, P'= 0.10 Pa CW4**

(a1) Mode 1 (6% total SE) (a2) Mode 2 (2% total SE)

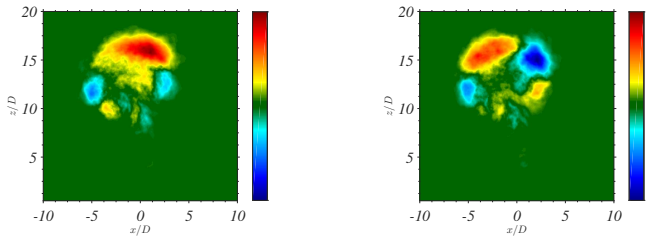

f_f **= 1750 Hz, P'= 0.10 Pa CCW4**

(b1) Mode 1 (7% total SE) (b2) Mode 2 (2% total SE)

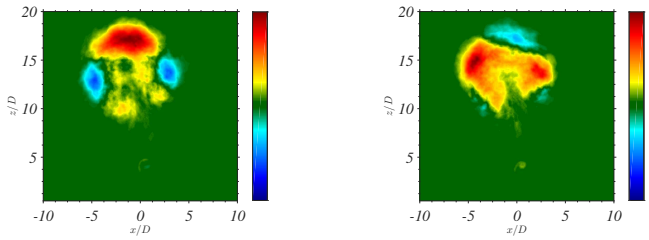

f_f **= 2300 Hz, P'= 0.42 Pa CW4**

(c1) Mode 1 (6% total SE) (c2) Mode 2 (5% total SE)

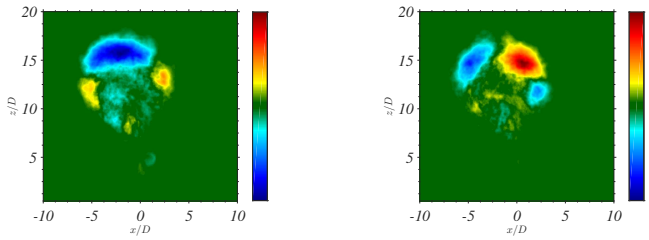

f_f **= 2300 Hz, P'= 0.42 Pa CCW4**

(d1) Mode 1 (5% total SE) (d2) Mode 2 (4% total SE)

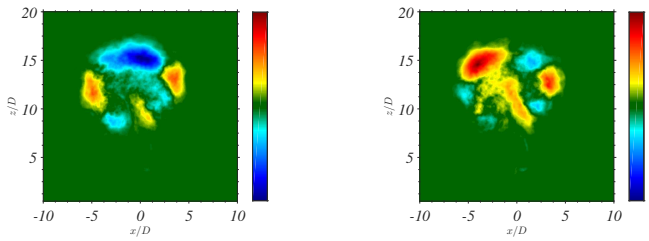

Figure D.15: PLIF POD mode structures from instantaneous cross-sectional view images at x/D = 5.5, of the $J = 61$ JICF (a,b) subject to external asymmetric forcing with all 4 speakers at f_f = 1750 Hz with amplitude P'= 0.10 Pa, and (c,d) asymmetric forcing at $f_f = 2300$ Hz with amplitude P'= 0.42 Pa. Percentage of total scalar fluctuation energy (SE) by each mode is indicated.

x/D **= 10.5**

f_f **= 1000 Hz, P'= 0.65 Pa CW4**

(a1) Mode 1 (16% total SE) (a2) Mode 2 (6% total SE)

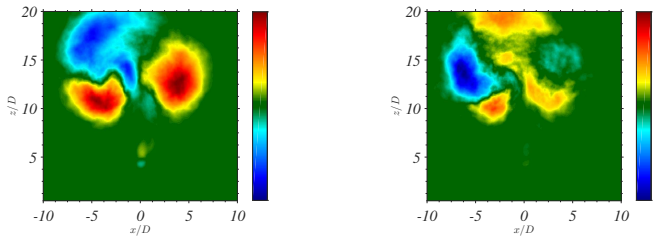

f_f **= 1000 Hz, P'= 0.65 Pa CCW4**

(b1) Mode 1 (10% total SE) (b2) Mode 2 (8% total SE)

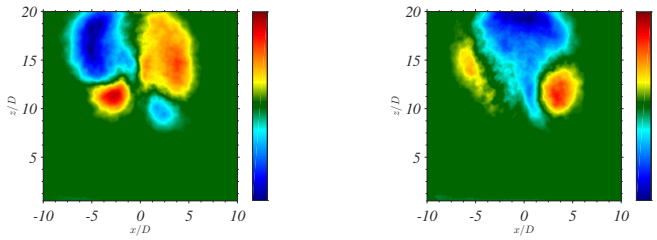

f_f **= 1600 Hz, P'= 0.075 Pa CW4**

(c1) Mode 1 (7% total SE) (c2) Mode 2 (6% total SE)

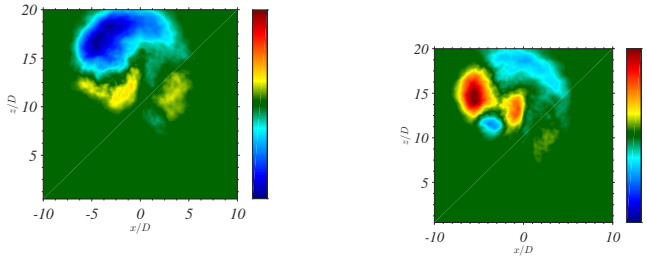

f_f **= 1600 Hz, P'= 0.075 Pa CCW4**

(d1) Mode 1 (7% total SE) (d2) Mode 2 (6% total SE)

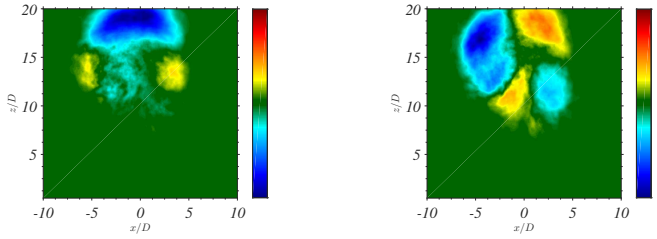

Figure D.16: PLIF POD mode structures from instantaneous cross-sectional view images at x/D = 10.5, of the $J = 61$ JICF (a,b) subject to external asymmetric forcing with all 4 speakers at f_f = 1000 Hz with amplitude P'= 0.65 Pa, and (c,d) asymmetric forcing at $f_f = 1600$ Hz with amplitude P'= 0.075 Pa. Percentage of total scalar fluctuation energy (SE) by each mode is indicated.

x/D **= 10.5**

f_f **= 1600 Hz, P'= 0.15 Pa CW4**

(a1) Mode 1 (8% total SE) (a2) Mode 2 (5% total SE)

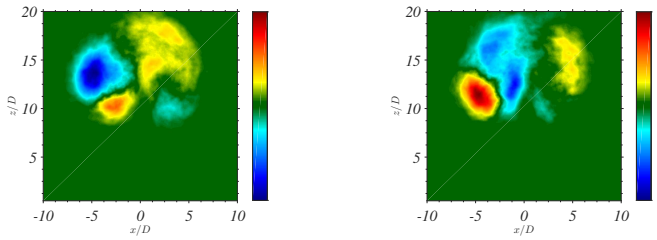

f_f **= 1600 Hz, P'= 0.15 Pa CCW4**

(b1) Mode 1 (15% total SE) (b2) Mode 2 (8% total SE)

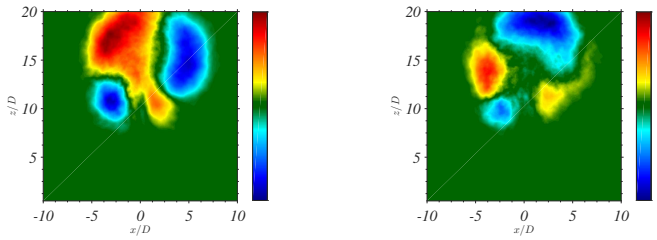

f_f **= 1900 Hz, P'= 0.15 Pa CW4**

(c1) Mode 1 (8% total SE) (c2) Mode 2 (5% total SE)

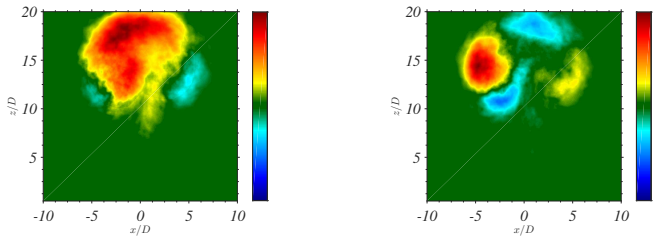

f_f **= 1900 Hz, P'= 0.15 Pa CCW4**

(d1) Mode 1 (14% total SE) (d2) Mode 2 (5% total SE)

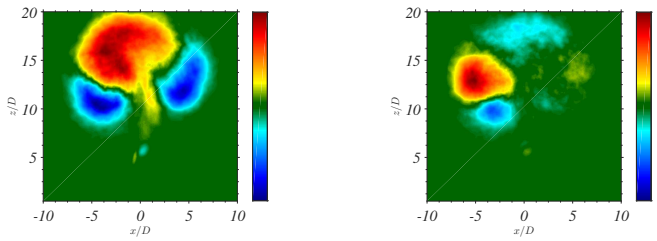

Figure D.17: PLIF POD mode structures from instantaneous cross-sectional view images at x/D = 10.5, of the $J = 61$ JICF (a,b) subject to external asymmetric forcing with all 4 speakers at f_f = 1600 Hz with amplitude P'= 0.15 Pa, and (c,d) asymmetric forcing at $f_f = 1900$ Hz with amplitude P'= 0.15 Pa. Percentage of total scalar fluctuation energy (SE) by each mode is indicated.

x/D **= 10.5**

f_f **= 1750 Hz, P'= 0.10 Pa CW4**

(a1) Mode 1 (9% total SE) (a2) Mode 2 (6% total SE)

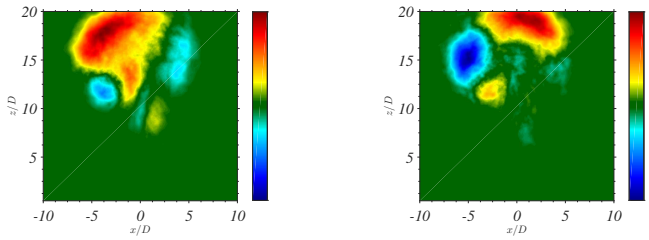

f_f **= 1750 Hz, P'= 0.10 Pa CCW4**

(b1) Mode 1 (8% total SE) (b2) Mode 2 (7% total SE)

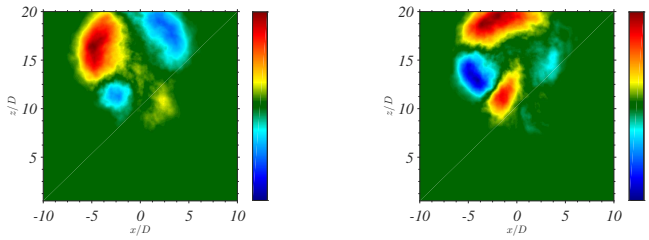

f_f **= 2300 Hz, P'= 0.42 Pa CW4**

(c1) Mode 1 (9% total SE) (c2) Mode 2 (6% total SE)

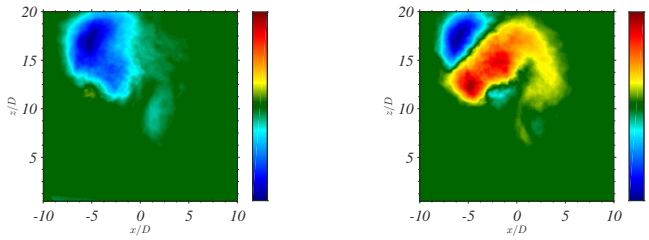

f_f **= 2300 Hz, P'= 0.42 Pa CCW4**

(d1) Mode 1 (7% total SE) (d2) Mode 2 (5% total SE)

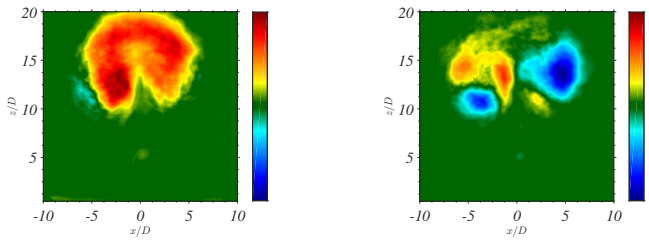

Figure D.18: PLIF POD mode structures from instantaneous cross-sectional view images at x/D = 10.5, of the $J = 61$ JICF (a,b) subject to external asymmetric forcing with all 4 speakers at f_f = 1750 Hz with amplitude P'= 0.10 Pa, and (c,d) asymmetric forcing at $f_f = 2300$ Hz with amplitude P'= 0.42 Pa. Percentage of total scalar fluctuation energy (SE) by each mode is indicated.

D.6 POD Analysis, 2-Speaker and 1-Speaker Study

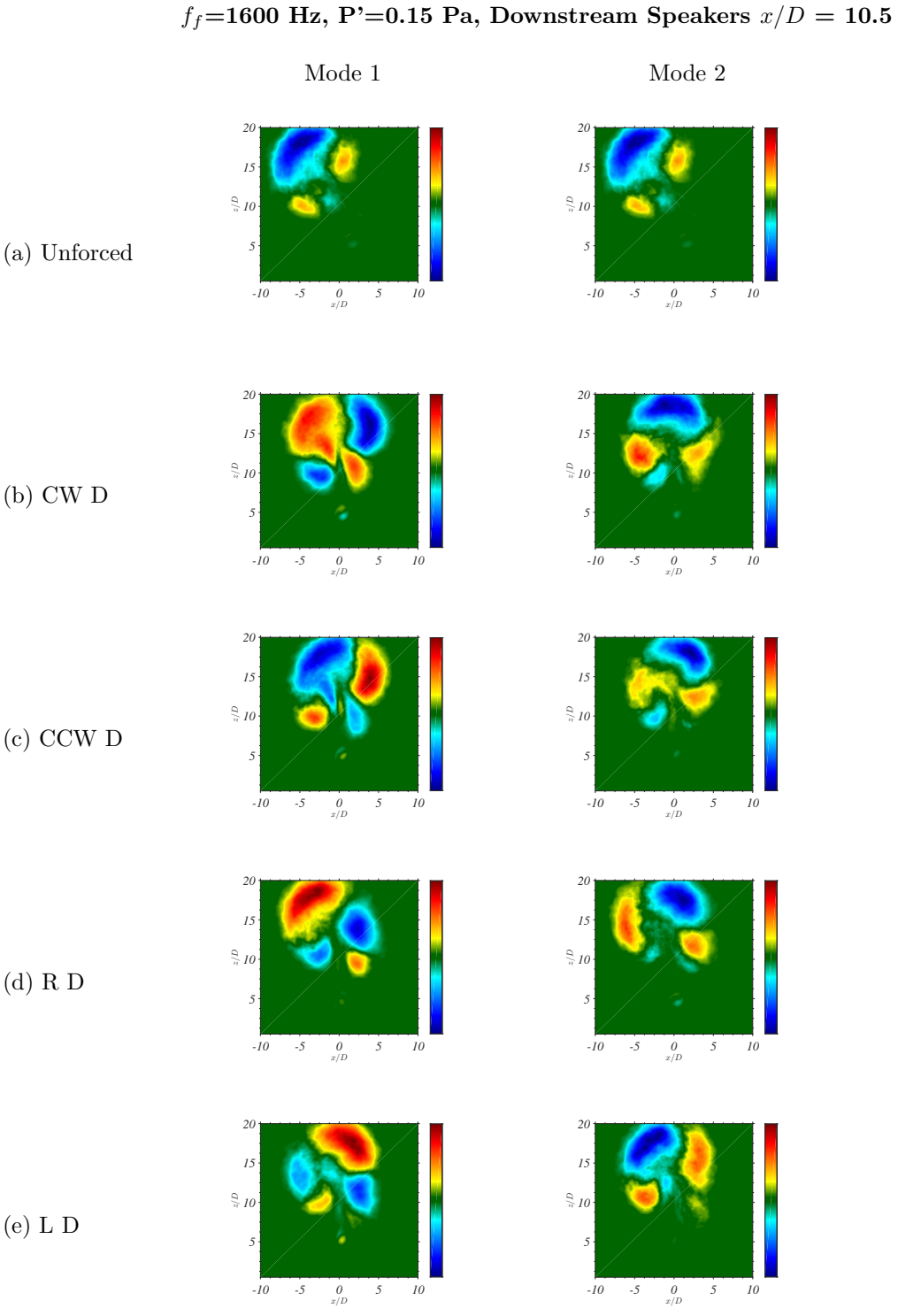

Figure D.19: PLIF POD mode structures from instantaneous cross-sectional view images at x/D = 10.5, of the J = 61 JICF (a) unforced and (b-f) subject to external asymmetric forcing in the jet downstream region at f_f = 1600 Hz with amplitude P'= 0.15 Pa.

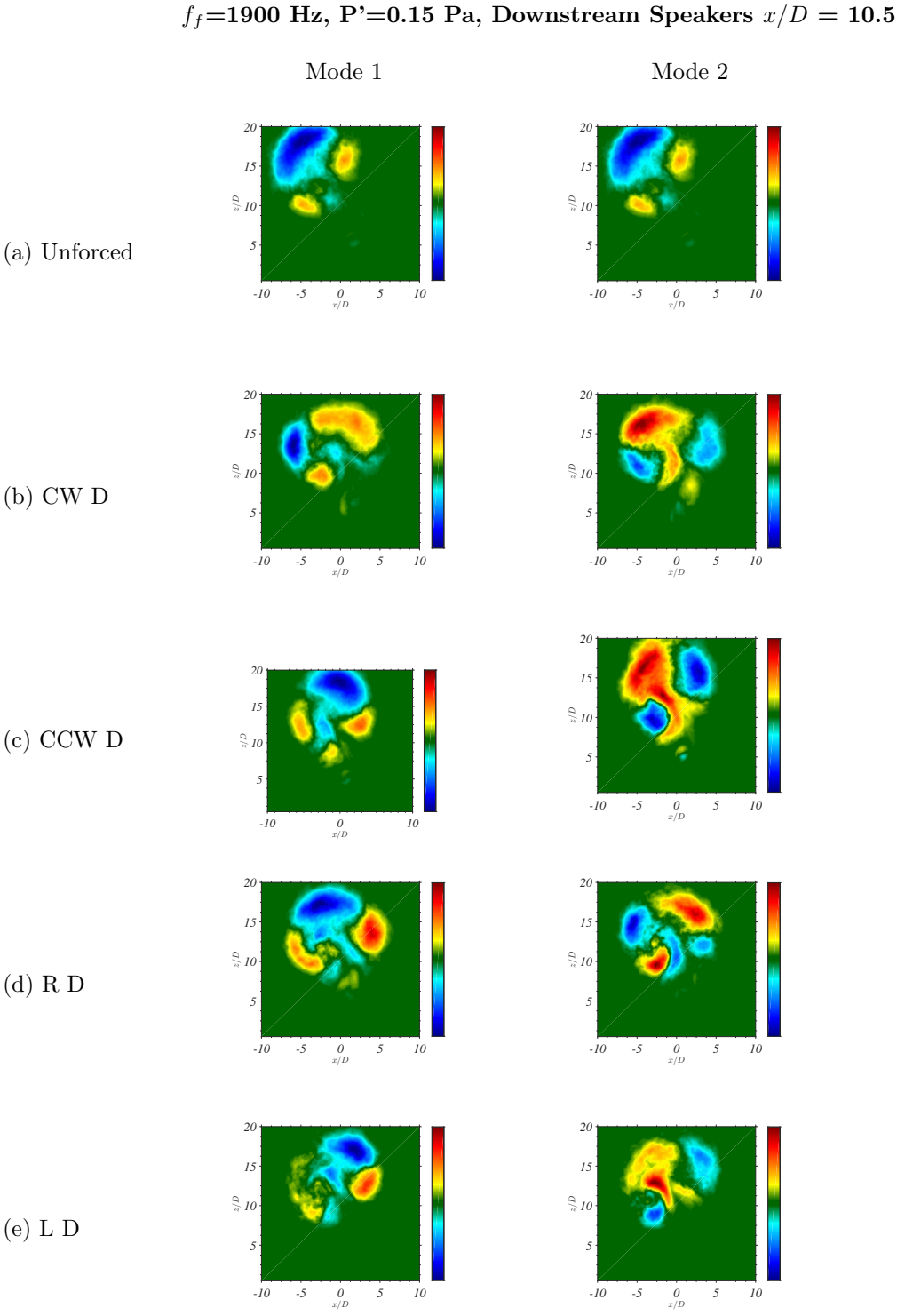

Figure D.20: PLIF POD mode structures from instantaneous cross-sectional view images at x/D = 10.5, of the J = 61 JICF (a) unforced and (b-f) subject to external asymmetric forcing in the jet downstream region at f_f = 1900 Hz with amplitude P'= 0.15 Pa.

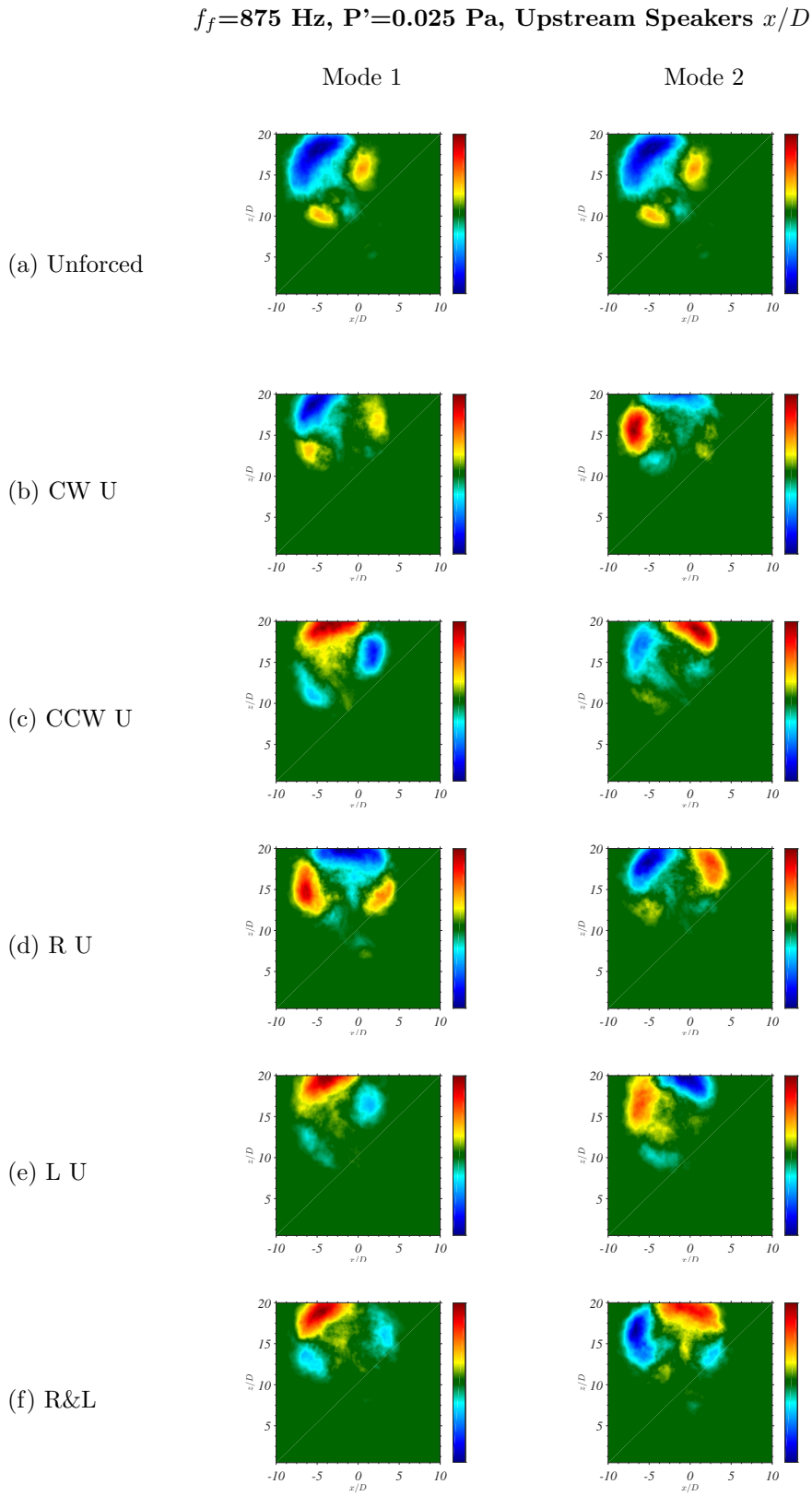

Figure D.21: PLIF POD mode structures from instantaneous cross-sectional view images at x/D = 10.5, of the J = 61 JICF (a) unforced and (b-f) subject to external asymmetric forcing in the jet upstream region at f_f = 875 Hz with amplitude P'= 0.025 Pa.

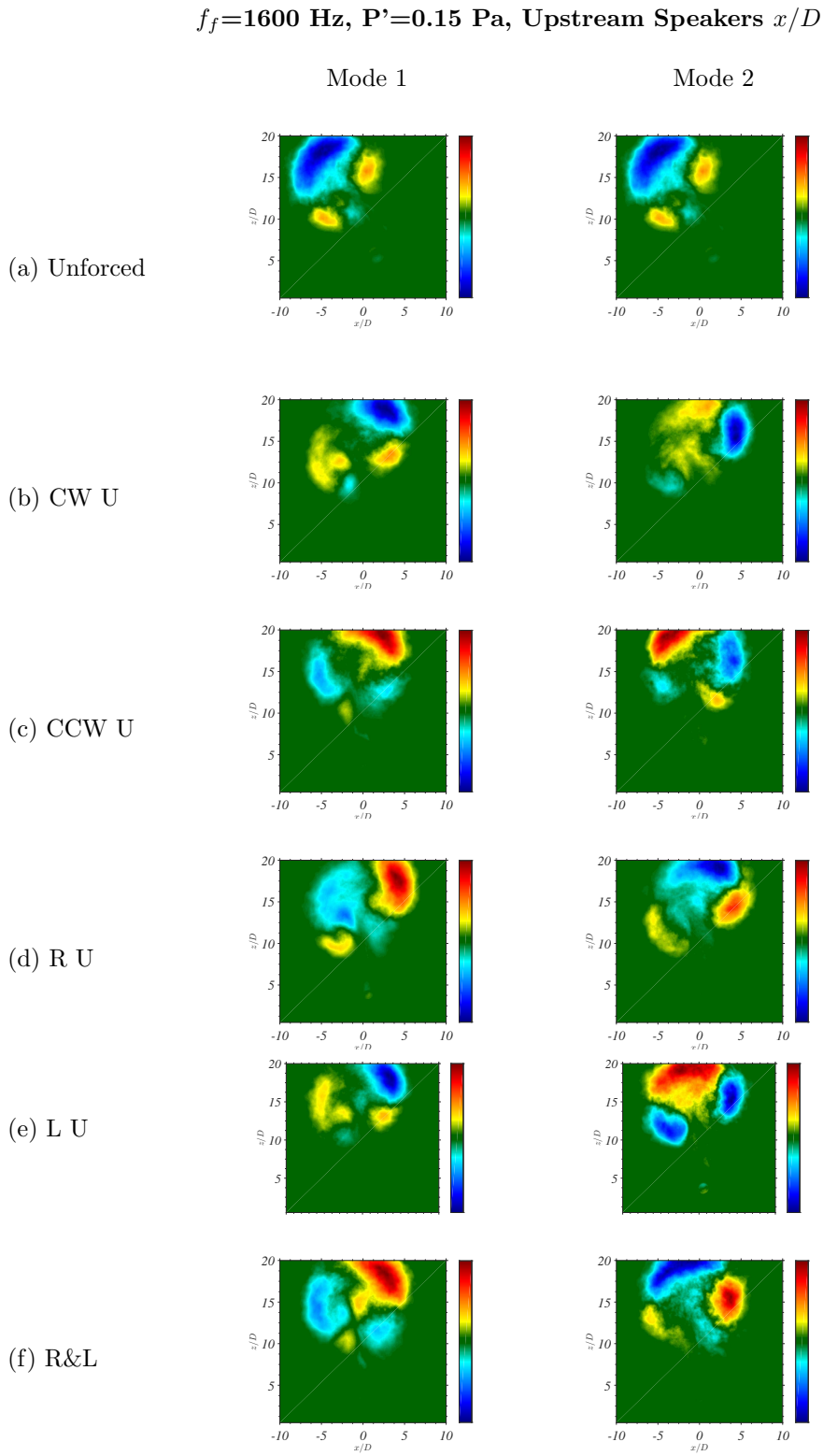

Figure D.22: PLIF POD mode structures from instantaneous cross-sectional view images at x/D = 10.5, of the $J = 61$ JICF (a) unforced and (b-f) subject to external asymmetric forcing in the jet upstream region at $f_f = 1600$ Hz with amplitude P'= 0.15 Pa.

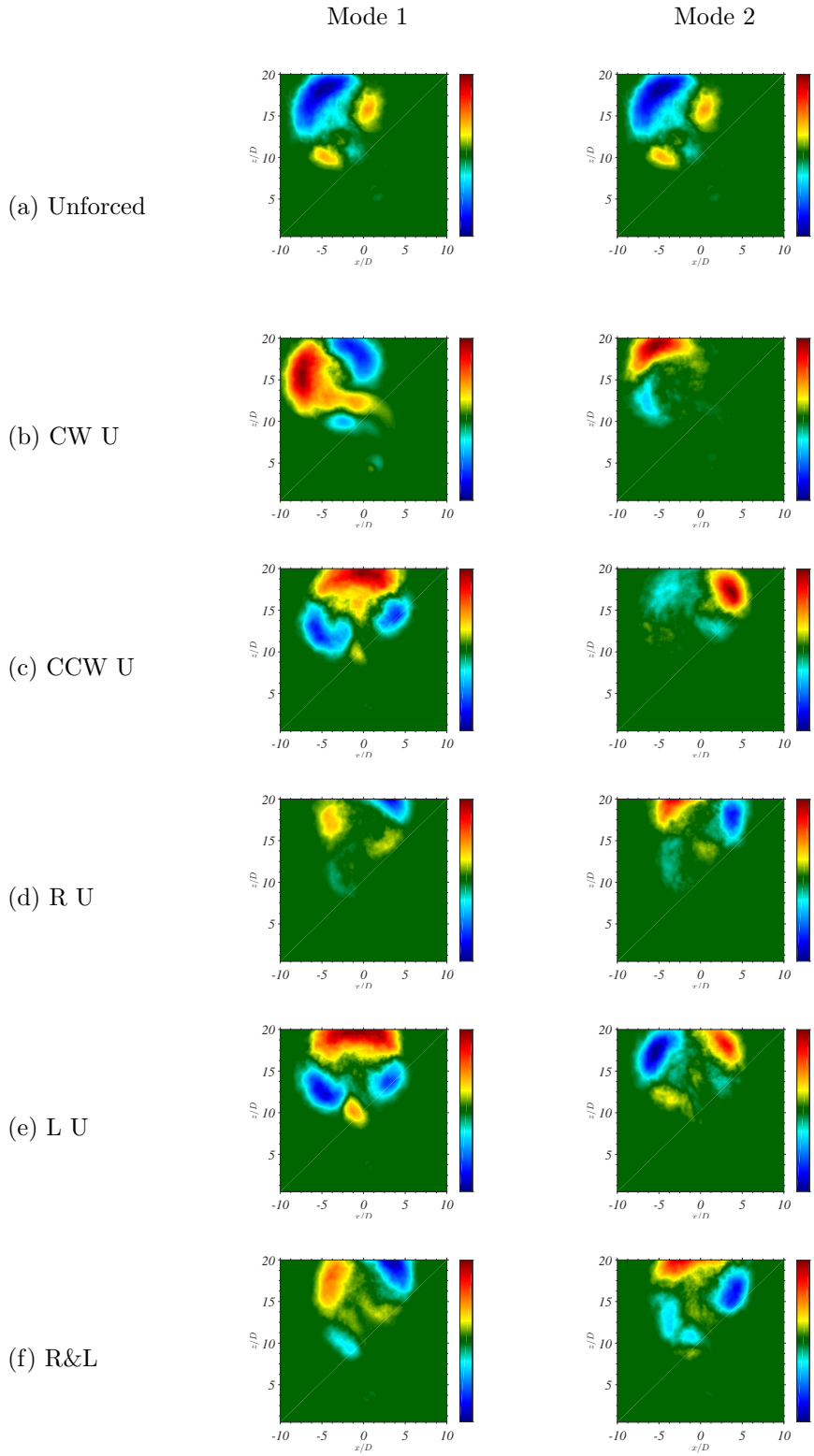

Figure D.23: PLIF POD mode structures from instantaneous cross-sectional view images at x/D = 10.5, of the J = 61 JICF (a) unforced and (b-f) subject to external asymmetric forcing in the jet upstream region at f_f = 1750 Hz with amplitude P'= 0.10 Pa.

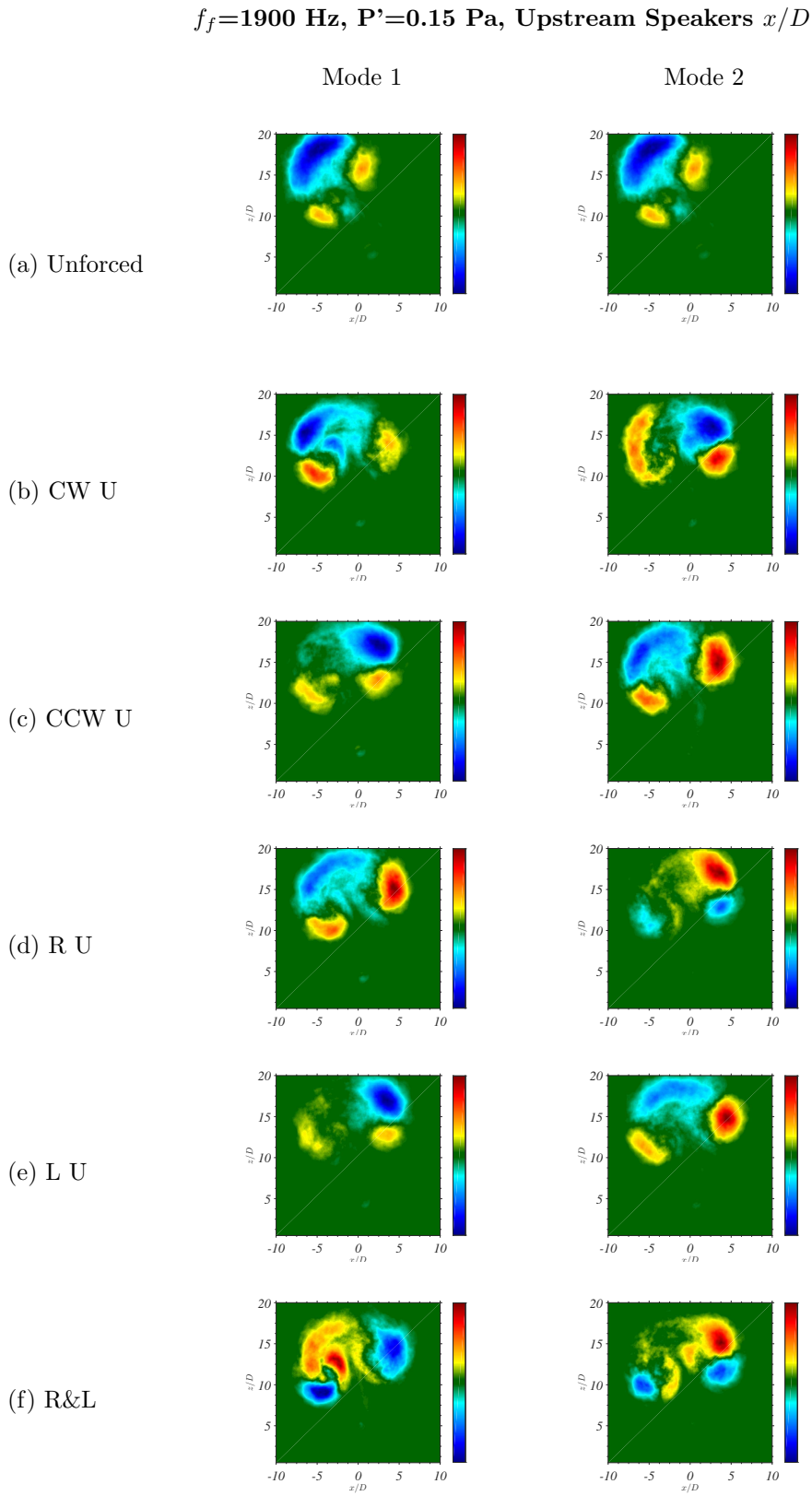

Figure D.24: PLIF POD mode structures from instantaneous cross-sectional view images at x/D = 10.5, of the J = 61 JICF (a) unforced and (b-f) subject to external asymmetric forcing in the jet upstream region at f_f = 1900 Hz with amplitude P'= 0.15 Pa.

D.7 POD Mode Coefficient Phase Space Plots

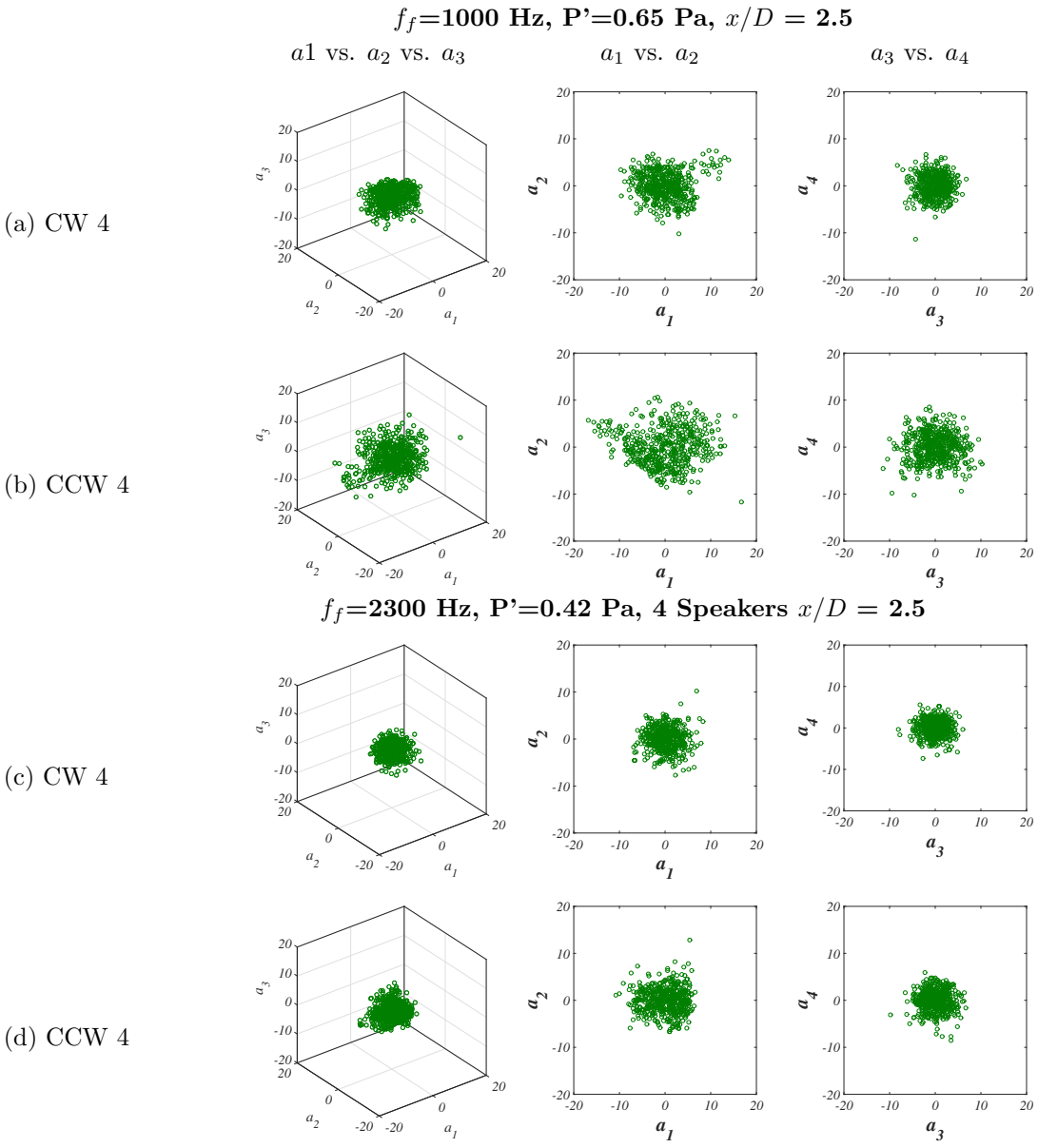

Figure D.25: PLIF POD coefficients for the first 4 modes plotted against each other, extracted from instantaneous $x/D = 2.5$ cross-sectional view images of the $J = 61$ JICF, subject to (a,b) $f_f = 1000$ Hz, and (c,d) $f_f = 2300$ Hz CW and CCW forcing. Black symbols represent the unforced condition, green colored symbols represent 1:1 lock-in of the USL, and green colored symbols represent 1:1 lock-in of the USL.

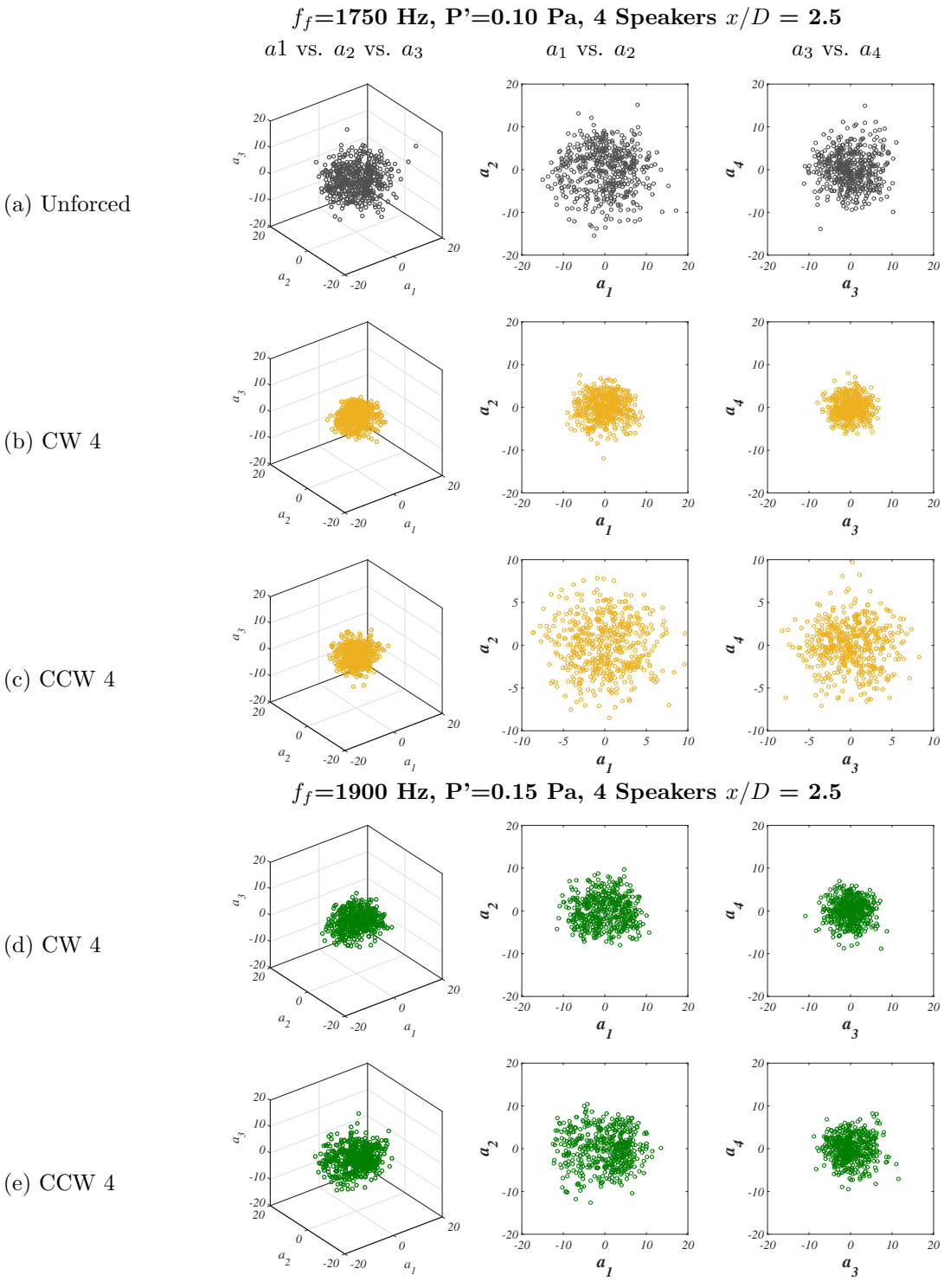

Figure D.26: PLIF POD coefficients for the first 4 modes plotted against each other, extracted from instantaneous $x/D = 2.5$ cross-sectional view images of the $J = 61$ JICF, (a) unforced, (b-c) subject to $f_f = 1750$ Hz, and (d-e) $f_f = 1900$ Hz CW and CCW forcing. Black symbols represent the unforced condition, green colored symbols represent 1:1 lock-in of the USL, and yellow symbols indicate the nature of the USL response spectra cannot be inferred from direct measurements.

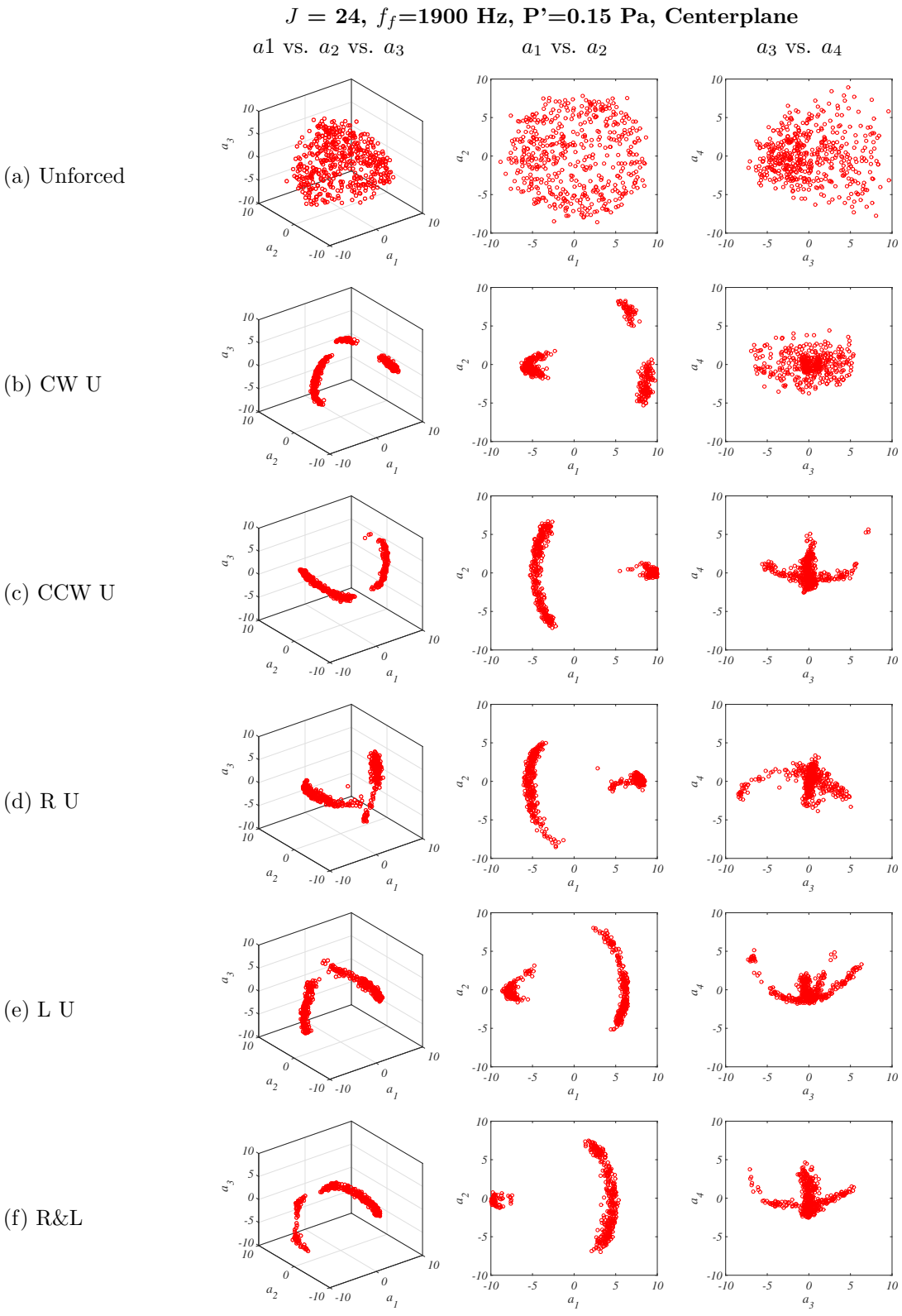

Figure D.27: PLIF POD coefficients for the first 4 modes plotted against each other, extracted from instantaneous centerplane images of the $J = 24$ JICF subject to $f_f = 1900$ Hz upstream forcing.

APPENDIX E

Simultaneous PLIF/PIV with Asymmetric Forcing

The following section provides additional results associated with the study of asymmetric external forcing effects on the simultaneous scalar and velocity fields of the $J = 41$ transverse jet in Chapter 6.

E.1 Scalar and Vorticity Fields, 4-Speaker Study

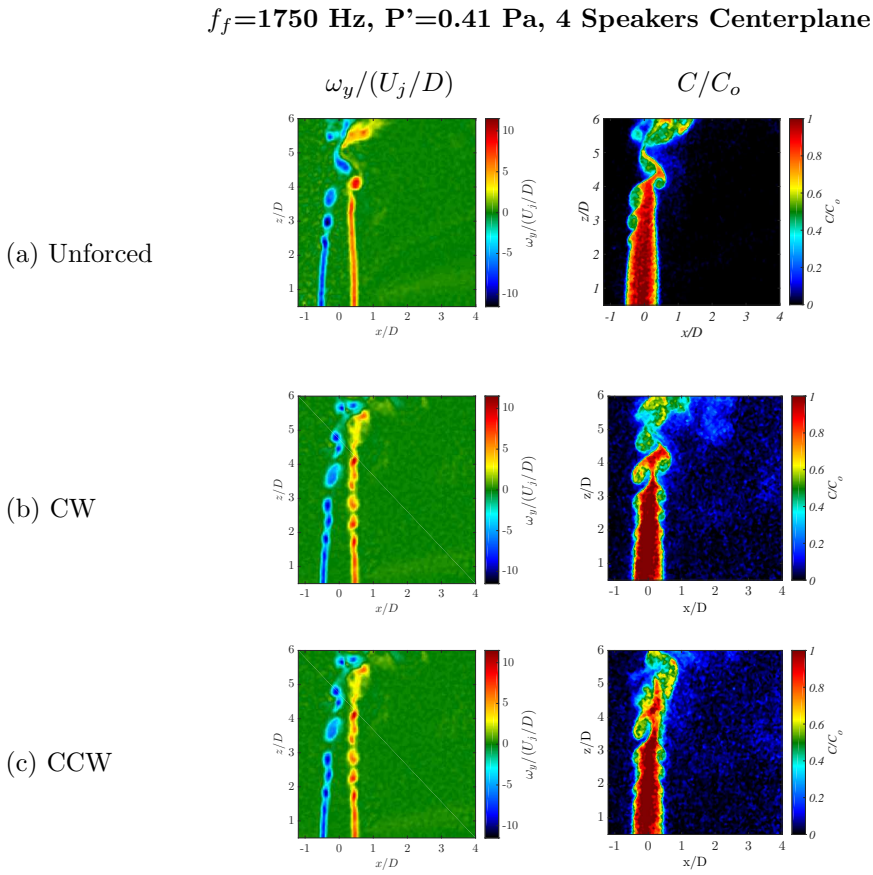

Figure E.1: Instantaneous centerplane simultaneous PLIF/PIV imaging of the $J = 41$ JICF. Data shown for scaled vorticity $\omega_y/(U_j/D)$ and scaled jet fluid concentration C/C_o for the (a) unforced jet, and jet subject to clockwise and counterclockwise directional forcing with excitation (b-c) f_f = 1750 Hz and P'= 0.41 Pa.

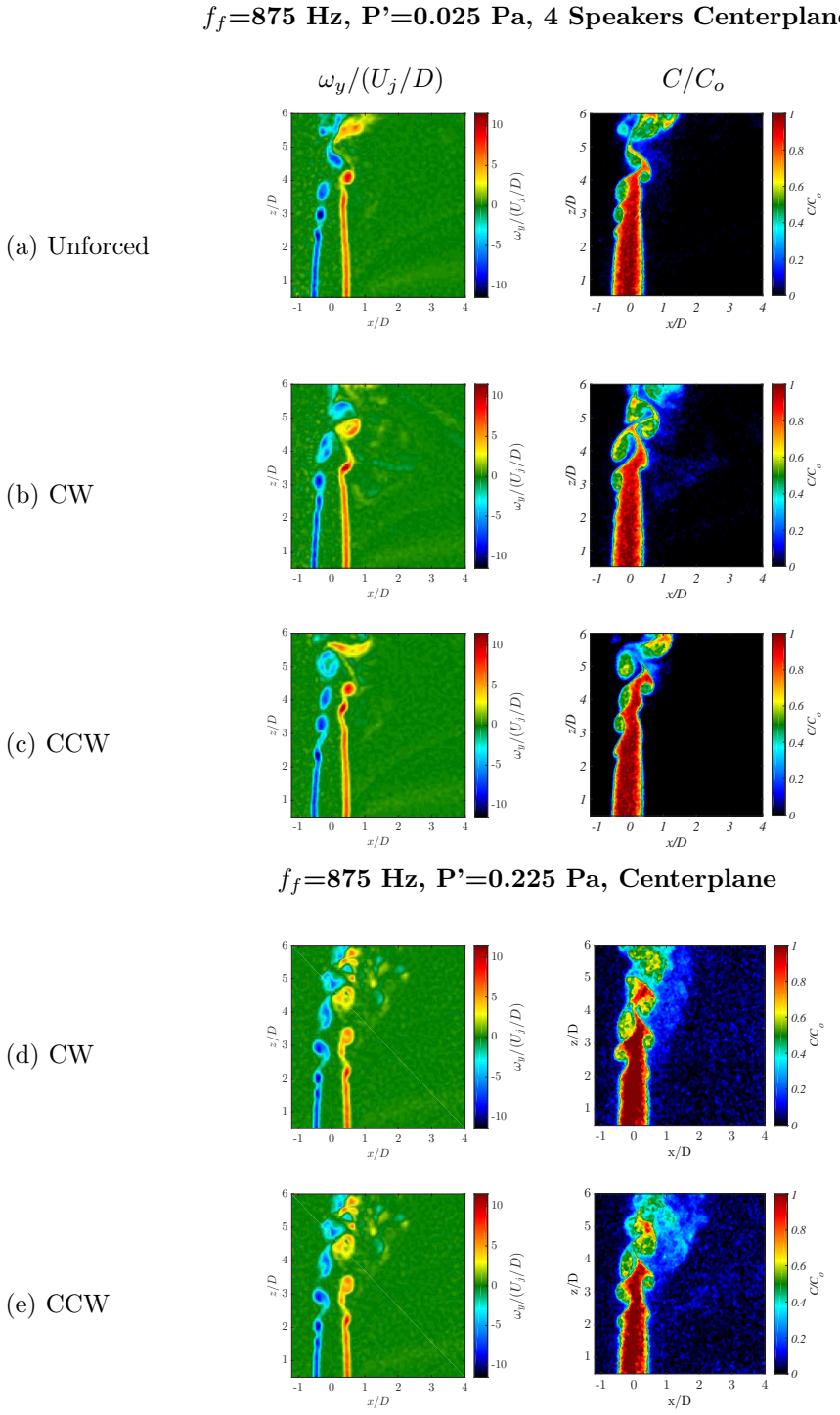

Figure E.2: Instantaneous centerplane simultaneous PLIF/PIV imaging of the $J = 41$ JICF. Data shown for scaled vorticity $\omega_y/(U_j/D)$ and scaled jet fluid concentration C/C_o for the (a) unforced jet, and jet subject to clockwise and counterclockwise directional forcing with excitation (b-c) f_f = 875 Hz and P'= 0.025 Pa, and (d-e) f_f = 875 Hz and P'= 0.225 Pa.

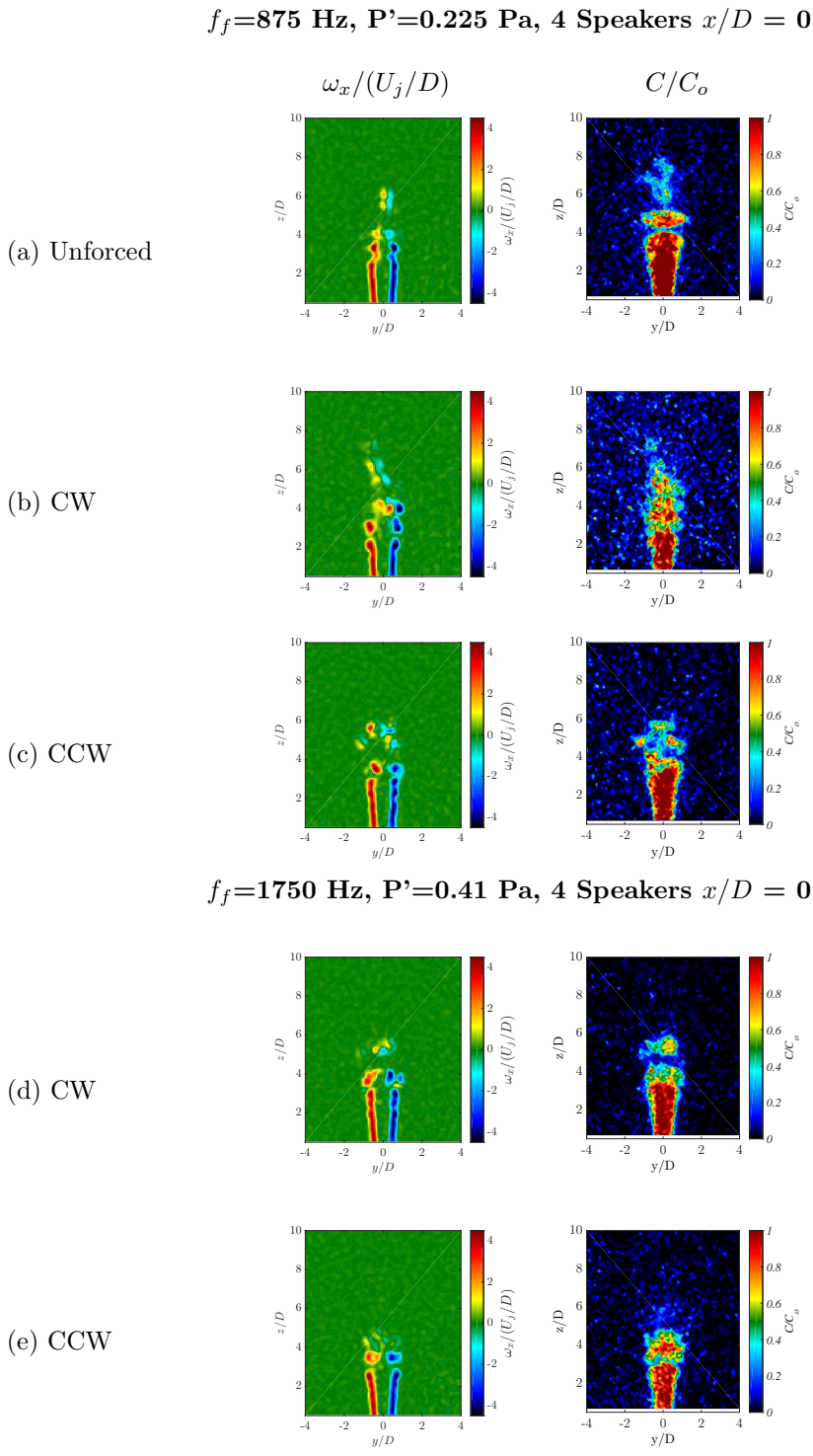

Figure E.3: Instantaneous cross-section view at $x/D = 0$ simultaneous PLIF/PIV imaging of the $J = 41$ JICF. Data shown for scaled vorticity $\omega_x/(U_j/D)$ and scaled jet fluid concentration C/C_o for the (a) unforced jet, and jet subject to clockwise and counterclockwise directional forcing with excitation (b-c) $f_f = 875$Hz and P'= 0.225 Pa, and (d-e) $f_f = 1750$ Hz and P'= 0.41 Pa.

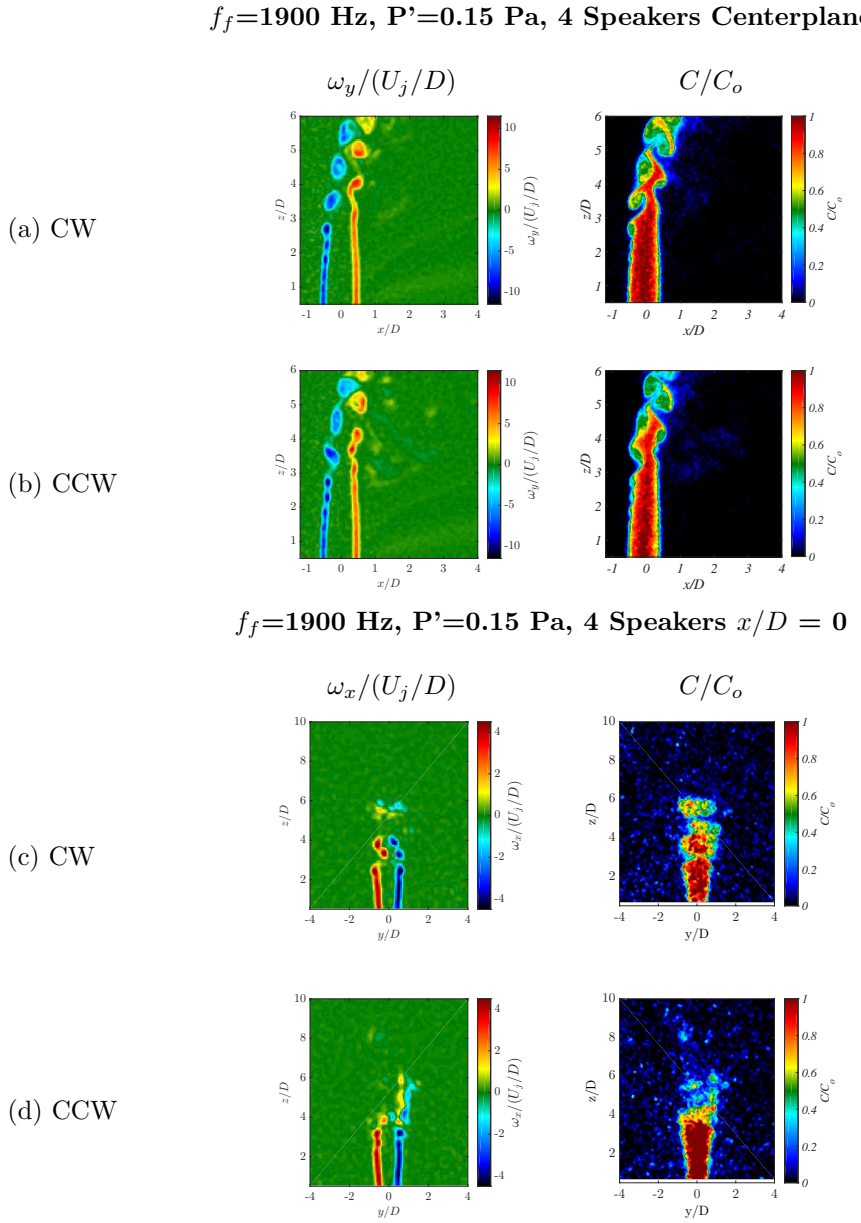

Figure E.4: Instantaneous centerplane simultaneous PLIF/PIV imaging of the $J = 41$ JICF. Data shown for scaled vorticity $\omega_y/(U_j/D)$ or $\omega_x/(U_j/D)$ and scaled jet fluid concentration C/C_o for the jet subject to clockwise and counterclockwise directional forcing with excitation (a-b) $f_f = 1600$ Hz and P'= 0.15 Pa, and (c-d) $f_f = 1900$ Hz and P'= 0.15 Pa.

E.2 Scalar and Vorticity Fields, 2-Speaker and 1-Speaker Study

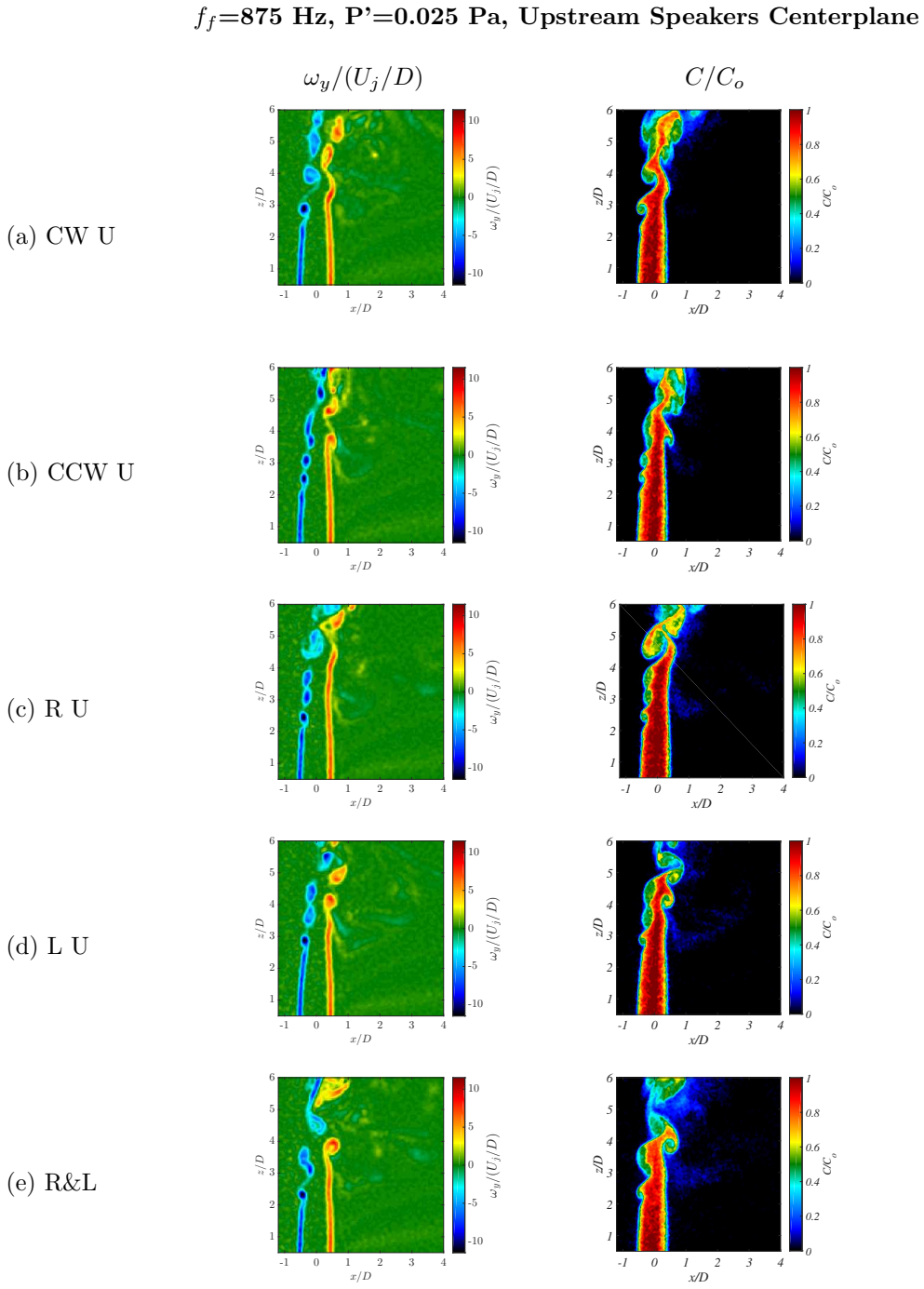

Figure E.5: Instantaneous centerplane simultaneous PLIF/PIV imaging of the $J = 41$ JICF. Data shown for scaled vorticity $\omega_y/(U_j/D)$ and scaled jet fluid concentration C/C_o for the (a) unforced jet, and jet subject to upstream directional forcing with excitation (b-f) $f_f = 875$ Hz and P'= 0.025 Pa.

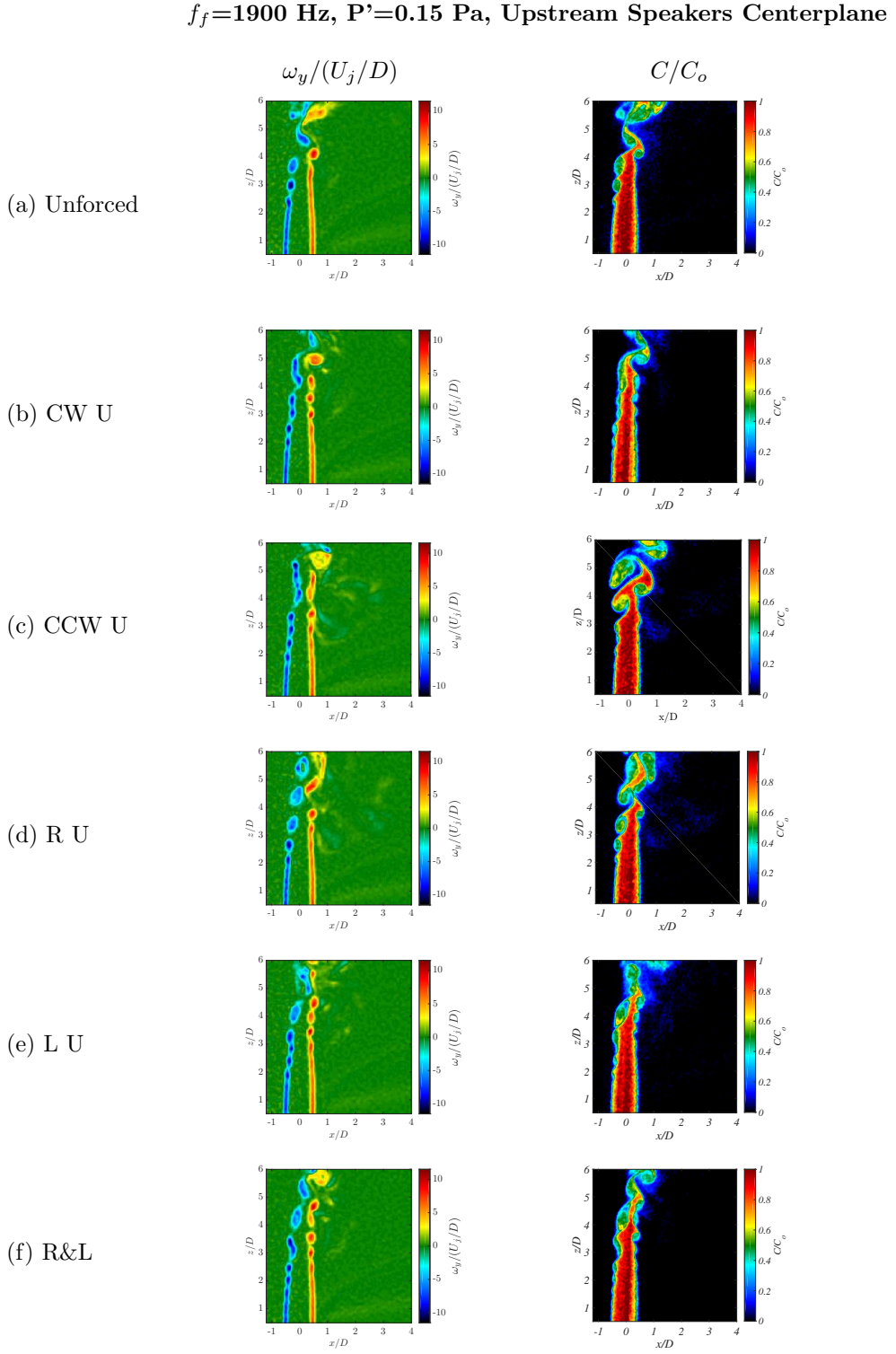

Figure E.6: Instantaneous centerplane simultaneous PLIF/PIV imaging of the $J = 41$ JICF. Data shown for scaled vorticity $\omega_y/(U_j/D)$ and scaled jet fluid concentration C/C_o for the (a) unforced jet, and jet subject to upstream directional forcing with excitation (b-f) f_f = 1900 Hz and P'= 0.15 Pa.

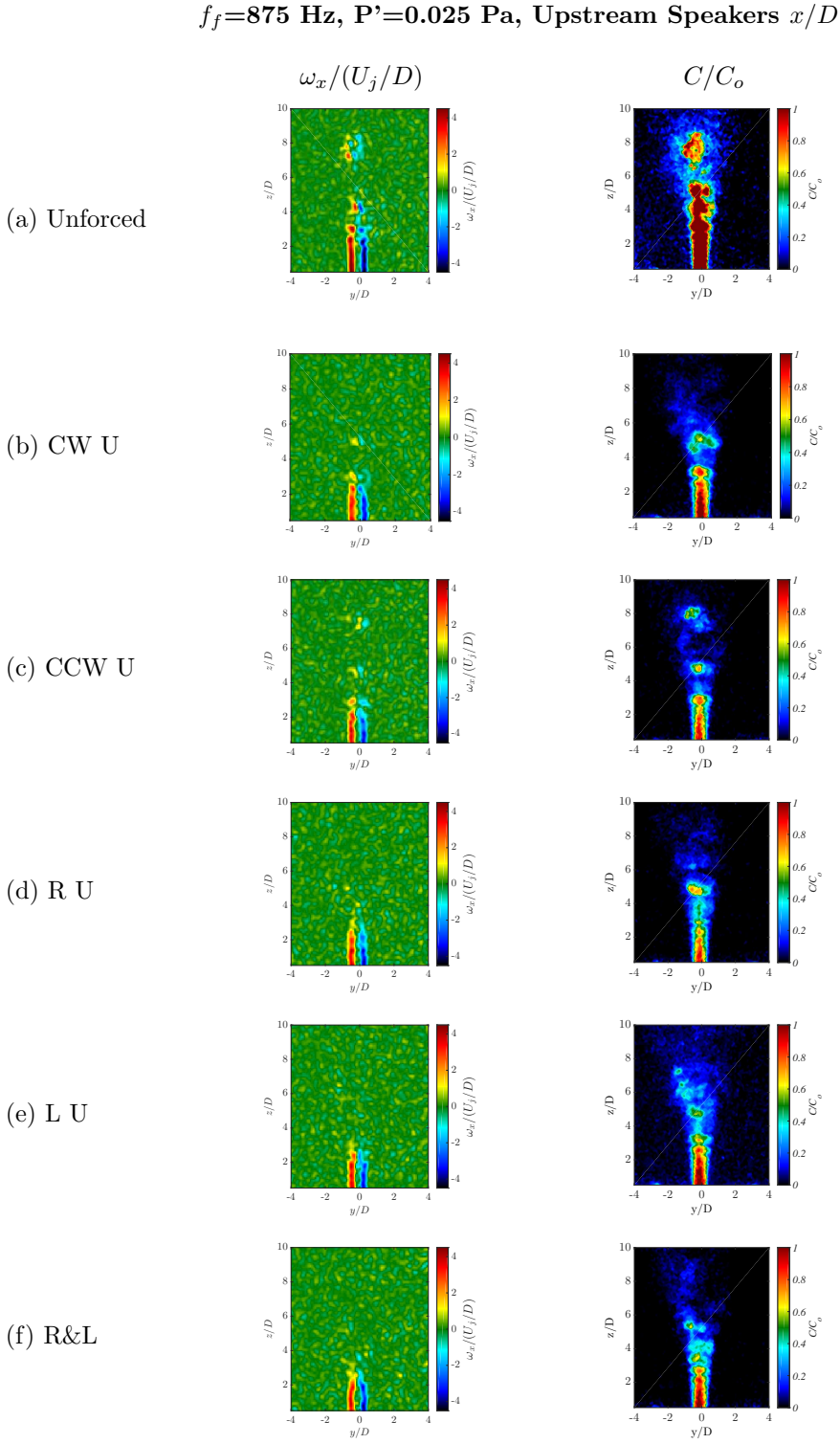

Figure E.7: Instantaneous cross-section view at x/D = -0.4 simultaneous PLIF/PIV imaging of the $J = 41$ JICF. Data shown for scaled vorticity $\omega_x/(U_j/D)$ and scaled jet fluid concentration C/C_o for the (a) unforced jet, and jet subject to upstream directional forcing with excitation (b-f) f_f = 875 Hz and P'= 0.025 Pa.

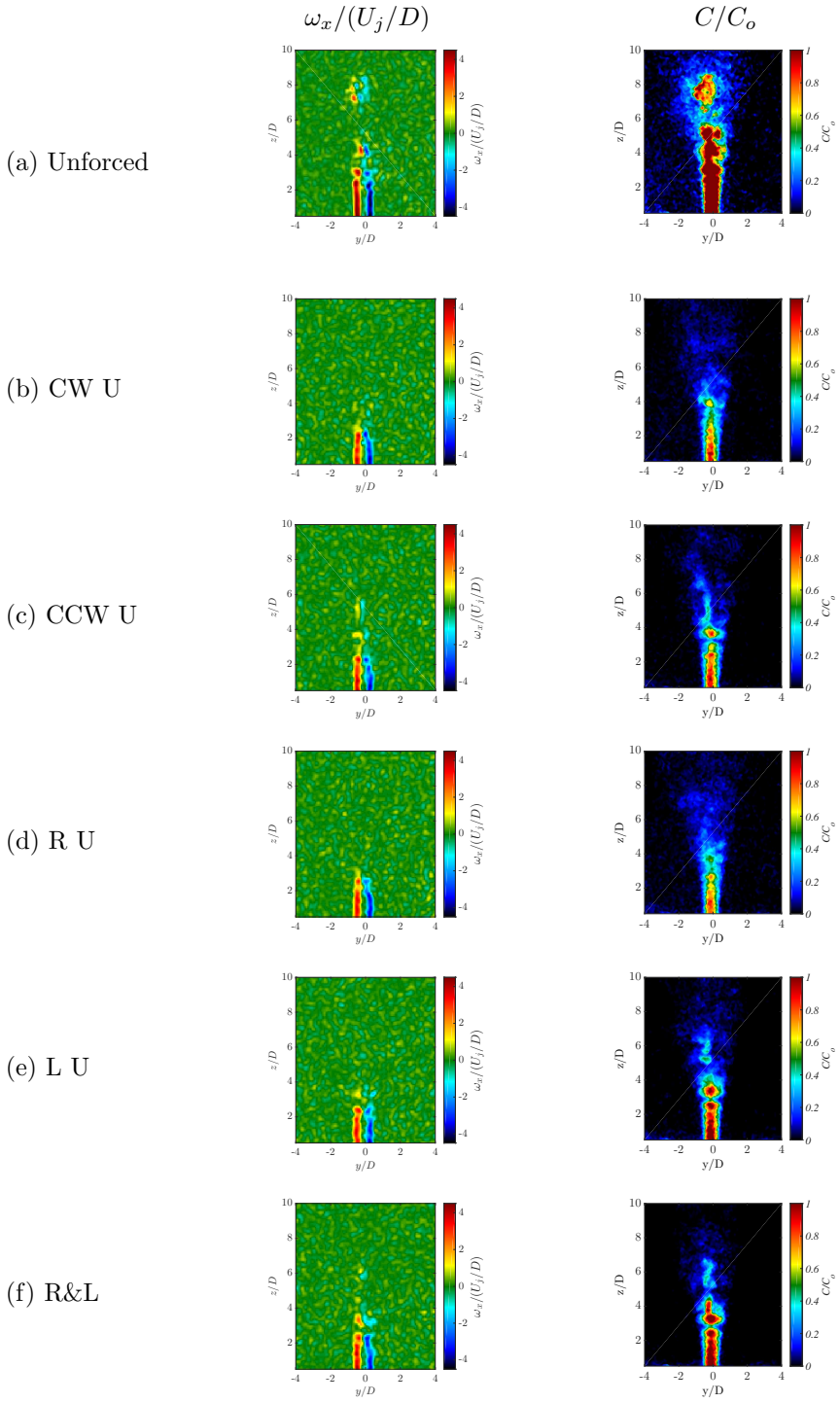

Figure E.8: Instantaneous cross-section view at x/D = -0.4 simultaneous PLIF/PIV imaging of the $J = 41$ JICF. Data shown for scaled vorticity $\omega_x/(U_j/D)$ and scaled jet fluid concentration C/C_o for the (a) unforced jet, and jet subject to upstream directional forcing with excitation (b-f) f_f = 1900 Hz and P'= 0.15 Pa.

E.3 POD Modes Structure, 4-Speaker Study

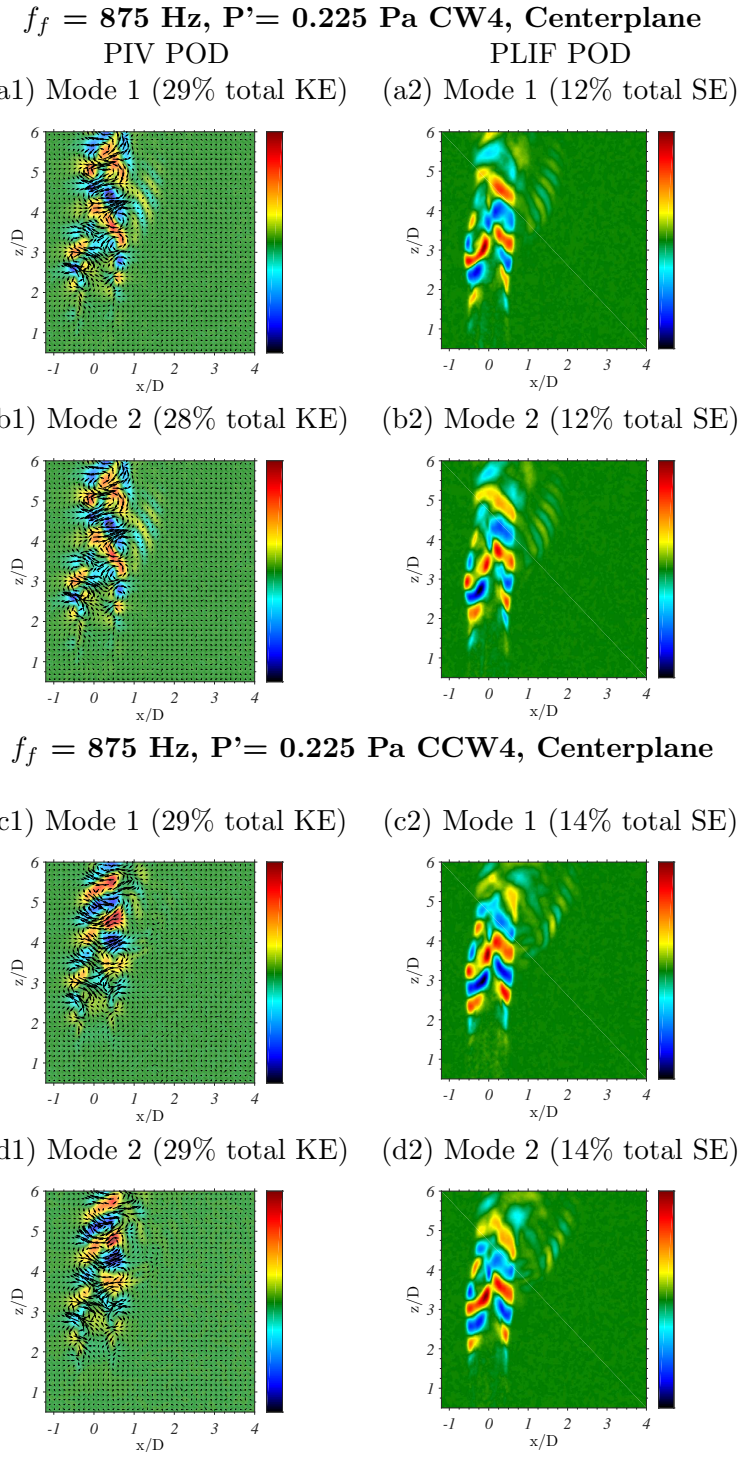

Figure E.9: PLIF and PIV POD mode structures from instantaneous centerplane images of the J = 41 JICF subject to external asymmetric forcing at f_f = 875 Hz with amplitude P'= 0.225 Pa in the (a-b) clockwise and (c-d) counterclockwise directions. Percentage of total kinetic energy (KE) or scalar fluctuation energy (SE) contributed by each mode is indicated..

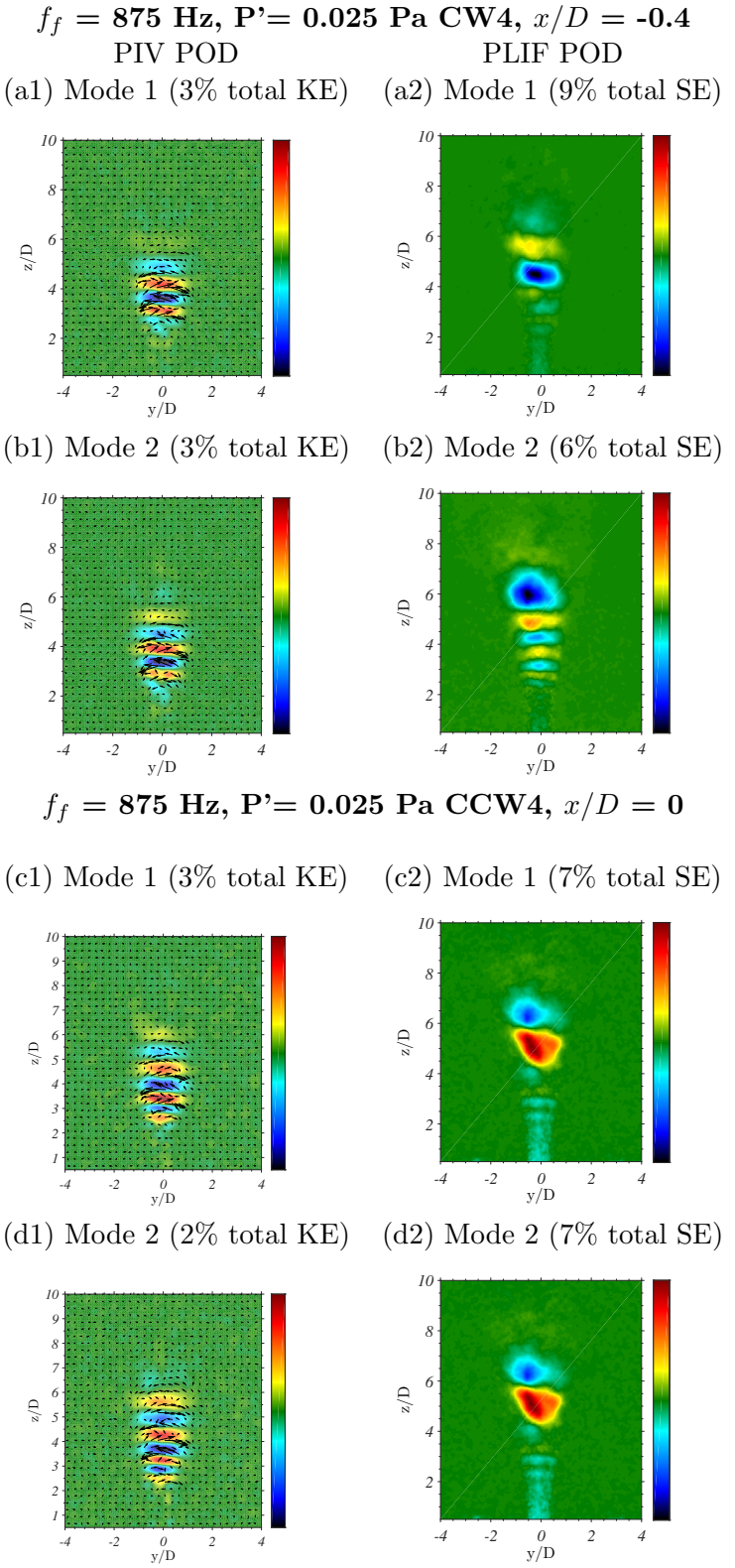

Figure E.10: PLIF and PIV POD mode structures from instantaneous x/D = -0.4 cross-sectional plane images of the J = 41 JICF subject to external asymmetric forcing at f_f = 875 Hz with amplitude P'= 0.025 Pa in the (a-b) clockwise and (c-d) counterclockwise directions. Percentage of total kinetic energy (KE) or scalar fluctuation energy (SE) contributed by each mode is indicated.

f_f = 1900 Hz, P'= 0.15 Pa CW4, x/D = -0.4

PIV POD PLIF POD

(a1) Mode 1 (7% total KE) (a2) Mode 1 (5% total SE)

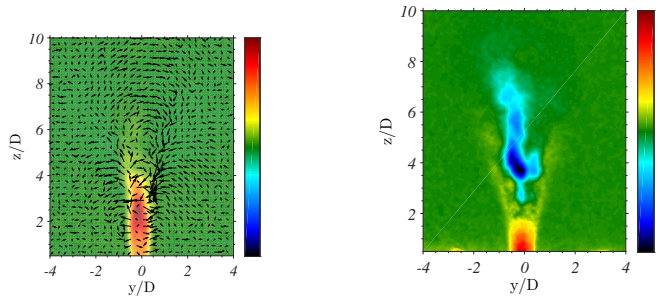

(b1) Mode 2 (3% total KE) (b2) Mode 2 (4% total SE)

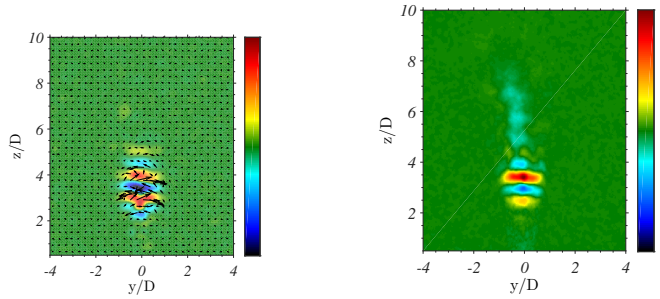

f_f = 1900 Hz, P'= 0.15 Pa CCW4, x/D = 0

(c1) Mode 1 (3% total KE) (c2) Mode 1 (4% total SE)

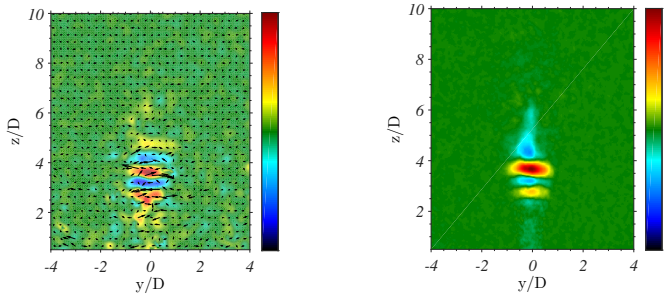

(d1) Mode 2 (3% total KE) (d2) Mode 2 (3% total SE)

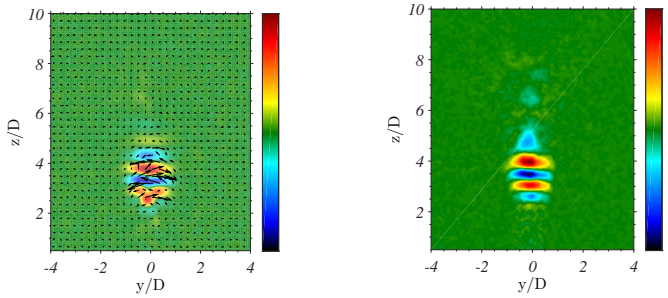

Figure E.11: PLIF and PIV POD mode structures from instantaneous x/D = -0.4 cross-sectional plane images of the J = 41 JICF subject to external asymmetric forcing at f_f = 1900 Hz with amplitude P'= 0.15 Pa in the (a-b) clockwise and (c-d) counterclockwise directions. Percentage of total kinetic energy (KE) or scalar fluctuation energy (SE) contributed by each mode is indicated.

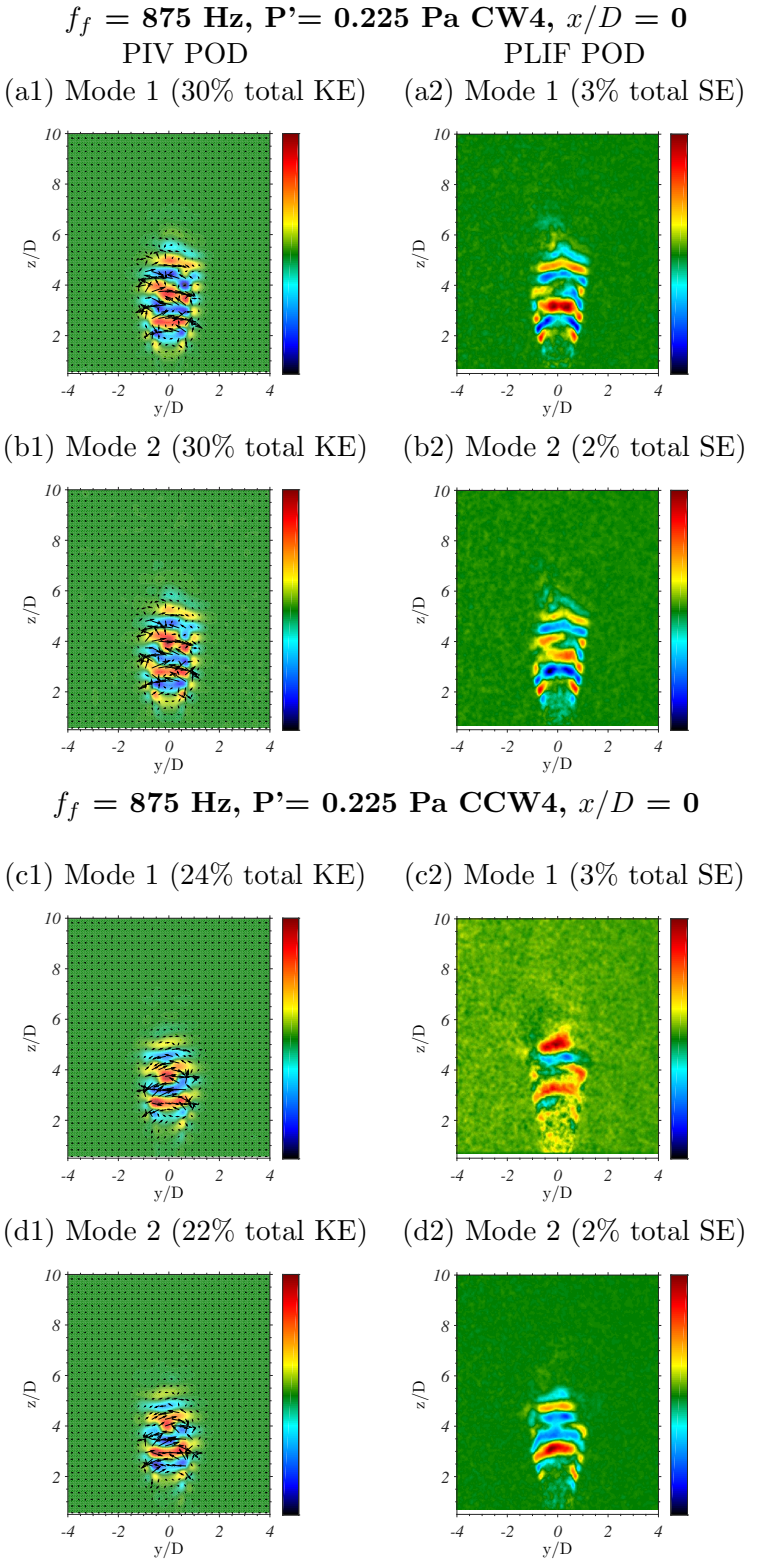

Figure E.12: PLIF and PIV POD mode structures from instantaneous $x/D = 0$ cross-sectional plane images of the $J = 41$ JICF subject to external asymmetric forcing at $f_f = 875$ Hz with amplitude P'= 0.225 Pa in the (a-b) clockwise and (c-d) counterclockwise directions. Percentage of total kinetic energy (KE) or scalar fluctuation energy (SE) contributed by each mode is indicated.

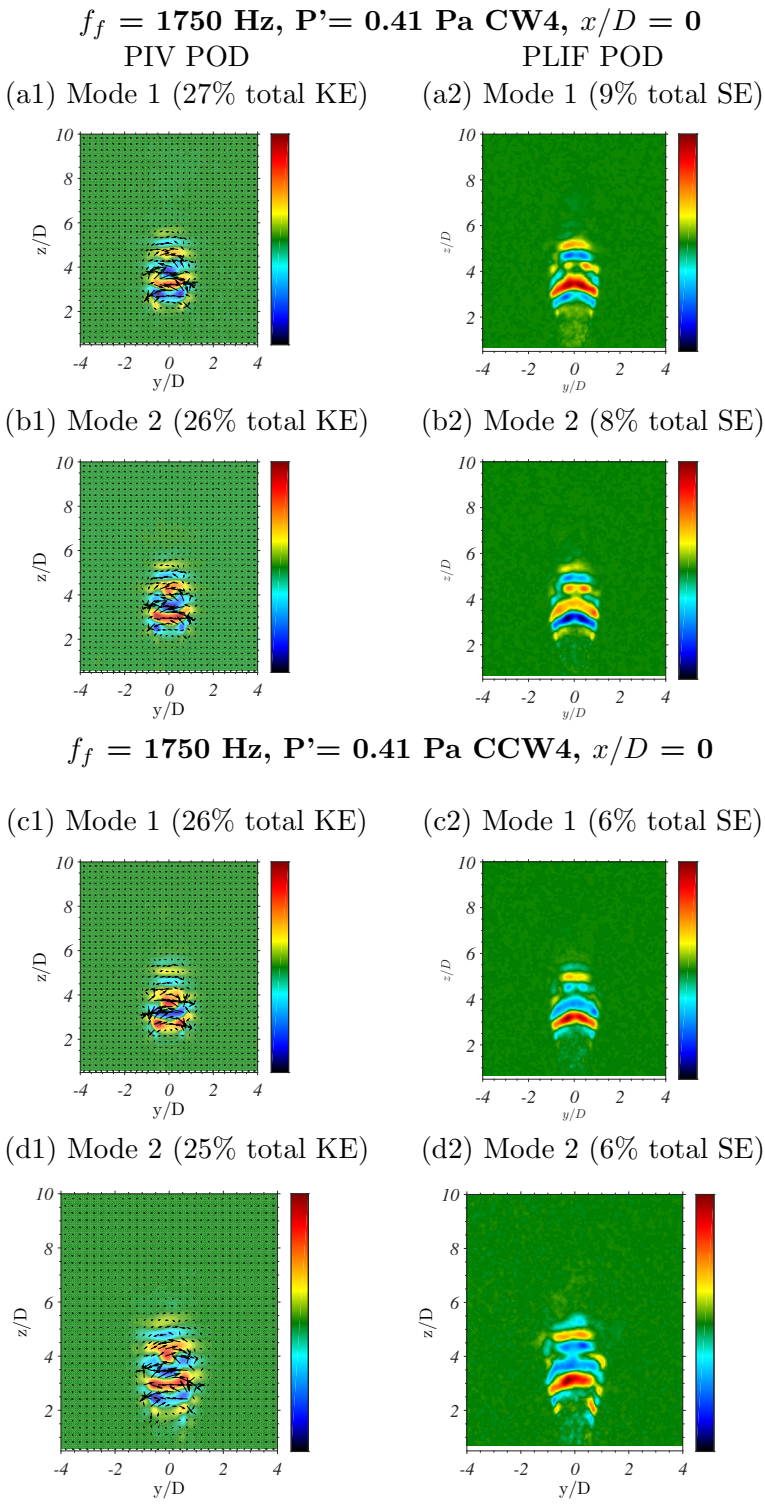

Figure E.13: PLIF and PIV POD mode structures from instantaneous $x/D = 0$ cross-sectional plane images of the $J = 41$ JICF subject to external asymmetric forcing at $f_f = 1750$ Hz with amplitude P'= 0.41 Pa in the (a-b) clockwise and (c-d) counterclockwise directions. Percentage of total kinetic energy (KE) or scalar fluctuation energy (SE) contributed by each mode is indicated.

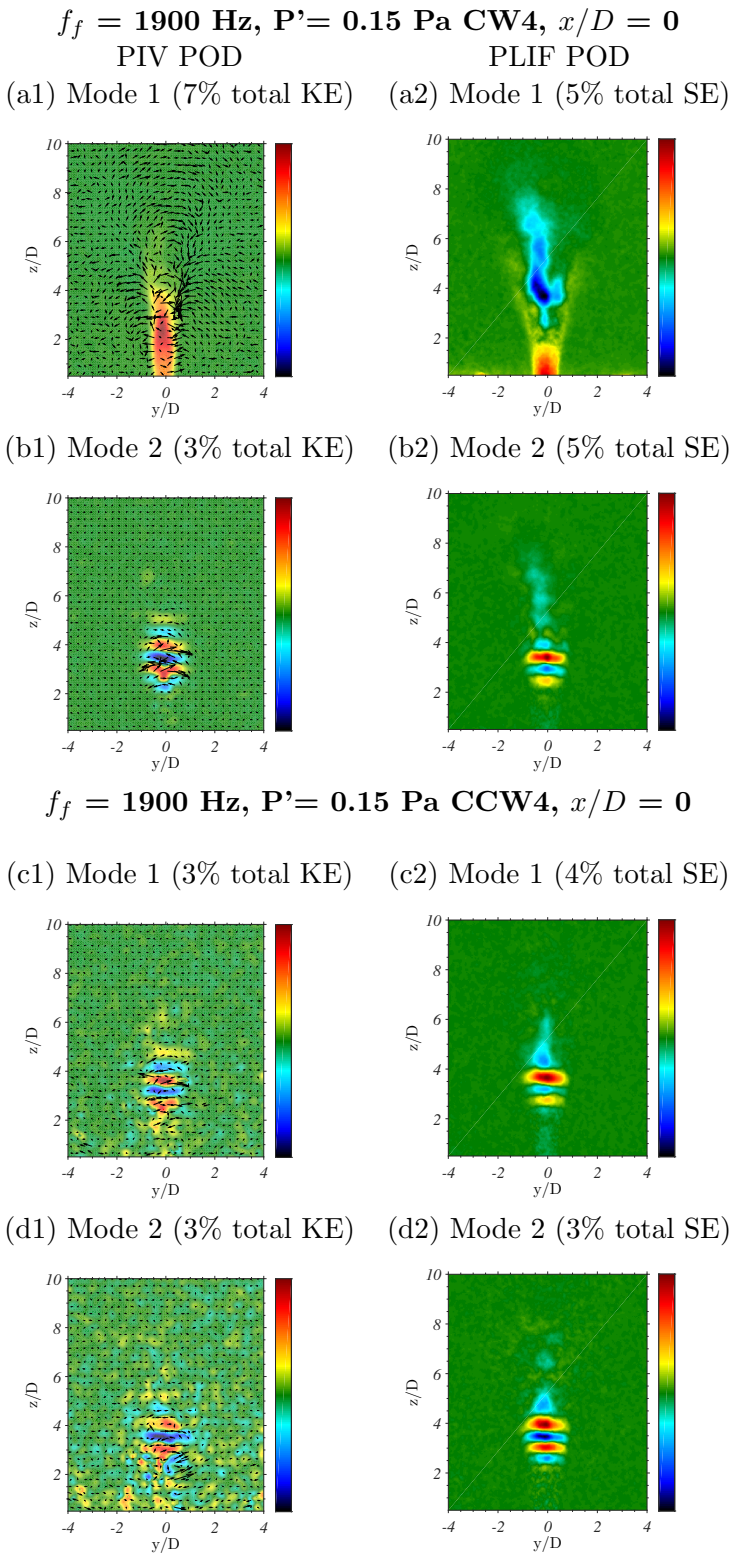

Figure E.14: PLIF and PIV POD mode structures from instantaneous $x/D = 0$ cross-sectional plane images of the $J = 41$ JICF subject to external asymmetric forcing at $f_f = 1900$ Hz with amplitude P'= 0.15 Pa in the (a-b) clockwise and (c-d) counterclockwise directions. Percentage of total kinetic energy (KE) or scalar fluctuation energy (SE) contributed by each mode is indicated.

E.4 POD Modes Structure, 2 Speaker and 1 Speaker Study

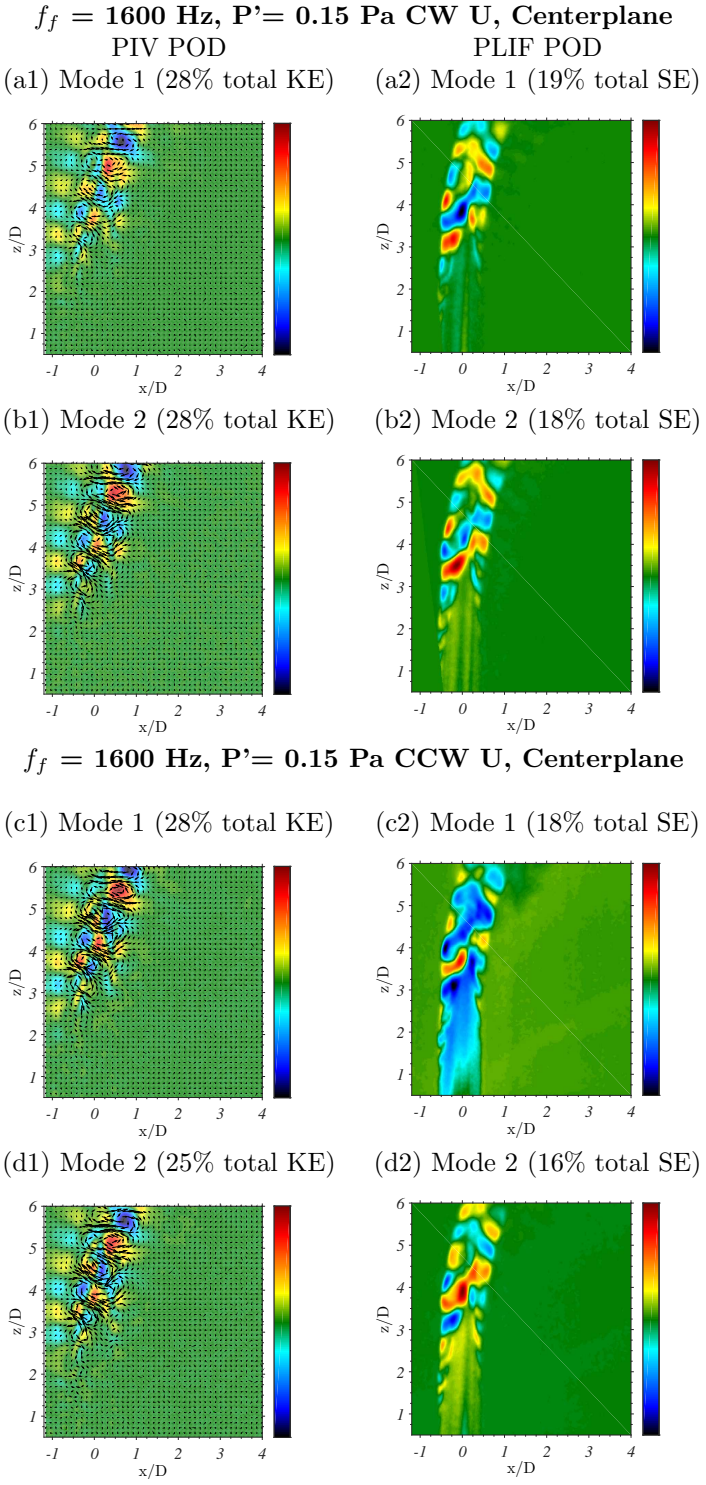

Figure E.15: PIV and PLIF POD mode structures from instantaneous centerplane images of the $J = 41$ JICF subject to external asymmetric forcing at $f_f = 1600$ Hz with amplitude P'= 0.15 Pa in the upstream region. Percentage of total kinetic energy (KE) or scalar fluctuation energy (SE) contributed by each mode is indicated.

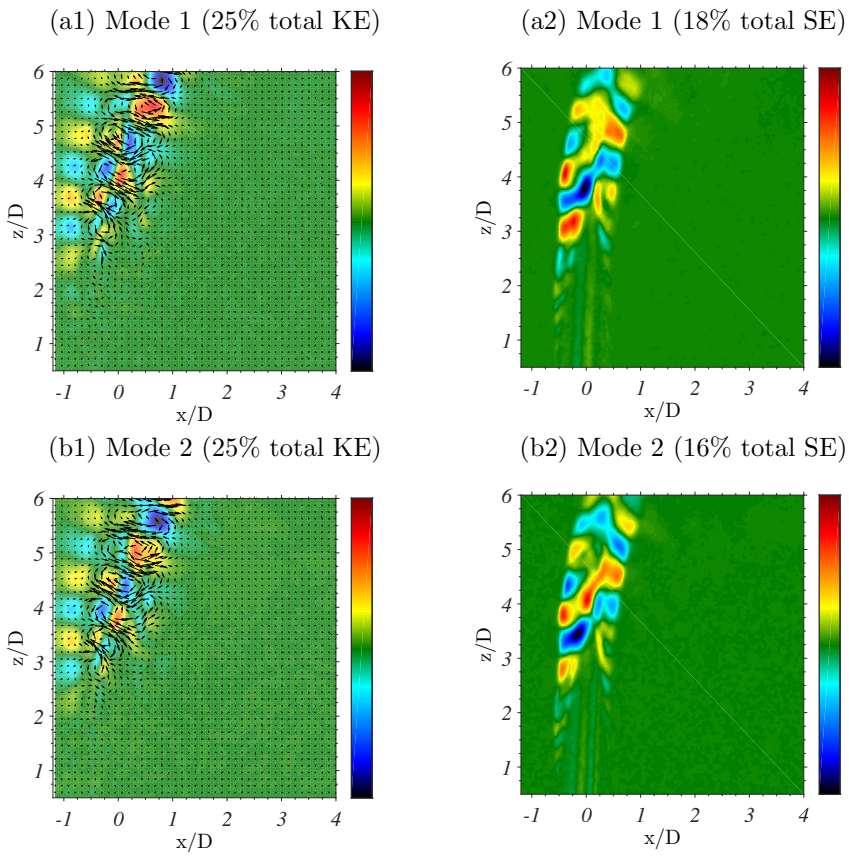

Figure E.16: PIV and PLIF POD mode structures from instantaneous centerplane images of the $J = 41$ JICF subject to external asymmetric forcing at $f_f = 1600$ Hz with amplitude P'= 0.15 Pa in the upstream region. Percentage of total kinetic energy (KE) or scalar fluctuation energy (SE) contributed by each mode is indicated.

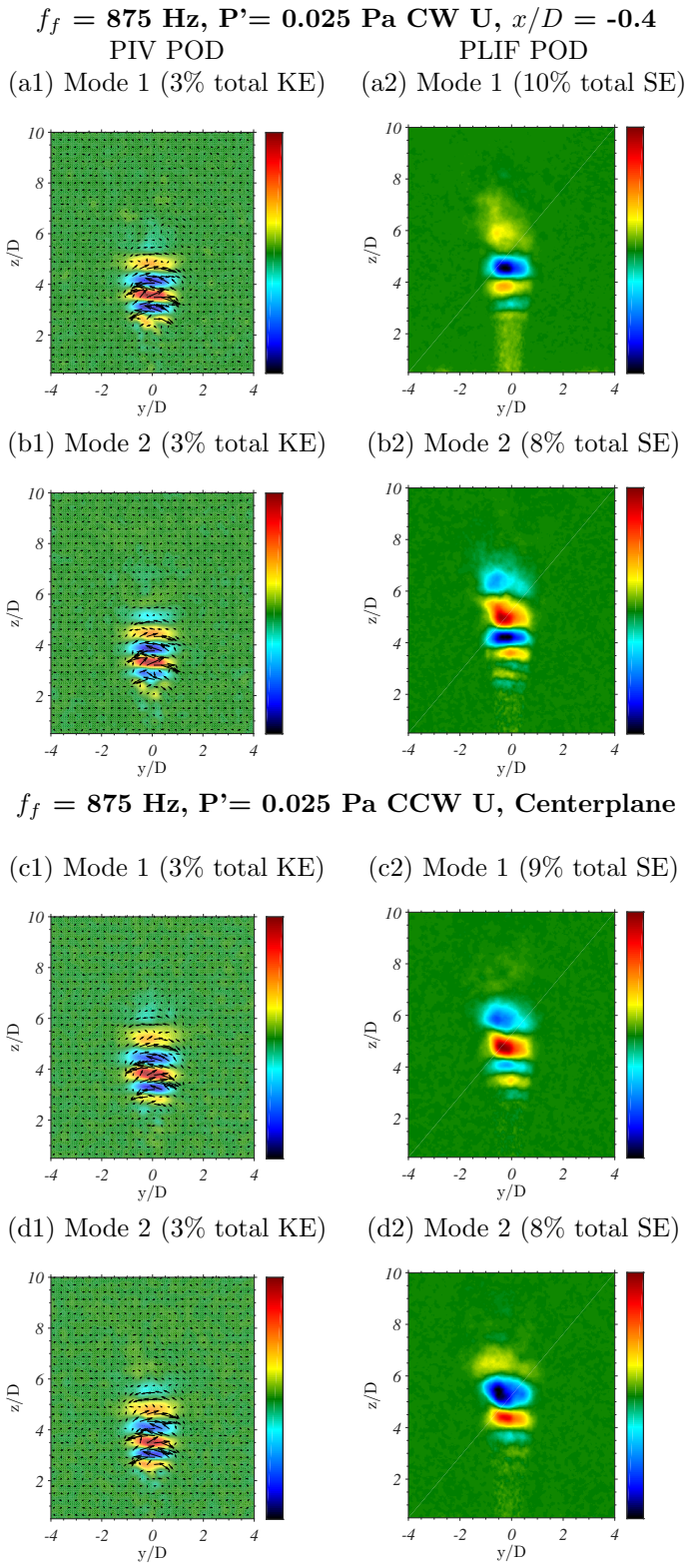

Figure E.17: PLIF and PIV POD mode structures from instantaneous x/D = -0.4 cross-sectional plane images of the J = 41 JICF subject to external asymmetric forcing at f_f = 875 Hz with amplitude P'= 0.025 Pa in the upstream region. Percentage of total kinetic energy (KE) or scalar fluctuation energy (SE) contributed by each mode is indicated.

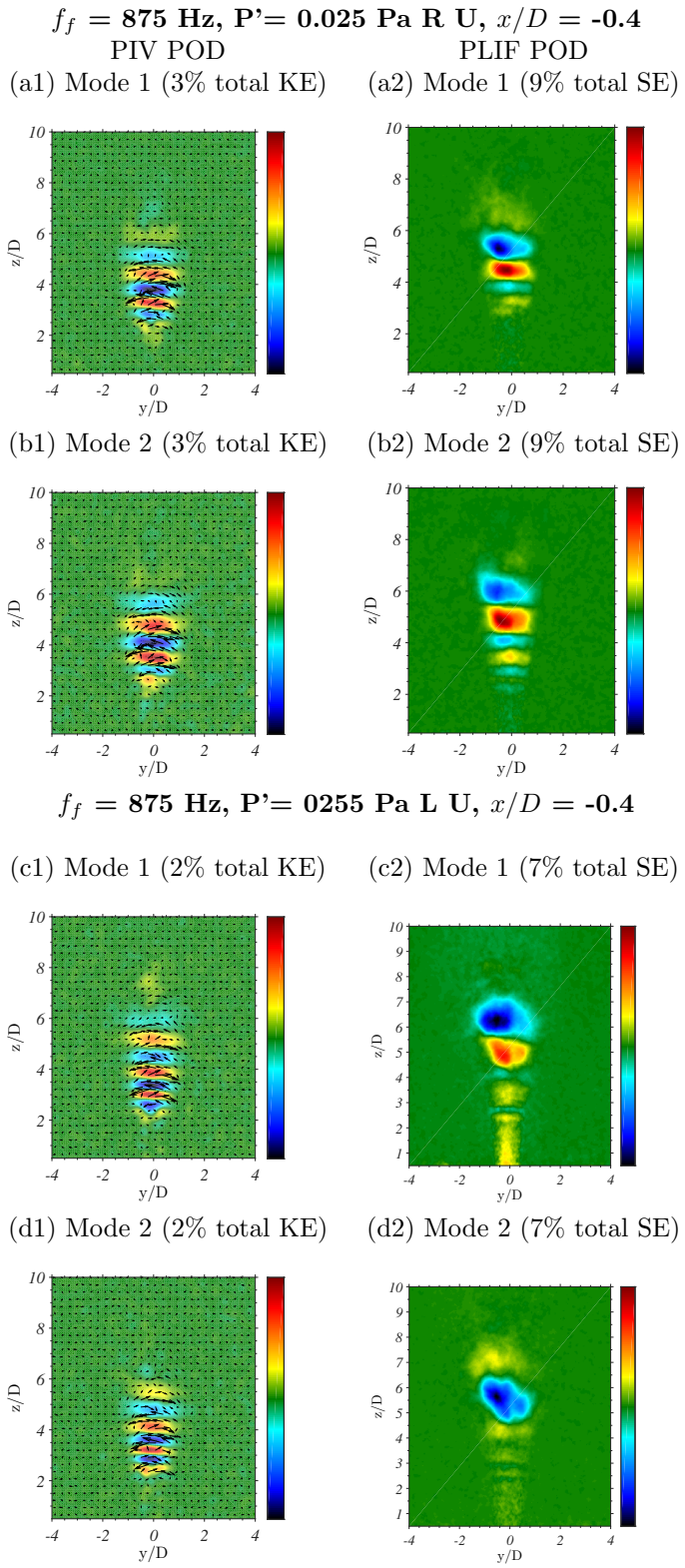

Figure E.18: PLIF and PIV POD mode structures from instantaneous x/D = -0.4 cross-sectional plane images of the J = 41 JICF subject to external asymmetric forcing at f_f = 875 Hz with amplitude P'= 0.225 Pa in the upstream region. Percentage of total kinetic energy (KE) or scalar fluctuation energy (SE) contributed by each mode is indicated.

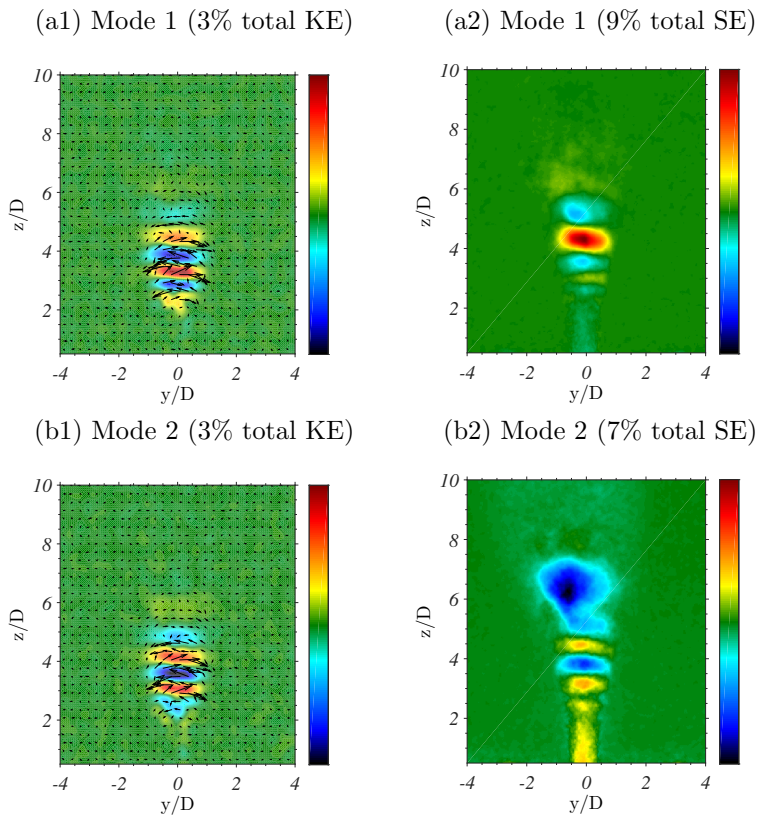

Figure E.19: PLIF and PIV POD mode structures from instantaneous x/D = -0.4 cross-sectional plane images of the J = 41 JICF subject to R&L U external asymmetric forcing at f_f = 875 Hz with amplitude P'= 0.225 Pa in the upstream region. Percentage of total kinetic energy (KE) or scalar fluctuation energy (SE) contributed by each mode is indicated.

f_f = 1600 Hz, P'= 0.15 Pa R&L U, x/D = -0.4

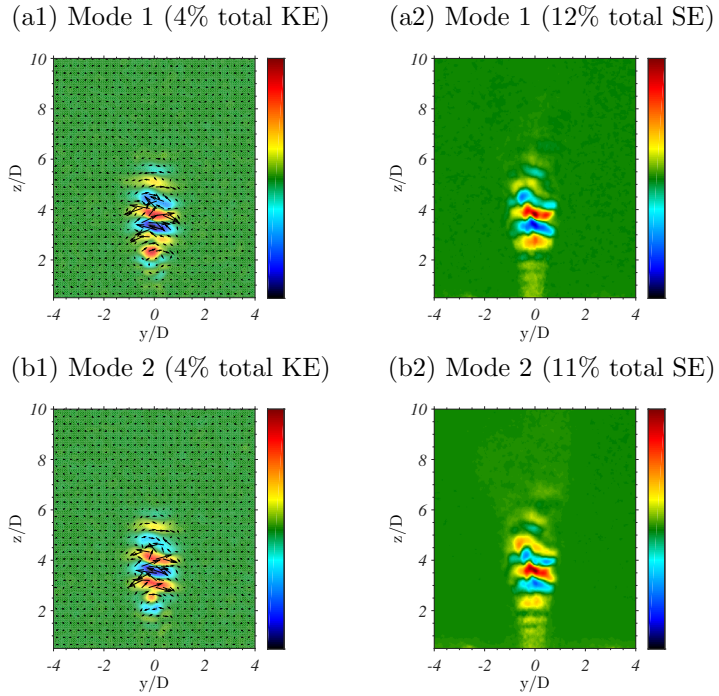

Figure E.20: PLIF and PIV POD mode structures from instantaneous x/D = -0.4 cross-sectional plane images of the $J = 41$ JICF subject to R&L U external asymmetric forcing at $f_f = 1600$ Hz with amplitude P'= 0.15 Pa in the upstream region. Percentage of total kinetic energy (KE) or scalar fluctuation energy (SE) contributed by each mode is indicated.

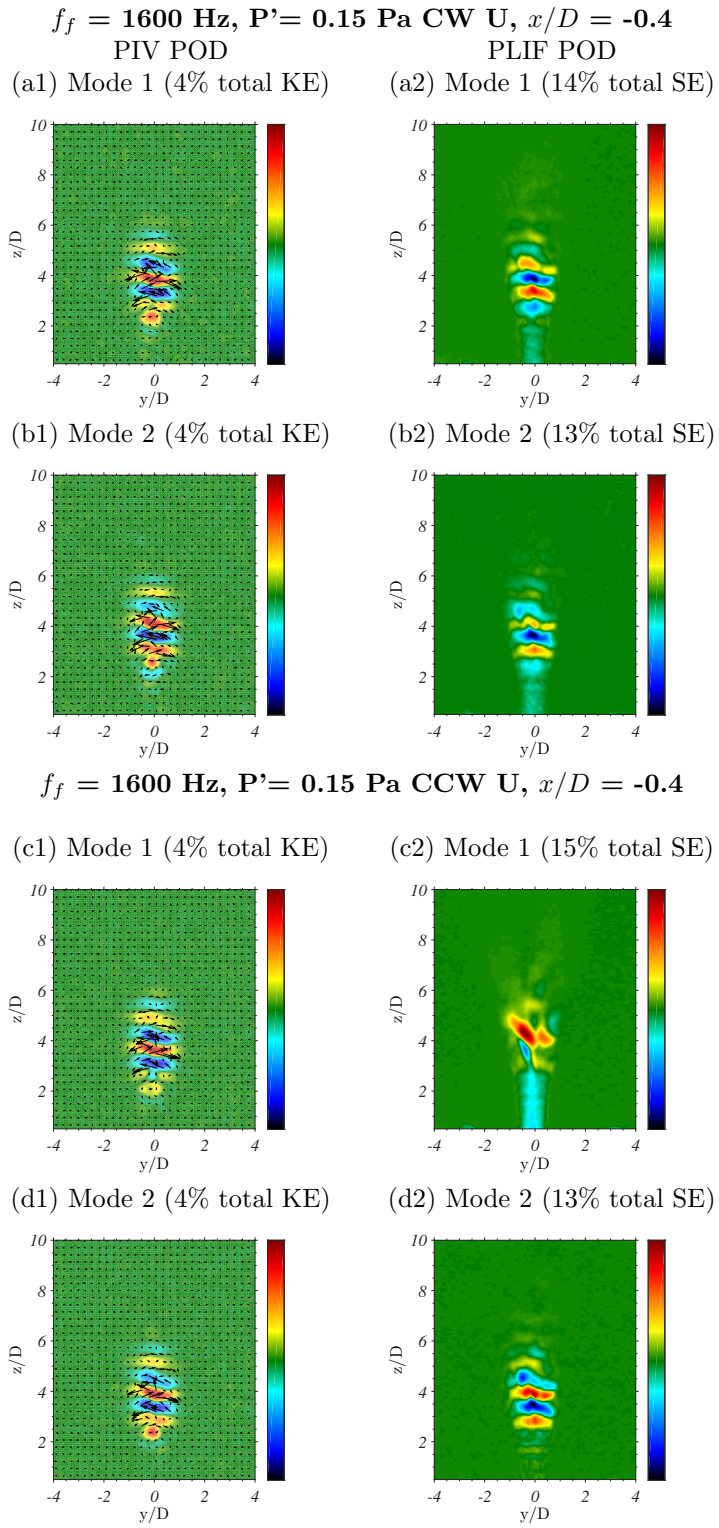

Figure E.21: PLIF and PIV POD mode structures from instantaneous x/D = -0.4 cross-sectional plane images of the J = 41 JICF subject to external asymmetric forcing at f_f = 1600 Hz with amplitude P'= 0.15 Pa in the upstream region. Percentage of total kinetic energy (KE) or scalar fluctuation energy (SE) contributed by each mode is indicated.

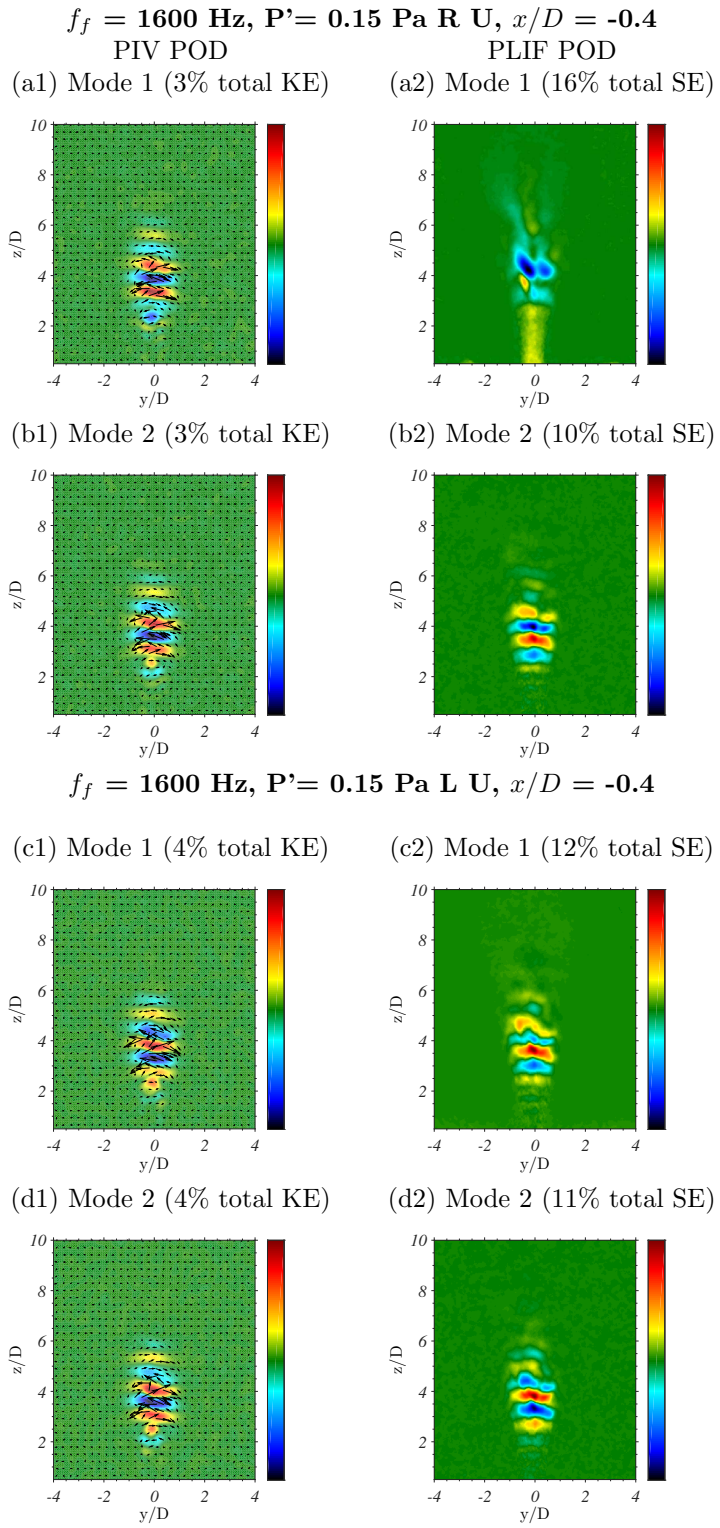

Figure E.22: PLIF and PIV POD mode structures from instantaneous x/D = -0.4 cross-sectional plane images of the J = 41 JICF subject to external asymmetric forcing at f_f = 1600 Hz with amplitude P'= 0.15 Pa in the upstream region. Percentage of total kinetic energy (KE) or scalar fluctuation energy (SE) contributed by each mode is indicated.

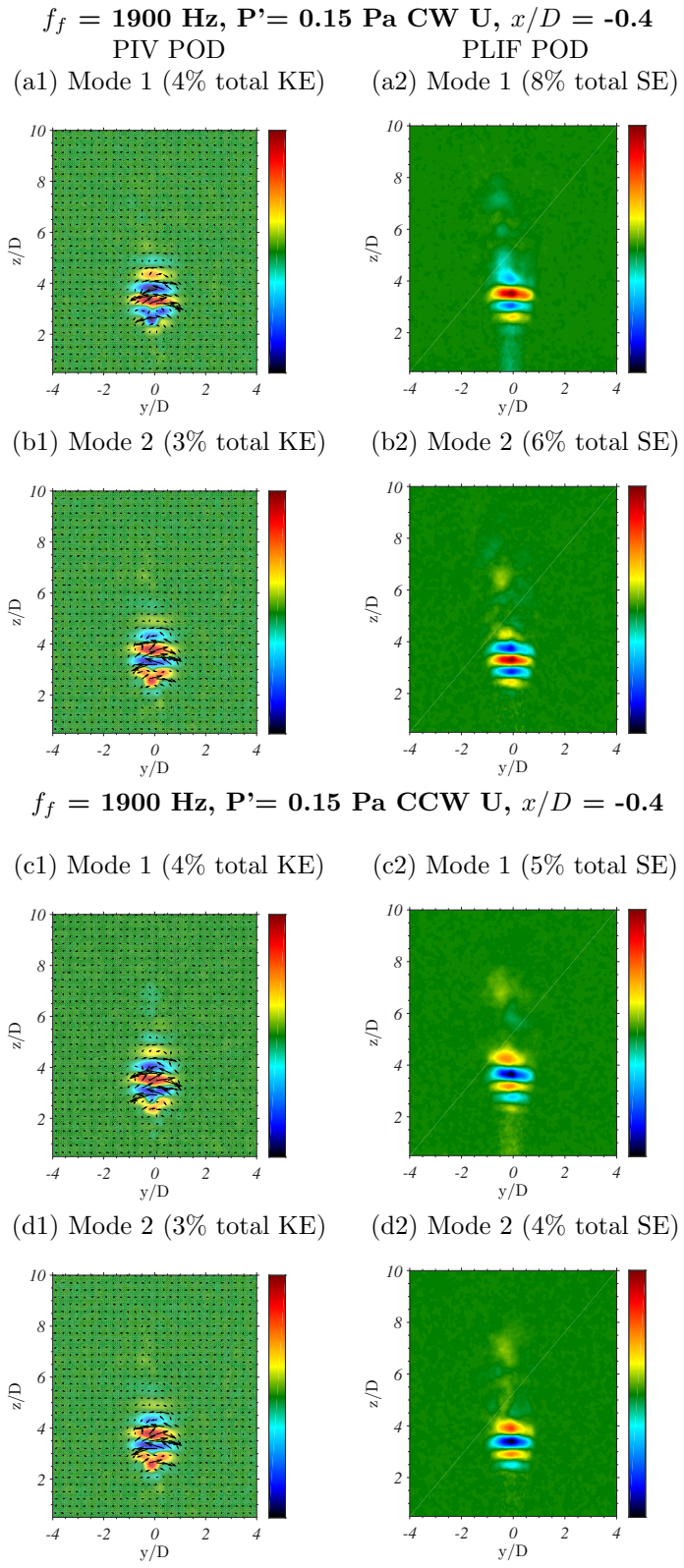

Figure E.23: PLIF and PIV POD mode structures from instantaneous x/D = -0.4 cross-sectional plane images of the J = 41 JICF subject to external asymmetric forcing at f_f = 1900 Hz with amplitude P'= 0.15 Pa in the upstream region. Percentage of total kinetic energy (KE) or scalar fluctuation energy (SE) contributed by each mode is indicated.

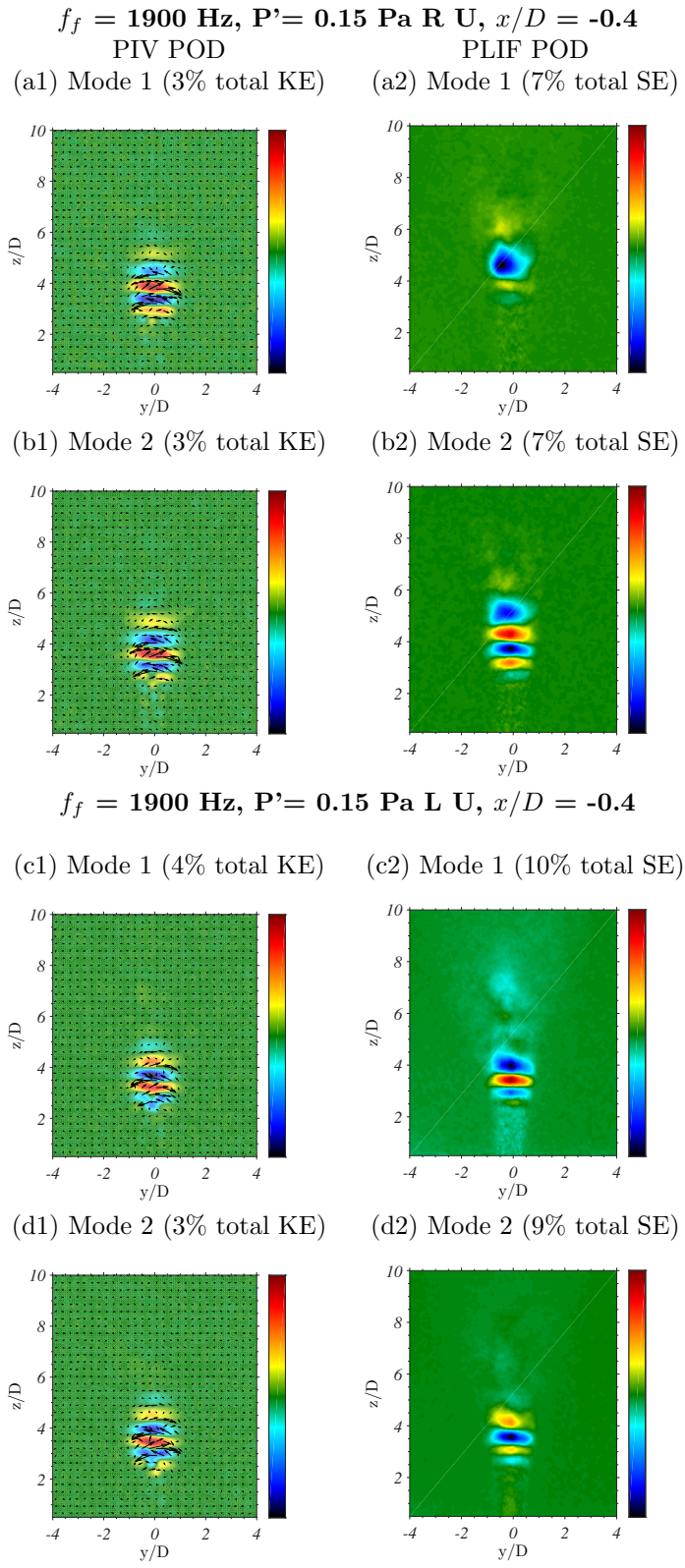

Figure E.24: PLIF and PIV POD mode structures from instantaneous x/D = -0.4 cross-sectional plane images of the J = 41 JICF subject to external asymmetric forcing at f_f = 1900 Hz with amplitude P'= 0.15 Pa in the upstream region. Percentage of total kinetic energy (KE) or scalar fluctuation energy (SE) contributed by each mode is indicated.

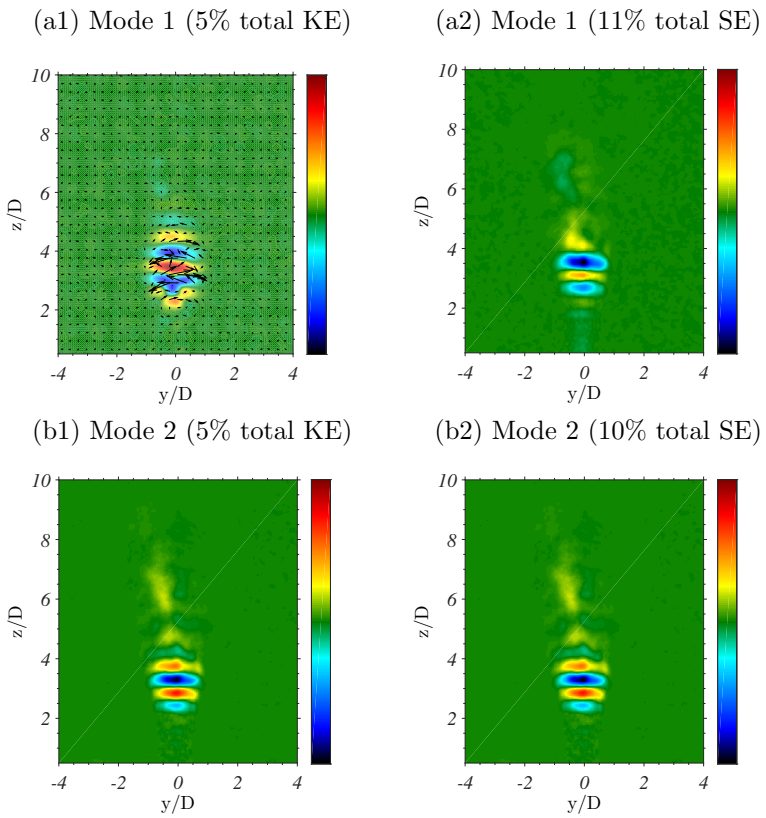

Figure E.25: PLIF and PIV POD mode structures from instantaneous x/D = -0.4 cross-sectional plane images of the $J = 41$ JICF subject to R&L U external asymmetric forcing at $f_f = 1900$ Hz with amplitude P'= 0.15 Pa in the upstream region. Percentage of total kinetic energy (KE) or scalar fluctuation energy (SE) contributed by each mode is indicated.

E.5 POD Coefficient Phase Portraits, 4 Speaker Study

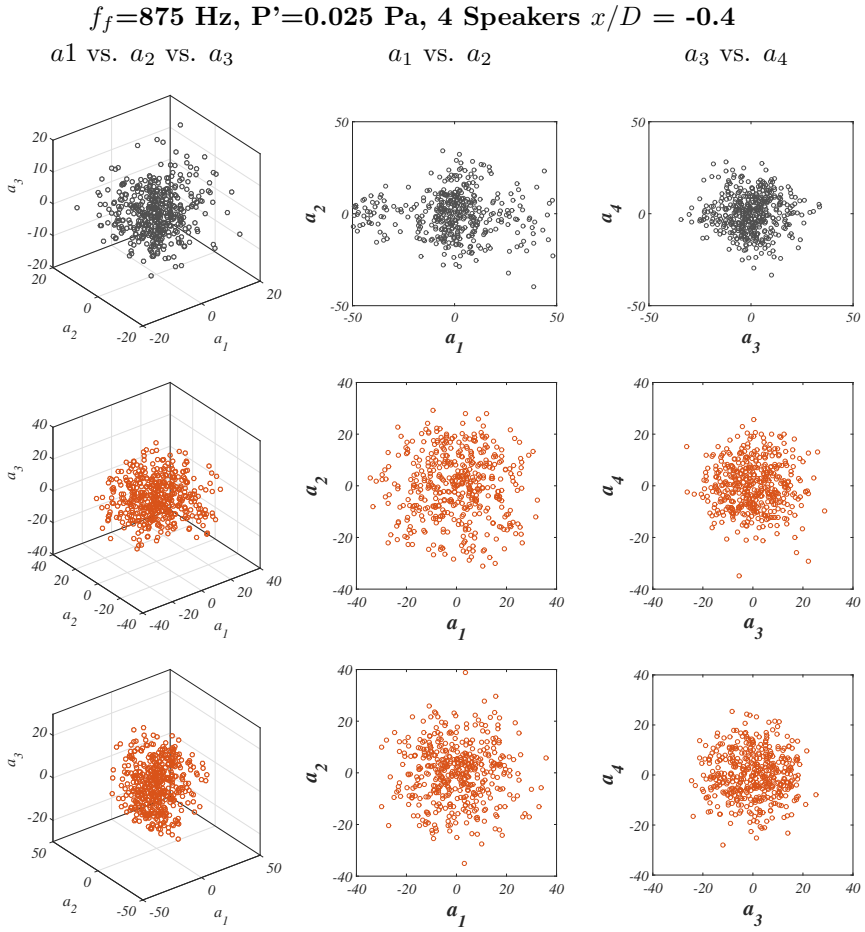

Figure E.26: PIV POD coefficients for the first 4 modes plotted against each other, extracted from instantaneous images of the $J = 41$ JICF, for the unforced jet in the $x/D = 0$ plane, and subject to CW4 and CCW4 excitation, where $f_f = 875$ Hz and P'= 0.025 Pa. Black symbols represent the unforced condition, orange symbols represent the jet subject to asymmetric forcing.

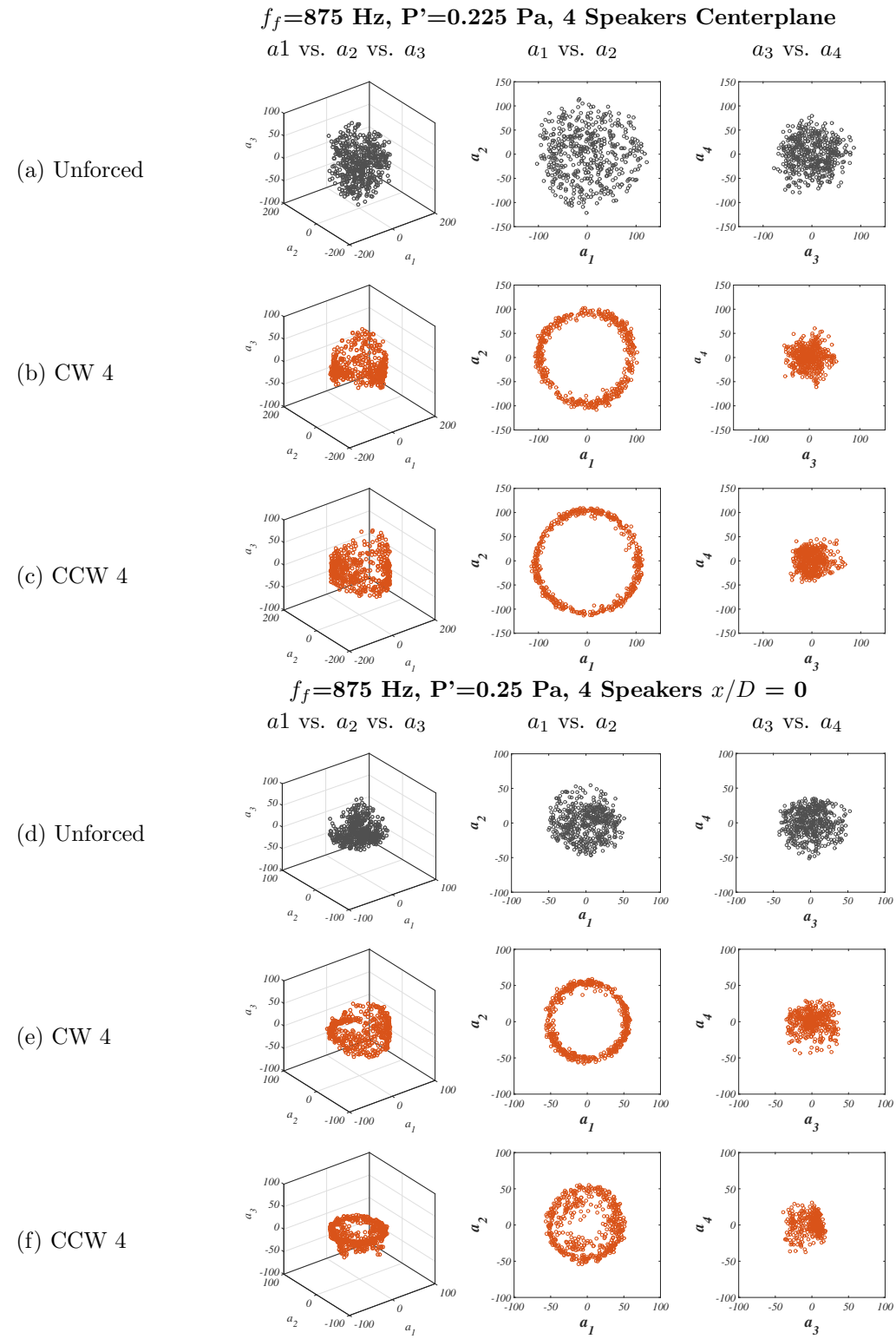

Figure E.27: PIV POD coefficients for the first 4 modes plotted against each other, extracted from instantaneous images of the $J = 41$ JICF, for the unforced jet in the (a) centerplane and (d) $x/D = 0$ plane, and subject to CW4 and CCW4 excitation in the (b-c) centerplane and (e-f) $x/D = 0$ plane, where $f_f = 875$ Hz and P'= 0.225Pa. Black symbols represent the unforced condition, orange symbols represent the jet subject to asymmetric forcing.

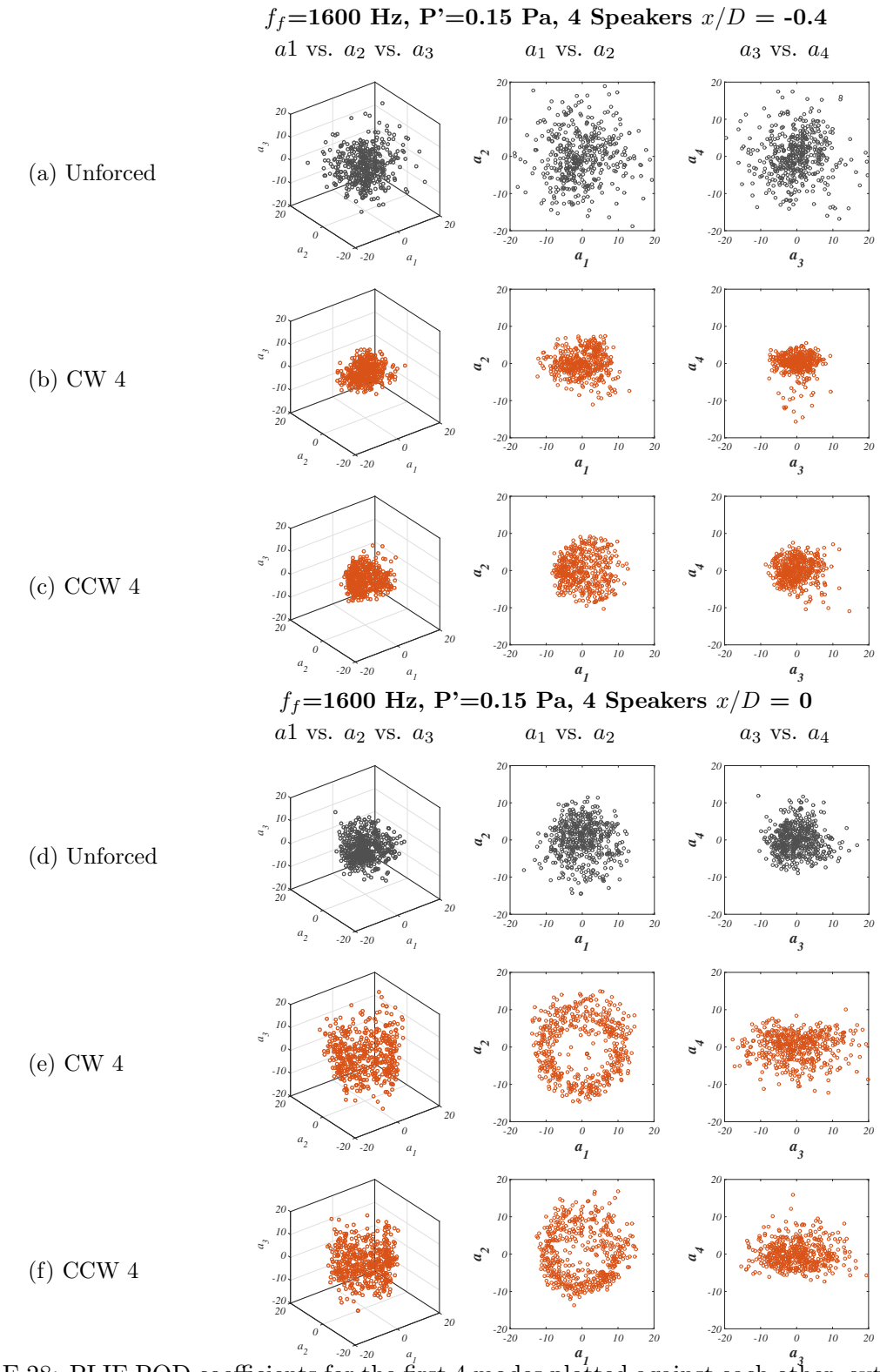

Figure E.28: PLIF POD coefficients for the first 4 modes plotted against each other, extracted from instantaneous cross-sectional plane images of the $J = 41$ JICF, for the unforced jet at (a) x/D = -0.4 and (d) $x/D = 0$, and subject to CW4 and CCW4 excitation in the (b-c) x/D = -0.4 plane and the (e-f) $x/D = 0$ plane, where $f_f = 1600$ Hz. Black symbols represent the unforced condition, orange symbols represent the jet subject to asymmetric forcing.

E.6 POD Coefficient Phase Portraits, 2/1 Speaker Study

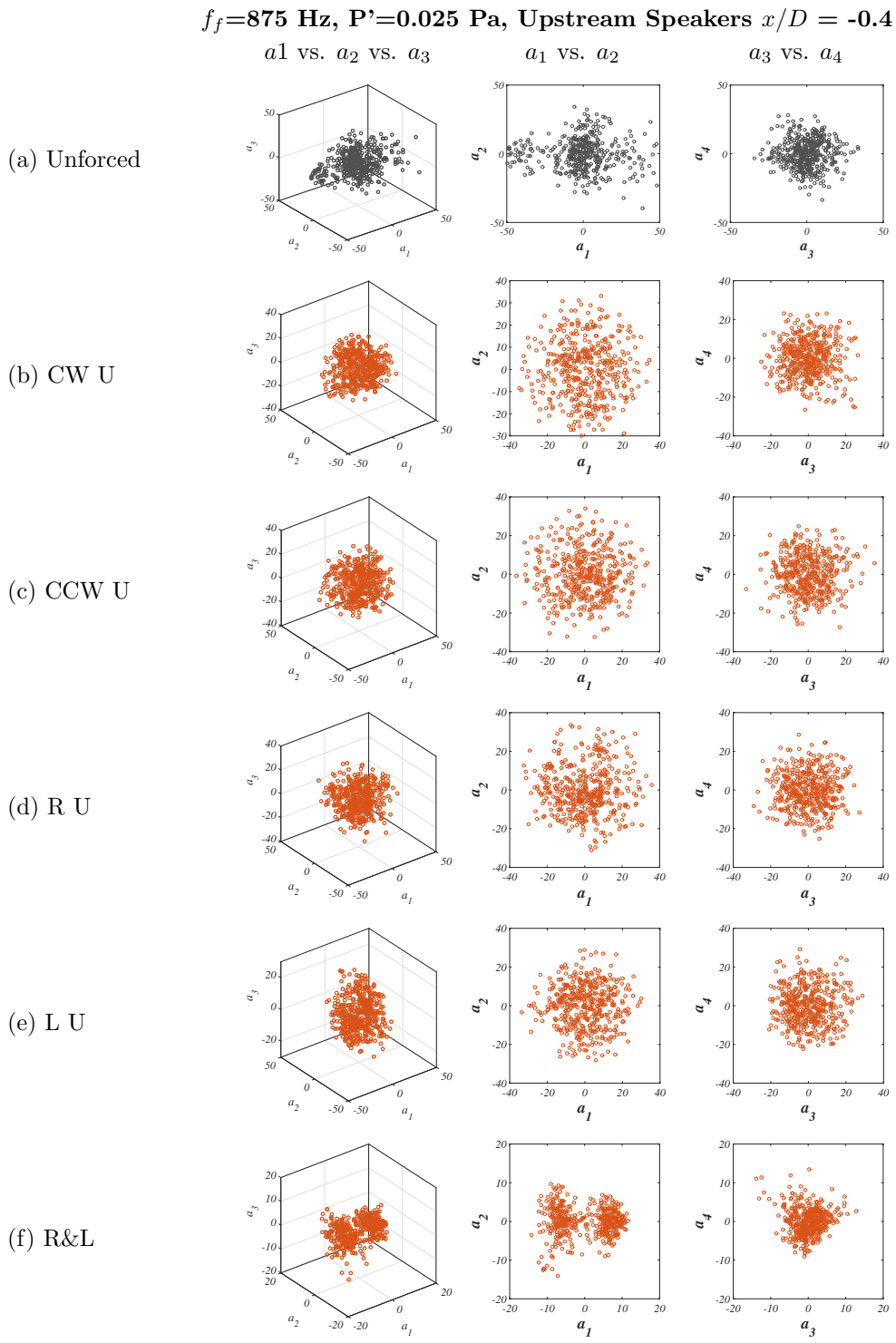

Figure E.29: PIV POD coefficients for the first 4 modes plotted against each other, extracted from instantaneous cross-sectional plane images of the $J = 41$ JICF, for the (a) unforced, and (b-f) subject to upstream speaker excitation in the x/D = -0.4 plane where $f_f = 875$ Hz. Black symbols represent the unforced condition, orange symbols represent the jet subject to asymmetric forcing.

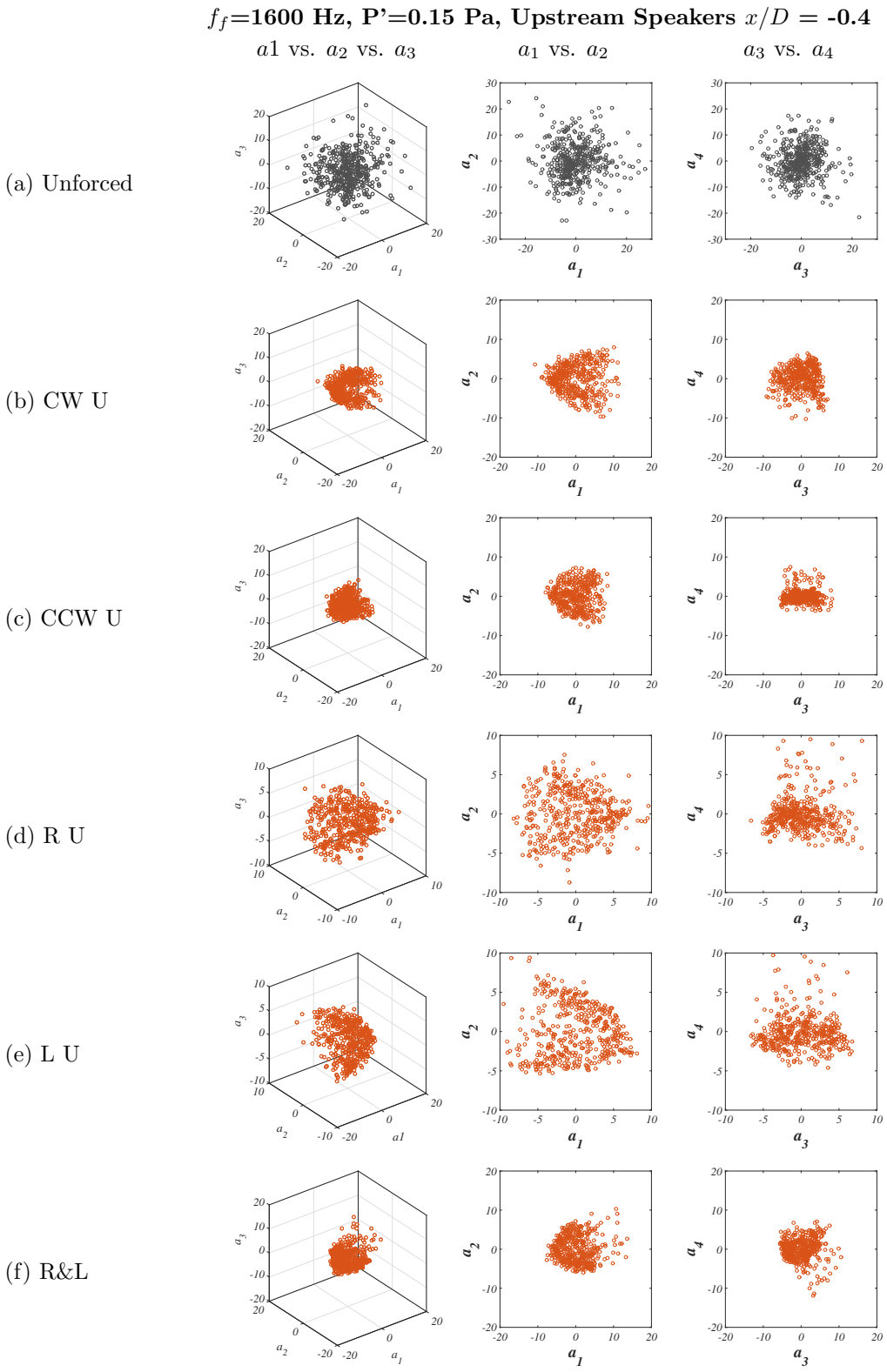

Figure E.30: PLIF POD coefficients for the first 4 modes plotted against each other, extracted from instantaneous cross-sectional plane images of the $J = 41$ JICF, for the (a) unforced, and (b-f) subject to upstream speaker excitation in the x/D = -0.4 plane where $f_f = 1600$ Hz. Black symbols represent the unforced condition, orange symbols represent the jet subject to asymmetric forcing.

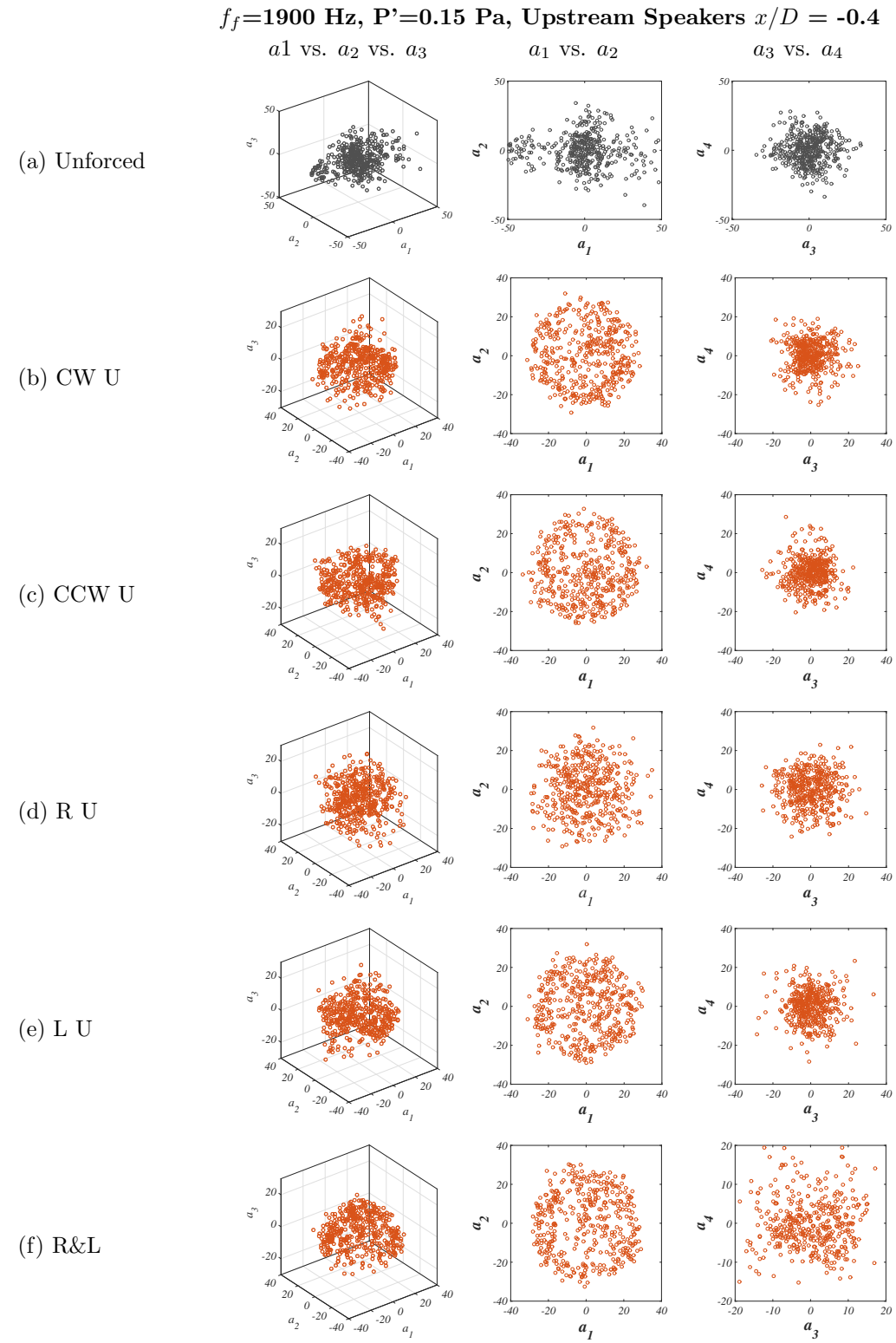

Figure E.31: PIV POD coefficients for the first 4 modes plotted against each other, extracted from instantaneous cross-sectional plane images of the $J = 41$ JICF, for the (a) unforced, and (b-f) subject to upstream speaker excitation in the x/D = -0.4 plane where $f_f = 1900$ Hz. Black symbols represent the unforced condition, orange symbols represent the jet subject to asymmetric forcing.

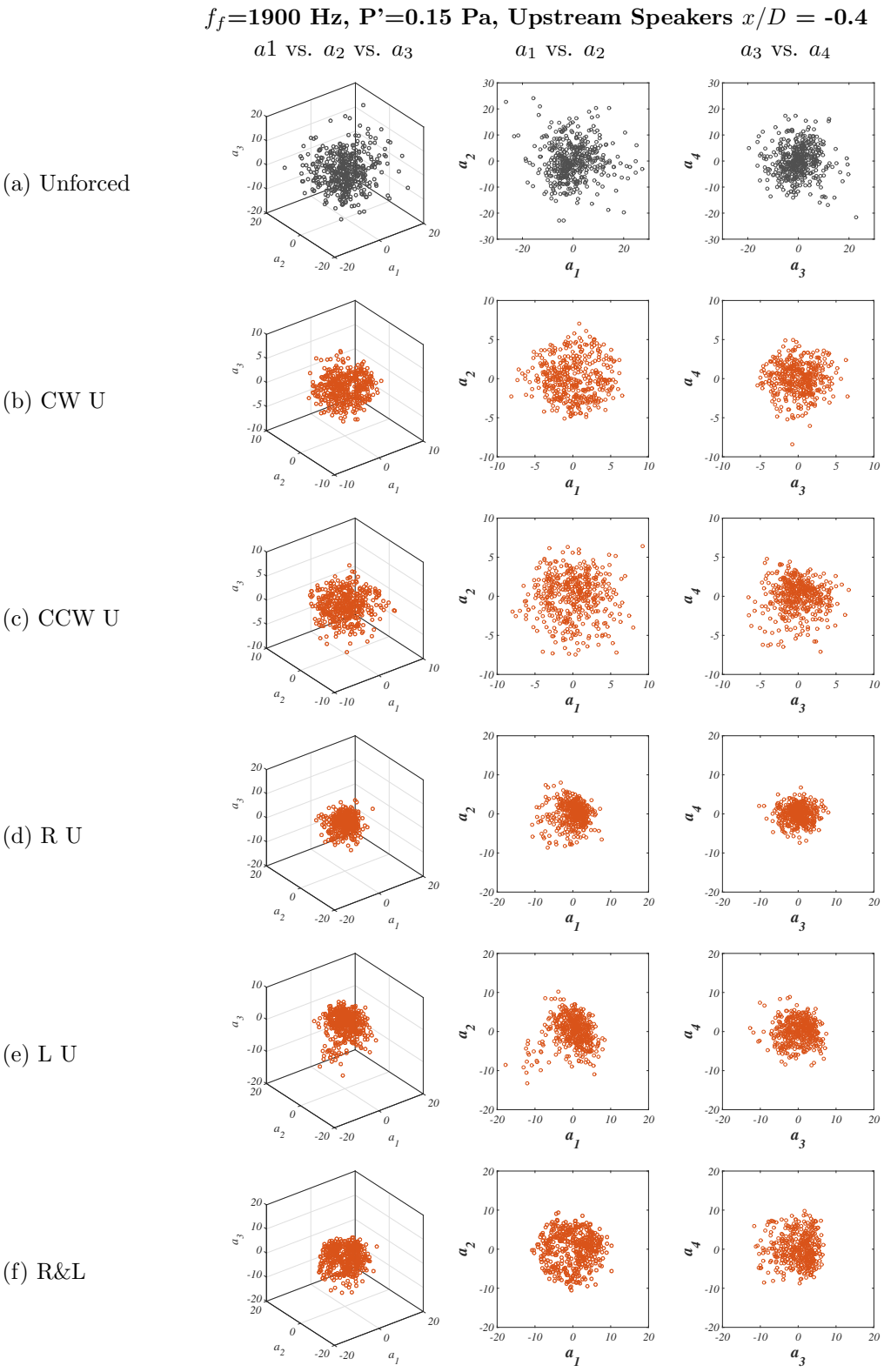

Figure E.32: PLIF POD coefficients for the first 4 modes plotted against each other, extracted from instantaneous cross-sectional plane images of the $J = 41$ JICF, for the (a) unforced, and (b-f) subject to upstream speaker excitation in the x/D = -0.4 plane where $f_f = 1900$ Hz. Black symbols represent the unforced condition, orange symbols represent the jet subject to asymmetric forcing.

E.7 Strain Rate and Scalar Dissipation Rate

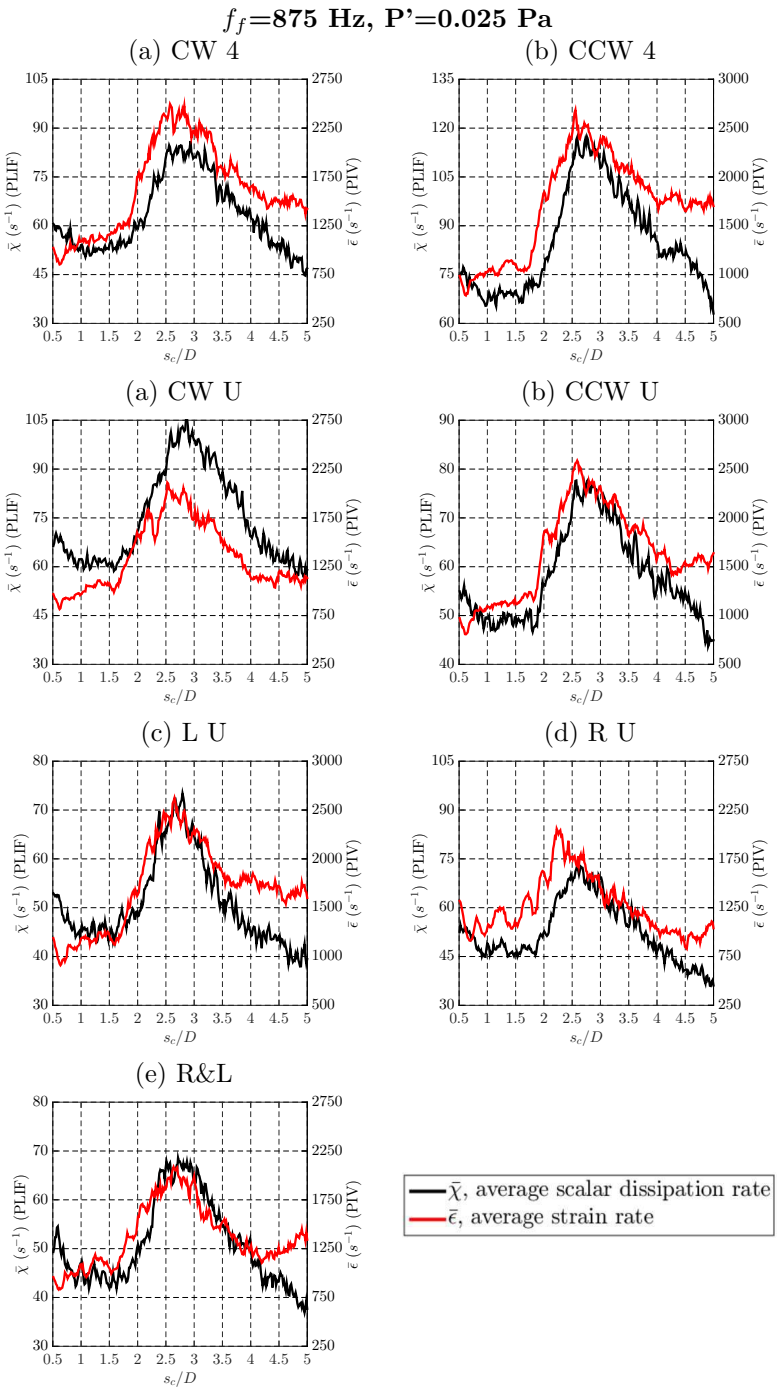

Figure E.33: Upstream mixing layer average maximum scalar dissipation rate, $\bar{\chi}$ and average strain rate normal to the scalar gradient direction, $\bar{\epsilon}$ for the $J = 41$ JICF subject to asymmetric forcing in the upstream region with $f_f = 875$ Hz and amplitude P'= 0.025 Pa. Data points with extensive strain in the scalar gradient direction are removed from the averaging process.

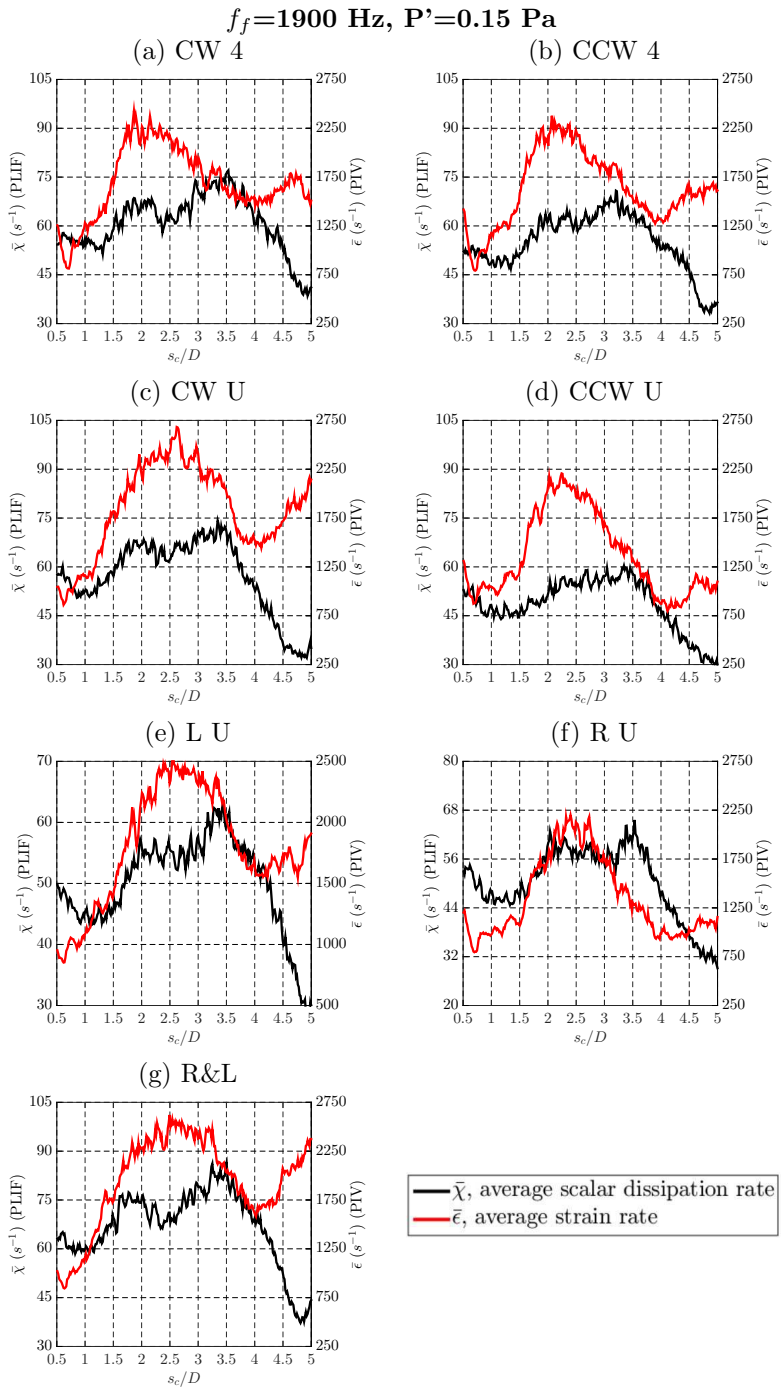

Figure E.34: Upstream mixing layer average maximum scalar dissipation rate, $\bar{\chi}$ and average strain rate normal to the scalar gradient direction, $\bar{\epsilon}$ for the $J = 41$ JICF subject to asymmetric forcing in the upstream region with $f_f = 1900$ Hz and amplitude P'= 0.15 Pa. Data points with extensive strain in the scalar gradient direction are removed from the averaging process.

BIBLIOGRAPHY

R. J Adrian and J. Westerweel. *Particle Image Velocimetry*. Cambridge University Press, New York, NY, 2011.

Leonardo S. De B. Alves, Robert E. Kelly, and Ann R. Karagozian. Local stability analysis of an inviscid transverse jet. *Journal of Fluid Mechanics*, 581:401–418, 2007.

Leonardo S. De B. Alves, Robert Kelly, and Ann R. Karagozian. Transverse-jet shear-layer instabilites. part 2. linear analysis for large jet-to-crossflow velocity ratio. *Journal of Fluid Mechanics*, 602:383–401, 2008.

H. Aref, M. Gharib, and C. W. Van Atta. Chaos in shear flows. In AIAA, editor, *AIAA 19th Fluid Dynamics, Plasma Dynamics and Lasers Conference*, number AIAA-87-1251, 1987.

D. G. Aronson, G. B. Ermentrout, and N. Kopell. Amplidute response of coupled oscillators. *Physica D*, 41(3):403–449, 1990.

C. W. Van Atta and M. Gharib. Ordered and chaotic vortex streets behind circular cylinders a low reynolds numbers. *Journal of Fluid Mechanics*, 174:113–133, 1987.

A. Balanov, N. Janson, D. Postnov, and O. Sosnovtseva. *Synchronization: From Simple to Complex*, chapter 1:1 Forced Synchonization of Periodic Oscillations, pages 21–73; 191–238. Springer, 2009.

S. Balusamy, L. K. B. Li, Z. Han, M. Juniper, and S. Hochgreb. Nonlinear dynamics of a self-excited thermoacoustic system subjected to acostic forcing. *Proceedings of the Combustion Institute*, 35:3229–3236, 2015.

G. Batchelor and A. Gill. Analysis of the stability of axisymmetric jets. *Journal of Fluid Mechanics*, 14(4):529–551, 1962.

G. Berkooz, P. Holmes, and J. L. Lumley. The proper orthogonal decompositin in the analysis of turbulent flows. *Annu. Rev. Fluid Mech.*, 25:539–575, 1996.

G. Bidan, C. Vezier, and D. Nikitopoulos. Study of unforced and modulated film-cooling jets using proper orthogoal decomposition- part 2: Forced jets. *Journal of Turbomachinery*, 135, 2013. doi: DOI: 10.1115/1.4006600.

Eric S. Bish and Merner J. A. Dahm. Strained dissipation and reaction layer analyses of nonequilibrium chemistry in turbulent reacting flows. *Combustion and Flame*, 100:457–464, 1995.

Marco Bonetti and Jean-Pierre Boon. Chaotic dynamics in open flow: The excited jet. *Physical Review A*, 40(6):3322–3346, 1989.

J. E. Broadwell and R. E. Breidenthal. Structure and mixing of a transverse jet in incompressible flow. *Journal of Fluid Mechanics*, 148:405–412, 1984.

John P. O'Connell Bruce E. Poling, John M. Prausnitz. *The Properties of Gases and Liquids*. McGraw-Hill, fifth edition, 2001.

J. Cohen and I. Wygnanski. The evolution of instabilites in the axisymmetric jet. part 1. the linear growth of distrubances near the nozzle. *Journal of Fluid Mechanics*, 176:191–219, 1987.

J. Cohen and I. Wygnaski. The evolution of instabilities in the axisymmetric jet. part 2. the flow resulting from the interaction between two waves. *Journal of Fluid Mechanics*, 176: 221–235, 1987.

T. C. Corke and S. M. Kusek. Resonance in axisymmetric jets with controlled helical-mode input. *Journal of Fluid Mechanics*, 249:307–336, 1993.

L. Cortelezzi and A. R. Karagozian. On the formation of the counter-rotating vortex pair in transverse jets. *Journal of Fluid Mechanics*, 446:347–373, 2001.

P. V. Danckwerts. The definition and measurement of some characteristics of mixtures. *Applied Scientific Research, Section A*, 3(4):279–296, 1952.

J. Davitian, D. Getsinger, C. Hendrickson, and A. R. Kargozian. Transition to global instability in transverse-jet shear layers. *Journal of Fluid Mechanics*, 661:294–315, 2010a.

J. Davitian, C. Hendrickson, D. Getsinger, and A. R. Karagozian. Strategic control of transverse jet shear layer instabilites. *AIAA Journal*, 49(9):2145–2156, 2010b.

Paul E. Dimotakis and Paul L. Miller. Some consequences of the boundedness of scalar fluctuations. *Physics of Fluids A*, 2(11):1919–1920, 1990.

Adnan Eroglu and Robert E. Breidenthal. Structure, penetration, and mixing of pulsed jets in crossflow. *AIAA Journal*, 39(3):417–423, 2001.

T. F. Fric and A. Roshko. Vortical structure in the wake of a transverse jet. *Journal of Fluid Mechanics*, 279:1–47, 1994.

Francois Gallaire and Jean-Marc Chomaz. Mode selection in swirling jet experiments: a linear stability analysis. *Journal of Fluid Mechanics*, 494:223–253, 2004.

D. R. Getsinger, L. Gevorkyan, O. I. Smith, and A. R. Karagozian. Structural and stability characteristics of jets in crossflow. *Journal of Fluid Mechanics*, 760:342–367, 2014.

Daniel Getsinger. *Shear Layer Instabilities and Mixing in Variable Density Transverse Jet Flows*. PhD thesis, University of California, Los Angeles, 2012.

Daniel R. Getsinger, Cory Hendrickson, and Ann R. Karagozian. Shear layer instabilites in low-density transverse jets. *Experiments in Fluids*, 53(3):783–801, 2012.

L. Gevorkyan, T. Shoji, W. Y. Peng, and A. R. Karagozian. Influence of the velocity field on scalar transport in gaseous transverse jets. *Journal of Fluid Mechanics*, 834:173–219, 2018.

Levon Gevorkyan. *Structure and Mixing Characterization of Variable Density Transverse Jet Flows*. PhD thesis, University of California, Los Angeles, 2015.

Levon Gevorkyan, Takeshi Shoji, Daniel Getsinger, O.I. Smith, and A. R. Karagozian. Transverse jet mixing characteristics. *Journal of Fluid Mechanics*, 790:237–274, 2016.

C. Grebogi, E. Ott, S. Pelikan, and J. A. Yorke. Strange attractors that are not chaotic. *Phys. D Nonlinear Phenom*, 13:261–268, 1984.

A. Gross and H. F. Fasel. Control-oriented proper orthogonal decomposition models for unsteady flows. *AIAA Journal*, 45(4):814–827, 2007. doi: 10.2514/1.22774 Controller.

Y. Guan, M. Murugesan, and L. K. B. Li. Strange nonchaotic and chaotic attractors in a self-excited thermoacoustic oscillator subjected to external periodic forcing. *Chaos*, 28, September 2018. doi: 10.1063/1.5026252.

Oleg Gubanov and Luca Cortelezzi. Towards the design of an optimal mixer. *Journal of Fluid Mechanics*, 651:27–53, 2010.

R. Gurka, A. Liberzon, and G. Hetsroni. Pod of vorticity fields: A method for spatial characterization of coherent structures. *International Journal of Heat and Fluid Flow*, 27: 416–423, 2006. doi: 10.1016/j.ijheatfluidflow.2006.01.0.

Ismet Gursul. Effect of nonaxisymmetric forcing on a swirling jet with vortex breakdown. *Journal of Fluids Engineering*, 118:316–321, 1996.

A. M. Guzman and C. H. Amon. Transition to chaos in convergin-divergin channel flows: Ruelle-takens-newhouse scenario. *Phys Fluids*, 6(6):1994–2002, 1994.

Cory Scott Hendrickson. *Identificaiton and Control of the Jet in Crossflow*. PhD thesis, University of California, Los Angeles, 2012.

Patrick Huerre and Peter A. Monkewitz. Local and global instabilities in spatially developing flows. *Annual Review of Fluid Mechanics*, 22:473–537, 1990.

A. K. M. F. Hussain and K. B. M. Q. Zaman. The free shear layer tone phenomenon and probe interference. *Journal of Fluid Mechanics*, 87:349–383, 1978.

P. S. Iyer and K. Mahesh. A numerical study of shear layer characteristics of low-speed transverse jets. *Journal of Fluid Mechanics*, 790:275–307, 2016. doi: 10.1017/jfm.2016.7.

Hamid Johari. Scaling of fully pulsed jets in crossflwo. *AIAA Journal*, 44(11):2719–2725, 2006.

M. P. Juniper, L. K. B. Li, and J. W. Nichols. Forcing of self-excited round jet diffusion flames. *Proceedings of the Combustion Institute*, 32:1191–1198, 2009.

Yasuhiro Kamotani and Isaac Greber. Experiments on a turbulent jet in a cross flow. *AIAA Journal*, 10(11), 1972.

Ann Karagozian. Transverse jets and their control. *Progress in Energy and Combustion Science*, 36(5):531–553, 2010.

Ann R. Karagozian and Frank E. Marble. Study of a diffusion flame in a stretched vortex. *Combustion Science and Technology*, 45:65–84, 1986.

G. E. Karniadakis and G. S. Triantafyllow. Frequency selection and asymptotic states in laminar wakes. *Journal of Fluid Mechanics*, 199:441–469, 1989.

R. M. Kelso and A. J. Smits. Horsehoe vortex systems resulting from the interaction between a laminar bounday layer and a transverse jet. *Physics of Fluids*, 7(1):153–158, 1995.

R. M. Kelso, T. T. Lim, and A. E. Perry. An experimental study of round jets in cross-flow. *Journal of Fluid Mechanics*, 306:111–144, 1996.

Alena Kukukova, Joelle Aubin, and Suzanne M. Kresta. A new definition of mixing and segregations: Three dimensions of a key process variable. *Chemical Engineering Research and Design*, 87:633–647, 2009.

S. M. Kusek, T. C. Corke, and P. Reisenthel. Seeding of helical modes in the initial region of an axisymmetric jet. *Experiments in Fluids*, 10:116–124, 1990.

David M. Kuzo. *An Experimental Study of the Turbulent Transverse Jet.* PhD thesis, California Institute of Technology, 1996.

S. Lardeau, F. Tessicini, and M. Leschziner. Analysis of cyclic events in turbulent flows using recurrence plots. *Journal of Turbulence*, 11(16):1–27, 2010. doi: 10.1080/14685248.2010.485201 To.

Sidney Leibovich. Vortex stability and breakdown: Survey and extension. *AIAA Journal*, 22(9):1192–1206, 1983.

L. K. B Li and M. P. Juniper. Phase trapping and slipping in a forced hydronamically self-excited jet. *Journal of Fluid Mechanics Rapids*, 735(R5), 2013a.

Larry K. B. Li and Matthew P. Juniper. Lock-in and quasiperiodicity in hydrodynamically self-excited flames:. In *Proceedings of the Combustion Institute*, volume 34, pages 947–954, 2013b.

Larry K. B. Li and Matthew P. Juniper. Lock-in and quasiperiodicity in a forced hydrodynamically self-excited jet. *Journal of Fluid Mechanics*, 726:624–655, 2013c.

E. N. Lorenz. Deterministic nonperiodic flow. *Journal of the Atmospheric Sciences*, 20, March 1963.

A. Lozano, B. Yip, and R.K. Hanson. Acetone: a tracer for concentration measurements in gaseous flows by planar laser-induced flourescence. *Experiments in Fluids*, 13:369–376, 1992.

Antonio Lozano. *Laser-excited lulminescent tracers for planar concentration measurements in gaseous jets.* PhD thesis, Stanford University, 1992.

Richard J. Margason. Fifty years of jet in crossflow research. In *AGARD-CP-534*, volume 1, pages 1–141, 1993.

George Mathew, Igor Mezic, and Linda Petzold. A multiscale measure for mixing. *Physica D*, 211:23–46, 2005.

G. E. Mattingly and C. C. Chang. Unstable waves on an axisymmetric jet column. *Journal of Fluid Mechanics*, 65(3):541–560, 1974.

R.T. M'Closkey, J. M. King, L. Cortelezzi, and A.R. Karagozian. The activley controlled jet in crossflow. *Journal of Fluid Mechanics*, 452:325–335, 2002.

S. Megerian, J. Davitian, L.S. de B. Alves, and A. R. Karagozian. Transverse-jet shear-layer instabilities. part 1. experimental studies. *Journal of Fluid Mechanics*, 593:93–129, 2007.

John Miles. Strange attractors in fluid dynamics. *Advances in Applied Mechanics*, 24:189–214, 1984.

Z. M. Moussa, John W. Trischka, and S. Eskinazi. The near field in the mixing of a round jet with a cross-stream. *Journal of Fluid Mechanics*, 80(1):49–80, 1977.

Frank Muldoon and Sumanta Acharya. Direct numerical simulation of pulsed jets-in-crosslfow. *Computers and Fluids*, 39:1745–1773, 2010.

S. Narayanan, P. Barooah, and J. M. Cohen. Dynamics and control of an isolated jet in crossflow. *AIAA Journal*, 41(12):2316–2330, 2003.

S. Newhouse, D. Ruelle, and F. Takens. Occurence of strange axiom attractors near quasi periodic flows. *Communications in Mathematical Physics*, 64:35–40, 1978.

Peter Plaschko. Helical instabilites of slowly divergent jets. *Journal of Fluid Mechanics*, 92 (2):209–215, 1979.

H. Poincare. Memoire sur les courbes definies par une equation differentielle. *J. de Math*, 7: 375–442, 1881.

M. A. Regan and K. Mahesh. Stability and sensitivity analysis of a low-speed jet in cross-flow. In *AIAA SciTech Forum*, 2019.

Marc Allen Regan. *Linear Stability and Sensitivity of a Low-speed Jet in Cross-flow*. PhD thesis, University of Minnesota, 2018.

D. Ruelle. Strange attractors. *The Mathematical Intelligencer*, 2:126–137, 1980.

D. Ruelle and F. Takens. On the nature of turbulence. *Comm. Math. Phys.*, 20, 1971.

Jerry W. Shan and Paul E. Dimotakis. Reynolds-number effects and anisotropy in transverse-jet mixing. *Journal of Fluid Mechanics*, 566:47–96, 2006.

S.R. Shapiro, J.M. King, R.T. M'Closkey, and A.R. Karagozian. Optimization of controlled jets in crossflow. *AIAA Journal*, 44(6):1292–1298, 2006.

T. Shoji, E. W. Harris, A. Besnard, and A. R. Karagozian. Effects of sinusiodal excitation on transverse jet structure and mixing, in preparation for journal submission. 2019a.

T. Shoji, E. W. Harris, A. Besnard, S. G. Schein, and A. R. Karagozian. Transverse jet lock-in and quasi-periodicity, in preparation for journal submission. 2019b.

Takeshi Shoji. *Mixing and Structural Characteristics of Unforced and Forced Jets in Cross-flow*. PhD thesis, University of California, Los Angeles, 2017.

Takeshi Shoji, Andrea Besnard, Elijah W. Harris, Robert T. M'Closkey, and Ann R. Karagozian. Effects of axisymmetric square-wave excitation on tranverse jet structure and mixing. *AIAA Journal*, 2019c. doi: DOI: 10.2514/1.J057982.

L. Sirovich. Turbulence and the dynamics of coherent sructures. part 1: Coherent structures. *Quarterly of Applied Mathematics*, 45(3):561–571, 1987.

Julius O. Smith. *Physical Audio Signal Processing*. W3K Publishing, 2010.

L. L. Smith, A. J. Majamaki, I. T. Lam, O. Delabroy, A. R. Karagozian, and F. E. Marble. Mixing enhancement in a lobed injector. *Physics of Fluids*, 9(3):667–768, 1997.

S. H. Smith and M. G. Mungal. Mixing, structure and scaling of the jet in crossflow. *Journal of Fluid Mechanics*, 357:83–122, 1998.

K. R. Sreenivasan, S. Raghu, and D. Kyle. Absolute instability in variable density round jets. *Experiments in Fluids*, 7:309–317, 1989.

P. J. R. Strange and D. G. Crighton. Spinning modes on axisymmetric jets. part 1. *Journal of Fluid Mechanics*, 134:231–245, 1983.

S. H. Strogatz. *Nonlinear Dynamics and Chaos*, pages 317–335. Perseus Books, 1994.

L. K. Su and N. T. Clemens. Planar measurements of the full three-dimensional scalar dissipaton rate in pas-phase turbulent flows. *Experiments in Fluids*, 27:507–521, 1999.

J Terry and G. Caras. Transpiratin and film cooling of liquid rocket nozzles. techreport RSIC-535, U.S. Army Missle Command, Redstone Scientific Information Center, Redstone Arsenal, AL, March 1966.

P.J Vermeulen, P. Grabinski, and V. Ramesh. Mixing of an actoustically excited air jet with a confined hot crossflow. *Journal of Engineering for Gas Turbines and Power*, 114:46–54, 1992.

R. Vernet, L. Thomas, and L. David. Analysis and reconstruction of a pulsed jet in crossflow by mulit-plane snapshot p.o.d. *Exp. Fluids*, 47:707–720, 2009. doi: 10.1007/s00348-009-0730-6.

J. Westerweel. Fundamentals of digital particle image velocimetry. *Measurement Science and Technology*, 8:1379–1392, 1997.

K. Williams-Stuber and M. Gharib. Transition from order to chaos in the wake of an airfoil. *Journal of Fluid Mechanics*, 213:29–57, 1990.

A. Wolf, J. B Swift, H. L. Swinney, and J. A. Vastano. Determining lyapunov exponents from a time series. *Physica*, 16D(285), 1985.

L. L. Yuan and R. L. Street. Trajectory and entrainment of a round jet in crossflow. *Physics of Fluids*, 10(9):2323–2335, 1998.